A Spectral Element Model for Ground Source Heat Pump Systems
Forward and Inverse Calculations

BniLam, Noori

DOI
10.4233/uuid:25e21d82-f203-4989-8eca-8508889def1f

Publication date
2020

Document Version
Final published version

Citation (APA)
BniLam, N. (2020). *A Spectral Element Model for Ground Source Heat Pump Systems: Forward and Inverse Calculations*. [Dissertation (TU Delft), Delft University of Technology]. https://doi.org/10.4233/uuid:25e21d82-f203-4989-8eca-8508889def1f

A Spectral Element Model for Ground Source Heat Pump Systems

Forward and Inverse Calculations

Noori Hussein Noori Bni Lam

ISBN 978-94-6384-110-8

Cover design: Saskia Bni Lam
Layout: Noori Bni Lam
Printed by: Gildeprint – The Netherlands

A Spectral Element Model for Ground Source Heat Pump Systems

Forward and Inverse Calculations

Proefschrift

ter verkrijging van de graad van doctor
aan de Technische Universiteit Delft,
op gezag van de Rector Magnificus Prof. dr.ir. T.H.J.J. van der Hagen;
voorzitter van het College voor Promoties,
in het openbaar te verdedigen op
woensdag 26 februari 2020 om 15:00 uur

door

Noori Hussein Noori Bni Lam

Master of Science in Electronics and Communication Engineering,
Baghdad University
geboren te Baghdad, Iraq

Dit proefschrift is goedgekeurd door de

promotor: Prof.dr.ir. L.J. Sluys
copromotor: Dr.ir. R.I.N. Al-Khoury

Samenstelling promotiecom

Rector Magnificus,	voorzitter
Prof.dr.ir. L.J. Sluys,	Technische Universiteit Delft, promotor
Dr.ir. R.I.N. Al-Khoury,	Technische Universiteit Delft, copromotor

Onafhankelijke leden:

Dr. H.J.L. Witte,	Groenholland, Netherlands
Prof.dr. D. Potts,	Imperial college London, UK
Prof.dr. L. Lamarche,	École de technologie supérieure, Montréal, Canada
Prof.dr. I. Berre,	University of Bergen, Norway
Prof.dr. M.A. Hicks,	Technische Universiteit Delft
Prof.dr. A. Metrikine	Technische Universiteit Delft, reserve lid

TU Delft Delft University of Technology

Summary

The ground source heat pump (GSHP) system is a well-established technology that utilizes a renewable energy source for heating and cooling of buildings. This technology is attractive because it relies on energy gain from shallow depths which are available nearly everywhere. Furthermore, it produces minimal CO_2 emissions into the atmosphere. Accordingly, this technology is thriving, and currently adopted in many countries all over the world. Nevertheless, due to the lack of accurate and efficient computational models, the design of GSHP systems is not yet optimal and requires further development, which constitutes the main goal of this thesis.

Over the years, several computational models have been developed to simulate the heat flow in GSHP systems. These models vary from detailed numerical 3D analyses to analytical solutions. Due to the peculiarity of the involved geometry, which constitutes highly slender borehole heat exchangers embedded in a vast soil mass, and the convection heat flow mechanism, the numerical models require extensive memory and CPU time. The analytical models, on the other hand, are computationally efficient, but their accuracy suffers from the over-simplified description of geometry and initial and boundary conditions. This thesis aims to bridge the gap between the numerical models in their generality, and the analytical models in their computational efficiency.

This thesis introduces a comprehensive and computationally efficient semi-analytical model based on the spectral element method and the superposition principle. The spectral element method is an elegant semi-analytical (semi-numerical) technique for solving linear partial differential equations based on the eigenfunction expansion and the fast Fourier transform. It requires one element to describe a homogeneous medium (single layer domain), and elements equal in number to the number of the layers to describe a nonhomogeneous medium (multilayers domain). The spectral element method is utilized to simulate heat flow in multilayer systems, and the superposition principle is utilized to simulate multiple borehole heat exchangers and their thermal interaction. Accordingly, the model can simulate heat flow in effectively 3D GSHP systems constituting multiple borehole heat exchangers embedded in multilayer soil mass using minimal memory and CPU time. In this thesis, both forward and inverse models are formulated, implement and tested against experimental and numerical results.

The forward model has the following features:

a) It can simulate heat flow in GSHP system constituting a single borehole heat exchanger embedded in a multilayer soil mass. The spectral element method is utilized for this purpose. The computational model describing this feature is presented in Chapter 2.

b) It can simulate any arbitrarily configured borehole heat exchangers and their thermal interaction. The superposition principle is utilized for this purpose. The computational model describing this feature is presented in Chapter 3.

c) Based on the above two computational models, the forward model is made to simulate heat flow in effectively 3D GSHP systems. The spectral element method and the superposition principle are coupled for this purpose. The computational model describing this feature is presented in Chapter 4.

d) The model can provide results from seconds to years simultaneously in a single run. The calculation can be conducted using prescribed heat flux derived from the heat pump power. The computational model describing this feature is presented in Chapter 5.

e) It can simulate the effect of friction heat gain in GSHP systems due to fluid flow in pipes. The computational model describing this feature is presented in Chapter 6.

The inverse model, on the other hand, is formulated based on the forward model and an iterative optimization algorithm. It has the following features:

a) It can estimate effective and detailed thermal parameters of GSHP systems

b) It can handle multilayer systems.

c) It can handle fluctuating heat pump power.

d) It can interpret data obtained from multiple heat extraction or injection pulses.

e) It can interpret data obtained at any spatial point in the GSHP system, including the surrounding soil mass.

f) It can produce accurate backcalculation for short and long duration experiments.

g) It is accurate, computationally efficient, stable and has a high convergence rate.

The inverse model is presented in Chapter 7.

Chapter 1 gives a brief introduction on the GSHP technology and the delineation of this thesis, and Chapter 8 gives conclusions and outlook.

Samenvatting

Het ondergrondse warmtepomp systeem (GSHP systeem, oftewel de aardwarmtepomp) is een sterk theoretisch gefundeerde technologie waarbij een duurzame energiebron wordt gebruikt voor het verwarmen en koelen van gebouwen. Deze technologie is aantrekkelijk, omdat hij afhankelijk is van energiewinning uit de ondiepe ondergrond die vrijwel overal bereikbaar is. Bovendien is er sprake van een minimale CO_2 uitstoot de dampkring in. Daarom floreert deze technologie en wordt deze momenteel in veel landen over de hele wereld toegepast. Toch is het ontwerp van GSHP systemen nog niet optimaal door een gebrek aan nauwkeurige en efficiënte computersimulatiemodellen. Er is verdere ontwikkeling nodig, wat het algemene doel is van dit proefschrift.

Door de jaren heen zijn er verschillende computersimulatiemodellen ontwikkeld om de warmtestroom in GSHP systemen te simuleren. Deze modellen variëren van gedetailleerde numerieke 3D technieken tot analytische oplossingen. Door de bijzondere bijbehorende geometrie, van bijzonder hoge maar smalle boorgat hitte uitwisselaars (borehole heat exchangers, BHE) die verankerd zijn in grootschalige aardmassa en door de convectiestromen, hebben de numerieke modellen bijzonder veel geheugen en CPU-tijd nodig. Aan de andere kant zijn de analytische modellen numeriek veel efficienter, maar lijdt hierbij de nauwkeurigheid onder de over-gesimplificeerde geometrie en begin- en randvoorwaarden. Het doel van dit proefschrift is om het gat te overbruggen tussen de algemeenheid van de numerieke modellen, en de numerieke efficiëntie van de analytische modellen.

Dit proefschrift introduceert een uitgebreid en numeriek efficient semi-analytisch model, dat gebaseerd is op de spectrale elementenmethode en het superpositie principe. De spectrale elementenmethode is een elegante semi-analytische (semi-numerieke) techniek voor het oplossen van lineaire partiële differentiaalvergelijkingen, gebaseerd op de methode van eigenfunctie-expansie en de snelle Fourier-transformatie. Het vereist één element om een homogeen medium te beschrijven (een enkellaags domein), en een gelijk aantal elementen aan het aantal media om een niet-homogeen medium te beschrijven (meerlaagse domeinen). De spectrale elementenmethode is gebruikt om de warmtestromen in meerlaagse systemen te simuleren, en het superpositie principe is gebruik om meerdere BHE's en hun thermische interactie te simuleren. Derhalve kan het model warmtestromen simuleren in effectief 3D GSHP systemen, bestaande uit meerdere BHE's welke zich bevinden in meerlaagse aardmassa, waarbij minimaal geheugen en CPU-tijd wordt vereist. In dit proefschrift formuleren we zowel voorwaartse als achterwaartse modellen, welke ook zijn geimplementeerd en getest met experimentele en numerieke data.

Het voorwaartse model heeft de volgende eigenschappen:

a) Het kan warmtestromen simuleren in GSHP systemen bestaande uit een enkele BHE die zich bevindt in meerlaagse aardmassa. Hiervoor is de spectrale elementenmethode gebruikt. Het numerieke model dat deze functie beschrijft is toegelicht in hoofdstuk 2.

b) Het kan willekeurige opgestelde BHE's en hun thermische interactie simuleren. Hiervoor is het superpositie principe gebruikt. Het numerieke model dat deze functie beschrijft is toegelicht in hoofdstuk 3.

c) Op basis van bovenstaande twee eigenschappen kan het voorwaartse model warmtestromen simuleren in effectief 3D GSHP systemen. Hiervoor zijn de spectrale elementenmethode en het superpositie principe gebruikt. Het numerieke model dat deze functie beschrijft is toegelicht in hoofdstuk 4.

d) Het model kan resultaten in seconden en jaren combineren in één enkele berekening. Deze berekening kan worden uitgevoerd gebruikmakend van voorgeschreven warmtestroomdichtheid, welke is afgeleid van het vermogen van de warmtepomp. Het numerieke model dat deze functie beschrijft is toegelicht in hoofdstuk 5.

e) Het kan de effecten simuleren van warmtetoename door wrijvingswarmte resulterend uit de stroming van vloeistoffen door de pijpen. Het numerieke model dat deze functie beschrijft is toegelicht in hoofdstuk 6.

Het achterwaartse model is gebaseerd op het voorwaartse model en iteratieve optimisatie algoritmes. Het heeft de volgende eigenschappen:

a) Het kan effectief en gedetailleerd thermische parameters van GSHP systemen bepalen

b) Het kan omgaan met meerlaagse systemen

c) Het kan omgaan met fluctuerend vermogen van warmtepompen

d) Het kan data interpreteren vanuit meerdere warmte extractie- of injectiepulsen

e) Het kan data interpreteren afkomstig uit elk ruimtelijk punt in het GSHP systeem, inclusief de omringende aardmassa.

f) Het kan accurate projectie produceren voor experimenten van zowel korte als lange duur

g) Het is nauwkeurig, numeriek efficient, stabiel en heeft een hoge convergentiewaarde

Het achterwaartse model is gepresenteerd in hoofdstuk 7.

Hoofdstuk 1 omvat een beknopte introductie in GSHP technologie en de afbakening van dit proefschrift, en hoofdstuk 8 omvat de conclusie en aanbevelingen.

Contents

1

Introduction

The ground source heat pump (GSHP) system is a well-established technology that utilizes the vastly available shallow geothermal energy for heating and cooling of buildings. The GSHP systems have many advantages, including low CO2 emissions, long lifetime (typically up to tens of years) and low costs for operation and maintenance. Even though the GSHP industry is relatively matured and efficient in extracting the shallow geothermal energy, accurate and efficient computational modelling of GSHP systems is still lagging. The design of this system is not yet optimal and requires further development. Developing a comprehensive and computationally efficient model that overcomes the current computational shortcomings constitutes the main objective of this thesis.

1.1 Objectives

The main objective of this thesis is to develop a detailed and accurate semi-analytical model for transient heat flow in ground source heat pump (GSHP) systems that is suitable for engineering practice. The model is comprehensive in describing the physics of the problem and efficient in its computations. It can simulate heat flow in an effectively 3D GSHP system constituting multiple borehole heat exchangers embedded in multilayer soil mass, and subjected to varying temperatures or heat pump power signals. The model possesses the exactness and computational efficiency of the analytical models, and (to a great extent) also the generality of numerical techniques in describing the geometry as well as initial and boundary conditions. As a consequence, the model is suitable for forward and inverse calculations. The forward calculation is appropriate for GSHP heat flow analysis and system design. The inverse calculation, on the other hand, is appropriate for GSHP thermal parameters identification.

1.2 Ground Source Heat Pumps (GSHP)

According to the Energy department of the European Commission, heating and cooling consumes around half of the EU's energy and much of it is wasted (European Commission 2016). The major share of heating and cooling is still generated from fossil fuels (mainly natural gas). Accordingly, researchers are actively investigating the deployment of different green and renewable energy sources with heat pumps for heating and cooling of buildings.

Heat pumps are mechanical systems that can extract (or reject) heat from (or to) energy sources. Different types of energy sources have been utilized with heat pumps for heating and cooling of buildings. The most known heating/cooling system is the one that extract heat from or reject heat to the ambient air using an air-source heat pump (ASHP) system. The main advantage of the ASHP system is the relatively low installation cost. Nevertheless, the ASHP system produces noise emissions and its energy efficiency is relatively low and dependent on the ambient air temperature (Rees 2016). The GSHP system, on the other hand, is a renewable energy system that employs the vastly available shallow geothermal energy for heating and cooling of buildings. It has many advantages including low in CO_2 emissions, long lifetime (typically up to tens years) and low cost for operation and maintenance. Furthermore, GSHP systems are energy efficient: for each input unit of conventional energy, a GSHP can produce on average 4 output units of renewable energy (Al-Khoury 2012b).

A GSHP system, as shown in Figure 1.1, works by circulating fluid (usually water with an antifreeze solution) through a closed loop of polyethylene U-tube pipe that is inserted in a borehole in a soil mass. The borehole is filled with grout (also referred to as backfilling) to fix the polyethylene pipe and to ensure a good thermal interaction with the soil. The circulating fluid in the U-tube collects heat from the surrounding soil mass via convection-conduction heat flow mechanism.

Over the years, several computational models have been developed to simulate the heat flow in GSHP systems. These models vary from detailed numerical 3D analyses to analytical solutions. Due to the peculiarity of the involved geometry, which constitutes highly slender borehole heat exchangers embedded in a vast nonhomogeneous soil mass, and the convection heat flow mechanism, the numerical models require extensive memory and CPU time. The analytical models, on the other hand, are computationally efficient, but their accuracy suffers from the over-simplified description of geometry and initial and boundary conditions. This thesis aims to bridge the gap between the numerical models in their generality, and the analytical models in their computational efficiency.

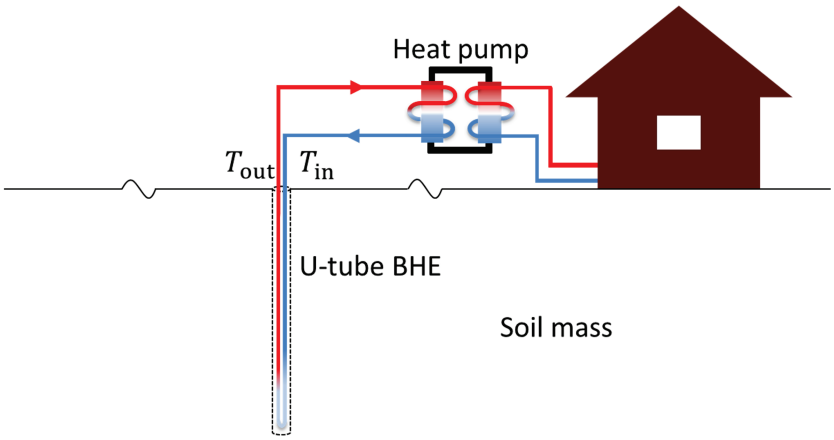

Figure 1.1: A schematic representation of a GSHP system

1.3 Modelling approach

Al-Khoury (2010, 2012a and 2012b) has formulated a computational model describing heat flow in a borehole heat exchanger (BHE) embedded in a semi-infinite homogeneous soil mass. The BHE is modelled as 1D with its axis coinciding on the vertical z-axis. The 1D assumption is valid because of the extreme slenderness of the borehole that makes the temperature gradient in the radial direction negligible. The BHE components (pipe-in, pipe-out and grout) coincide geometrically on each other, but they are thermally interacting via their surface areas. The soil mass is modelled as a semi-infinite, axial symmetric domain with its axis of symmetry coinciding with the centreline of the borehole heat exchanger (z-axis), Figure 1.2. The spectral analysis is utilized to solve the governing equations on the basis of the fast Fourier transform (FFT). The BHE heat equations are solved using the eigenfunction expansion, and the soil mass heat equation is solved using the Bessel function.

In this thesis, the spectral analysis approach of Al-Khoury has been adopted to formulate a semi-analytical model for simulating effectively 3D heat flow in GSHP systems constituting multiple borehole heat exchangers embedded in multilayer soil mass. The spectral element method is utilized to simulate heat flow in a multilayer system, and the superposition principle is utilized to simulate multiple borehole heat exchangers and their thermal interaction.

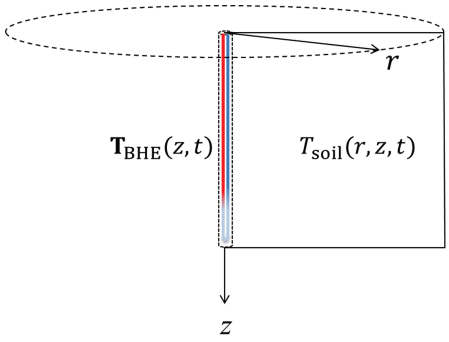

Figure 1.2: A schematic representation of an axial symmetric shallow geothermal system.

Due to the linearity of the system, the 3D geometry is decomposed into two sub-systems, Figure 1.3. Sub-system 1 represents a single BHE embedded in a multilayer system; and Sub-system 2 represents a soil mass subjected to multiple heat sources.

Sub-system 1:

This sub-system represents a BHE embedded in a multilayer domain. The heat flow is formulated based on the spectral element method (SEM) (Doyle1997). SEM is utilized to extend the spectral analysis model of Al-Khoury (Al-Khoury 2012a and 2012b) to incorporate multiple layers with different thermal properties. The spectral element method is a semi-numerical (semi-analytical) technique which combines the spectral analysis method, basically the discrete Fourier transform, with the finite element method. One of the important features of this method is that its solution to the governing partial differential equations leads to a set of algebraic equations ($\boldsymbol{Ax} = \boldsymbol{b}$), similar to those of the conventional finite element method. The fundamental difference, however, is that the spectral element stiffness matrix is exact and frequency dependent. Due to the exact formulation of the system, one element is sufficient to describe a whole homogenous domain. For a nonhomogeneous domain consisting of several layers, the number of the

spectral elements is equal to the number of the involved layers. This feature significantly reduces the size of the problem and rendering this method computationally very efficient.

Modelling heat flow in this sub-system is presented in Chapter 2.

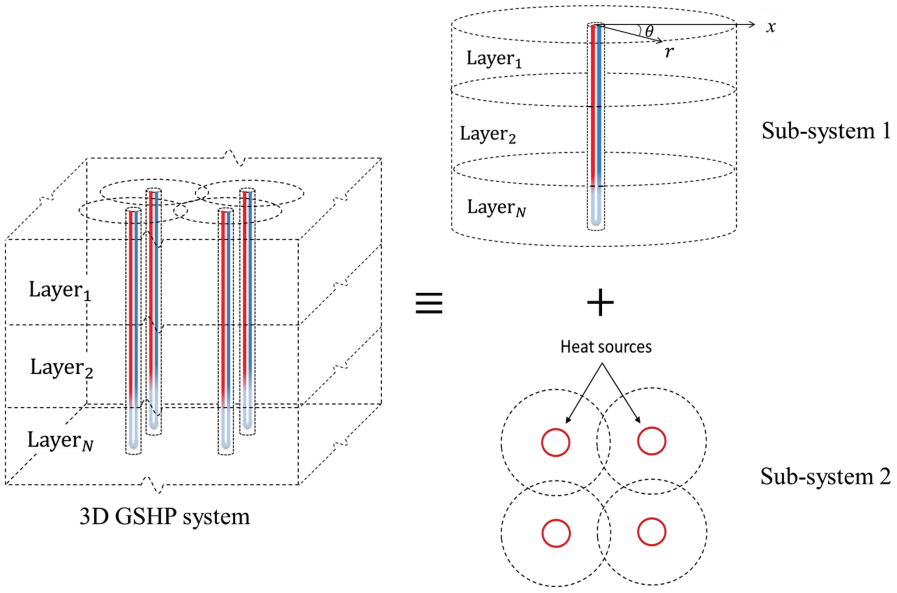

Figure 1.3: A schematic representation of the modelling approach.

Sub-system 2:

This sub-system is a manifestation of multiple borehole heat exchangers embedded in a half space. The heat flow is formulated based on the superposition principle. The superposition principle indicates that, for a linear system, the total heat flow in a medium caused by multiple heat sources is the sum of heat flow that is caused by every individual heat source. Thus, this principle is typically applicable to heat sources with Neumann boundary conditions (prescribed heat flux). For heat sources with Dirichlet boundary conditions (prescribed temperature), the superposition cannot be applied directly and requires a special treatment. In this thesis, heat sources with Dirichlet boundary conditions are coupled using a matrix technique.

Heat sources with both Neumann and Dirichlet boundary conditions are treated in Chapter 3.

3D GSHP system:

The models in Sub-system 1 and Sub-system 2 are coupled to formulate heat flow in an effectively 3D GSHP system. Details of the coupling is given in Chapter 4. The term "effectively 3D" in this thesis indicates that the geometry is basically three-dimensional constituting multiple borehole heat exchangers embedded in a multilayer soil mass. However, the layers are horizontal and go from $-\infty$ to $+\infty$. Even though heat flow in a single BHE and its surrounding soil mass is considered axial symmetric, the use of the superposition principle results into a non-symmetrical heat flow. As it will be discussed in-detail in Chapter 5, modelling a 2 x 2 BHE layout configuration (see Figure 5.6) would, upon thermal interaction, result to a non-symmetric temperature distribution in the system. Figure 1.4 shows the evolution of temperature in this system with time. It clearly shows that before thermal interaction between the boreholes takes place, the temperature is axial-symmetric, but with time, this symmetric behaviour around the borehole becomes gradually non-symmetric.

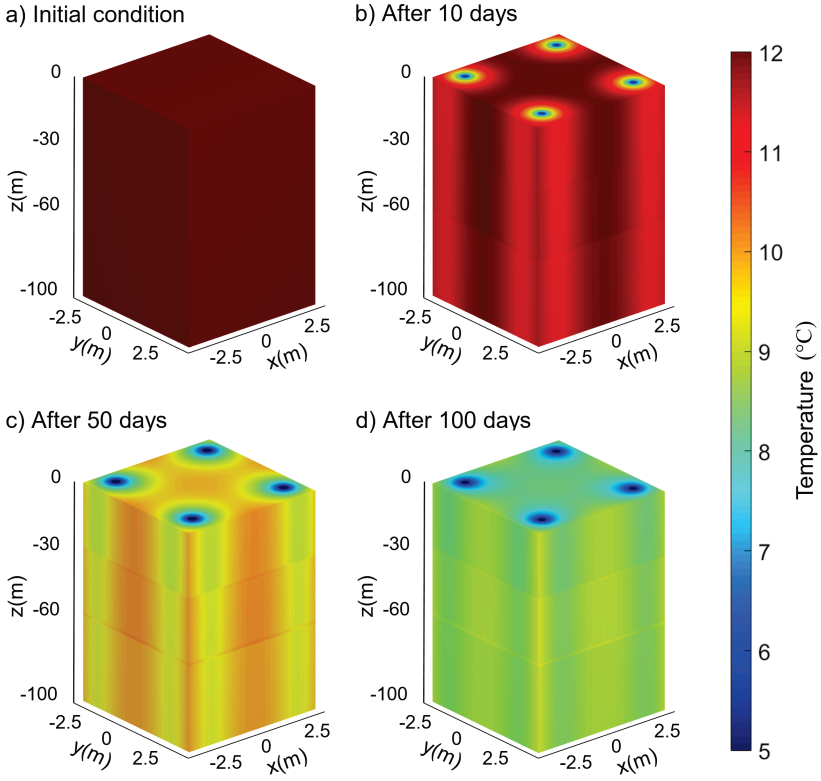

Figure 1.4: The 3D soil temperature distribution for the GSHP system presented in Figure 5.6, at different operation's time.

The key for obtaining such an exact, computationally efficient and practically general model is the unique mix between the conceptual model, the mathematical formulation and the solution technique:

1. The conceptual model includes coupling a 1D domain (representing the borehole heat exchanger) to an axial symmetric 2D domain (representing a homogeneous soil layer) and a 3D domain (representing multiple borehole heat exchangers embedded in multilayers soil mass). This coupling makes the model computationally more efficient compared to detailed numerical 3D models.
2. The mathematical formulation is designed to describe heat flow in all GSHP components, including the detailed heat equations of the individual borehole heat exchangers components and the soil mass (as well as their thermal interactions). This formulation results to a comprehensive description of the involved physical features of the system.
3. The solution technique is designed to be accurate and computationally efficient. The use of the spectral element method for modelling multilayer systems together with the superposition technique for modelling multiple borehole heat exchangers makes the solution technique fit for this problem. It enables the simulation of heat flow in effectively 3D GSHP systems subjected to any arbitrary time dependant boundary condition. It gives accurate computation of the governing equations and makes the model suitable for forward and inverse calculations.

1.4 Parameter Identification of GSHP system

Proficient design of a GSHP system depends mainly on the accuracy of the thermal and physical parameters of its components. Thermal parameters of the BHE components are usually known a priori, but thermal parameters of the soil mass are not readily known and need to be determined. Estimating the thermal parameters of the soil mass requires an innovative interplay between a forward model, to simulate heat flow in the GSHP system, and an inverse model, to estimate the thermal parameter based on the forward model and the measured data.

The measured data is usually collected using the in-situ Thermal Response Test (TRT). A typical TRT consists of a vertical borehole heat exchanger embedded in which a single U-tube. The device is equipped with thermometers to measure the fluid temperatures at the inlet and outlet of the U-tube, though modern TRT devices are equipped with fibre optics to measure the temperature along the BHE.

In this thesis, a new parameter identification (PI) algorithm capable of estimating effective and detailed thermal parameters of GSHP systems is introduced. The PI algorithm comprises an iterative scheme, coupling the proposed 3D GSHP semi-analytical forward model to an inverse model. Figure 1.5 presents schematically the iterative procedure of the proposed PI algorithm. The procedure starts with an initial guess

of the GSHP thermal parameters ($\mathbf{x}^0$, not presented in Figure 1.5), and based on the measured inlet temperature (T_{in} in Figure 1.5), temperature distributions are calculated at points of interest in the system. Then, the measured and calculated temperatures are combined to formulate the objective function of the system.

The objective function is expressed as the Euclidean distance (norm 2) between the measured, $\hat{T}_{\text{m}}(\omega_n, z)$, and theoretical, $\hat{T}_{\text{th}}(\omega_n, z, \mathbf{x})$, temperatures, described in the frequency domain. Theoretically, $\hat{T}_{\text{m}}(\omega_n, z)$ and $\hat{T}_{\text{th}}(\omega_n, z, \mathbf{x})$ can be at any frequency, ω_n, at any depth, z, and for any component of the GSHP system, including the soil mass.

The objective function is minimized using an optimization algorithm capable of systematically choosing input parameters from within an allowed set to be forwarded to the forward model to re-compute the values of the function. This process is repeated iteratively until the objective function satisfies a predefined tolerance ε. The obtained values of the parameters are considered to be a good representation of the material parameters in site.

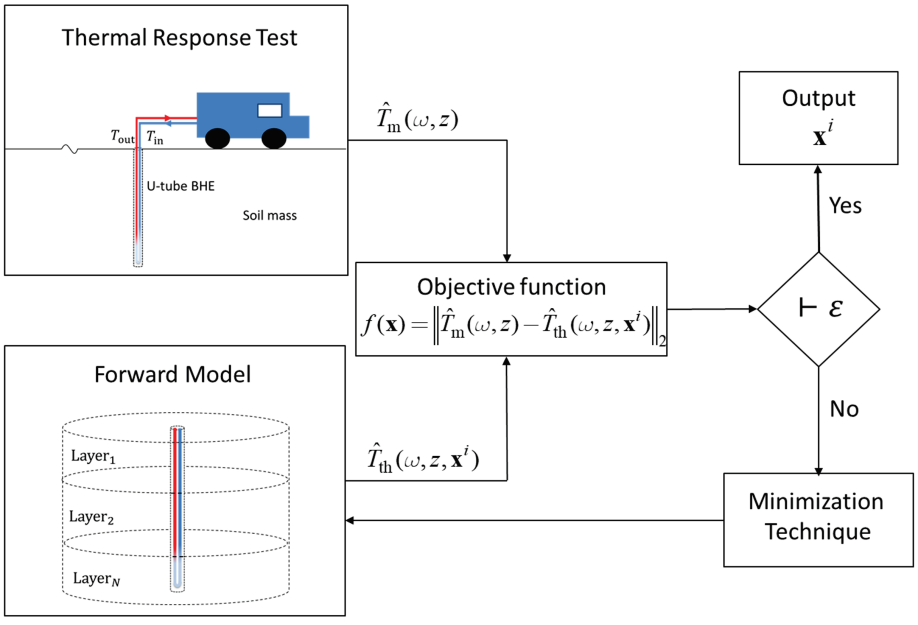

Figure 1.5: A schematic representation of the iterative process of GSHP parameter identification.

1.5 Thesis delineation

This thesis consists of mainly two parts; Part I: heat flow in GSHP systems: Forward calculations, and Part II: Parameter identification of GSHP systems: Inverse calculations.

Part I introduces five computational models. These models utilize the spectral analysis, the spectral element method and the superposition principle to describe heat flow in GSHP systems.

Chapter 2 introduces a comprehensive spectral element formulation for the simulation of transient conduction–convection heat flow in an axisymmetric shallow geothermal system consisting of a single U-tube borehole heat exchanger embedded in a layered soil mass.

Chapter 3 introduces analytical solutions based on the superposition principle for transient heat conduction in an infinite solid mass subjected to multiple cylindrical heat sources. The solutions are formulated for two types of boundary conditions: Neumann boundary condition, and Dirichlet boundary condition.

Chapter 4 introduces a comprehensive and computationally efficient semi-analytical model for heat flow in effectively 3D GSHP systems. The two aforementioned computational models were elaborated and put together to formulate this model. The model can simulate transient heat flow in an effectively 3D GSHP systems constituting multiple borehole heat exchanger embedded in a multilayer soil mass.

Chapter 5 introduces two engineering features to the semi-analytical model. First, the calculation can be conducted from seconds to years simultaneously in a single run using tailored, multiple time stepping fast Fourier transform (FFT) algorithm. Second, the calculation can be conducted using prescribed heat flux derived from the heat pump power.

Chapter 6 investigates the effect of friction heat gain on the heat flow in GSHP systems due to the fluid flow in U-tube pipes. A spectral model for the simulation of transient heat transfer with friction heat gain in a single U-tube BHE is introduced.

Part II introduces a detailed parameter identification algorithm for GSHP systems using TRT measured data.

Chapter 7 introduces a new parameter identification (PI) algorithm for estimating effective and detailed thermal parameters of GSHP systems. The PI is implemented in an iterative algorithm, coupling the forward model to an inverse model. The proposed PI algorithm can handle fluctuating heat pump power, interpret data obtained from multiple heat injection or extraction pulses, produce accurate backcalculation for short and long duration experiments and handle multilayer systems.

Chapter 8 highlights the conclusions and provides an outlook for possible improvements.

Part I
Heat flow in GSHP systems:

Forward Calculations

2

A spectral element model for heat flow in layered shallow geothermal systems

This chapter introduces a comprehensive spectral element formulation for nonhomogeneous heat flow in a shallow geothermal system consisting of a borehole heat exchanger embedded in a multilayer soil mass. The spectral element method is utilized to solve the governing heat equations in the borehole heat exchanger and the soil mass simultaneously using the fast Fourier transform, the eigenfunction expansion, the Fourier Bessel series and the complex Fourier series, together with the finite element method. Only one spectral element is necessary to describe heat flow in a homogeneous domain. For a nonhomogeneous multilayer system, the number of spectral elements is equal to the number of layers. The proposed spectral element model combines the exactness of the analytical methods with an important extent of generality in describing the geometry and boundary conditions of the numerical methods. Verification examples illustrating the model accuracy, and numerical examples illustrating its capability to simulate multilayer systems are given. Despite the apparent rigor of the proposed model, it is robust, computationally efficient and easy to implement in computer codes.

This chapter is based on BniLam N. and Al-Khoury R. (2017). A spectral element model for nonhomogeneous heat flow in shallow geothermal systems. International Journal of Heat and Mass Transfer Volume 104, Pages 703-717.

2.1 Introduction

Heat flow in nonhomogeneous domains consisting of components with different physical properties is central among numerous engineering applications. Heat flow in pipes, heat exchangers, solids and layered domains are only few examples of such applications. Solution of the involved heat equations vary between analytical, semi-analytical and numerical, depending on the complexity of the problem. In this chapter, we present a semi-analytical methodology for solving transient conductive-convective heat flow in nonhomogeneous domains, which might consist of multiple components with different geometrical and physical properties. The proposed methodology is applicable to a wide range of engineering applications, but the focus here is on shallow geothermal systems.

A shallow geothermal system, known as geothermal heat pump (GHP) or ground source heat pump (GSHP), is a source of renewable energy that utilizes the earth heat energy from shallow depths for heating and cooling of buildings. It works by circulating a fluid, mostly water with antifreeze solution, through a closed loop of polyethylene U-tube pipe that is inserted in a borehole in a soil mass. The borehole is filled with grout to fix the polyethylene pipe and to ensure a good thermal interaction with the soil.

The borehole heat exchanger is a slender heat pipe with dimensions of the order of 30 mm in diameter for the U-tube, and 150 mm in diameter and 100 m in length for the borehole. The circulating fluid in the U-tube extract or reject heat from the surrounding soil mass via convection-conduction heat flow mechanisms. Physically, the heat flow mechanism in such a system is well understood, but computationally, and in spite of the bulk of existing models, still creeping due to the combination of the slenderness of the boreholes heat exchangers and the involved thermal convection. This combination of geometry and physics constitutes the main source of computational challenges in this field. Consequently, several geometrical and physical simplifications have been introduced in order to circumvent this problem and obtain feasible solutions.

All known solution techniques, such as analytical, semi-analytical and numerical, have been utilized for this purpose. Nevertheless, in spite of the versatility of the numerical methods, analytical and semi-analytical solutions are yet preferable because of their comparatively little demands on computational power and ease of use in engineering practice.

Most of the current analytical and semi-analytical models for heat flow in geothermal heat pumps are based on the work of Carslaw and Jaeger (1959) for modelling heat flow in finite, semi-infinite and infinite domains subjected to point, line, plane and cylindrical heat sources. In these models, the BHE detailed composition and heat transfer mechanisms are totally ignored and considered as a constant heat source. Gu and O'Neal (1995) introduced an analytical model simulating transient heat flow in a composite domain subjected to a constant heat source, resembling U-tubes surrounded by grout, and a soil mass bounded by a far field boundary. They utilized the eigenfunction expansion to solve the governing partial differential equation. Based on Gu and O'Neal's approach,

Lamarche and Beauchamp (2007) solved the composite domain problem using Laplace transform. They solved both forward and inverse Laplace transforms analytically. Bandyopadhyay et al. (2008) solved the same problem using dimensionless equations, and employed the Gaver–Stehfest numerical algorithm for solving the inverse Laplace transform.

Eskilson and Claesson (1988) diverged from the Carslaw and Jaeger solutions and introduced a semi-analytical model for ground source heat pumps that approximates heat flow in the borehole heat exchangers by two interacting channels conveying a circulating fluid in the vertical axis and embedded in an axisymmetric soil mass. Heat flow in the channels is assumed steady state convective, and in the soil, transient conductive. They utilized Laplace transform to solve the heat equations of the channels, and the explicit forward difference method to solve the heat equations of the soil mass. Zeng et al. (2003) solved the same problem but using dimensionless heat equations for the channels.

Marcotte and Pasquier (2008a) introduced a semi-analytical model for a transient pseudo convection using the fast Fourier transform for discretizing the time domain, and the cubic spline for interpolating results obtained at selected spatial samples. They utilized the principle of superposition to simulate the response to multiple heat fluxes. Javed and Claesson (2011) solved Gu and O'Neal's problem using a similar pseudo convective approach.

Recently, notable attempts have been introduced to account for the inevitable presence of multiple soil layers in shallow geothermal systems. Raymond and Lamarche (2013) analyzed the effect of multiple layers in determining the thermal parameters from the thermal response test (TRT) results. They adopted an analytical computer code for transient well flow in layered aquifer systems to describe conductive heat transfer in shallow geothermal systems constituting multiple layers and subjected to a variable heat injection rate. The Laplace transform is utilized to solve the system of partial differential equations describing heat flow in the layered system. Abdelaziz et al. (2014) extended the finite line heat source solution to a multiple segment finite line heat source resembling a layered soil profile. The temperature of the heterogeneous domain is obtained by summing up the temperature of the typical homogeneous domain with that obtained due to the presence of other layers. The latter is calculated by assuming a composite system constituting smeared thermal parameters, described as a function of the relative distances of the layers from the point of interest.

Despite the appeal of these endeavors, current analytical and semi-analytical models are in general limited in describing the geometry and physics of heat flow in shallow geothermal systems. The main shortcomings are twofold: (1) Not all the details of heat transfer mechanisms in the BHE are taken into consideration. The BHE is considered as a line or cylindrical heat source, ignoring the heat flow in its components and their thermal interactions. (2) The soil mass is in general considered infinite or semi-infinite. Even if a

multilayer system is adopted, the BHE is assumed a line or a cylindrical heat source with a constant or a variable heat flux. Here, these two shortcomings are treated.

In a previous work, Al-Khoury (2012 a, b) introduced a semi-analytical model for transient conductive-convective heat flow in shallow geothermal systems based on the spectral analysis. The model is valid for a semi-infinite domain, where the system can extend to infinity in the vertical and the radial directions. No soil layers with different physical parameters are permitted. However, it is likely that the soil mass surrounding the BHE consists of several layers with different thermal interaction effects. To tackle this, here, the spectral element method is utilized to formulate a semi-analytical model for shallow geothermal systems consisting of a single U-tube borehole heat exchanger embedded in a layered soil mass.

The spectral element method (SEM) is a semi-numerical (semi-analytical) technique which combines the spectral analysis method, basically the discrete Fourier transform, with the finite element method. In the literature, the spectral element method corresponds to two different techniques. The first corresponds to the work introduced by Patera (1984), and the second corresponds to the work introduced by Doyle (1997). Patera's spectral element method deals mainly with spectral formulations in the spatial domain. In this, the domain is discretized into a number of elements, and the field variable in each element is represented by a high-order Lagrangian interpolation through Chebyshev collocation points. It is thus a finite element method with high degree piecewise polynomial basis functions capable of producing high order accuracy.

Doyle's spectral element method, on the other hand, deals mainly with a spectral formulation in the temporal domain. It is a combination of the spectral analysis method, the dynamic stiffness method and the finite element method. In this work, we adopt the temporal SEM of Doyle. For more account of the historical and theoretical background of the spectral element method, see Lee (2009).

The spectral element method is an elegant technique used mainly for solving wave propagation problems. One of the important features of this method is that its formulation leads to a set of equations, similar to that of the conventional finite element method. The fundamental difference, however, is that the spectral element stiffness matrix is exact and frequency dependent. Due to the exact formulation of the system, one element is sufficient to describe a whole homogenous domain. For a nonhomogeneous domain consisting of several layers or members, the number of the spectral elements is equal to the number of the involved layers or members. This feature significantly reduces the size of the problem, and rendering this method computationally very efficient.

The spectral element method discretizes a space–time field variable into a frequency domain and an eigenmode domain. The discretization of the time domain to the frequency domain is done using the fast Fourier transform (FFT) algorithm, and the discretization of the spatial domain to the eigenmode domain is done using the eigenfunction expansion.

The general solution of the system can be obtained by summing over all significant frequencies and eigenvalues.

In this chapter, we formulate a two-node spectral element for transient conduction–convection heat flow in a single U-tube borehole heat exchanger embedded in a layered soil mass. A detailed modelling approach is given hereafter.

2.2 Modelling approach

A shallow geothermal system, particularly a geothermal heat pump, consists basically of two thermally interacting domains: the borehole heat exchanger and the soil mass.

Upon operating the geothermal heat pump, the temperature in the soil mass changes as a result of the thermal interaction with the borehole heat exchanger. The temperature in borehole heat exchanger, on the other hand, changes as a result of the inlet fluid temperature coming from a heat pump, and the thermal interaction with the soil mass.

For a geothermal system consisting of one borehole heat exchanger embedded in a soil mass, the geometry can be described by an axial-symmetric coordinate system. We assume that the borehole heat exchanger is one-dimensional with its axis coincides on the vertical z-axis. This assumption is valid because of the extreme slenderness of the borehole that makes the temperature gradient in the radial direction minimal. The vertical axis of the borehole heat exchanger coincides with the axis of symmetry of the soil mass, as shown in Figure (2.1a) (Al-Khoury 2012 b).

The borehole heat exchanger is modelled as a single U-tube, representing pipe-in and pipe-out, surrounded by a grout and a thin film of soil, Figure (2.1b). This thin soil film is added to the borehole heat exchanger model for two reasons: 1) to accurately model the thermal interaction between the BHE and soil mass, and 2) as it will be apparent later, to formulate one spectral element describing heat flow in the BHE and its surrounding soil layer simultaneously. The computed thin soil film temperature within the BHE model acts as an amplitude to the radial soil mass temperature.

The soil mass is modelled as an axial-symmetric domain, where the axis of symmetry coincides with the centerline of the borehole heat exchanger. The soil mass is in thermal contact with the BHE thin soil film. It can consist of many layers with different physical properties, such as different thermal conductivity, mass density and specific heat capacity. This entails that different parts of the soil mass can have different effects on the borehole heat exchanger.

Solving heat flow in a such nonhomogeneous geometry typically requires the use of a numerical solution method, such as the finite element, the finite volume or the finite difference. However, these methods, and due to the above described complicated geometry and physical processes, require significant memory and CPU time. To avoid this, here, the spectral element method is utilized. A new spectral element for heat flow in an axial-symmetric domain consisting of a borehole heat exchanger and a soil layer is

formulated. The spectral element is designed to calculate a propagating heat flow in the vertical z-direction, along the borehole heat exchanger, and a diffusive heat flow in the radial r-direction, through the soil layer. Temperature distributions in all shallow geothermal components: pipe-in, pipe-out, grout and soil, are calculated simultaneously.

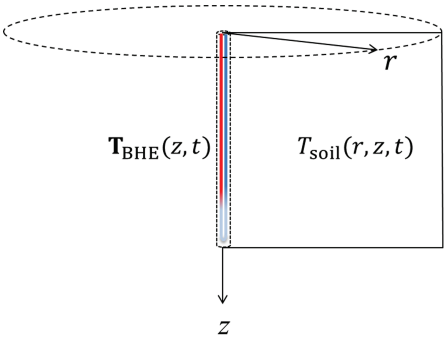

(a)

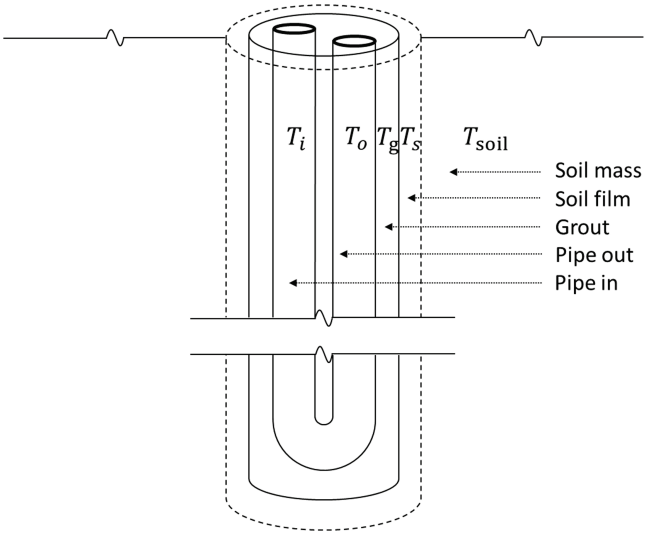

(b)

Figure 2.1: BHE Modelling approach. (a) A schematic representation of an axial symmetric shallow geothermal system. (b) A schematic representation of a single U-tube BHE and its surrounding soil mass

2.3 Governing equations

Heat flow in a single U-tube borehole heat exchanger, consisting of four components (pipe-in, pipe-out, grout, and a thin soil film) in contact with a soil mass can be described as

Pipe-in

$$\rho c\frac{\partial T_i}{\partial t}dV_i-\lambda\frac{\partial^2 T_i}{\partial z^2}dV_i+\rho cu\frac{\partial T_i}{\partial z}dV_i+b_{ig}\left(T_i-T_g\right)dS_{ig}=0 \tag{2.1}$$

Pipe-out

$$\rho c\frac{\partial T_o}{\partial t}dV_o-\lambda\frac{\partial^2 T_o}{\partial z^2}dV_o-\rho cu\frac{\partial T_o}{\partial z}dV_o+b_{og}\left(T_o-T_g\right)dS_{og}=0 \tag{2.2}$$

Grout

$$\begin{aligned}\rho_g c_g\frac{\partial T_g}{\partial t}dV_g-\lambda_g\frac{\partial^2 T_g}{\partial z^2}dV_g+b_{ig}\left(T_g-T_i\right)dS_{ig}\\+b_{og}\left(T_g-T_o\right)dS_{og}+b_{gs}\left(T_g-T_s\right)dS_{gs}=0\end{aligned} \tag{2.3}$$

Soil film

$$\rho_s c_s\frac{\partial T_s}{\partial t}dV_s-\lambda_s\frac{\partial^2 T_s}{\partial z^2}dV_s+b_{gs}\left(T_s-T_g\right)dS_{gs}+b_{ss}\left(T_s-T_{\text{soil}}\big|_{r=0}\right)dS_s=0 \tag{2.4}$$

Soil mass

$$\frac{1}{\alpha}\frac{\partial T_{\text{soil}}}{\partial t}-\frac{\partial^2 T_{\text{soil}}}{\partial r^2}-\frac{1}{r}\frac{\partial T_{\text{soil}}}{\partial r}-\frac{\partial^2 T_{\text{soil}}}{\partial z^2}=0 \tag{2.5}$$

where the subscripts i, o, g and s represent pipe-in, pipe-out, grout and soil film, respectively, and $T_i=T_i(z,t)$, $T_o=T_o(z,t)$, $T_{\text{g}}=T_{\text{g}}(z,t)$, $T_s=T_s(z,t)$ are their corresponding temperatures; and $T_{\text{soil}}=T_{\text{soil}}(r,t)$ is the temperature in the soil mass. λ, λ_{g} and λ_s (W/mK) are the thermal conductivity of the circulating fluid, grout and soil film, respectively; u (m/s) is the circulating fluid velocity; b_{ig}, b_{og}, b_{gs}, b_{ss} (W/m^{2}K) are the thermal interaction coefficients between pipe in-grout, pipe out-grout, grout-soil film, and soil film-soil mass, respectively; ρc (J/m^{3}K) is the volume heat capacity, with c (J/kg K) the specific heat capacity and ρ (kg/m^3) the mass density; dV_i , dV_o , dV_{g} , dV_s (m^3) are the control volumes of pipe-in, pipe-out, grout and soil film, respectively, and $dS_{ig}, dS_{og}, dS_{gs}, dS_s$ (m^2) are their associated surface areas; and α (m^2/s) is the thermal diffusivity of the soil, described as

$$\alpha = \frac{\lambda_s}{\rho_s c_s} \tag{2.6}$$

The associated initial and boundary conditions are:

$$T_i(z,0) = T_o(z,0) = T_g(z,0) = T_s(z,0) = T_{\text{soil}}(r,z,0) \tag{2.7}$$

$$T_i(0,t) = T_{\text{in}}(t) \tag{2.8}$$

$$T_i(L,t) = T_o(L,t) \tag{2.9}$$

$$T_{\text{soil}}\big|_{r=0} = T_s \tag{2.10}$$

$$T_{\text{soil}}(R,z,t) = 0 \tag{2.11}$$

where, initially, the temperature distribution in the BHE components is equal to that of the steady state condition of the soil mass before heating/cooling operation starts; T_{in} is the fluid temperature at z = 0, coming from the heat pump. At the bottom of the BHE, ($z = L$) the fluid temperature in pipe-in is equal to that in pipe-out, neglecting the elbow part since it is too small compared to the BHE length. Eq. (2.10) implies that the temperature of the soil film acts as the amplitude of the soil mass temperature in the radial direction. In Eq.(2.11), we utilized the concept of region-of-interest (Al-Khoury 2012a and 2012b), where R represents a fictitious homogeneous boundary, far away from the borehole heat exchanger, where it is known, intuitively or analytically, that heat flux from the BHE vanishes. This choice, as it will be apparent later, results to an algebraic summation over Fourier-Bessel series, alleviating the need to solve semi-infinite integrals of oscillatory transcendental functions.

The thermal interaction coefficient for pipe-in - grout is described as

$$b_{ig} = \frac{1}{R_i} \tag{2.12}$$

where

$$R_i = R_{\text{convection}} + R_{\text{pipe material}} = \frac{1}{r_o / r_i \, \bar{h}} + \frac{r_o \ln(r_o/r_i)}{\lambda_{\text{p}}} \tag{2.13}$$

in which r_i and r_o are the inner and outer radius of pipe-in, respectively; λ_{p} is the thermal conductivity of pipe-in material; and $\bar{h} = \text{Nu}\lambda/D$ is the convective heat transfer coefficient, where D is the inner diameter of the pipe. Nu is the Nusselt Number and can be expressed as (Al-Khoury 2012b):

$$\mathrm{Nu} = 4.36 \qquad \text{for laminar} \tag{2.14}$$

$$\mathrm{Nu}=0.023\,\mathrm{Re}^{0.8}\,\mathrm{Pr}^{n} \qquad \text{for turbulent} \tag{2.15}$$

where Pr is the Prandtl number and Re is the Reynolds number, defined as:

$$\mathrm{Pr} = \frac{c\mu}{\lambda} \tag{2.16}$$

$$\mathrm{Re} = \frac{\rho u D}{\mu} \tag{2.17}$$

in which μ is the dynamic viscosity and where n=0.4 for heating, and n=0.3 for cooling.

A similar formulation is valid for pipe-out-grout, b_{og}.

The thermal interaction coefficient for grout –soil film can be expressed as

$$b_{gs} = \frac{1}{R_g} \tag{2.18}$$

where

$$R_g = \frac{r_\mathrm{b} \ln(r_\mathrm{b} / r_{eq})}{\lambda_g} \tag{2.19}$$

in which r_b is the radius of the grout (borehole), and $r_{eq} = 2\sqrt{r_\mathrm{in}^2 + r_\mathrm{out}^2}$ with r_in the pipe-in inner radius and r_out the pipe-out inner radius.

The thermal interaction coefficient for the soil film-soil mass can be expressed as

$$b_{ss} = \frac{1}{R_s} \tag{2.20}$$

where

$$R_s = \frac{r_\mathrm{f} \ln(r_\mathrm{f} / r_\mathrm{b})}{\lambda_s} \tag{2.21}$$

in which r_f is the radius of the soil film.

Note that the above formulation of the thermal interaction coefficients have been modified following an intensive verifications with detailed numerical analysis and they are somewhat different than the coefficients presented in BniLam and al Khoury (2017).

2.4 Two-node spectral element formulation

The spectral element method is utilized to formulate an axial-symmetric spectral element for heat flow in a coupled borehole heat exchanger and a soil mass. The element consists of two nodes located at its boundaries, and denoting two parallel circular planes within which the heat is constrained to flow, Figure 2.2. In the vertical z-direction, the element extends to cover a whole layer depth, h, and in the radial direction, the element is assumed to extend to a fictitious finite boundary, R, where the BHE heat flux is known a priori to vanish. The response at any point within the element is described as a superposition of an incident flux from one boundary node and a reflected flux, if occurs, from the other boundary node.

The procedure for formulating a spectral element starts by the Fourier transform of the governing partial differential equations, to convert them from the time domain to the frequency domain. Then, an eigenfunction expansion is employed on the homogeneous part of the equations, to obtain the eigenvalues. This is followed by discretizing the resulting equations into the nodal values, to formulate an algebraic spectral element equation, similar to that of the force-displacement finite element method. This equation is complex and frequency dependent.

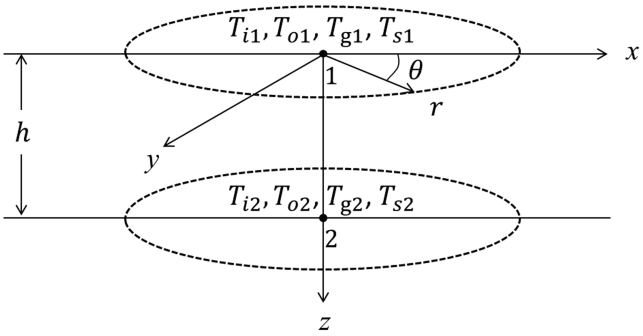

Figure 2.2: Two-node spectral element

Eqs. (2.1)-(2.4) are functions of z only, and act as a source to the soil mass. While Eq.(2.5) is a function of r and z, and acts as a source to the borehole heat exchanger. These equations are solved simultaneously, using the eigenfunction expansion, to solve Eqs. (2.1)-(2.4); and the separation of variables and the Fourier-Bessel series expansion, to solve Eq.(2.5). Eq. (2.4) is nonhomogeneous due to the presence of T_{soil}. To make it homogeneous, T_{soil} needs to be given in terms of T_{s}.

In the following, we first solve the soil heat equation, Eq.(2.5), followed by solving Eqs.(2.1)-(2.4) for the borehole heat exchanger. Then, a two-node spectral element is formulated. But first, a brief description of the spectral analysis is given.

2.4.1 Spectral analysis

Using the discrete Fourier transform, the temperature, which is a function of time and space, can be discretized as

$$T(z,t_m)=\sum_n \hat{T}(z,\omega_n)e^{i\omega_n t_m}\ , \qquad \hat{T}(z,\omega_n)=\frac{1}{N}\sum_m T(z,t_m)e^{-i\omega_n t_m} \tag{2.22}$$

in which N is the number of the discrete samples, where, in the fast Fourier transform, it is usually made $N=2^{\gamma}=2,4,8,\cdots,2048,\cdots$. For a real signal, such as the one treated in this work, the transform is symmetric about a middle frequency, referred to as the Nyquist frequency. This means that N real points are transformed into $N/2$ complex points.

The spectral representation of the time derivative is given by

$$\frac{\partial T}{\partial t}=\frac{\partial}{\partial t}\sum \hat{T}_n e^{i\omega_n t}=\sum i\omega_n \hat{T}_n e^{i\omega_n t}\Rightarrow i\omega\hat{T} \tag{2.23}$$

and of the spatial derivative is given by

$$\frac{\partial^m T}{\partial z^m}=\frac{\partial^m}{\partial z^m}\sum \hat{T}_n\, e^{i\omega_n t}=\sum \frac{\partial^m \hat{T}_n}{\partial z^m}\, e^{i\omega_n t}\Rightarrow \frac{\partial^m \hat{T}}{\partial z^m} \tag{2.24}$$

For clarity of notation, the summation, the exponential term and the subscripts are ignored, and the transform is represented as $T\Leftrightarrow\hat{T}$.

2.4.2 Solution of soil heat equation

Fourier transform of Eq. (2.5), gives

$$\frac{i\omega}{\alpha}\hat{T}_{\text{soil}}-\frac{\partial^2\hat{T}_{\text{soil}}}{\partial r^2}-\frac{1}{r}\frac{\partial\hat{T}_{\text{soil}}}{\partial r}-\frac{\partial^2\hat{T}_{\text{soil}}}{\partial z^2}=0 \tag{2.25}$$

The general solution of the soil heat equations in the frequency domain can be expressed as (Al-Khoury 2012 a, b)

$$\hat{T}_{\text{soil}}(r,z,\omega)=\sum_m A_m J_o(\xi_m r)e^{i\zeta_m z} \tag{2.26}$$

where

$$\begin{aligned}&\zeta_m=(-\kappa^2-\xi_m^2)^{1/2}\\&\kappa=\sqrt{i\omega/\alpha}\\&\xi_m=\frac{\beta_m}{R}\end{aligned} \tag{2.27}$$

in which β_m is the roots of the Bessel function of the first kind, J_o. Note that the solution of Eq. (2.25) in the radial direction is the Bessel functions J_o and Y_o of the first and second kind of order zero. Since the temperature at the origin, $r = 0$, is finite, and since Y_o is infinite at this point, the Y_o solution is discarded (Al-Khoury 2012a and 2012b).

Relating the soil mass temperature, T_{soil}, to the soil film temperature, T_{s}, in Eq.(2.4) can be done by substituting Eq.(2.26) into Eq.(2.10), giving

$$\sum_m A_m e^{i\zeta_m z} = \hat{T}_S \tag{2.28}$$

This equation is a typical complex Fourier series, and its coefficient can be expressed as

$$A_m = \frac{1}{h}\int_0^h \hat{T}_s e^{-i\zeta_m z} dz \tag{2.29}$$

where h is the height of the element. Solving for the integral, it yields

$$A_m = \frac{\left(e^{-i\zeta_m h} - 1\right)\hat{T}_S}{-i\zeta_m h} \tag{2.30}$$

Substituting Eq.(2.30) into Eq.(2.26), gives

$$\hat{T}_{\text{soil}} = \hat{T}_S \sum_m \overline{A}_m J_0(\xi_m r) \tag{2.31}$$

where

$$\overline{A}_m = \frac{\left(e^{-i\zeta_m h} - 1\right)}{-i\zeta_m h} \tag{2.32}$$

It can be noticed that the exponential term over z in Eq.(2.26) has disappeared in Eq.(2.31), because it is included in $\hat{T}_s$, as it is apparent in Eq.(2.38), given below.

At the boundary between the soil film and the soil mass, Eq. (2.31) yields

$$\hat{T}_{\text{soil}}\Big|_{r=0} = \hat{T}_S \sum_m \overline{A}_m \tag{2.33}$$

2.4.3 Solution of BHE heat equation

Applying Eq. (2.22) to Eqs. (2.1)-(2.4) and substituting Eq. (2.33) into Eq. (2.4), gives

$$-\lambda\frac{d^2\hat{T}_i}{dz^2}dV_i+\rho cu\frac{d\hat{T}_i}{dz}dV_i+\left(i\omega\rho cdV_i+b_{ig}dS_{ig}\right)\hat{T}_i-b_{ig}\hat{T}_g dS_{ig}=0 \tag{2.34}$$

$$-\lambda\frac{d^2\hat{T}_o}{dz^2}dV_i-\rho cu\frac{d\hat{T}_i}{dz}dV_o+\left(i\omega\rho cdV_o+b_{og}dS_{og}\right)\hat{T}_o-b_{og}\hat{T}_g dS_{og}=0 \tag{2.35}$$

$$\begin{aligned}-\lambda_g\frac{d^2\hat{T}_g}{dz^2}dV_g+\left(i\omega\rho_g c_g dV_g+b_{ig}dS_{ig}+b_{og}dS_{og}+b_{gs}dS_{gs}\right)\hat{T}_g\\ -b_{ig}dS_{ig}\hat{T}_i-b_{og}dS_{og}\hat{T}_o-b_{gs}dS_{gs}\hat{T}_s=0\end{aligned} \tag{2.36}$$

$$-\lambda_s\frac{d^2\hat{T}_s}{dz^2}dV_s+\left(i\omega\rho_s c_s dV_s+b_{gs}dS_{gs}+b_{ss}dS_s\left(1-\sum_m\overline{A}_m\right)\right)\hat{T}_s-b_{gs}dS_{gs}\hat{T}_g=0 \tag{2.37}$$

which forms a homogeneous set of equations that can be solved using the eigenfunction expansion.

The utilization of the spectral analysis has reduced the partial differential equations, Eqs.(2.1)-(2.4), into ordinary differential equations, Eqs.(2.34)-(2.37). However, the resulting equations are frequency dependent and need to be solved for every frequency ω_n.

2.4.3.1 Eigenfunction expansion

The solution of the primary variables in Eqs.(2.34)-(2.37) can be given by:

$$\hat{T}_i=A_i e^{-ikz},\quad \hat{T}_o=A_o e^{-ikz},\quad \hat{T}_g=A_g e^{-ikz},\quad \hat{T}_s=A_s e^{-ikz} \tag{2.38}$$

in which A_i, A_o, A_g and A_s are the integral constants, which are related to $\hat{T}_i$, $\hat{T}_o$, $\hat{T}_g$ and $\hat{T}_s$, respectively; and *k* denotes the system eigenvalues, which need to be determined.

Substituting Eq.(2.38) into Eqs.(2.34)-(2.37), gives

$$\begin{aligned}k^2\lambda dV_i A_i e^{-ikz}-ik\rho cudV_i A_i e^{-ikz}+\left(i\omega\rho cdV_i+b_{ig}dS_{ig}\right)A_i e^{-ikz}\\ -b_{ig}dS_{ig}A_g e^{-ikz}=0\end{aligned} \tag{2.39}$$

$$\begin{aligned}k^2\lambda dV_i A_o e^{-ikz}+ik\rho cudV_o A_i e^{-ikz}+\left(i\omega\rho cdV_o+b_{og}dS_{og}\right)A_o e^{-ikz}\\ -b_{og}dS_{og}A_g e^{-ikz}=0\end{aligned} \tag{2.40}$$

$$k^2\lambda_g dV_g A_g e^{-ikz} + \left(i\omega\rho_g c_g dV_g + b_{ig}dS_{ig} + b_{og}dS_{og} + b_{gs}dS_{gs}\right)A_g e^{-ikz} - b_{ig}dS_{ig}A_i e^{-ikz} - b_{og}dS_{og}A_o e^{-ikz} - b_{gs}dS_{gs}A_s e^{-ikz} = 0 \tag{2.41}$$

$$k^2\lambda_s dV_s A_s e^{-ikz} + \left(i\omega\rho_s c_s dV_s + b_{gs}dS_{gs} + b_{ss}dS_s\left(1-\sum_m \bar{A}_m\right)\right)A_s e^{-ikz} - b_{gs}dS_{gs}A_g e^{-ikz} = 0 \tag{2.42}$$

Dividing Eqs.(2.39)-(2.42) by e^{-ikz}, rearranging and putting it in a matrix form, gives

$$\begin{pmatrix} a_{11} & 0 & a_{13} & 0 \\ 0 & a_{22} & a_{23} & 0 \\ a_{31} & a_{32} & a_{33} & a_{34} \\ 0 & 0 & a_{43} & a_{44} \end{pmatrix}\begin{bmatrix} A_i \\ A_o \\ A_g \\ A_s \end{bmatrix} = 0 \tag{2.43}$$

where

$$a_{11} = k^2\lambda dV_i - ik\rho cudV_i + i\omega\rho cdV_i + b_{ig}dS_{ig}$$
$$a_{13} = -b_{ig}dS_{ig}$$
$$a_{22} = k^2\lambda dV_o + ik\rho cudV_o + i\omega\rho cdV_o + b_{og}dS_{og}$$
$$a_{23} = -b_{og}dS_{og}$$
$$a_{31} = -b_{ig}dS_{ig}$$
$$a_{32} = -b_{og}dS_{og}$$
$$a_{33} = k^2\lambda_g dV_g + i\omega\rho_g c_g dV_g + b_{ig}dS_{ig} + b_{og}dS_{og} + b_{gs}dS_{gs}$$
$$a_{34} = -b_{gs}dS_{gs}$$
$$a_{43} = -b_{gs}dS_{gs}$$
$$a_{44} = k^2\lambda_s dV_s + i\omega\rho_s c_s dV_s + b_{gs}dS_{gs} + b_{ss}dS_s\left(1-\sum_m \bar{A}_m\right)$$

Since $\hat{T}_i$, $\hat{T}_g$, $\hat{T}_o$ and $\hat{T}_s$ are coupled, the constants, A_i, A_o, A_g and A_s are related to each other. Using Eqs.(2.39) -(2.43), the following relationships exist:

Pipe in-grout

$$A_i = Y^{ig} A_g$$

$$Y^{ig} = \frac{b_{ig} dS_{ig}}{k^2 \lambda dV_i \mp ik\rho cudV_i + i\omega\rho cdV_i + b_{ig} dS_{ig}} \tag{2.44}$$

Pipe out-grout

$$A_o = Y^{og} A_g$$

$$Y^{og} = \frac{b_{og} dS_{og}}{k^2 \lambda dV_o \pm ik\rho cudV_o + i\omega\rho cdV_o + b_{og} dS_{og}} \tag{2.45}$$

Soil film-grout

$$A_s = Y^{sg} A_g$$

$$Y^{sg} = \frac{b_{gs} dS_{gs}}{k^2 \lambda_s dV_s + i\omega\rho_s c_s dV_s + b_{gs} dS_{gs} + b_{ss} dS_s \left(1 - \sum_m \bar{A}_m\right)} \tag{2.46}$$

For each k there is a corresponding Y^{ig}, Y^{og} and Y^{sg}, i.e. there are Y_1^{ig}, Y_1^{og}, Y_1^{sg} for k_1, etc. (Doyle, 1988).

The $\mp$ signs in Eq.(2.44) and Eq.(2.45) refer to the fluid velocity direction at the nod. The fluid velocity in pipe-in at nod 1 is $(-)$, while it is $(+)$ at nod 2. For pipe-out, the signs are opposite.

Non-trivial solution of Eq. (2.43) can only be obtained by letting the determinate equal to zero, giving a complex eight degree polynomial of the form:

$$a_8 k^8 + a_7 k^7 + a_6 k^6 + a_5 k^5 + a_4 k^4 + a_3 k^3 + a_2 k^2 + a_1 k + a_0 = 0 \tag{2.47}$$

This polynomial represents the eigenfunction of the single U-tube BHE system with k denoting its set of eigenvalues, which can be obtained by solving for the roots of Eq.(2.47). Only for this set of eigenvalues do the eigenfunction exist that satisfy the boundary conditions of the problem. Eight eigenvalues in two groups of four, differ in sign, are obtained from Eq.(2.47). The first group is related to the positive fluid velocity, and the second to the negative fluid velocity. The exact forms of the coefficients of Eq. (2.47) are given in BniLam and Al-Khoury (2017). They are obtained using MAPLE software (Maple 2019).

2.4.3.2 Spectral element formulation in z-direction

Consider a one-dimensional heat flow in an element of length h bounded by two nodes: node 1 and node 2, Figure 2.2. At each node, there are four degrees of freedom, representing the temperatures in pipe-in, pipe-out, grout and soil film. Using Eq.(2.38), the temperatures at any point along the element are calculated by the superposition of an incident flux, from node 1, and a reflective flux, from node 2, as

$$\begin{aligned}\hat{T}_i = {} & A_{i1}e^{-ik_1 z} + B_{i1}e^{-ik_2 z} + C_{i1}e^{-ik_3 z} + D_{i1}e^{-ik_4 z} \\ & + A_{i2}e^{-ik_5(h-z)} + B_{i2}e^{-ik_6(h-z)} + C_{i2}e^{-ik_7(h-z)} + D_{i2}e^{-ik_8(h-z)}\end{aligned} \tag{2.48}$$

$$\begin{aligned}\hat{T}_o = {} & A_{o1}e^{-ik_1 z} + B_{o1}e^{-ik_2 z} + C_{o1}e^{-ik_3 z} + D_{o1}e^{-ik_4 z} \\ & + A_{o2}e^{-ik_5(h-z)} + B_{o2}e^{-ik_6(h-z)} + C_{o2}e^{-ik_7(h-z)} + D_{o2}e^{-ik_8(h-z)}\end{aligned} \tag{2.49}$$

$$\begin{aligned}\hat{T}_g = {} & A_{g1}e^{-ik_1 z} + B_{g1}e^{-ik_2 z} + C_{g1}e^{-ik_3 z} + D_{g1}e^{-ik_4 z} \\ & + A_{g2}e^{-ik_5(h-z)} + B_{g2}e^{-ik_6(h-z)} + C_{g2}e^{-ik_7(h-z)} + D_{g2}e^{-ik_8(h-z)}\end{aligned} \tag{2.50}$$

$$\begin{aligned}\hat{T}_s = {} & A_{s1}e^{-ik_1 z} + B_{s1}e^{-ik_2 z} + C_{s1}e^{-ik_3 z} + D_{s1}e^{-ik_4 z} \\ & + A_{s2}e^{-ik_5(h-z)} + B_{s2}e^{-ik_6(h-z)} + C_{s2}e^{-ik_7(h-z)} + D_{s2}e^{-ik_8(h-z)}\end{aligned} \tag{2.51}$$

As for the finite element method, the governing equations are solved in terms of the nodal values.

At node 1, z = 0, substituting Eqs. (2.44)-(2.45) into Eqs.(2.48), (2.49) and (2.51), the nodal temperatures become

$$\begin{aligned}\hat{T}_{i1} = {} & A_{g1}Y_1^{ig} + B_{g1}Y_2^{ig} + C_{g1}Y_3^{ig} + D_{g1}Y_4^{ig} \\ & + A_{g2}Y_5^{ig}e^{-ik_5 h} + B_{g2}Y_6^{ig}e^{-ik_6 h} + C_{g2}Y_7^{ig}e^{-ik_7 h} + D_{g2}Y_8^{ig}e^{-ik_8 h} \\ \hat{T}_{o1} = {} & A_{g1}Y_1^{og} + B_{g1}Y_2^{og} + C_{g1}Y_3^{og} + D_{g1}Y_4^{og} \\ & + A_{g2}Y_5^{og}e^{-ik_5 h} + B_{g2}Y_6^{og}e^{-ik_6 h} + C_{g2}Y_7^{og}e^{-ik_7 h} + D_{g2}Y_8^{og}e^{-ik_8 h} \\ \hat{T}_{g1} = {} & A_{g1} + B_{g1} + C_{g1} + D_{g1} \\ & + A_{g2}e^{-ik_5 h} + B_{g2}e^{-ik_6 h} + C_{g2}e^{-ik_7 h} + D_{g2}e^{-ik_8 h} \\ \hat{T}_{s1} = {} & A_{g1}Y_1^{sg} + B_{g1}Y_2^{sg} + C_{g1}Y_3^{sg} + D_{g1}Y_4^{sg} \\ & + A_{g2}Y_5^{sg}e^{-ik_5 h} + B_{g2}Y_6^{sg}e^{-ik_6 h} + C_{g2}Y_7^{sg}e^{-ik_7 h} + D_{g2}Y_8^{sg}e^{-ik_8 h}\end{aligned} \tag{2.52}$$

At node 2, z = h, and similarly, upon substituting Eqs. (2.44)-(2.45) into Eqs.(2.48), (2.49) and (2.51), the nodal temperatures become

$$
\begin{aligned}
\hat{T}_{i2} &= A_{g1}Y_1^{ig}e^{-ik_1h} + B_{g1}Y_2^{ig}e^{-ik_2h} + C_{g1}Y_3^{ig}e^{-ik_3h} + D_{g1}Y_4^{ig}e^{-ik_4h} \\
&\quad + A_{g2}Y_5^{ig} + B_{g2}Y_6^{ig} + C_{g2}Y_7^{ig} + D_{g2}Y_8^{ig} \\
\hat{T}_{o2} &= A_{g1}Y_1^{og}e^{-ik_1h} + B_{g1}Y_2^{og}e^{-ik_2h} + C_{g1}Y_3^{og}e^{-ik_3h} + D_{g1}Y_4^{og}e^{-ik_4h} \\
&\quad + A_{g2}Y_5^{og} + B_{g2}Y_6^{og} + C_{g2}Y_7^{og} + D_{g2}Y_8^{og} \\
\hat{T}_{g2} &= A_{g1}e^{-ik_1h} + B_{g1}e^{-ik_2h} + C_{g1}e^{-ik_3h} + D_{g1}e^{-ik_4h} \\
&\quad + A_{g2} + B_{g2} + C_{g2} + D_{g2} \\
\hat{T}_{s2} &= A_{g1}Y_1^{sg}e^{-ik_1h} + B_{g1}Y_2^{sg}e^{-ik_2h} + C_{g1}Y_3^{sg}e^{-ik_3h} + D_{g1}Y_4^{sg}e^{-ik_4h} \\
&\quad + A_{g2}Y_5^{sg} + B_{g2}Y_6^{sg} + C_{g2}Y_7^{sg} + D_{g2}Y_8^{sg}
\end{aligned}
\tag{2.53}
$$

In a matrix form, Eq.(2.52) and eq.(2.53) can be presented as

$$
\begin{pmatrix} \hat{T}_{i1} \\ \hat{T}_{o1} \\ \hat{T}_{g1} \\ \hat{T}_{s1} \\ \hat{T}_{i2} \\ \hat{T}_{g2} \\ \hat{T}_{o2} \\ \hat{T}_{s2} \end{pmatrix} = \begin{pmatrix} h_{11} & h_{12} & h_{13} & h_{14} & h_{15} & h_{16} & h_{17} & h_{18} \\ h_{21} & h_{22} & h_{23} & h_{24} & h_{25} & h_{26} & h_{27} & h_{28} \\ h_{31} & h_{32} & h_{33} & h_{34} & h_{35} & h_{36} & h_{37} & h_{38} \\ h_{41} & h_{42} & h_{43} & h_{44} & h_{45} & h_{46} & h_{47} & h_{48} \\ h_{51} & h_{52} & h_{53} & h_{54} & h_{55} & h_{56} & h_{57} & h_{58} \\ h_{61} & h_{62} & h_{63} & h_{64} & h_{65} & h_{66} & h_{67} & h_{68} \\ h_{71} & h_{72} & h_{73} & h_{74} & h_{75} & h_{76} & h_{77} & h_{78} \\ h_{81} & h_{82} & h_{83} & h_{84} & h_{85} & h_{86} & h_{87} & h_{88} \end{pmatrix} \begin{pmatrix} A_{g1} \\ B_{g1} \\ C_{g1} \\ D_{g1} \\ A_{g2} \\ B_{g2} \\ C_{g2} \\ D_{g2} \end{pmatrix} \tag{2.54}
$$

Where

$$
\begin{aligned}
&h_{11} = Y_1^{ig}, \quad h_{12} = Y_2^{ig}, \quad h_{13} = Y_3^{ig}, \quad h_{14} = Y_4^{ig} \\
&h_{15} = Y_5^{ig}e^{-ik_5h}, \quad h_{16} = Y_6^{ig}e^{-ik_6h}, \quad h_{17} = Y_7^{ig}e^{-ik_7h}, \quad h_{18} = Y_8^{ig}e^{-ik_8h}
\end{aligned}
$$

$$
\begin{aligned}
&h_{21} = Y_1^{og}, \quad h_{22} = Y_2^{og}, \quad h_{23} = Y_3^{og}, \quad h_{24} = Y_4^{og} \\
&h_{25} = Y_5^{og}e^{-ik_5h}, \quad h_{26} = Y_6^{og}e^{-ik_6h}, \quad h_{27} = Y_7^{og}e^{-ik_7h}, \quad h_{28} = Y_8^{og}e^{-ik_8h}
\end{aligned}
$$

$$
\begin{aligned}
&h_{31} = 1, \quad h_{32} = 1, \quad h_{33} = 1, \quad h_{34} = 1 \\
&h_{35} = e^{-ik_5h}, \quad h_{36} = e^{-ik_6h}, \quad h_{37} = e^{-ik_7h}, \quad h_{38} = e^{-ik_8h}
\end{aligned}
$$

$$h_{41}=Y_1^{sg},\quad h_{42}=Y_2^{sg},\quad h_{43}=Y_3^{sg},\quad h_{44}=Y_4^{sg}$$
$$h_{45}=Y_5^{sg}e^{-ik_5h},\quad h_{46}=Y_6^{sg}e^{-ik_6h},\quad h_{47}=Y_7^{sg}e^{-ik_7h},\quad h_{48}=Y_8^{sg}e^{-ik_8h}$$

$$h_{51}=Y_1^{ig}e^{-ik_1h},\quad h_{52}=Y_2^{ig}e^{-ik_2h},\quad h_{53}=Y_3^{ig}e^{-ik_3h},\quad h_{54}=Y_4^{ig}e^{-ik_4h}$$
$$h_{55}=Y_5^{ig},\quad h_{56}=Y_6^{ig},\quad h_{57}=Y_7^{ig},\quad h_{58}=Y_8^{ig}$$

$$h_{61}=Y_1^{og}e^{-ik_1h},\quad h_{62}=Y_2^{og}e^{-ik_2h},\quad h_{63}=Y_3^{og}e^{-ik_3h},\quad h_{64}=Y_4^{og}e^{-ik_4h}$$
$$h_{65}=Y_5^{og},\quad h_{66}=Y_6^{og},\quad h_{67}=Y_7^{og},\quad h_{68}=Y_8^{og}$$

$$h_{71}=e^{-ik_1h},\quad h_{72}=e^{-ik_2h},\quad h_{73}=e^{-ik_3h},\quad h_{74}=e^{-ik_4h}$$
$$h_{75}=1,\quad h_{76}=1,\quad h_{77}=1,\quad h_{78}=1$$

$$h_{81}=Y_1^{sg}e^{-ik_1h},\quad h_{82}=Y_2^{sg}e^{-ik_2h},\quad h_{83}=Y_3^{sg}e^{-ik_3h},\quad h_{84}=Y_4^{sg}e^{-ik_4h}$$
$$h_{85}=Y_5^{sg},\quad h_{86}=Y_6^{sg},\quad h_{87}=Y_7^{sg},\quad h_{88}=Y_8^{sg}$$

Eq.(2.54) indicates that the temperatures of pipe-in, pipe-out and soil film are represented in terms of the grout coefficients. This equation can be written as

$$\hat{\mathbf{T}}_{\text{node}}=\mathbf{H}\left(k,\omega_n\right)\mathbf{A} \tag{2.55}$$

Solving for $\mathbf{A}$, gives

$$\mathbf{A}=\mathbf{H}\left(k,\omega_n\right)^{-1}\hat{\mathbf{T}}_{\text{node}} \tag{2.56}$$

The next step is to relate the heat flux to the temperature at the nodes. The heat fluxes for the BHE components are

$$\begin{aligned} q_i&=\mp\lambda\frac{\partial T_i}{\partial z}dA_i, & q_o&=\mp\lambda\frac{\partial T_o}{\partial z}dA_o\\ q_g&=\mp\lambda_g\frac{\partial T_g}{\partial z}dA_g, & q_s&=\mp\lambda_s\frac{\partial T_s}{\partial z}dA_s \end{aligned} \tag{2.57}$$

where dA_i, dA_o, dA_{g} and dA_s are the cross sectional areas of pipe-in, pip-out, grout and soil film respectively. The $\mp$ sign refers to the direction of the heat flux: the heat flux at node 1 is $(-)$ while at node 2, it is $(+)$.

Substituting Eqs. (2.44)-(2.46) and Eqs.(2.48) -(2.51) into Eq. (2.57) gives

$$q_i = \mp\lambda dA_i \begin{pmatrix} -ik_1 A_{g1} Y_1^{ig} e^{-ik_1 z} - ik_2 B_{g1} Y_2^{ig} e^{-ik_2 z} \\ -ik_3 C_{g1} Y_3^{ig} e^{-ik_3 z} - ik_4 D_{g1} Y_4^{ig} e^{-ik_4 z} \\ +ik_5 A_{g2} Y_5^{ig} e^{-ik_5 (h-z)} + ik_6 B_{g2} Y_6^{ig} e^{-ik_6 (h-z)} \\ +ik_7 C_{g2} Y_7^{ig} e^{-ik_7 (h-z)} + ik_8 D_{g2} Y_8^{ig} e^{-ik_8 (h-z)} \end{pmatrix} \tag{2.58}$$

$$q_o = \mp\lambda dA_o \begin{pmatrix} -ik_1 A_{g1} Y_1^{og} e^{-ik_1 z} - ik_2 B_{g1} Y_2^{og} e^{-ik_2 z} \\ -ik_3 C_{g1} Y_3^{og} e^{-ik_3 z} - ik_4 D_{g1} Y_4^{og} e^{-ik_4 z} \\ +ik_5 A_{g2} Y_5^{og} e^{-ik_5 (h-z)} + ik_6 B_{g2} Y_6^{og} e^{-ik_6 (h-z)} \\ +ik_7 C_{g2} Y_7^{og} e^{-ik_7 (h-z)} + ik_8 D_{g2} Y_8^{og} e^{-ik_8 (h-z)} \end{pmatrix} \tag{2.59}$$

$$q_g = \mp\lambda_g dA_g \begin{pmatrix} -ik_1 A_{g1} e^{-ik_1 z} - ik_2 B_{g1} e^{-ik_2 z} \\ -ik_3 C_{g1} e^{-ik_3 z} - ik_4 D_{g1} e^{-ik_4 z} \\ +ik_5 A_{g2} e^{-ik_5 (h-z)} + ik_6 B_{g2} e^{-ik_6 (h-z)} \\ +ik_7 C_{g2} e^{-ik_7 (h-z)} + ik_8 D_{g2} e^{-ik_8 (h-z)} \end{pmatrix} \tag{2.60}$$

$$q_s = \mp\lambda_s dA_s \begin{pmatrix} -ik_1 A_{g1} Y_1^{sg} e^{-ik_1 z} - ik_2 B_{g1} Y_2^{sg} e^{-ik_2 z} \\ -ik_3 C_{g1} Y_3^{sg} e^{-ik_3 z} - ik_4 D_{g1} Y_4^{sg} e^{-ik_4 z} \\ +ik_5 A_{g2} Y_5^{sg} e^{-ik_5 (h-z)} + ik_6 B_{g2} Y_6^{sg} e^{-ik_6 (h-z)} \\ +ik_7 C_{g2} Y_7^{sg} e^{-ik_7 (h-z)} + ik_8 D_{g2} Y_8^{sg} e^{-ik_8 (h-z)} \end{pmatrix} \tag{2.61}$$

At the element nodes, Eq. (2.58)-(2.61) becomes:

At node 1, z = 0:

$$
\begin{aligned}
q_{i1} &= -\lambda dA_i \begin{pmatrix} -ik_1 A_{g1} Y_1^{ig} - ik_2 B_{g1} Y_2^{ig} - ik_3 C_{g1} Y_3^{ig} \\ -ik_4 D_{g1} Y_4^{ig} + ik_5 A_{g2} Y_5^{ig} e^{-ik5h} + ik_6 B_{g2} Y_6^{ig} e^{-ik6h} \\ +ik_7 C_{g2} Y_7^{ig} e^{-ik7h} + ik_8 D_{g2} Y_8^{ig} e^{-ik8h} \end{pmatrix} \\
q_{o1} &= -\lambda dA_o \begin{pmatrix} -ik_1 A_{g1} Y_1^{og} - ik_2 B_{g1} Y_2^{og} - ik_3 C_{g1} Y_3^{og} \\ -ik_4 D_{g1} Y_4^{og} + ik_5 A_{g2} Y_5^{og} e^{-ik5h} + ik_6 B_{g2} Y_6^{og} e^{-ik6h} \\ +ik_7 C_{g2} Y_7^{og} e^{-ik7h} + ik_8 D_{g2} Y_8^{og} e^{-ik8h} \end{pmatrix} \\
q_{g1} &= -\lambda_g dA_g \begin{pmatrix} -ik_1 A_{g1} - ik_2 B_{g1} - ik_3 C_{g1} - ik_4 D_{g1} + ik_5 A_{g2} e^{-ik5h} \\ +ik_6 B_{g2} e^{-ik6h} + ik_7 C_{g2} e^{-ik7h} + ik_8 D_{g2} e^{-ik8h} \end{pmatrix} \\
q_{s1} &= -\lambda_s dA_s \begin{pmatrix} -ik_1 A_{g1} Y_1^{sg} - ik_2 B_{g1} Y_2^{sg} - ik_3 C_{g1} Y_3^{sg} \\ -ik_4 D_{g1} Y_4^{sg} + ik_5 A_{g2} Y_5^{sg} e^{-ik5h} + ik_6 B_{g2} Y_6^{sg} e^{-ik6h} \\ +ik_7 C_{g2} Y_7^{sg} e^{-ik7h} + ik_8 D_{g2} Y_8^{sg} e^{-ik8h} \end{pmatrix}
\end{aligned}
\tag{2.62}
$$

At node 2, z = h:

$$
\begin{aligned}
q_{i2} &= \lambda dA_i \begin{pmatrix} -ik_1 A_{g1} Y_1^{ig} e^{-ik1h} - ik_2 B_{g1} Y_2^{ig} e^{-ik2h} - ik_3 C_{g1} Y_3^{ig} e^{-ik3h} \\ -ik_4 D_{g1} Y_4^{ig} e^{-ik4h} + ik_5 A_{g2} Y_5^{ig} + ik_6 B_{g2} Y_6^{ig} \\ +ik_7 C_{g2} Y_7^{ig} + ik_8 D_{g2} Y_8^{ig} \end{pmatrix} \\
q_{o2} &= \lambda dA_o \begin{pmatrix} -ik_1 A_{g1} Y_1^{og} e^{-ik1h} - ik_2 B_{g1} Y_2^{og} e^{-ik2h} - ik_3 C_{g1} Y_3^{og} e^{-ik3h} \\ -ik_4 D_{g1} Y_4^{og} e^{-ik4h} + ik_5 A_{g2} Y_5^{og} + ik_6 B_{g2} Y_6^{og} \\ +ik_7 C_{g2} Y_7^{og} + ik_8 D_{g2} Y_8^{og} \end{pmatrix} \\
q_{g2} &= \lambda_g dA_g \begin{pmatrix} -ik_1 A_{g1} e^{-ik1h} - ik_2 B_{g1} e^{-ik2h} - ik_3 C_{g1} e^{-ik3h} \\ -ik_4 D_{g1} e^{-ik4h} + ik_5 A_{g2} + ik_6 B_{g2} + ik_7 C_{g2} + ik_8 D_{g2} \end{pmatrix} \\
q_{s2} &= \lambda_s dA_s \begin{pmatrix} -ik_1 A_{g1} Y_1^{sg} e^{-ik1h} - ik_2 B_{g1} Y_2^{sg} e^{-ik2h} - ik_3 C_{g1} Y_3^{sg} e^{-ik3h} \\ -ik_4 D_{g1} Y_4^{sg} e^{-ik4h} + ik_5 A_{g2} Y_5^{sg} + ik_6 B_{g2} Y_6^{sg} \\ +ik_7 C_{g2} Y_7^{sg} + ik_8 D_{g2} Y_8^{sg} \end{pmatrix}
\end{aligned}
\tag{2.63}
$$

In a matrix form:

$$\hat{\mathbf{q}}_{\text{node}} = \mathbf{M}(k,\omega_n)\mathbf{A} \tag{2.64}$$

Substituting Eq.(2.56) into Eq.(2.64), yields

$$\hat{\mathbf{q}}_{\text{node}} = \mathbf{K}(k,\omega_n)\hat{\mathbf{T}}_{\text{node}} \tag{2.65}$$

in which $\mathbf{K}(k,\omega_n) = \mathbf{M}(k,\omega_n)\mathbf{H}^{-1}(k,\omega_n)$, representing the spectral element stiffness matrix, in resemblance to that of the finite element method. However, the spectral element matrix is exact and frequency-dependent.

The matrix components of Eq. (2.64) are

$$\begin{pmatrix} q_{i1} \\ q_{o1} \\ q_{g1} \\ q_{s1} \\ q_{i2} \\ q_{o2} \\ q_{g2} \\ q_{s2} \end{pmatrix} = \begin{pmatrix} b_{11} & b_{12} & b_{13} & b_{14} & b_{15} & b_{16} & b_{17} & b_{18} \\ b_{21} & b_{22} & b_{23} & b_{24} & b_{25} & b_{26} & b_{27} & b_{28} \\ b_{31} & b_{32} & b_{33} & b_{34} & b_{35} & b_{36} & b_{37} & b_{38} \\ b_{41} & b_{42} & b_{43} & b_{44} & b_{45} & b_{46} & b_{47} & b_{48} \\ b_{51} & b_{52} & b_{53} & b_{54} & b_{55} & b_{56} & b_{57} & b_{58} \\ b_{61} & b_{62} & b_{63} & b_{64} & b_{65} & b_{66} & b_{67} & b_{68} \\ b_{71} & b_{72} & b_{73} & b_{74} & b_{75} & b_{76} & b_{77} & b_{78} \\ b_{88} & b_{82} & b_{83} & b_{84} & b_{85} & b_{86} & b_{87} & b_{88} \end{pmatrix} \begin{pmatrix} A_{g1} \\ B_{g1} \\ C_{g1} \\ D_{g1} \\ A_{g2} \\ B_{g2} \\ C_{g2} \\ D_{g2} \end{pmatrix} \tag{2.66}$$

where

$$b_{11} = ik_1 Y_1^{ig},\ b_{12} = ik_2 Y_2^{ig},\ b_{13} = ik_3 Y_3^{ig},\ b_{14} = ik_4 Y_4^{ig}$$
$$b_{15} = -ik_5 Y_5^{ig} e^{-ik5h},\ b_{16} = -ik_6 Y_6^{ig} e^{-ik6h},\ b_{17} = -ik_7 Y_7^{ig} e^{-ik7h},\ b_{18} = -ik_8 Y_8^{ig} e^{-ik8h}$$

$$b_{21} = ik_1 Y_1^{og},\ b_{22} = ik_2 Y_2^{og},\ b_{23} = ik_3 Y_3^{og},\ b_{24} = ik_4 Y_4^{og}$$
$$b_{25} = -ik_5 Y_5^{og} e^{-ik5h},\ b_{26} = -ik_6 Y_6^{og} e^{-ik6h},\ b_{27} = -ik_7 Y_7^{og} e^{-ik7h},\ b_{28} = -ik_8 Y_8^{og} e^{-ik8h}$$

$$b_{31} = ik_1,\ b_{32} = ik_2,\ b_{33} = ik_3,\ b_{34} = ik_4$$
$$b_{35} = -ik_5 e^{-ik5h},\ b_{36} = -ik_6 e^{-ik6h},\ b_{37} = -ik_7 e^{-ik7h},\ b_{38} = -ik_8 e^{-ik8h}$$

$$b_{41} = ik_1 Y_1^{sg},\ b_{42} = ik_2 Y_2^{sg},\ b_{43} = ik_3 Y_3^{sg},\ b_{44} = ik_4 Y_4^{sg}$$
$$b_{45} = -ik_5 Y_5^{sg} e^{-ik5h},\ b_{46} = -ik_6 Y_6^{sg} e^{-ik6h},\ b_{47} = -ik_7 Y_7^{sg} e^{-ik7h},\ b_{48} = -ik_8 Y_8^{sg} e^{-ik8h}$$

$$b_{51} = -ik_1 Y_1^{ig} e^{-ik_1 h},\ b_{52} = -ik_2 Y_2^{ig} e^{-ik_2 h},\ b_{53} = -ik_3 Y_3^{ig} e^{-ik_3 h},\ b_{54} = -ik_4 Y_4^{ig} e^{-ik_4 h}$$
$$b_{55} = ik_5 Y_5^{ig},\ b_{56} = ik_6 Y_6^{ig},\ b_{57} = ik_7 Y_7^{ig},\ b_{58} = ik_8 Y_8^{ig}$$

$$b_{61} = -ik_1 Y_1^{og} e^{-ik_1 h},\ b_{62} = -ik_2 Y_2^{og} e^{-ik_2 h},\ b_{63} = -ik_3 Y_3^{og} e^{-ik_3 h},\ b_{64} = -ik_4 Y_4^{og} e^{-ik_4 h}$$
$$b_{65} = ik_5 Y_5^{og},\ b_{66} = ik_6 Y_6^{og},\ b_{67} = ik_7 Y_7^{og},\ b_{68} = ik_8 Y_8^{og}$$

$$b_{71} = -ik_1 e^{-ik_1 h},\ b_{72} = -ik_2 e^{-ik_2 h},\ b_{73} = -ik_3 e^{-ik_3 h},\ b_{74} = -ik_4 e^{-ik_4 h}$$
$$b_{75} = ik_5,\ b_{76} = ik_6,\ b_{77} = ik_7,\ b_{78} = ik_8$$

$$b_{81} = -ik_1 Y_1^{sg} e^{-ik_1 h},\ b_{82} = -ik_2 Y_2^{sg} e^{-ik_2 h},\ b_{83} = -ik_3 Y_3^{sg} e^{-ik_3 h},\ b_{84} = -ik_4 Y_4^{sg} e^{-ik_4 h}$$
$$b_{85} = ik_5 Y_5^{sg},\ b_{86} = ik_6 Y_6^{sg},\ b_{87} = ik_7 Y_7^{sg},\ b_{88} = ik_8 Y_8^{sg}$$

2.4.3.3 General solution BHE heat equations

Having determined the eigenvalues and the integration constants, the general solution of the single U-tube BHE system of equations can then be obtained by summing over all eigenfunctions (corresponding to k_1 , k_2 , …, k_8) and frequencies, as

$$\mathbf{T}(z,t) = \sum_n \begin{pmatrix} \mathbf{A}_1 e^{-ik_1 z} + \mathbf{B}_1 e^{-ik_2 z} + \mathbf{C}_1 e^{-ik_3 z} + \mathbf{D}_1 e^{-ik_4 z} \\ + \mathbf{A}_2 e^{-ik_5 (L-z)} + \mathbf{B}_2 e^{-ik_6 (L-z)} + \mathbf{C}_2 e^{-ik_7 (L-z)} + \mathbf{D}_2 e^{-ik_8 (L-z)} \end{pmatrix} e^{i\omega_n t} \tag{2.67}$$

where $\mathbf{T}(z,t)$ represents T_i, T_o, T_g and T_s.

2.5 Spectral element mesh assembly and solution

Eqs.(2.31) and (2.67) solve the temperature distributions in all BHE components and the surrounding soil layer. For a multilayer system, assembly of the global system of equations is necessary. For this, the finite element techniques for element numbering, node numbering and mesh assembly are utilized (Fagan, 1992). The solution of the global system of equations is conducted using the IMSL mathematical library subroutine, *lin_sol_gen*, which solves a general system of linear equations $\boldsymbol{Ax} = \boldsymbol{b}$, (IMSL 2019). Eq.(2.47) is solved using the IMSL subroutine, DZPOCC, which solves for the roots of a polynomial with complex coefficients. The reconstruction of the time domain is carried out using the inverse FFT algorithm.

2.6 Model Verification

Exact solution describing heat flow in a single U-tube BHE embedded in a multilayer soil mass has not been introduced before. Accordingly, verification of the proposed model is done by comparing its computational results with those obtained from analytical solutions of simplified cases. The BHE model is verified against the van Genuchten and Alves (1982) solution of a one-dimensional advective-dispersive solute transport equation. The soil mass model is verified against the Carslaw and Jaeger (1959) solution of an infinite line source embedded in a semi-infinite solid.

2.6.1 Verification against van Genuchten and Alves solution

van Genuchten and Alves provided an analytical solution to a one-dimension advective-diffusive partial differential equation of the form:

$$R\frac{\partial c}{\partial t}-D\frac{\partial^2 c}{\partial z^2}+F\frac{\partial c}{\partial z}+\mu c-\gamma=0 \tag{2.68}$$

The initial and boundary conditions are:

$$\begin{aligned} &c(z,0)=A(z)=\frac{\gamma}{\mu}+\left(C_{\text{int}}-\frac{\gamma}{\mu}\right)e^{\frac{(F-\overline{u})}{2D}z} \\ &c(0,t)=\begin{cases} C_{\text{in}} & 0<t<t_o \\ 0 & t>t_o \end{cases} \\ &\frac{\partial c}{\partial z}(\infty,t)=0 \end{aligned} \tag{2.69}$$

where R, D, F, μ and γ are constants, and $\overline{u}=F\sqrt{1+\frac{4\mu D}{F^2}}$. The initial value, $A(z)$ in Eq.(2.69), is determined by solving the steady state condition of Eq.(2.68).

Their solution is:

$$c(z,t)=A(z)+\frac{1}{2}(C_{\text{in}}-C_{\text{int}})\left(\begin{aligned} &e^{\frac{(F-\overline{u})}{2D}z}\operatorname{erfc}\left[\frac{Rz-\overline{u}t}{2(DRt)^{\frac{1}{2}}}\right] \\ &+e^{\frac{(F+\overline{u})}{2D}z}\operatorname{erfc}\left[\frac{Rz+\overline{u}t}{2(DRt)^{\frac{1}{2}}}\right] \end{aligned}\right) \quad 0<t\le t_o \tag{2.70}$$

and

$$c(z,t)=A(z)+\frac{1}{2}(C_{\text{in}}-C_{\text{int}})\left(e^{\frac{(F-\overline{u})}{2D}z}\operatorname{erfc}\left[\frac{Rz-\overline{u}t}{2(DRt)^{\frac{1}{2}}}\right]+e^{\frac{(F+\overline{u})}{2D}z}\operatorname{erfc}\left[\frac{Rz+\overline{u}t}{2(DRt)^{\frac{1}{2}}}\right]\right)$$
$$-\frac{1}{2}C_{\text{in}}\left(e^{\frac{(F-\overline{u})}{2D}z}\operatorname{erfc}\left[\frac{Rz-\overline{u}(t-t_o)}{2(DR(t-t_o))^{\frac{1}{2}}}\right]+e^{\frac{(F+\overline{u})}{2D}z}\operatorname{erfc}\left[\frac{Rz+\overline{u}(t-t_o)}{2(DR(t-t_o))^{\frac{1}{2}}}\right]\right)\quad t>t_0 \tag{2.71}$$

The van Genuchten and Alves model and the proposed spectral element model are employed to solve heat flow in a heat pipe embedded in a constant temperature environment. The geometry and material parameters are:

Pipe length	= 100m
Pipe radius, r_i	= 0.016 m
Fluid ρc	= 4.1298E6 J/m^3 K
Fluid λ	= 0.56 W/m K
Fluid velocity, u	= 0.1 and 1 m/s
b_{ig}	=12 W/m^2 K

The initial steady state temperature, and the temperature at the pipe inlet are:

$$T_{st}(t=0,z)=\ 10\,^{\circ}\text{C}$$
$$T_{\text{in}}(t,z=0)=\begin{cases}20\,^{\circ}\text{C} & 0<t\le 4000\,s\\ 0\,^{\circ}\text{C} & 4000<t<\infty\,s\end{cases} \tag{2.72}$$

In the spectral element model, T_{in} is equal to $T_{st}+\Delta T_{\text{in}}$, where, in this case, ΔT_{in} = 10 ºC.

To compare between the two models, the van Genuchten and Alves parameters need to be adjusted to match the physical parameters of the spectral element model. Comparing Eq. (2.1) to Eq.(2.68), yields:

$$R=\rho c dV_i;\qquad D=\lambda dV_i;$$
$$F=\rho c u\, dV_i;\qquad \mu=b_{ig}dS_{ig};$$
$$\gamma=0;\qquad C_{\text{int}}=T_{st};\qquad C_{\text{in}}=T_{\text{in}} \tag{2.73}$$

Also, and as the proposed model is general and applicable to a multiple component domain, the following adjustments are necessary:

a) The thermal interaction coefficient, b_{og}, is made relatively small (0.01 W/m^{2}K) to insure insulation, such that there is no heat flow between pipe-in and pipe-out.

b) The thermal interaction coefficients of the grout-soil film and the soil film-soil mass are made relatively high ($b_{gs} = b_{ss} = 1000$ W/m^{2}K) so insure a full contact.

c) The soil mass temperature is made constant, by setting $\overline{A}_m$ in Eq.(2.32), equal to zero.

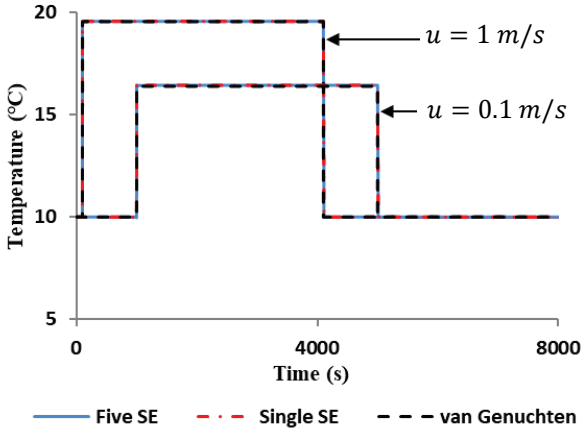

(a)

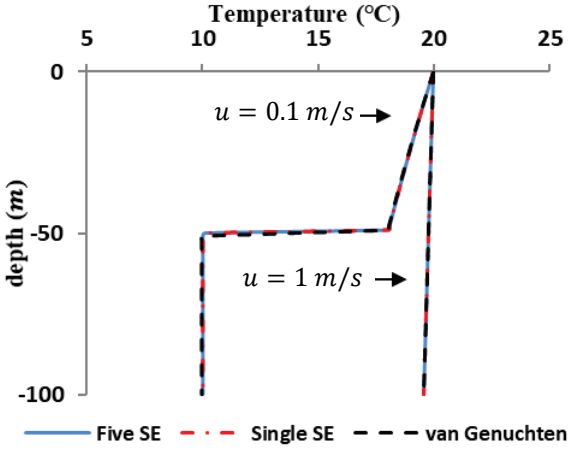

(b)

Figure 2.3: Spectral element model vs. van Genuchten and Alves solution: (a) with time, (b) along the pipe

Using the spectral element model, two analyses were conducted: one using one spectral element only, with element length equal to 100 m; and another using 5 elements, with an element length equal to 20 m. Two fluid velocities were analyzed: 0.1 m/s and 1 m/s.

The input temperature time histories of T_{in} and T_{st} were transformed to the frequency domain using the forward FFT. 16384 samples, with a sample rate of 1s, were used, giving a time window of 16384s.

Figure 2.3a, shows the temperature distributions versus time at $z = 100\,m$, obtained from the van Genuchten and Alves solution and the spectral element model, for both mesh sizes and fluid velocities. Figure 2.3b, shows the temperature distributions along the depth of the BHE, at time $t = 500\,s$, obtained from both models. Apparently, the computational results are nearly identical.

2.6.2 Verification against Carslaw and Jaeger infinite line source (ILS) model

Carslaw and Jaeger (1959) provided an analytical solution to heat flow in a semi-infinite solid, subjected to a constant heat flow from an infinite line source. In such a domain, only radial heat flow exists, and the temperature distribution is described as

$$T = T_{st} + \frac{q}{2\pi\lambda}\int_{\beta}^{\infty}\frac{e^{-\beta^2}}{\beta}d\beta \tag{2.74}$$

in which

$$\beta = \frac{r}{2\sqrt{\alpha t}}, \quad \text{and} \quad \alpha = \frac{\lambda}{\rho c} \tag{2.75}$$

with r is the radial distance from the source, t is the time, λ is the soil heat conductivity, ρ is the mass density, c is the heat capacity, T_{st} is the initial soil temperature, and q is the heat flux per meter length of the line source (pipe). Solution for this semi-infinite upper limit integral is available in exact form for $\beta < 0.2$, and in tables, for larger values of β. For $\beta < 0.2$, the solution to the integrand of Eq. (2.74) is:

$$I(\beta) = \ln\frac{1}{\beta} + \frac{\beta^2}{2} - \frac{\beta^4}{8} - 0.2886 \tag{2.76}$$

The tabulated values $\beta < 3.1$ are available in Ingersoll *et al*. (1954).

In such a domain, it is assumed that there is a full contact between the heat source and the medium. To simulate such a domain, the temperature along the pipe must be constant. This can be done by assuming a high flow rate, generated by the circulating fluid.

The ILS model and the proposed spectral element model are employed to solve heat flow in a soil mass consisting of two layers, and subjected to a constant line heat source equal to 0 ºC. The initial temperature, T_{st} , is assumed 10 ºC. The material and geometrical parameter of the system are shown in Table 2.1, and illustrated in Figure 2.4.

The ILS model does not recognize the layers, and hence the temperature distributions are obtained for each layer, regardless of the other layer. In the spectral element model, however, this is possible, but requires two spectral elements.

Table 2.1. Material and geometrical parameters

Parameter	Value	Parameter	Value
Borehole:		**Grout:**	
Borehole length	100 m	Density, ρ_g	1420 kg/m^3
Borehole diameter	0.12 m	Specific thermal capacity, c_g	1197 J/(kg.K)
Pipe external diameter	0.026 m	Thermal conductivity, λ_g	0.62 W/(m.K)
Pipe roughness	3 E-6	**Soil:**	
Pipe thermal conductivity, λ_p	0.42 W/(mK)	Film thickness	0.5 cm
Fluid:		density , ρ_s	1680 kg/m^3
Density, ρ	1000 kg/m^3	Specific thermal capacity , c_s	400 J/(kg.K)
Specific thermal capacity, c	4186 J/(kg.K)	Thermal conductivity, λ_s at $z \geq -50m$	2.5 W/(m.K)
Thermal conductivity, λ	0.56 W/(mK)	Thermal conductivity, λ_s at $z \leq -50m$	5 W/(m.K)
Dynamic viscosity, μ	0.001 Pa.s		

In the spectral model, the inlet temperature, T_{in}, is equal to 0 ºC, and the fluid velocity, u, is equal to 5 m/s, a relatively high velocity to insure a constant 0 ºC along the whole length of the BHE. The thermal interaction coefficients, b_{ig}, b_{og}, b_{gs} and b_{ss}, are calculated using Eq.(2.12)-(2.21). The homogeneous fictitious boundary of the soil layer, R, is calculated by:

$$R = \sqrt{6\alpha t} \tag{2.77}$$

where α is the thermal diffusivity of the soil and t is the time when the temperature at point R reaches its maximum (Carslaw and Jaeger 1959).

The number of FFT samples is 16384, with a sample rate of 1 hr, giving a time window of 16384 hr. The number of the Fourier-Bessel series terms is 500. Four calculations with different transient times of 5 days, 25 days, 50 days and 100 days were conducted.

Figure 2.5 shows the computational results at $z = 49m$ (top layer) and at $z = 51m$ (bottom layer), along the radial direction, obtained from both models. The radial distances from the line heat source are chosen such that they are solvable by Eq.(2.76), or available in the Carslaw and Jaeger tables. Apparently, the two results are nearly identical.

Note that as the ILS model adopts a Neumann boundary condition with constant heat flux and our model adopts a time dependent Dirichlet boundary condition, we compared the results by first running our model with a prescribed T_{in} at the inlet of pipe-in. Then we calculate the resulting heat flux at a certain time and depth along the BHE as a post processing. This heat flux is applied to the ILS model to calculate the soil temperature.

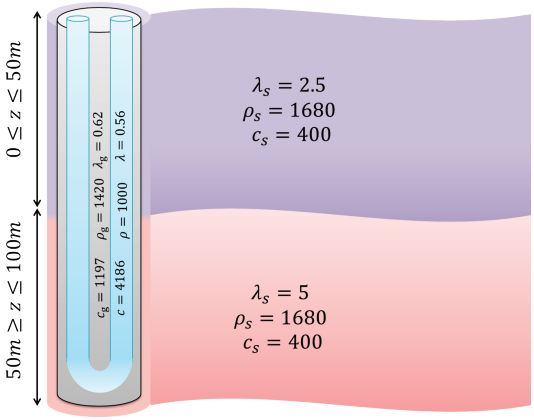

Figure 2.4: A schematic representation of a semi-infinite solid subjected to a constant heat source

2.7 Numerical examples

To illustrate the model computational capabilities, a numerical example illustrating the behavior of a shallow geothermal system subjected to a varying temperature signal is introduced. A 100 m single U-tube BHE embedded in a soil mass consisting of 5 layers with different physical properties, Figure 2.6, is studied. The material and geometrical properties are given in Table 2.2. Relatively short and long terms were studied.

For the short term, the initial and boundary conditions are:

$$T_{st} = 10 \qquad t = 0$$

$$T_{\text{in}} = \begin{cases} 20 & t < 5h \\ 10 & 5h \le t < 7h \\ 18 & 7h \le t < 12h \\ 10 & 12\ h \le t < 14h \\ 16 & 14h \le t < 19h \\ 10 & 19h \le t \end{cases} \tag{2.78}$$

where it can be seen that the BHE has a 2 hours off after every 5 hours of operation.

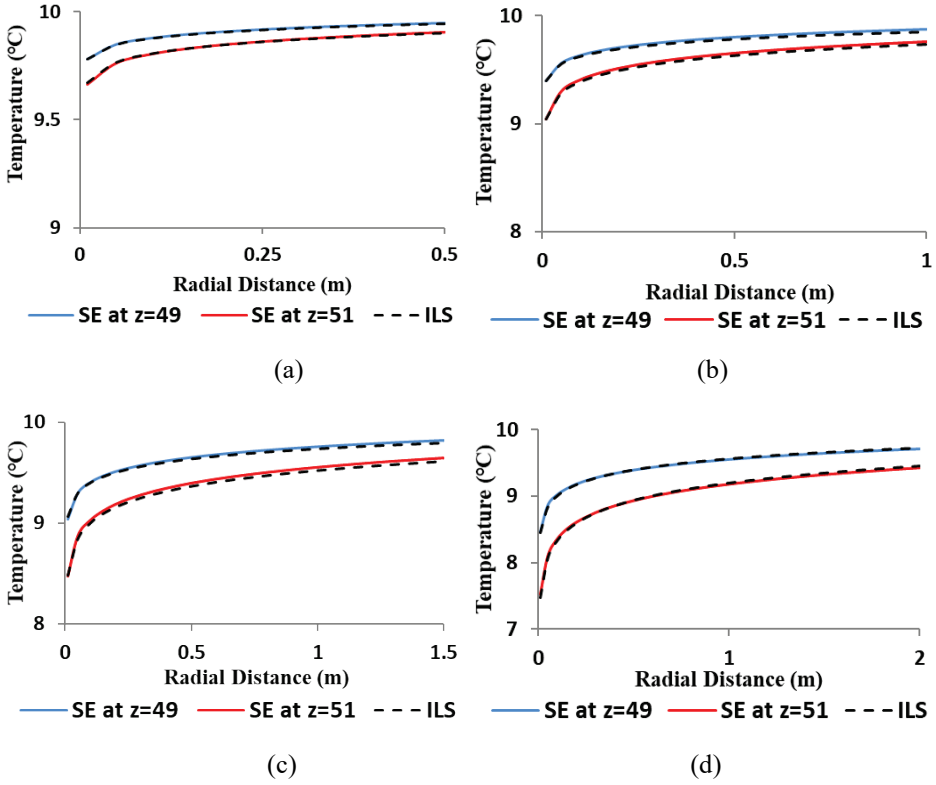

Figure 2.5: SE model vs. ILS model. (a) 5 days, (b) 25 days, (c) 50 days, (d) 100 days

The frequency discretization of T_{in} was conducted using 16,384 (214) FFT samples with a sample rate of 10 seconds, giving a time window of approximately 45.5 hours. The thermal coefficients b_{ig}, b_{og} , b_{gs} and b_{ss} are determined using Eq.(2.12)-(2.21). The domain is discretized using 5 spectral elements, one for each layer.

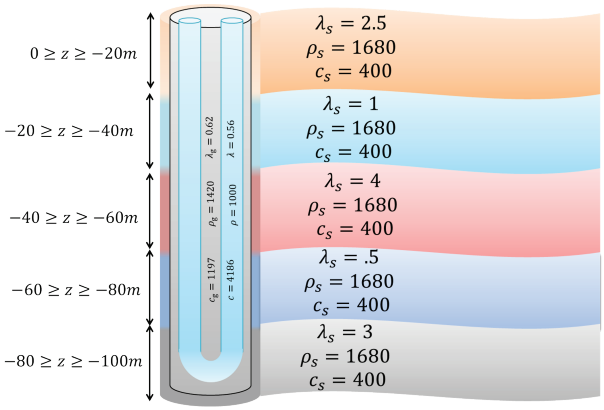

Figure 2.6: A schematic representation of a 5 layers shallow geothermal system

Table 2.2: Material and geometrical parameters

Parameter	Value	Parameter	Value
Borehole:		**Soil:**	
Borehole length	100 m	Film thickness	0.5 cm
Borehole diameter	0.126 m	Density , ρ_s	1680 kg/m^3
Pipe external diameter	0.032 m	Specific thermal capacity , c_s	400 J/(kg.K)
Pipe roughness	3 E-6		
Pipe thermal conductivity	0.42 W/(mK)	$0 \geq z \geq -20m$	
		Thermal conductivity, λ_s	2.5 W/(m.K)
Fluid:			
Density, ρ	1000 kg/m^3	$-20 \geq z \geq -40m$	
Specific thermal capacity, c	4186 J/(kg.K)	Thermal conductivity, λ_s	1 W/(m.K)
Thermal conductivity, λ	0.56 W/(mK)	$-40 \geq z \geq -60m$	
Dynamic viscosity, μ	0.001 Pa.s	Thermal conductivity, λ_s	4 W/(m.K)
Velocity, u	0.5 m/s	$-60 \geq z \geq -80m$	
		Thermal conductivity, λ_s	0.5 W/(m.K)
Grout:			
Density, ρ_{g}	1420 kg/m^3	$-80 \geq z \geq -100m$	
Specific thermal capacity, c_{g}	1197 J/(kg.K)	Thermal conductivity, λ_s	3 W/(m.K)
Thermal conductivity, λ_{g}	0.62 W/(m.K)		

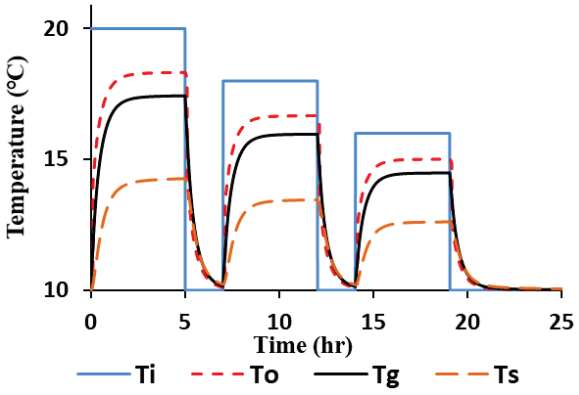

(a)

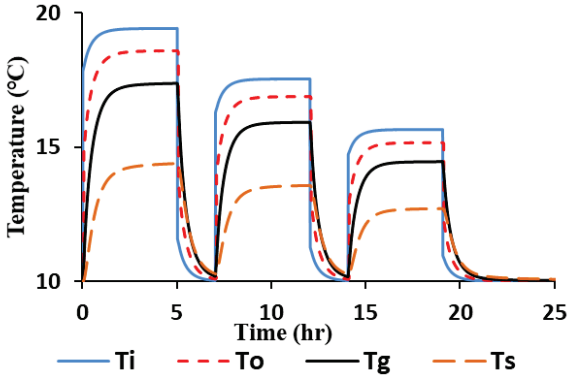

(b)

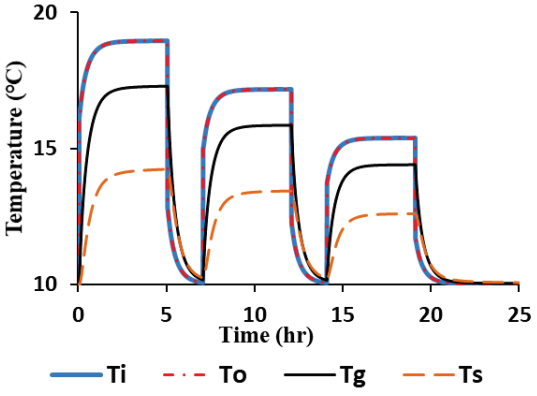

(c)

Figure 2.7 : T_i, T_o, T_g and T_s at (a) $z = 0\ m$, (b) $z = 50\ m$, (c) $z = 100\ m$

Figure 2.7 shows the temperature distributions versus time for pipe-in (T_i), pipe-out (T_o), grout (T_g) and soil film (T_s) at different depths: $z = 0,\ 50$ and 100 m. The figure shows that, although not verified quantitatively, the response signals are smooth and exhibit thermal dissipation with distance.

For the relatively long term, the inlet temperature varies as

$$T_{\text{in}} = \begin{cases} 20 & t < 15000 \text{ hours} \\ 10 & 15000 \text{ hours} \le t \end{cases} \tag{2.79}$$

The frequency discretization of T_{in} was conducted using 32,768 (2^{15}) FFT samples with a sample rate of 1 hour, giving a time window of approximately 3.5 years.

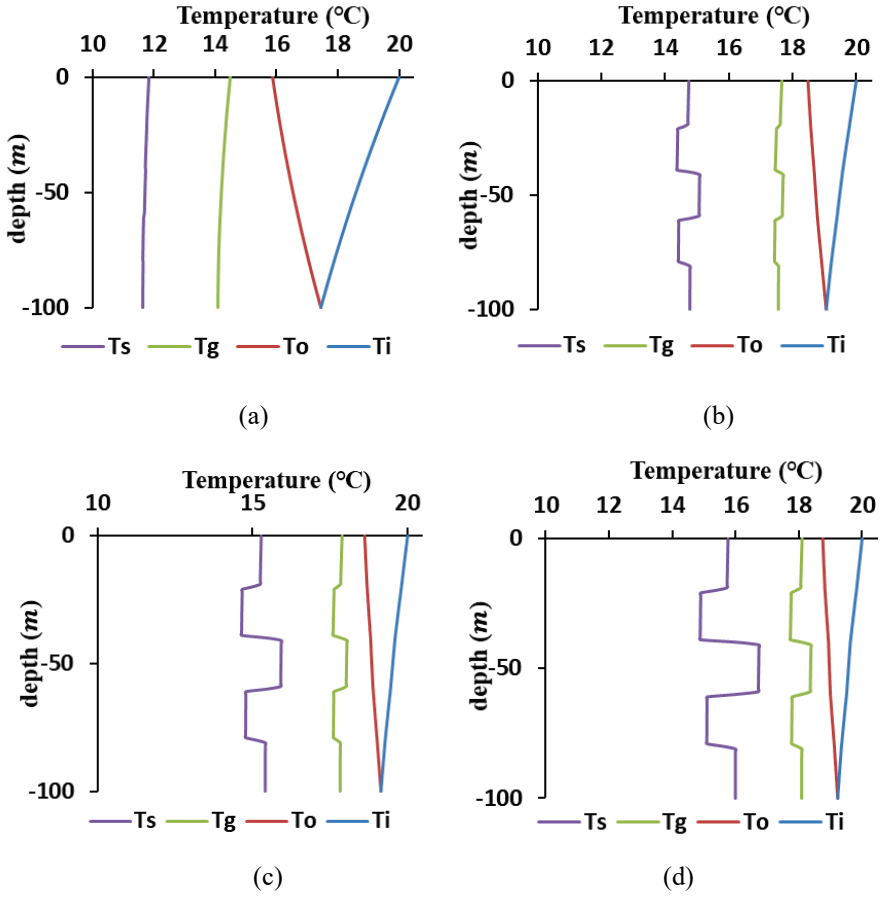

Figure 2.8 : T_i, T_o, T_g and T_s along the BHE at (a) 1 hour , (b) 1 day , (c) 1 month, (d) 1 year

Figure 2.8 shows the temperature distributions along the BHE in z direction for pipe-in (T_i), pipe-out (T_o), grout (T_g) and soil film temperature (T_s) at different times: 1 hour, 1 day, 1 month and 1 year. It can be seen that at the first hour, the effect of the different thermal parameters of the surrounding soil layers was not apparent, but became significant with increasing time.

This example shows that the model is capable of calculating heat flow in a relatively complicated geometry, consisting of multiple layers, and subjected to a complicated boundary conditions consisting of multiple pulses. The CPU time of conducting this example was on average less than 1 minute for 100 output values in z domain, and 30 output values in *r* domain, using Intel core 2.66 GHz processor.

2.8 Conclusion

In this chapter, a spectral element model for the simulation of transient conduction–convection heat flow in an axisymmetric shallow geothermal system consisting of a single U-tube borehole heat exchanger embedded in a layered soil mass is introduced. A new two-node spectral element is formulated. For a homogeneous domain, the heat equations are solved analytically. For a multiple nonhomogeneous domain with different physical properties, the finite element technique is utilized to assemble an algebraic system of linear equations, $\mathbf{A}x = \mathbf{b}$, which can be solved using standard solvers. One element is sufficient to describe heat flow in all BHE components and its surrounding soil layer. For a multilayer system, the number of elements is equal to the number of layers, making the model highly efficient.

Despite the apparent rigor of the model, it is relatively easy to implement in computer codes. Standard MAPLE commands and IMSL subroutines can be utilized to solve the eigenfunction and the global system of equations. As a result of the model accuracy and computationally efficiency, it can be utilized directly for forward analysis, or in an iterative scheme for parameter identification of system thermal parameters. Also, it is generic and can be utilized for modelling a wide range of engineering mechanics applications involving linear heat flow or other diffusive-advective processes occurring in relatively complicated geometries.

3

A superposition model for heat flow in an infinite medium subjected to multiple Cylindrical Heat Sources

This chapter introduces analytical solutions for transient heat conduction in an infinite solid mass subjected to a varying single or multiple cylindrical heat sources. The solutions are formulated for two types of boundary conditions: a time-dependent Neumann boundary condition, and a time-dependent Dirichlet boundary condition. The initial and boundary value problem have been solved for a single heat source using the modified Bessel function, for the spatial domain, and the fast Fourier transform, for the temporal domain. For multiple heat sources, the superposition principle has been applied directly for the Neumann boundary condition, but for the Dirichlet boundary condition, an analytical coupling was conducted, which allows for the exact thermal interaction between all involved heat sources. The heat sources can exhibit different time-dependent signals and can have any distribution in space. The solutions are verified against the analytical solution given by Carslaw and Jaeger for a constant Neumann boundary condition, and the finite element solution for both types of boundary conditions. Compared to these two solutions, the proposed solutions are exact at all radial distances, highly elegant, robust and easy to implement.

This chapter is based on BniLam N. and Al-Khoury R. (2016). Transient heat conduction in an infinite medium subjected to multiple cylindrical heat sources: An application to shallow geothermal systems. Renewable Energy, Volume 97, Pages 145-154.

3.1 Introduction

Most of the currently utilized analytical solutions for heat equations in solid domains are based on the work provided by Carslaw and Jaeger (1959), who seem to be the first to introduce a comprehensive treatment of heat conduction in solids subjected to different combinations of initial and boundary conditions. They introduced solutions to heat flow in finite, semi-infinite and infinite domains subjected to point, line, plane, spherical and cylindrical heat sources. In this chapter, the focus is placed on heat flow in an infinite domain subjected to cylindrical heat sources, a topic which is central in many engineering applications, mainly in modelling shallow geothermal systems (Deerman and Kavanaugh 1991, Gu and O'Neal 1995, Kavanaugh and Rafferty 1997, Zanchini and Pulvirenti 2013).

A shallow geothermal system, known as geothermal heat pump (GHP), and also ground source heat pump (GSHP), is a source of renewable energy that utilizes the earth heat energy from shallow depths for heating and cooling of buildings. It works by circulating a fluid in a borehole heat exchanger (BHE) which ensures a good thermal interaction with the surrounding soil mass. In many of the currently available models for shallow geothermal systems, the BHE is considered as a constant heat source.

Usually, shallow geothermal systems consist of multiple borehole heat exchangers. Modelling such a system typically requires numerical methods, such as the finite difference (Yavuzturk et al 1999, Lee and Lam 2008), finite volume (Nabi and Al-Khoury 2012a and 2012b), or finite element (Diersch et al. 2011a and 2011b, Al-Khoury 2012b). Nevertheless, some limited number of analytical and semi-analytical models has been introduced, notably those given by Eskilson and Claesson (1988), Pasquier and Marcotte (2013) and Erol et al (2015). The basic idea behind the possibility of utilizing analytical methods for solving multiple heat sources problems is the use of the superposition principle.

Eskilson and Claesson (1988) introduced a semi-analytical model for heat flow in a 1D finite line heat source embedded in an axisymmetric solid mass. They utilized the principle of superposition to account for multiple heat sources. They introduced what they termed "error" to approximate the difference between heat flow due to a single heat source and that of multiple heat sources. The approximation is made using the Fourier expansion to the first order of the thermal interaction between the heat sources. Their solution is effective for symmetric heat sources distribution, and necessitates separation between heat sources at the corners of the geometry and those in the middle.

Pasquier and Marcotte (2013) introduced a semi-analytical model for heat flow in a solid mass subjected to multiple heat sources with time-varying heat fluxes and temperatures. The model allows for the imposition of heat sources with different heat fluxes or temperatures. They applied the fast Fourier transform for the temporal domain and the superposition principle for the spatial domain. The multiple heat sources system is solved using an iterative algorithm, which couples the thermal interaction between the involved heat sources. The algorithm has been applied to the infinite line source model, but can be

extended to any model that can be decomposed into an incremental heat flux function, and the involved integral can be evaluated for a unit rectangular heat pulse, such as the finite line source and the infinite cylindrical line source.

Erol et al. (2015) introduced a modified Green's function for heat flow in a porous domain subjected to a constant line heat source with a finite length. The prescribed heat flux is discontinuous, described by a rectangular pulses function. The convolution theory in time domain is utilized to solve the initial and boundary value problem for a single heat source. For the multiple heat sources, they utilized the superposition principle by summing up the temporal convolved functions of the heat sources.

In this chapter, we elaborate on these models and introduce analytical solutions for transient heat flow in an infinite solid mass subjected to a varying single or multiple cylindrical heat sources. Solutions for two types of boundary conditions are introduced: a prescribed heat flux (Neumann boundary condition), and a prescribed temperature (Dirichlet boundary condition). We solve the initial and boundary value problem using the modified Bessel series and the fast Fourier transform. For multiple heat sources, we apply directly the superposition principle for the Neumann boundary condition. For the Dirichlet boundary condition, an analytical coupling allowing for the thermal interaction between all involved heat sources, is conducted. The heat sources can exhibit different time-dependent signals, and can have any distribution in space.

3.2 Single heat source in a solid mass

Heat conduction in an infinite cylinder constituting a homogeneous, isotropic solid is described as

$$\frac{1}{\alpha}\frac{\partial T}{\partial t}-\frac{\partial^2 T}{\partial r^2}-\frac{1}{r}\frac{\partial T}{\partial r}=0 \tag{3.1}$$

where $T=T(r,t)$ is the temperature of the solid mass; r is the radial distance; and α (m^2/s) is its thermal diffusivity, defined as

$$\alpha=\frac{\lambda}{\rho c} \tag{3.2}$$

in which λ (W/mK) is the thermal conductivity; ρ (kg/m^3) is the mass density; and c (J/kg.K) is the specific heat capacity.

The initial condition is:

$$T\left(r, t=0\right)=T_{st} \tag{3.3}$$

in which T_{st} is the initial steady state temperature before operating the heat sources.

The boundary condition at infinity is:

$$\Delta T\big|_{r=\infty,t} = T\big|_{r=\infty,t} - T_{st} = 0 \tag{3.4}$$

which implies that the heat source effect vanishes at far distances.

The boundary condition at the sources might be any of two types:

Neumann boundary condition:

$$-\lambda \frac{dT}{dr}\bigg|_{r=r_s} = q_s(t) \tag{3.5}$$

Dirichlet boundary condition:

$$T\big|_{r=r_s} = T_s(t) \tag{3.6}$$

where $q_s(t)$ is the heat source flux (W/m); $T_s(t)$ is the heat source temperature; and r_s is the radius of the heat source (for a line source, r_s approaches zero).

Applying Fourier transform of Eq. (3.1), gives (Al-Khoury 2012b):

$$\frac{i\omega}{\alpha}\hat{T} - \frac{\partial^2 \hat{T}}{\partial r^2} - \frac{1}{r}\frac{\partial \hat{T}}{\partial r} = 0 \tag{3.7}$$

where $\hat{T}$ is the temperature frequency response. Eq. (3.7) is a complex ordinary differential equation, describing a modified Bessel equation. The solution of this equation can be expressed as

$$\hat{T}(r,\omega) = AK_o(kr) + BI_o(kr) \tag{3.8}$$

where

$$k = \sqrt{\frac{i\omega}{\alpha}} \tag{3.9}$$

and I_o and K_o are the first and second kind of modified Bessel functions.

Applying the boundary condition, Eq.(3.4), to Eq.(3.8), leads to

$$\Delta \hat{T}\big|_{r=\infty} = AK_o(\infty) + BI_o(\infty) = 0 \tag{3.10}$$

As $K_o(\infty) = 0$ and $I_o(\infty) = \infty$, it implies that $B = 0$, yielding

$$\hat{T}(r,\omega) = AK_o(kr) \tag{3.11}$$

Applying the prescribed heat flux boundary condition, Eq.(3.5), to Eq.(3.11), leads to

$$A = \frac{\hat{q}_s(\omega)}{\lambda k K_1(k r_s)} \tag{3.12}$$

Substituting this equation into Eq. (3.11), gives

$$\hat{T}(r,\omega) = \frac{\hat{q}_s(\omega)}{\lambda k} \frac{K_o(k r)}{K_1(k r_s)} \tag{3.13}$$

Applying the prescribed temperature boundary condition, Eq. (3.6), to Eq. (3.11), leads to

$$A = \frac{\hat{T}_s(\omega)}{K_o(k r_s)} \tag{3.14}$$

Substituting this equation into Eq. (3.11), gives

$$\hat{T}(r,\omega) = \hat{T}_s(\omega) \frac{K_o(k r)}{K_o(k r_s)} \tag{3.15}$$

Eqs. (3.13) and (3.15) are the spectral solutions to the heat conduction equation in an infinite solid domain subjected to a single cylindrical heat source, describing a prescribed heat flux and a prescribed temperature, respectively.

Applying the inverse fast Fourier transform to these equations gives:

Prescribed heat source flux:

$$T(r,t) = \sum\nolimits_n \frac{\hat{q}_s(\omega_n)}{\lambda k} \frac{K_o(k r)}{K_1(k r_s)} e^{i\omega_n t} \tag{3.16}$$

Prescribed heat source temperature:

$$T(r,t) = \sum\nolimits_n \hat{T}_s(\omega_n) \frac{K_o(k r)}{K_o(k r_s)} e^{i\omega_n t} \tag{3.17}$$

Compared to the solution given by Carslaw and Jaeger (1959) using the Laplace transform (see Section 3.4.1), two advantages can be deduced from the proposed solutions. First, the solution using the Fourier transform is elegant and straightforward. Second, the heat source, whether prescribed temperature or heat flux, can be constant or time-dependent. These advantages make the proposed solutions more general and easy to implement in computer codes or commercial software's, such as (MATLAB 2019), (COMSOL 2019), (Maple 2019), etc...

3.3 Multiple heat sources in a solid mass

Eqs. (3.16) and (3.17) describe the temperature distribution in an infinite solid subjected to a cylindrical heat source for a Neumann boundary condition and a Dirichlet boundary condition, respectively. Here, we extend these solutions to multiple heat sources.

The geometry of a multiple heat sources system can have any distribution, but for the sake of description, the heat sources are distributed on a plane to form a matrix of heat sources in a polar coordinate system, as shown in Figure 3.1. The radial distance between heat source S_i and source S_j is calculated as

$$r_{ij} = \sqrt{x_{ij}^2 + y_{ij}^2} \tag{3.18}$$

in which x_{ij} and y_{ij} are the rectangular displacements of the two sources in the planar array.

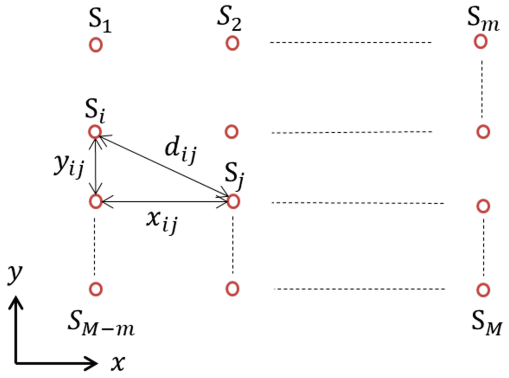

Figure 3.1: Heat sources geometry

3.3.1 Multiple heat sources with prescribed heat flux

As the system of equations governing heat conduction in an infinite solid is linear, the superposition principle applies. This simply implies summing the temperatures exerted by all involved heat sources on a point in space, as

$$\hat{T}(r,\omega) = \sum_{s=1}^{M} \frac{\hat{q}_s(\omega)}{\lambda k} \frac{K_o(k\,r)}{K_1(k\,r_s)} \tag{3.19}$$

Applying the inverse fast Fourier transform to Eq. (19) yields the general solution in the time domain, as

$$T(r,t)=\sum_n\sum_s \frac{\hat{q}_s(\omega)}{\lambda k}\frac{K_o(k\,r)}{K_1(k\,r_s)}e^{i\omega_n t} \tag{3.20}$$

3.3.2 Multiple heat sources with prescribed temperature

In the prescribed temperature boundary condition case, the superposition principle is not directly applicable. The superposition in this case would algebraically add the temperatures exerted by the sources, giving rise to an unphysical increase or decrease of temperature. For instance, if a point in space with an initial temperature equal to zero is subjected to two equally distanced heat sources, with each prescribed by 10 °C, and if we assume that its distance to any of the sources implies raising its temperature by 8 °C, the superposition in this case would imply 16 °C, which is clearly not correct. Therefore, to solve this problem, coupling between the sources is carried out to modify their temperature amplitudes by considering the effect of the thermal interaction between them. The thermal interaction between the sources is described by the exact solution given in Eq. (3.15).

Eq. (3.15), for a single heat source, can be written as

$$\hat{T}(r,\omega)=AK_o(k\,r) \tag{3.21}$$

where $A=A(r_s,\omega)=\hat{T}_s(\omega)/K_o(k\,r_s)$ represents the temperature amplitude at the heat source, and $K_o(k\,r)$ represents the dissipation of temperature at r away from the source.

For multiple heat sources, the temperature at a point in the system is described as

$$\hat{T}(r,\omega)=A_1K_o(k\,r_1)+A_2K_o(k\,r_2)+\cdots+A_MK_o(k\,r_M) \tag{3.22}$$

where $r_1, r_2, \ldots\ r_M$ are the radial distance between a reference point and the heat sources $s_1, s_2, \ldots\ s_M$ respectively, and $A_1, A_2, \ldots\ A_M$ are their amplitudes.

Solving Eq.(3.22) at the heat sources, yields

$$\begin{aligned}
\hat{T}_{s_1} &= A_1 &&+A_2K_o(k\,r_{12}) &&+\ \cdots\ &&+A_MK_o(k\,r_{1M})\\
\hat{T}_{s_2} &= A_1K_o(k\,r_{21}) &&+A_2 &&+\ \cdots\ &&+A_MK_o(k\,r_{2M})\\
&\vdots &&\vdots &&\ &&\vdots\\
\hat{T}_{s_M} &= A_1K_o(k\,r_{M1}) &&+A_2K_o(k\,r_{M2}) &&+\ \cdots\ &&+A_M
\end{aligned} \tag{3.23}$$

which implies that the temperature at a heat source is a superposition of its temperature amplitude, A, and temperatures raised by the other sources; not solely its prescribed value. r_{12}, for instance, indicates the distance between heat source 1 and heat source 2, described by Eq. (3.18)

In a matrix format, Eq. (3.23) becomes

$$\begin{pmatrix} \hat{T}_{s_1} \\ \hat{T}_{s_2} \\ \vdots \\ \hat{T}_{s_M} \end{pmatrix} = \begin{pmatrix} 1 & K_o(k r_{12}) & \cdots & K_o(k r_{1M}) \\ K_o(k r_{21}) & 1 & \cdots & K_o(k r_{2M}) \\ \vdots & \vdots & \vdots & \vdots \\ K_o(k r_{M1}) & K_o(k r_{M2}) & \cdots & 1 \end{pmatrix} \begin{pmatrix} A_1 \\ A_2 \\ \vdots \\ A_M \end{pmatrix} \tag{3.24}$$

Solving for $A's$, yields

$$\begin{pmatrix} A_1 \\ A_2 \\ \vdots \\ A_M \end{pmatrix} = \begin{pmatrix} 1 & K_o(k r_{12}) & \cdots & K_o(k r_{1M}) \\ K_o(k r_{21}) & 1 & \cdots & K_o(k r_{2M}) \\ \vdots & \vdots & \vdots & \vdots \\ K_o(k r_{M1}) & K_o(k r_{M2}) & \cdots & 1 \end{pmatrix}^{-1} \begin{pmatrix} \hat{T}_{s_1} \\ \hat{T}_{s_2} \\ \vdots \\ \hat{T}_{s_M} \end{pmatrix} \tag{3.25}$$

Substituting these temperature amplitudes into Eq. (3.22), and applying the inverse fast Fourier transform, yields the general solution in the time domain, as

$$T(r,t) = \sum_n \sum_m A_m K_o(k r_m) e^{i\omega_n t} \tag{3.26}$$

The temperature at any point in the system can be obtained. With this coupling technique, there is no need for distinguishing between corner or central heat sources. Also, the coupling is made analytically, alleviating the need for an iterative scheme.

3.4 Model verification

Three verification examples are studied:

1) The prescribed heat flux solution for a single cylindrical heat source is verified against the solution given by Carslaw and Jaeger (1959).

2) The prescribed temperature solution for a single cylindrical heat source is verified against the solution given by the finite element package COMSOL Multiphysics (COMSOL 2019).

3) Both, the prescribed heat flux and the prescribed temperature solutions for multiple cylindrical heat sources are verified against the solutions given by COMSOL Multiphysics.

3.4.1 Verification against Carslaw and Jaeger infinite cylindrical heat source solution

The prescribed heat flux solution for a single cylindrical heat source, Eq. (3.16), is verified against the solution given by Carslaw and Jaeger (1959) using the Laplace transform.

Using the Laplace transform, the forward solution to Eq. (3.1), leads to

$$\hat{T}(r,s)=\frac{\hat{q}_s}{\lambda s}\frac{K_o\left(r\sqrt{s/\alpha}\right)}{K_1\left(r_s\sqrt{s/\alpha}\right)} \tag{3.27}$$

in which s is the Laplace parameter. The inverse Laplace transform of this equation can be obtained using the Bromwich integral, which gives

$$\hat{T}(r,s)=\frac{\hat{q}_s}{2\pi\lambda}\int_{\gamma-i\infty}^{\gamma+i\infty}e^{st}\frac{K_o\left(r\sqrt{s/\alpha}\right)}{sK_1\left(r_s\sqrt{s/\alpha}\right)}ds \tag{3.28}$$

Using contour integration, Carslaw and Jaeger (1959) provided a solution to this integral for a constant heat flux, of the form,

$$T(r,t)=T_{st}+\frac{q_o}{\pi^2 r_s\lambda}\int_0^{\infty}\left(1-e^{-\alpha\beta^2 t}\right)\frac{J_o(\beta r)Y_1(\beta r_s)-Y_o(\beta r)J_1(\beta r_s)}{\beta^2\left[J_1^2(\beta r_s)+Y_1^2(\beta r_s)\right]}d\beta \tag{3.29}$$

in which

$$\beta=\sqrt{s/\alpha} \tag{3.30}$$

where J_o, J_1 , Y_o and Y_1 are the Bessel functions of the order 0 and 1, of the first and second kind respectively, and q_o is a constant cylindrical heat flux per meter length.

Exact solution of the integral in Eq. (3.29) is, if possible, complicated. Carslaw and Jaeger provided approximate solutions for short and long time scales. For the long time scale, the approximated solution is:

$$T(r,t)=T_{st}+\frac{q_o r_s}{2\lambda}\left\{\ln\frac{4\alpha t}{Cr^2}+\frac{r_s^2}{2\alpha t}\ln\frac{4\alpha t}{Cr^2}+\frac{1}{2\alpha t}\left[r_s^2+r^2-2r_s^2\ln\frac{r_s}{r}\right]+\cdots\right\} \tag{3.31}$$

in which $\ln C=0.57722\cdots$

This solution has been intensively utilized for analyzing heat flow in shallow geothermal systems, and commonly known as the infinite cylindrical source model (ICS).

The ICS model and the proposed spectral model are employed to solve heat flow in a solid mass, subjected to a constant cylindrical heat flux source, $q_0 = -20$ (W/m). The cylinder radius, $r_s = 10$ cm, and the initial temperature, $T_{st} = 10$ °C. The thermal parameters of the medium are: λ =2.5 (W/mK), $\rho = 1680$ (kg/m^3), and $c = 400$ (J/kg.K).

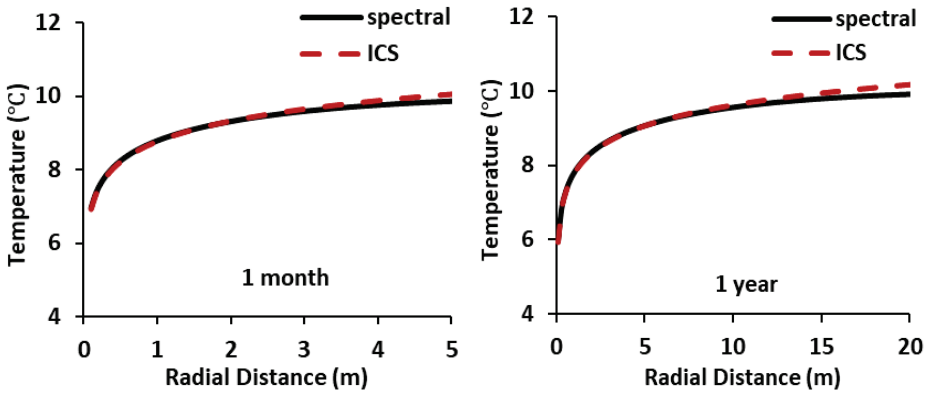

Figure 3.2: Spectral model vs. Carslaw and Jaeger infinte cylindrical source model.

In the spectral model, the number of the FFT samples is 16384, with two sample rates: 1hr and 1 day, giving time windows of 16384 hours and 16384 days, respectively. Two calculations for different physical times were conducted: 1 month, and 1 year.

Figure 3.2 shows the computational results obtained from both models. Apparently, the two results are nearly identical, especially at relatively short distances from the source. The ICS model exceeds the initial steady state temperature at larger distances, which is physically incorrect. Apparently, the use of three terms in the approximation solution in Eq. (3.31) is not sufficient at larger radial distances.

3.4.2 Verification against the finite element method for a single heat source

The prescribed temperature solution for a single cylindrical heat source, Eq.(3.17), is verified against the solution given by the finite element package COMSOL Multiphysics.

The physical system is assumed to consist of a solid cylinder, 100 m in diameter, with an initial temperature $T_{st} = 10$ °C subjected to a constant temperature heat source, $T_s =$ 0 °C, 10 cm in diameter, going through its central vertical axis. The material parameters of the medium are: λ =1.5 (W/mK), $\rho = 1800$ (kg/m3) , and $c = 600$ (J/kg.K).

As the problem deals with an infinite domain, the finite element analysis is conducted using a two-dimensional mesh. The finite element mesh consists of 230,861 linear triangular elements. This, relatively fine mesh is utilized to ensure high accuracy in the numerical solution.

Figure 3.3 shows the computational results obtained from both calculations. Apparently, the two results are nearly identical.

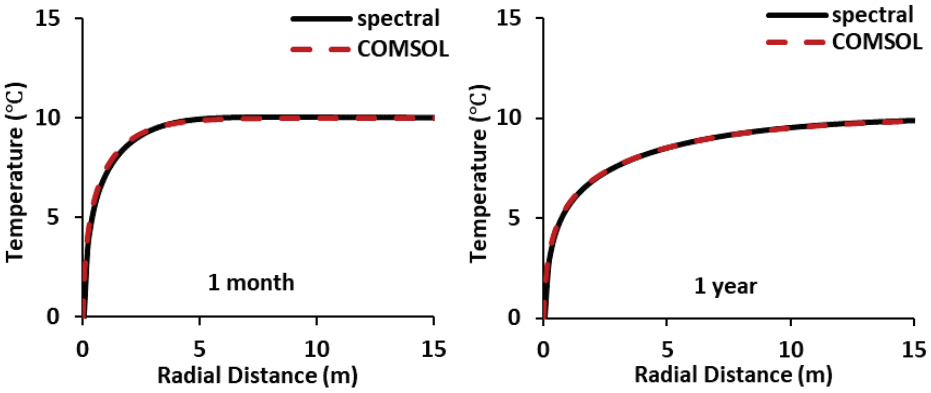

Figure 3.3: Spectral model vs. COMSOL constant temperature single cylinder heat source model.

3.4.3 Verification against the finite element method for multiple heat sources

The prescribed heat flux and the prescribed temperature solutions for multiple cylindrical heat sources, Eqs. (3.20) and (3.26), respectively, are verified against the finite element solutions given by COMSOL Multiphysics.

A. Prescribed heat flux analysis

Heat flow due to nine heat sources, each 3 cm in radius, and inducing a constant heat flux $q_s = 100$ (W/m), distributed in a 3×3 symmetric matrix, is studied, Figure 3.4a. The initial temperature, $T_{st} = 10$ °C and the material parameters of the medium are: λ =2 (W/m.K), $\rho = 2000$ (kg/m3) , and $c = 1000$ (J/kg.K).

The finite element calculation is conducted for a 100 m in diameter solid mass, using a 2D finite element mesh, consisting of 269,431 linear triangular elements, Figure 3.4b.

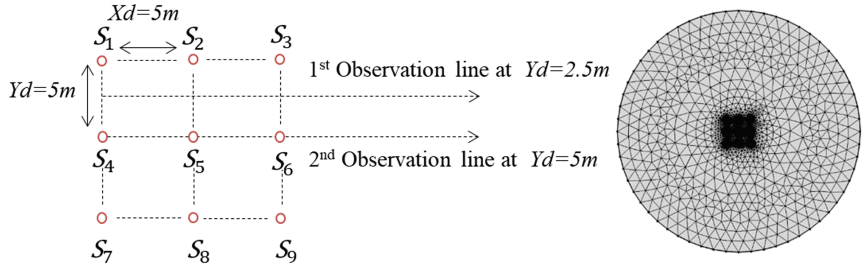

(a) (b)

Figure 3.4: (a) heat sources geometry, (b) finite element mesh

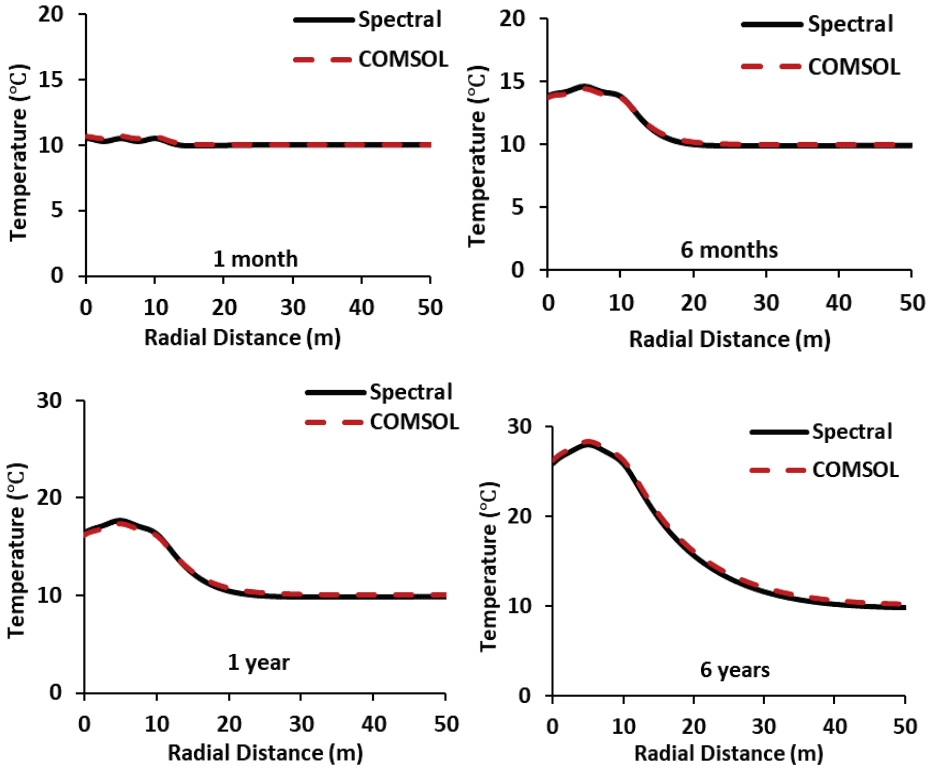

Figure 3.5: Prescribed heat flux spectral model vs. COMSOL finite element model, for the 1'st observation line

Figures 3.5 and 3.6 show the computational results obtained from the proposed spectral model and the finite element model. They show the temperature distribution along the first observation line at y=2.5m, and the second observation line at y=5m, after 1 month, 6 months, 1 year and 6 years, respectively. Apparently, the two results are nearly identical. Figure 3.6 demonstrates the significant effect of the individual heat sources on the temperature distribution. This effect is less pronounced in the first observation line (Figure 3.5), which exhibits some ripples near the heat sources in the first 6 months and disappears later on. The temperature in the region near the heat sources exhibits a significant increase, but further away, it is in the first year at its initial value (T_{st} = 10 °C), but after 6 years, it exceeds this value. This entails that the effect of the heat sources has reached, in this example, to 50m from the left edge of the geometry.

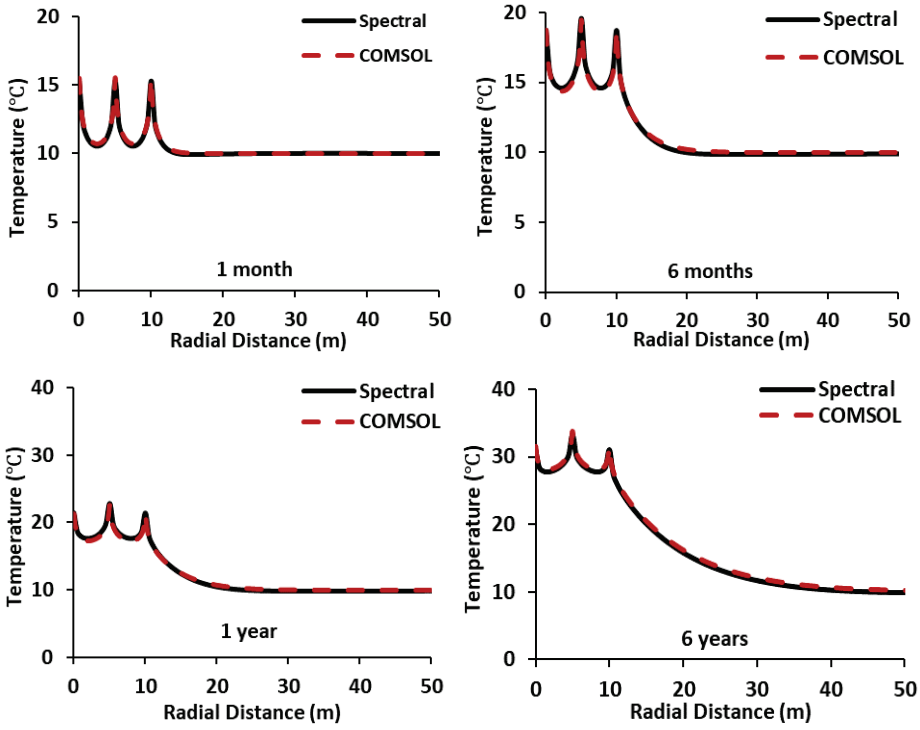

Figure 3.6: Prescribed heat flux spectral model vs. COMSOL finite element model, for the 2'nd observation line

B. Prescribed temperature analysis

A similar analysis as the one conducted in the previous verification example has been conducted, but now the heat sources induce a constant temperature, $T_s = 20°C$ for each.

Figures 3.7 and 3.8 show the computational results obtained from the proposed spectral and the COMSOL models, for the first and second observation lines, respectively. Apparently, the two results are nearly identical. A similar observation for the temperature distribution in both observation lines as that in the previous example is applied here. However, the temperature at the heat sources locations is fixed to the prescribed value.

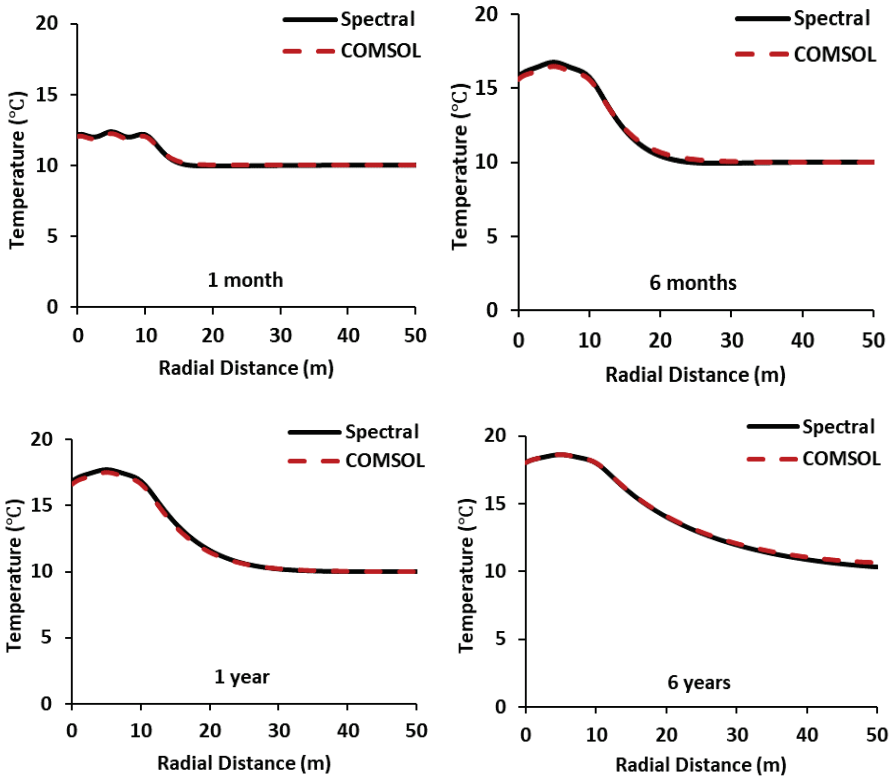

Figure 3.7: Prescribed temperature spectral model vs. COMSOL finite element model, for the 1'st observation line

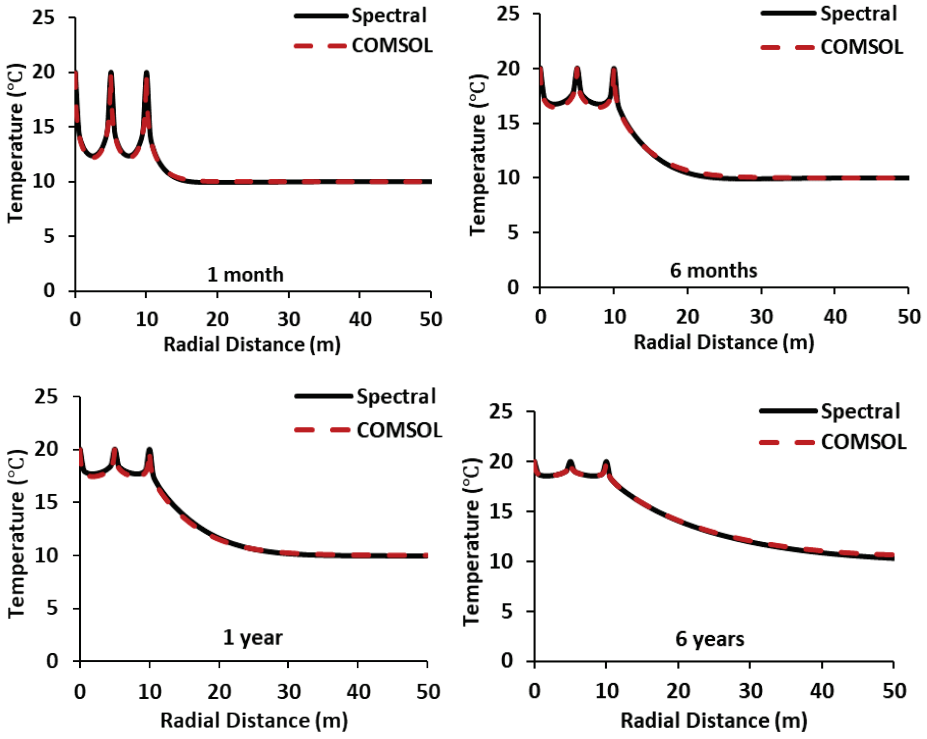

Figure 3.8: Prescribed temperature spectral model vs. COMSOL finite element model, for the 2'nd observation line

3.5 Numerical Examples

Two numerical examples are given here, describing two important features of the model: non-identical heat sources, and time varying heat signals.

A. Non-identical heat sources

The physical system is assumed to consist of three heat sources inducing temperatures: $T_s = 20, 30$ and 15 °C Figure 3.9. The cylindrical sources radius is 7 cm. The initial temperature, $T_{st} = 10$ °C. The material parameters of the medium are: λ =2.5 (W/m K), $\rho = 1680$ (kg/m^3) , and $c = 400$ (J/kg K).

Figure 3.10 shows the temperature radial distribution for 1 day, 1 month, 1 year and 20 years operation time. The figure shows that after 1 day, there are three peak temperatures, clearly representing the prescribed values at the heat sources. The temperature in the regions immediately surrounding the heat sources has increased but further away, it is just above the initial temperature. After 1 month, the three peak values are observable but less obvious for the first and third heat sources. After 1 year, the first two heat sources

exhibit peaks, but the third exhibits a dip. The heat source in the middle tempt to increase the temperature in the region on the right side, but the prescribed temperature on the right side heat source brings it to its prescribed value. After 20 years, the temperature seems to reach its equilibrium. We observe one peak and one dip, and the regions in between had reached their steady states.

The CPU time for the spectral analysis was 45 seconds for 100 observation points using Intel core 2.66 GHz processor. Using the same PC, it took 1 hour of CPU time for the finite element calculation for 20 years of operation with 1 day sampling rate.

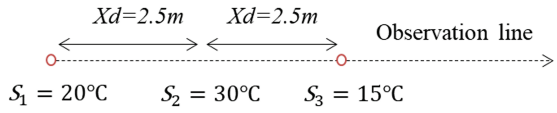

Figure 3.9: Heat sources geometry and their prescribed temperatures

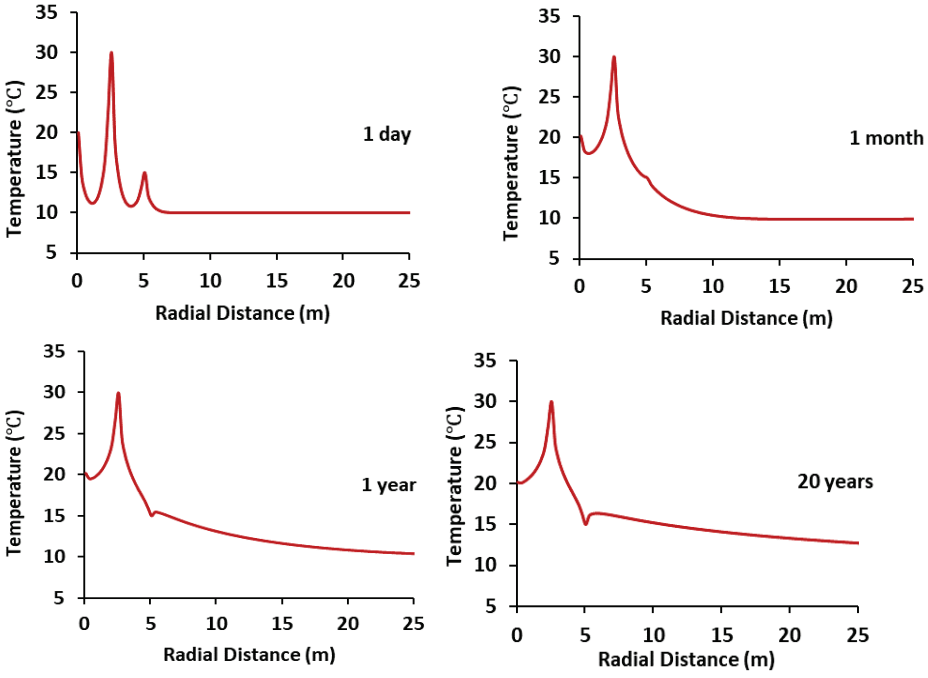

Figure 3.10: Radial temperature distribution for 3 heat sources with different prescribed temperatures

B. Time varying signals

The physical system is assumed to consist of ten heat sources as shown in Figure 3.11. The initial temperature and the material thermal parameters of the medium are similar to those of the previous numerical example. The temperature variation with time is given by

$$T_{in} = \begin{cases} 20 & 0 < t < 100 \text{ day} \\ 10 & 100 < t < 150 \text{ day} \\ 25 & t = 200 \text{ day} \\ 10 & 250 < t < 300 \text{ day} \\ 15 & 300 < t < 400 \text{ day} \\ 10 & 400 < t < 500 \text{ day} \end{cases} \tag{3.32}$$

which is depicted in Figure 3.12.

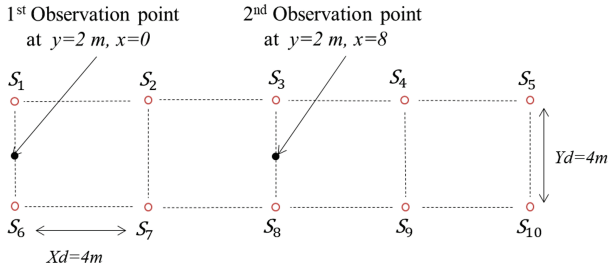

Figure 3.11: Heat sources geometry

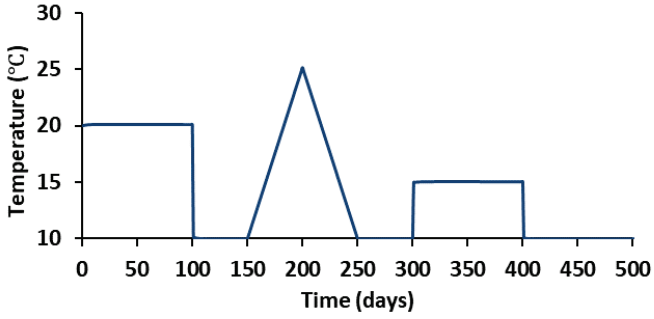

Figure 3.12: Temperature signal

This numerical example is introduced to illustrate the capability of the model to tackle complicated time varying boundary conditions. Figure 3.13 shows the temperature variation with time at the two observation points (see Figure 3.11). The figure shows that the observation point in the middle exhibits higher temperature than that at the edge. It also shows that the rectangular pulse signals show dissipation on their unloading parts, while that for the triangular signal, it shows a bell shape.

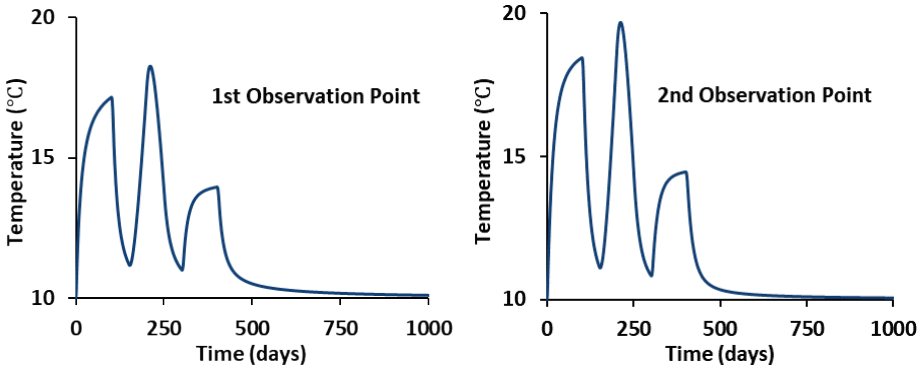

Figure 3.13: Time varying temperature response for two observation points

3.6 Conclusions

In this chapter, analytical solutions for transient heat conduction in an infinite solid mass subjected to a varying single or multiple cylindrical heat sources have been introduced. The solutions are formulated for two types of boundary conditions: a time-dependent Neumann boundary condition, and a time-dependent Dirichlet boundary condition. The governing heat equation for a single heat source is solved using the modified Bessel function, for the spatial domain, and the fast Fourier transform, for the temporal domain. For multiple heat sources, we apply directly the superposition principle for the Neumann boundary condition, but for the Dirichlet boundary condition, we conduct an analytical coupling, which allows for the exact thermal interaction between all involved heat sources.

There are several features distinguishing the proposed solutions from others. Compared to the Carslaw and Jaeger analytical solution, the proposed analytical solution, using the modified Bessel function and the fast Fourier transform, is exact at all radial points, highly elegant, robust and easy to implement in computer codes.

Compared to the finite element solution, the proposed analytical solution is exact and computationally very efficient. The CPU time for the three heat sources case given in Section 3.5, for instance, was 1 hour for the finite element calculation, while for the proposed solution, using the same PC, it was 45 seconds.

Compared to Eskilson and Claesson and Pasquier and Marcotte, the superposition for the Dirichlet boundary condition is analytical. Eskilson and Claesson used an approximate function to simulate the thermal interaction between the heat sources, and Pasquier and Marcotte applied an iterative scheme to simulate this interaction.

The heat sources can exhibit different time-dependent signals, and can have any distribution in space. Eskilson and Claesson model needs to differentiate between heat sources at the corners and those in the middle.

As a consequence, the proposed analytical solution is suitable for implementation in computer codes, which can be utilized for forward heat flow analysis and design of geothermal borehole heat exchangers. And also, it can be utilized for inverse calculation of material parameters.

4

A coupled spectral element – superposition model for detailed 3D heat flow in GSHP Systems

This chapter introduces a semi-analytical model for simulating transient conductive-convective heat flow in a three-dimensional shallow geothermal system consisting of multiple borehole heat exchangers (BHE) embedded in a multilayer soil mass. The model is formulated in three steps, starting from an axial symmetric system and ending in a 3D multilayer, multiple BHE system. In step 1, the model is formulated as a single BHE embedded in an axial symmetric homogeneous soil layer, and the governing heat equations are solved analytically using the fast Fourier transform, the eigenfunction expansion and the modified Bessel function. In step 2, the model is extended to incorporate multiple layers using the spectral element method. And in step 3, the model is extended to incorporate multiple borehole heat exchangers using a superposition technique suitable for Dirichlet boundary conditions. The ensuing computational model solves detailed three-dimensional heat flow using minimal CPU time and capacity. The number of the required spectral elements is equal to the number of soil layers embedded in which any number of borehole heat exchangers with any configuration. A verification example illustrating the model accuracy and numerical examples illustrating its computational capabilities are given. Despite the apparent rigor of the proposed model, its high accuracy and computational efficiency make it suitable for engineering practice.

This chapter is based on BniLam N., Al-Khoury R., Shiri A. and Sluys L.J. (2018). A semi-analytical model for detailed 3D heat flow in shallow geothermal systems. International Journal of Heat and Mass Transfer Volume 123, Pages 911-927.

4.1 Introduction

Extracting thermal energy from relatively shallow depths has become an established technology, and shallow geothermal systems known as geothermal heat pumps (GHP), ground source heat pumps (GSHP) or borehole heat exchangers (BHE) are in use all over the world. A BHE works by circulating a fluid, mostly water with antifreeze, through a closed loop of polyethylene pipe that is inserted in a borehole embedded in a soil mass. The borehole is filled with grout to fix the polyethylene pipe and to ensure a good thermal interaction with the soil. Several types of BHE are available in practice. In this work, the BHE is assumed to consist of a vertical single U-tube filled with circulating water and embedded in grout.

The borehole heat exchanger is a slender heat pipe with dimensions of the order of 30 mm in diameter for the U-tube, and 150 mm in diameter and 100 m in length for the borehole. The U-tube carries a circulating fluid that collects heat (or rejects heat) from (or to) the surrounding soil via convection-conduction heat transfer mechanisms.

In practice, shallow geothermal systems consist of multiple borehole heat exchangers embedded in a multilayer soil mass. Computational modelling of such a system, in spite of the bulk of existing models, is state of the art due to the combination of the extreme slenderness of the boreholes heat exchangers, the presence of multiple components with different thermal properties and the involved heat convection. Consequently, several theoretical and computational assumptions and approximations have been introduced in order to circumvent this computationally challenging combination and obtain feasible solutions. All known solution techniques, such as analytical, semi-analytical and numerical, have been utilized for this purpose. Nevertheless, in spite of the versatility of the numerical methods, analytical and semi-analytical solutions are yet preferable because of their comparatively little demands on computational power and ease of use in engineering practice. In Al-Khoury (2012b) a thorough review of models utilized in this field is given. In this chapter, focus is placed on models based on the semi-analytical solution technique.

Eskilson and Claesson (1988) introduced a semi-analytical model for heat flow in a borehole heat exchanger constituting two fluid channels and a borehole wall, embedded in an axial symmetric soil mass. The governing heat equations of the two fluid channels are solved using the Laplace transform and that for the soil mass using the finite difference method. They extended the model to 3D by use of the principle of superposition to account for multiple heat sources. Their solution is effective for relatively long term analyses and for a symmetric heat sources configuration.

Pasquier and Marcotte (2013) introduced a semi-analytical model for heat flow in a solid mass subjected to multiple infinite line heat sources with time-varying heat fluxes and temperatures. They applied the fast Fourier transform for the temporal domain and the superposition principle for the spatial domain. The thermal interaction between the involved heat sources is solved using an iterative algorithm.

Erol et al (2015) introduced a modified Green's function for heat flow in a porous domain subjected to a constant line heat source with a finite length. The convolution theory is utilized to solve the initial and boundary value problem for a single heat source. For multiple heat sources, they utilized the superposition principle by summing up the temporal convolved functions of the heat sources.

Raymond and Lamarche (2013) analyzed the effect of multiple layers in determining the thermal parameters from the thermal response test (TRT) results. They adopted an analytical computer code (MLU), which was originally developed for transient water flow in layered aquifers, to describe conductive heat transfer in shallow geothermal systems constituting multiple layers and subjected to a variable heat injection rate. The Laplace transform is utilized to solve the system of partial differential equations describing heat flow in the layered system.

Abdelaziz et al. (2014) extended the finite line heat source solution to a multiple segment finite line heat source resembling a layered soil profile. The temperature of the heterogeneous domain is obtained by summing up the temperature in a typical homogeneous domain with that obtained due to the presence of other layers. The latter is calculated by assuming a composite system constituting smeared thermal parameters, described as a function of the relative distances of the layers from the point of interest.

Apparently, semi-analytical solutions for heat flow in multiple heat sources embedded in a homogeneous soil mass exist. Also, semi-analytical solutions for a single heat source embedded in a multilayer system exist. However, semi-analytical solutions for multiple heat sources embedded in a multilayer soil mass do not exist. This constitutes the objective of this chapter.

In a previous work, BniLam and Al-Khoury (2016) introduced an analytical model for transient heat flow in an infinite soil mass subjected to multiple cylindrical heat sources. In a later work, BniLam and Al-Khoury (2017) introduced an axial-symmetric spectral element model for heat flow in a borehole heat exchanger embedded in a multilayer system. In this chapter, these two models are elaborated and put together to formulate a detailed three-dimensional shallow geothermal system with any arbitrary layout configuration. The multiple infinite cylindrical heat sources of the first model are replaced by multiple finite borehole heat exchangers, and are incorporated in the multilayer system of the second model. This entails establishing a tailored thermal interaction between the borehole and the surrounding soil mass, and between the boreholes themselves. The superposition principle for Dirichlet boundary conditions, introduced in BniLam and Al-Khoury (2016), is tailored to the multiple BHE case. By this, the soil temperature amplitudes at the borehole locations are coupled to the temperatures in the BHE components, then coupling all involved boreholes via a matrix technique. Additionally, in this chapter, we modified the formulation of the 2-noded spectral element. In BniLam and Al-Khoury (2017), the spectral element was formulated based on the first kind Bessel function J_o, which is suitable for a line source case where the borehole and the soil mass

share and coincide on the axis of symmetry. Here, the solution is modified to lead to the use of the modified Bessel function K_o, which is suitable for a cylindrical source case where the borehole and the soil mass share the axis of symmetry, but the soil mass starts at the radius of the borehole. The latter function is more physical in representing the cylindrical nature of the BHE-soil interaction, and it has no roots to be determined and summed over. Details of the modelling approach are given hereafter.

4.2 Modelling approach

A shallow geothermal system, particularly a geothermal heat pump, consists basically of two thermally interacting domains: the borehole heat exchanger and the soil mass. In practice, the system consists of several borehole heat exchangers embedded in a multilayer layer soil mass. Solving heat flow in such a three-dimensional, nonhomogeneous geometry typically requires the use of a numerical method, such as the finite element, the finite volume or the finite difference method. However, these methods, and due to the disproportionate geometry of the system and the presence of the convective heat transfer mechanism, might require significant CPU time and capacity. To avoid this, here, a semi-analytical solution is proposed. The heat flow in this system is modelled in three steps, starting from an axial symmetric system and ending in a 3D multilayer, multiple BHE system, as outlined hereafter.

Step 1: The model is first formulated as a single BHE embedded in a semi-infinite homogeneous soil mass. The borehole heat exchanger is modelled as 1D with its axis coinciding on the vertical z-axis. The 1D assumption is reasonably valid because of the extreme slenderness of the borehole that makes the temperature gradient in the radial direction of the BHE components negligible. A single U-tube consisting of pipe-in, pipe-out and grout is considered in this study, but extension to other BHE types is straightforward. The BHE components coincide geometrically on each other, but thermally interacting with each other.

The soil mass, on the other hand, is modelled as a semi-infinite, axial symmetric domain with its axis of symmetry coinciding with the centerline of the borehole heat exchanger (z-axis). In principle, the heat equation for this domain must be formulated in the r, z-coordinate system. Solving this equation analytically would require an extra separation of variables and the determination of an additional Fourier coefficient. To circumvent this, we introduced a soil film connecting the BHE to the soil mass, as shown in Figure 4.1. The soil film has the soil mass properties, and its heat equation describes the temperature distribution in the soil mass along the z direction, which acts as the amplitude to the radial direction (r-coordinate). By this, the soil mass heat equation can be formulated in the radial direction only, making it relatively easy to solve. However, adding a soil film entails assigning a thickness, which is apparently hypothetical (see Figure 4.2). As the soil film temperature acts as the amplitude to the soil mass temperature, the choice of its thickness can affect the temperature distributions in the soil mass and the BHE

components. To tackle this issue, a thorough study has been conducted and it was found that with the use of a proper thermal interaction coefficient at the BHE-soil interface, the temperature distributions in the BHE components and the soil mass become effectively independent of the soil film thickness. In Section 4.10, a numerical example highlighting this independency is given.

The spectral analysis is utilized to solve the governing equations on the basis of the fast Fourier transform (FFT). The BHE heat equations are solved using the eigenfunction expansion, and the soil mass heat equation is solved using the modified Bessel function. See Sections 4.4 and 4.5.

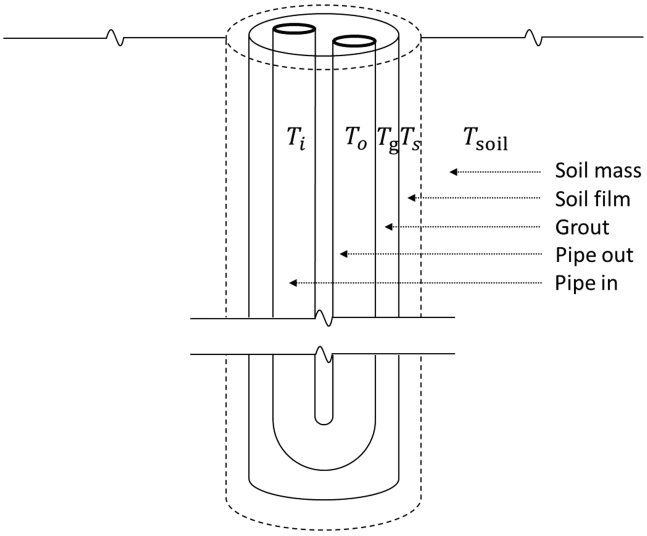

Figure 4.1: A schematic representation of a single U-tube BHE and its surrounding soil mass (recall from Chapter 2)

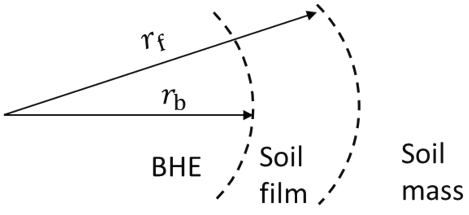

Figure 4.2: The boundary between the BHE and the soil film, and the hypothetical boundary between the soil film and the soil mass

Step 2: The model in Step 1 is extended to incorporate multiple layers exhibiting different thermal properties using the spectral element method. The spectral element method is an elegant technique combining analytical solutions of a homogeneous domain to the finite element solution of nonhomogeneous domains. Here, the spectral analysis of the BHE-soil domain of Step 1 is discretized into a 2-node spectral element (see Figure 4.3). Each soil layer is described by a single spectral element, and a soil mass constituting several layers is described by spectral elements equal in number to the soil layers. The assembly of the spectral element matrices is done similar to the finite element method. See Section 4.6.

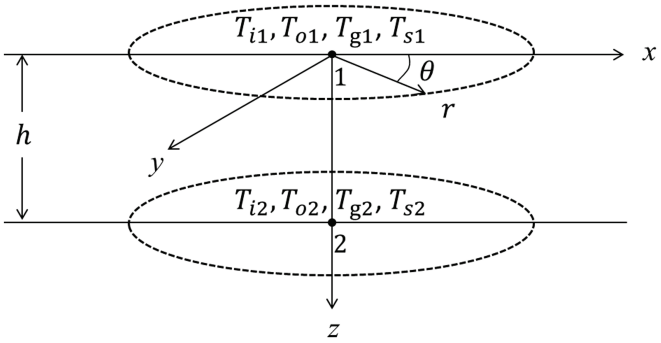

Figure 4.3: Two-node spectral element (recall from chapter 2)

Step 3: The model in Step 2 is extended to incorporate multiple borehole heat exchangers using a superposition technique. The superposition principle is typically applicable to heat sources with Neumann boundary conditions. For Dirichlet boundary conditions, as for the case in this chapter, the superposition can only be applied by modifying the temperature amplitude at each heat source by considering the thermal interaction with other heat sources. Using the superposition technique makes the model three-dimensional. See Section 4.7.

4.3 Governing equations

The governing equations for the GSHP system are given in detail in Chapter 2 but for completeness they are re-stated here.

Heat equations of a shallow geothermal system consisting of a single U-tube borehole heat exchanger, made of pipe-in, pipe-out, grout, and a soil film, embedded in a soil mass can be described as:

Pipe-in

$$\rho c\frac{\partial T_i}{\partial t}dV_i-\lambda\frac{\partial^2 T_i}{\partial z^2}dV_i+\rho cu\frac{\partial T_i}{\partial z}dV_i+b_{ig}\left(T_i-T_g\right)dS_{ig}=0 \tag{4.1}$$

Pipe-out

$$\rho c\frac{\partial T_o}{\partial t}dV_o-\lambda\frac{\partial^2 T_o}{\partial z^2}dV_o-\rho cu\frac{\partial T_o}{\partial z}dV_o+b_{og}\left(T_o-T_g\right)dS_{og}=0 \tag{4.2}$$

Grout

$$\begin{aligned}\rho_g c_g\frac{\partial T_g}{\partial t}dV_g-\lambda_g\frac{\partial^2 T_g}{\partial z^2}dV_g+b_{ig}\left(T_g-T_i\right)dS_{ig}\\+b_{og}\left(T_g-T_o\right)dS_{og}+b_{gs}\left(T_g-T_s\right)dS_{gs}=0\end{aligned} \tag{4.3}$$

Soil film

$$\rho_s c_s\frac{\partial T_s}{\partial t}dV_s-\lambda_s\frac{\partial^2 T_s}{\partial z^2}dV_s+b_{gs}\left(T_s-T_g\right)dS_{gs}+b_{ss}\left(T_s-T_{\text{soil}}\big|_{r=r_{\text{f}}}\right)dS_s=0 \tag{4.4}$$

Soil mass

$$\frac{1}{\alpha}\frac{\partial T_{\text{soil}}}{\partial t}-\frac{\partial^2 T_{\text{soil}}}{\partial r^2}-\frac{1}{r}\frac{\partial T_{\text{soil}}}{\partial r}=0 \tag{4.5}$$

where the subscripts i, o, g and s represent pipe-in, pipe-out, grout and soil film, respectively; and $T_i = T_i(z,t)$, $T_o = T_o(z,t)$, $T_{\text{g}} = T_{\text{g}}(z,t)$, $T_s = T_s(z,t)$ and $T_{\text{soil}} = T_{\text{soil}}(r,t)$ are the temperatures in pipe-in, pipe-out, grout, soil film and soil mass, respectively. λ, λ_{g} and λ_s (W/mK) are the thermal conductivity of the circulating fluid, grout and soil film, respectively; u (m/s) is the circulating fluid velocity; b_{ig}, b_{og}, b_{gs}, b_{ss} (W/m^{2}K) are the reciprocal of the thermal resistance between pipe-in-grout, pipe-out-grout, grout-soil film, and soil film-soil mass, respectively (see Section 2.3 for their determination); ρc (J/m^{3}K) is the volume heat capacity, with c (J/kg K) the specific heat and ρ (kg/m^3) the mass density; dV_i , dV_o , dV_{g} , dV_s (m^3) are the control volumes of pipe-in, pipe-out, grout and soil film, respectively; $dS_{\text{ig}}, dS_{\text{og}}, dS_{\text{gs}}, dS_s$ (m^2) are the surface areas of the control volumes of pipe-in, pipe-out, grout and soil film, respectively; r_{f} is the soil film radius, describing the location of a hypothetical boundary between the soil film and the soil mass (see Figure 4.2); and α(m^2/s) is the thermal diffusivity of the soil, described as

$$\alpha = \frac{\lambda_s}{\rho_s c_s} \tag{4.6}$$

Eq. (4.4) is a nonhomogeneous partial differential equation due to the presence of $T_{\text{soil}}|_{r=r_f}$. As it will be shown later, this equation will be converted to a homogeneous equation by relating T_{soil} to T_s .

The initial condition is

$$T_i(z,0) = T_o(z,0) = T_g(z,0) = T_s(z,0) = T_{\text{soil}}(r,0) \tag{4.7}$$

where initially the temperature distribution in the BHE components is equal to that of the steady state condition of the soil mass before the heating/cooling operation has been started.

The boundary conditions in the BHE are

$$T_i(0,t) = T_{\text{in}}(t) \tag{4.8}$$

$$T_i(L,t) = T_o(L,t) \tag{4.9}$$

where T_{in} is the fluid temperature at $z = 0$, coming from the heat pump. It can have any arbitrary shape in time. Eq. (4.9) implies that at the bottom of the BHE, $z = L$, the temperature of the fluid in pipe-in is equal to the temperature of the fluid in pipe-out.

The boundary conditions in the soil mass are

$$T_{\text{soil}}\big|_{r=r_b} = T_s \tag{4.10}$$

$$T_{\text{soil}}\left(r = \infty, t\right) = 0 \tag{4.11}$$

where Eq. (4.10) indicates that the soil mass physically includes the soil film and its temperature is equal to the soil film temperature at the boundary with the borehole ($r = r_b$). However, as the soil film has a thickness, the soil mass is hypothetically in contact with the soil film at $r = r_f$, as shown in Figure 4.2, and mathematically indicated in Eq. (4.4). In what follows it will be shown how these two boundaries will be utilized for the determination of the integration constants. Eq.(4.11) implies that the temperature variation in the soil mass at an infinitely far distance is zero.

4.4 Solution of soil heat equation

Fourier transform of Eq.(4.5) gives

$$k_s^2 \hat{T}_{\text{soil}} - \frac{\partial^2 \hat{T}_{\text{soil}}}{\partial r^2} - \frac{1}{r}\frac{\partial \hat{T}_{\text{soil}}}{\partial r} = 0 \tag{4.12}$$

in which $\hat{T}$ represents the temperature in the frequency domain, and

$$k_s = \sqrt{\frac{i\omega}{\alpha}} \tag{4.13}$$

is the eigenvalue of the soil mass.

Assume $S = k_s\, r$, from which the following identities can be derived:

$$\begin{aligned} &\frac{\partial S}{\partial r} = k_s; \quad \left(\frac{\partial S}{\partial r}\right)^2 = k_s^2 \\ &\frac{\partial T}{dS} = \frac{\partial T}{\partial r}\frac{\partial r}{\partial S} = \frac{1}{k_s}\frac{\partial T}{\partial r} \\ &\frac{\partial^2 T}{\partial S^2} = \frac{\partial^2 T}{\partial r^2}\frac{\partial r^2}{\partial S^2} = \frac{1}{k_s^2}\frac{\partial^2 T}{\partial r^2} \end{aligned} \tag{4.14}$$

Substituting these identities into Eq.(4.12) gives

$$\hat{T}_{\text{soil}} - \frac{\partial^2 \hat{T}_{\text{soil}}}{\partial S^2} - \frac{1}{S}\frac{\partial \hat{T}_{\text{soil}}}{\partial S} = 0 \tag{4.15}$$

This equation is a standard modified Bessel function with a general solution expressed as

$$\hat{T}_{\text{soil}}(r) = A\, I_o(k_s r) + B\, K_o(k_s r) \tag{4.16}$$

where I_o and K_o are the modified Bessel functions of the first and second kind.

Applying the boundary condition in Eq. (4.11) to Eq. (4.16) leads to

$$\hat{T}_{\text{soil}}\Big|_{r=\infty} = AI_o(\infty) + BK_o(\infty) = 0 \tag{4.17}$$

but since $I_o(\infty) = \infty$, A in Eq. (4.17) must be 0, giving:

$$\hat{T}_{\text{soil}}(r) = B\, K_o(k_s r) \tag{4.18}$$

At $r = r_{\text{b}}$, Eq. (4.18) becomes

$$\hat{T}_{\text{soil}}\Big|_{r=r_{\text{b}}} = B\, K_o(k_s r_{\text{b}}) \tag{4.19}$$

Applying the boundary condition in Eq.(4.10) to Eq.(4.19) yields

$$B = \frac{\hat{T}_s}{K_o(k_s r_{\text{b}})} \tag{4.20}$$

Substituting Eq.(4.20) into Eq. (4.18), the soil temperature at any radial point can be calculated as

$$\hat{T}_{\text{soil}}(r) = \frac{\hat{T}_s}{K_o(k_s r_{\text{b}})} K_o(k_s r) \tag{4.21}$$

At the hypothetical boundary between the soil film and the soil mass, $r = r_{\text{f}}$, Eq. (4.21) gives

$$\hat{T}_{\text{soil}}\Big|_{r=r_{\text{f}}} = \frac{K_o(k_s r_{\text{f}})}{K_o(k_s r_{\text{b}})} \hat{T}_s \tag{4.22}$$

or, equivalently

$$\hat{T}_{\text{soil}}\Big|_{r=r_{\text{f}}} = A_f \hat{T}_s \tag{4.23}$$

with

$$A_f = \frac{K_o(k_s r_{\text{f}})}{K_o(k_s r_{\text{b}})} \tag{4.24}$$

which can be substituted into the transformed form of Eq. (4.4).

4.5 Solution of BHE heat equations

Applying Fourier transform to Eqs. (1)-(4), and substituting Eq.(4.23) into the transformed form of Eq. (4), gives

$$-\lambda \frac{\partial^2 \hat{T}_i}{\partial z^2} dV_i + \rho c u \frac{\partial \hat{T}_i}{\partial z} dV_i + \left(i\omega \rho c dV_i + b_{ig} dS_{ig}\right)\hat{T}_i - b_{ig}\hat{T}_g dS_{ig} = 0 \tag{4.25}$$

$$-\lambda \frac{\partial^2 \hat{T}_o}{\partial z^2} dV_i - \rho c u \frac{\partial \hat{T}_i}{\partial z} dV_o + \left(i\omega \rho c dV_o + b_{og} dS_{og}\right)\hat{T}_o - b_{og}\hat{T}_g dS_{og} = 0 \tag{4.26}$$

$$\begin{aligned} -\lambda_g \frac{\partial^2 \hat{T}_g}{\partial z^2} dV_g + \left(i\omega \rho_g c_g dV_g + b_{ig} dS_{ig} + b_{og} dS_{og} + b_{gs} dS_{gs}\right)\hat{T}_g \\ - b_{ig} dS_{ig}\hat{T}_i - b_{og} dS_{og}\hat{T}_o - b_{gs} dS_{gs}\hat{T}_s = 0 \end{aligned} \tag{4.27}$$

$$-\lambda_s \frac{\partial^2 \hat{T}_s}{\partial z^2} dV_s + \left(i\omega \rho_s c_s dV_s + b_{gs} dS_{gs} + b_{ss} dS_s \left(1 - A_f\right)\right)\hat{T}_s - b_{gs} dS_{gs}\hat{T}_g = 0 \tag{4.28}$$

which forms a set of homogeneous equations that can be solved using the eigenfunction expansion. This set of homogeneous equations was obtained by converting Eq. (4.4) from

a nonhomogeneous differential equation, due to the presence of the $T_{\text{soil}}|_{r=r_f}$ to a homogeneous equation by incorporating Eq.(4.23) into Eq.(4.28).

The solutions to Eqs. (4.25)-(4.28) can be expressed as (Doyle 1997)

$$\hat{T}_i = A_i e^{-ikz},\ \hat{T}_o = A_o e^{-ikz},\ \hat{T}_g = A_g e^{-ikz},\ \hat{T}_s = A_s e^{-ikz} \tag{4.29}$$

in which A_i, A_o, A_g and A_s are the integral constants, and k denotes the system eigenvalues, which need to be determined.

Substituting Eq. (4.29) into Eqs. (4.25)-(4.28), gives

$$k^2\lambda dV_i A_i e^{-ikz} - ik\rho cudV_i A_i e^{-ikz} + \left(i\omega\rho cdV_i + b_{ig}dS_{ig}\right)A_i e^{-ikz} - b_{ig}dS_{ig}A_g e^{-ikz} = 0 \tag{4.30}$$

$$k^2\lambda dV_i A_o e^{-ikz} + ik\rho cudV_o A_i e^{-ikz} + \left(i\omega\rho cdV_o + b_{og}dS_{og}\right)A_o e^{-ikz} - b_{og}dS_{og}A_g e^{-ikz} = 0 \tag{4.31}$$

$$k^2\lambda_g dV_g A_g e^{-ikz} + \left(i\omega\rho_g c_g dV_g + b_{ig}dS_{ig} + b_{og}dS_{og} + b_{gs}dS_{gs}\right)A_g e^{-ikz} - b_{ig}dS_{ig}A_i e^{-ikz} - b_{og}dS_{og}A_o e^{-ikz} - b_{gs}dS_{gs}A_s e^{-ikz} = 0 \tag{4.32}$$

$$k^2\lambda_s dV_s A_s e^{-ikz} + \left(i\omega\rho_s c_s dV_s + b_{gs}dS_{gs} + b_{ss}dS_s\left(1-A_f\right)\right)A_s e^{-ikz} - b_{gs}dS_{gs}A_g e^{-ikz} = 0 \tag{4.33}$$

Dividing Eqs. (4.30)-(4.33) by e^{-ikz}, rearranging and putting it in a matrix form, gives

$$\begin{pmatrix} a_{11} & 0 & a_{13} & 0 \\ 0 & a_{22} & a_{23} & 0 \\ a_{31} & a_{32} & a_{33} & a_{34} \\ 0 & 0 & a_{43} & a_{44} \end{pmatrix}\begin{bmatrix} A_i \\ A_o \\ A_g \\ A_s \end{bmatrix} = 0 \tag{4.34}$$

where

$$a_{11} = k^2\lambda dV_i - ik\rho cudV_i + i\omega\rho cdV_i + b_{ig}dS_{ig}$$
$$a_{13} = -b_{ig}dS_{ig}$$
$$a_{22} = k^2\lambda dV_o + ik\rho cudV_o + i\omega\rho cdV_o + b_{og}dS_{og}$$
$$a_{23} = -b_{og}dS_{og}$$

$$a_{31} = -b_{ig} dS_{ig}$$
$$a_{32} = -b_{og} dS_{og}$$

$$a_{33} = k^2 \lambda_g dV_g + i\omega \rho_g c_g dV_g + b_{ig} dS_{ig} + b_{og} dS_{og} + b_{gs} dS_{gs}$$
$$a_{34} = -b_{gs} dS_{gs}$$

$$a_{43} = -b_{gs} dS_{gs}$$
$$a_{44} = k^2 \lambda_s dV_s + i\omega \rho_s c_s dV_s + b_{gs} dS_{gs} + b_{ss} dS_s \left(1 - A_f\right)$$

Since $\hat{T}_i$, $\hat{T}_g$, $\hat{T}_o$ and $\hat{T}_s$ are coupled, the constants, A_i, A_o, A_g and A_s are related to each other. Using Eqs. (4.30)-(4.33), the following relationships exist:

Pipe-in-grout

$$A_i = Y^{ig} A_g$$
$$Y^{ig} = \frac{b_{ig} dS_{ig}}{k^2 \lambda dV_i \mp ik\rho cudV_i + i\omega \rho cdV_i + b_{ig} dS_{ig}} \tag{4.35}$$

Pipe-out-grout

$$A_o = Y^{og} A_g$$
$$Y^{og} = \frac{b_{og} dS_{og}}{k^2 \lambda dV_o \pm ik\rho cudV_o + i\omega \rho cdV_o + b_{og} dS_{og}} \tag{4.36}$$

Soil film-grout

$$A_s = Y^{sg} A_g$$
$$Y^{sg} = \frac{b_{gs} dS_{gs}}{k^2 \lambda_s dV_s + i\omega \rho_s c_s dV_s + b_{gs} dS_{gs} + b_{ss} dS_s \left(1 - A_f\right)} \tag{4.37}$$

For each k there is a corresponding Y^{ig}, Y^{og} and Y^{sg}, i.e. there are Y_1^{ig}, Y_1^{og}, Y_1^{sg} for k_1, etc. (Doyle, 1988).

The $\mp$ signs in Eqs. (4.35) and (4.36) refer to the fluid velocity direction at the nod. The fluid velocity in pipe-in at nod 1 is $(-)$, while it is $(+)$ at nod 2 (see Figure 4.2). For pipe-out, the signs are opposite.

Non-trivial solution of Eq. (4.34) can only be obtained by letting the determinate equal to zero, giving a complex eight degree polynomial of the form:

$$a_0 + a_1 k + a_2 k^2 + a_3 k^3 + a_4 k^4 + a_5 k^5 + a_6 k^6 + a_7 k^7 + a_8 k^8 = 0 \tag{4.38}$$

This polynomial represents the eigenfunction of a single U-tube BHE, with k denoting its set of eigenvalues determined by solving for the roots of Eq. (4.38). Only for this set of eigenvalues do the eigenfunction exist and satisfy the boundary conditions of the problem. Eight eigenvalues in two groups of four conjugates are obtained from Eq. (4.38). The first group is related to the positive heat flow, and the second to the negative heat flow. The exact form of the coefficients of Eq. (4.38) are given by BniLam and Al-Khoury (2017), noting that the term $\sum \bar{A}_m$ should be exchanged by A_f. Though, the exact form of the coefficients can be obtained easily using MAPLE software (Maple 2019).

4.6 Modelling multilayer system: the spectral element formulation

To clarify, the spectral element formulation that given in Chapter 2 is presented below.

The spectral element method is utilized to extend the model from a single borehole heat exchanger embedded in a homogenous soil layer to a multilayer system constituting layers with different physical parameters.

The spectral element method is utilized to formulate an axial symmetric spectral element for heat flow in a coupled borehole heat exchanger and a soil mass. The element consists of two nodes located at its boundaries, and denoting two parallel circular planes within which the heat is constrained to flow, Figure 4.3. In the vertical direction, the element extends to cover a whole layer depth, h, and in the radial direction, the element is assumed to extend to infinity.

Consider a one-dimensional heat flow in an element of length h bounded by two nodes: node 1 and node 2. At each node, there are four degrees of freedom, representing the temperatures in pipe-in, pipe-out, grout and soil film. Using Eq. (4.29) and the eight eigenvalues obtained from solving Eq.(4.38), the temperatures at any point along the element can be calculated by the superposition of an incident flux from node 1 and a reflective flux from node 2, as

$$\begin{aligned}\hat{T}_i = {} & A_{i1}e^{-ik_1 z} + B_{i1}e^{-ik_2 z} + C_{i1}e^{-ik_3 z} + D_{i1}e^{-ik_4 z} \\ & + A_{i2}e^{-ik_5(h-z)} + B_{i2}e^{-ik_6(h-z)} + C_{i2}e^{-ik_7(h-z)} + D_{i2}e^{-ik_8(h-z)}\end{aligned} \tag{4.39}$$

$$\begin{aligned}\hat{T}_o = {} & A_{o1}e^{-ik_1 z} + B_{o1}e^{-ik_2 z} + C_{o1}e^{-ik_3 z} + D_{o1}e^{-ik_4 z} \\ & + A_{o2}e^{-ik_5(h-z)} + B_{o2}e^{-ik_6(h-z)} + C_{o2}e^{-ik_7(h-z)} + D_{o2}e^{-ik_8(h-z)}\end{aligned} \tag{4.40}$$

$$\begin{aligned}\hat{T}_g = {} & A_{g1}e^{-ik_1 z} + B_{g1}e^{-ik_2 z} + C_{g1}e^{-ik_3 z} + D_{g1}e^{-ik_4 z} \\ & + A_{g2}e^{-ik_5(h-z)} + B_{g2}e^{-ik_6(h-z)} + C_{g2}e^{-ik_7(h-z)} + D_{g2}e^{-ik_8(h-z)}\end{aligned} \tag{4.41}$$

$$\begin{aligned}\hat{T}_s &= A_{s1}e^{-ik_1 z} + B_{s1}e^{-ik_2 z} + C_{s1}e^{-ik_3 z} + D_{s1}e^{-ik_4 z} \\ &\quad + A_{s2}e^{-ik_5(h-z)} + B_{s2}e^{-ik_6(h-z)} + C_{s2}e^{-ik_7(h-z)} + D_{s2}e^{-ik_8(h-z)}\end{aligned} \tag{4.42}$$

As for the finite element method, the governing equations are solved in terms of the nodal values.

At node 1, z = 0, substituting Eqs. (4.35)- (4.37) into Eqs.(4.39), (4.40) and (4.42), the nodal temperatures become

$$\begin{aligned}\hat{T}_{i1} &= A_{g1}Y_1^{ig} + B_{g1}Y_2^{ig} + C_{g1}Y_3^{ig} + D_{g1}Y_4^{ig} \\ &\quad + A_{g2}Y_5^{ig}e^{-ik_5 h} + B_{g2}Y_6^{ig}e^{-ik_6 h} + C_{g2}Y_7^{ig}e^{-ik_7 h} + D_{g2}Y_8^{ig}e^{-ik_8 h} \\ \hat{T}_{o1} &= A_{g1}Y_1^{og} + B_{g1}Y_2^{og} + C_{g1}Y_3^{og} + D_{g1}Y_4^{og} \\ &\quad + A_{g2}Y_5^{og}e^{-ik_5 h} + B_{g2}Y_6^{og}e^{-ik_6 h} + C_{g2}Y_7^{og}e^{-ik_7 h} + D_{g2}Y_8^{og}e^{-ik_8 h} \\ \hat{T}_{g1} &= A_{g1} + B_{g1} + C_{g1} + D_{g1} \\ &\quad + A_{g2}e^{-ik_5 h} + B_{g2}e^{-ik_6 h} + C_{g2}e^{-ik_7 h} + D_{g2}e^{-ik_8 h} \\ \hat{T}_{s1} &= A_{g1}Y_1^{sg} + B_{g1}Y_2^{sg} + C_{g1}Y_3^{sg} + D_{g1}Y_4^{sg} \\ &\quad + A_{g2}Y_5^{sg}e^{-ik_5 h} + B_{g2}Y_6^{sg}e^{-ik_6 h} + C_{g2}Y_7^{sg}e^{-ik_7 h} + D_{g2}Y_8^{sg}e^{-ik_8 h}\end{aligned} \tag{4.43}$$

At node 2, z = h, and similarly, upon substituting Eqs. (4.35)- (4.37) into Eqs.(4.39), (4.40) and (4.42), the nodal temperatures become

$$\begin{aligned}\hat{T}_{i2} &= A_{g1}Y_1^{ig}e^{-ik_1 h} + B_{g1}Y_2^{ig}e^{-ik_2 h} + C_{g1}Y_3^{ig}e^{-ik_3 h} + D_{g1}Y_4^{ig}e^{-ik_4 h} \\ &\quad + A_{g2}Y_5^{ig} + B_{g2}Y_6^{ig} + C_{g2}Y_7^{ig} + D_{g2}Y_8^{ig} \\ \hat{T}_{o2} &= A_{g1}Y_1^{og}e^{-ik_1 h} + B_{g1}Y_2^{og}e^{-ik_2 h} + C_{g1}Y_3^{og}e^{-ik_3 h} + D_{g1}Y_4^{og}e^{-ik_4 h} \\ &\quad + A_{g2}Y_5^{og} + B_{g2}Y_6^{og} + C_{g2}Y_7^{og} + D_{g2}Y_8^{og} \\ \hat{T}_{g2} &= A_{g1}e^{-ik_1 h} + B_{g1}e^{-ik_2 h} + C_{g1}e^{-ik_3 h} + D_{g1}e^{-ik_4 h} \\ &\quad + A_{g2} + B_{g2} + C_{g2} + D_{g2} \\ \hat{T}_{s2} &= A_{g1}Y_1^{sg}e^{-ik_1 h} + B_{g1}Y_2^{sg}e^{-ik_2 h} + C_{g1}Y_3^{sg}e^{-ik_3 h} + D_{g1}Y_4^{sg}e^{-ik_4 h} \\ &\quad + A_{g2}Y_5^{sg} + B_{g2}Y_6^{sg} + C_{g2}Y_7^{sg} + D_{g2}Y_8^{sg}\end{aligned} \tag{4.44}$$

In a matrix form, Eqs. (4.43) and (4.44) can be presented as

$$\begin{pmatrix} \hat{T}_{i1} \\ \hat{T}_{o1} \\ \hat{T}_{g1} \\ \hat{T}_{s1} \\ \hat{T}_{i2} \\ \hat{T}_{g2} \\ \hat{T}_{o2} \\ \hat{T}_{s2} \end{pmatrix} = \begin{pmatrix} h_{11} & h_{12} & h_{13} & h_{14} & h_{15} & h_{16} & h_{17} & h_{18} \\ h_{21} & h_{22} & h_{23} & h_{24} & h_{25} & h_{26} & h_{27} & h_{28} \\ h_{31} & h_{32} & h_{33} & h_{34} & h_{35} & h_{36} & h_{37} & h_{38} \\ h_{41} & h_{42} & h_{43} & h_{44} & h_{45} & h_{46} & h_{47} & h_{48} \\ h_{51} & h_{52} & h_{53} & h_{54} & h_{55} & h_{56} & h_{57} & h_{58} \\ h_{61} & h_{62} & h_{63} & h_{64} & h_{65} & h_{66} & h_{67} & h_{68} \\ h_{71} & h_{72} & h_{73} & h_{74} & h_{75} & h_{76} & h_{77} & h_{78} \\ h_{81} & h_{82} & h_{83} & h_{84} & h_{85} & h_{86} & h_{87} & h_{88} \end{pmatrix} \begin{pmatrix} A_{g1} \\ B_{g1} \\ C_{g1} \\ D_{g1} \\ A_{g2} \\ B_{g2} \\ C_{g2} \\ D_{g2} \end{pmatrix} \tag{4.45}$$

Where

$$h_{11} = Y_1^{ig}, \quad h_{12} = Y_2^{ig}, \quad h_{13} = Y_3^{ig}, \quad h_{14} = Y_4^{ig}$$
$$h_{15} = Y_5^{ig} e^{-ik_5 h}, \quad h_{16} = Y_6^{ig} e^{-ik_6 h}, \quad h_{17} = Y_7^{ig} e^{-ik_7 h}, \quad h_{18} = Y_8^{ig} e^{-ik_8 h}$$

$$h_{21} = Y_1^{og}, \quad h_{22} = Y_2^{og}, \quad h_{23} = Y_3^{og}, \quad h_{24} = Y_4^{og}$$
$$h_{25} = Y_5^{og} e^{-ik_5 h}, \quad h_{26} = Y_6^{og} e^{-ik_6 h}, \quad h_{27} = Y_7^{og} e^{-ik_7 h}, \quad h_{28} = Y_8^{og} e^{-ik_8 h}$$

$$h_{31} = 1, \quad h_{32} = 1, \quad h_{33} = 1, \quad h_{34} = 1$$
$$h_{35} = e^{-ik_5 h}, \quad h_{36} = e^{-ik_6 h}, \quad h_{37} = e^{-ik_7 h}, \quad h_{38} = e^{-ik_8 h}$$

$$h_{41} = Y_1^{sg}, \quad h_{42} = Y_2^{sg}, \quad h_{43} = Y_3^{sg}, \quad h_{44} = Y_4^{sg}$$
$$h_{45} = Y_5^{sg} e^{-ik_5 h}, \quad h_{46} = Y_6^{sg} e^{-ik_6 h}, \quad h_{47} = Y_7^{sg} e^{-ik_7 h}, \quad h_{48} = Y_8^{sg} e^{-ik_8 h}$$

$$h_{51} = Y_1^{ig} e^{-ik_1 h}, \quad h_{52} = Y_2^{ig} e^{-ik_2 h}, \quad h_{53} = Y_3^{ig} e^{-ik_3 h}, \quad h_{54} = Y_4^{ig} e^{-ik_4 h}$$
$$h_{55} = Y_5^{ig}, \quad h_{56} = Y_6^{ig}, \quad h_{57} = Y_7^{ig}, \quad h_{58} = Y_8^{ig}$$

$$h_{61} = Y_1^{og} e^{-ik_1 h}, \quad h_{62} = Y_2^{og} e^{-ik_2 h}, \quad h_{63} = Y_3^{og} e^{-ik_3 h}, \quad h_{64} = Y_4^{og} e^{-ik_4 h}$$
$$h_{65} = Y_5^{og}, \quad h_{66} = Y_6^{og}, \quad h_{67} = Y_7^{og}, \quad h_{68} = Y_8^{og}$$

$$h_{71} = e^{-ik_1 h}, \quad h_{72} = e^{-ik_2 h}, \quad h_{73} = e^{-ik_3 h}, \quad h_{74} = e^{-ik_4 h}$$
$$h_{75} = 1, \quad h_{76} = 1, \quad h_{77} = 1, \quad h_{78} = 1$$

$$h_{81} = Y_1^{sg} e^{-ik_1 h}, \quad h_{82} = Y_2^{sg} e^{-ik_2 h}, \quad h_{83} = Y_3^{sg} e^{-ik_3 h}, \quad h_{84} = Y_4^{sg} e^{-ik_4 h}$$
$$h_{85} = Y_5^{sg}, \quad h_{86} = Y_6^{sg}, \quad h_{87} = Y_7^{sg}, \quad h_{88} = Y_8^{sg}$$

Eq.(4.45) indicates that the temperatures of pipe-in, pipe-out and soil film are represented in terms of the grout coefficients. This equation can be written as

$$\hat{\mathbf{T}}_{\text{node}} = \mathbf{H}(k, \omega_n)\mathbf{A} \tag{4.46}$$

Solving for $\mathbf{A}$, gives

$$\mathbf{A} = \mathbf{H}(k, \omega_n)^{-1} \hat{\mathbf{T}}_{\text{node}} \tag{4.47}$$

The next step is to relate the heat flux to the temperature at the nodes. The heat fluxes for the BHE components are

$$\begin{aligned} q_i &= \mp\lambda \frac{\partial T_i}{\partial z} dA_i, \qquad q_o = \mp\lambda \frac{\partial T_o}{\partial z} dA_o \\ q_g &= \mp\lambda_g \frac{\partial T_g}{\partial z} dA_g, \quad q_s = \mp\lambda_s \frac{\partial T_s}{\partial z} dA_s \end{aligned} \tag{4.48}$$

where dA_i, dA_o, dA_g and dA_s are the cross sectional areas of pipe-in, pip-out, grout and soil film respectively. The $\mp$ sign refers to the direction of the heat flux: the heat flux at node 1 is $(-)$ while at node 2, it is $(+)$.

Substituting Eqs. (4.35)- (4.37) into Eqs.(4.39), (4.40) and (4.42), gives

$$q_i = \mp\lambda dA_i \begin{pmatrix} -ik_1 A_{g1} Y_1^{ig} e^{-ik_1 z} - ik_2 B_{g1} Y_2^{ig} e^{-ik_2 z} \\ -ik_3 C_{g1} Y_3^{ig} e^{-ik_3 z} - ik_4 D_{g1} Y_4^{ig} e^{-ik_4 z} \\ +ik_5 A_{g2} Y_5^{ig} e^{-ik_5 (h-z)} + ik_6 B_{g2} Y_6^{ig} e^{-ik_6 (h-z)} \\ +ik_7 C_{g2} Y_7^{ig} e^{-ik_7 (h-z)} + ik_8 D_{g2} Y_8^{ig} e^{-ik_8 (h-z)} \end{pmatrix} \tag{4.49}$$

$$q_o = \mp\lambda dA_o \begin{pmatrix} -ik_1 A_{g1} Y_1^{og} e^{-ik_1 z} - ik_2 B_{g1} Y_2^{og} e^{-ik_2 z} \\ -ik_3 C_{g1} Y_3^{og} e^{-ik_3 z} - ik_4 D_{g1} Y_4^{og} e^{-ik_4 z} \\ +ik_5 A_{g2} Y_5^{og} e^{-ik_5 (h-z)} + ik_6 B_{g2} Y_6^{og} e^{-ik_6 (h-z)} \\ +ik_7 C_{g2} Y_7^{og} e^{-ik_7 (h-z)} + ik_8 D_{g2} Y_8^{og} e^{-ik_8 (h-z)} \end{pmatrix} \tag{4.50}$$

$$q_g = \mp\lambda_g dA_g \begin{pmatrix} -ik_1 A_{g1} e^{-ik_1 z} - ik_2 B_{g1} e^{-ik_2 z} \\ -ik_3 C_{g1} e^{-ik_3 z} - ik_4 D_{g1} e^{-ik_4 z} \\ +ik_5 A_{g2} e^{-ik_5 (h-z)} + ik_6 B_{g2} e^{-ik_6 (h-z)} \\ +ik_7 C_{g2} e^{-ik_7 (h-z)} + ik_8 D_{g2} e^{-ik_8 (h-z)} \end{pmatrix} \tag{4.51}$$

$$q_s = \mp\lambda_s dA_s \begin{pmatrix} -ik_1 A_{g1} Y_1^{sg} e^{-ik_1 z} - ik_2 B_{g1} Y_2^{sg} e^{-ik_2 z} \\ -ik_3 C_{g1} Y_3^{sg} e^{-ik_3 z} - ik_4 D_{g1} Y_4^{sg} e^{-ik_4 z} \\ +ik_5 A_{g2} Y_5^{sg} e^{-ik_5 (h-z)} + ik_6 B_{g2} Y_6^{sg} e^{-ik_6 (h-z)} \\ +ik_7 C_{g2} Y_7^{sg} e^{-ik_7 (h-z)} + ik_8 D_{g2} Y_8^{sg} e^{-ik_8 (h-z)} \end{pmatrix} \tag{4.52}$$

At the element nodes, Eqs. (4.49)-(4.52) become:

At node 1, z = 0:

$$q_{i1} = -\lambda dA_i \begin{pmatrix} -ik_1 A_{g1} Y_1^{ig} - ik_2 B_{g1} Y_2^{ig} - ik_3 C_{g1} Y_3^{ig} \\ -ik_4 D_{g1} Y_4^{ig} + ik_5 A_{g2} Y_5^{ig} e^{-ik_5 h} + ik_6 B_{g2} Y_6^{ig} e^{-ik_6 h} \\ +ik_7 C_{g2} Y_7^{ig} e^{-ik_7 h} + ik_8 D_{g2} Y_8^{ig} e^{-ik_8 h} \end{pmatrix}$$

$$q_{o1} = -\lambda dA_o \begin{pmatrix} -ik_1 A_{g1} Y_1^{og} - ik_2 B_{g1} Y_2^{og} - ik_3 C_{g1} Y_3^{og} \\ -ik_4 D_{g1} Y_4^{og} + ik_5 A_{g2} Y_5^{og} e^{-ik_5 h} + ik_6 B_{g2} Y_6^{og} e^{-ik_6 h} \\ +ik_7 C_{g2} Y_7^{og} e^{-ik_7 h} + ik_8 D_{g2} Y_8^{og} e^{-ik_8 h} \end{pmatrix} \tag{4.53}$$

$$q_{g1} = -\lambda_g dA_g \begin{pmatrix} -ik_1 A_{g1} - ik_2 B_{g1} - ik_3 C_{g1} \\ -ik_4 D_{g1} + ik_5 A_{g2} e^{-ik_5 h} + ik_6 B_{g2} e^{-ik_6 h} \\ +ik_7 C_{g2} e^{-ik_7 h} + ik_8 D_{g2} e^{-ik_8 h} \end{pmatrix}$$

$$q_{s1} = -\lambda_s dA_s \begin{pmatrix} -ik_1 A_{g1} Y_1^{sg} - ik_2 B_{g1} Y_2^{sg} - ik_3 C_{g1} Y_3^{sg} \\ -ik_4 D_{g1} Y_4^{sg} + ik_5 A_{g2} Y_5^{sg} e^{-ik_5 h} + ik_6 B_{g2} Y_6^{sg} e^{-ik_6 h} \\ +ik_7 C_{g2} Y_7^{sg} e^{-ik_7 h} + ik_8 D_{g2} Y_8^{sg} e^{-ik_8 h} \end{pmatrix}$$

At node 2, z = h:

$$
\begin{aligned}
q_{i2} &= \lambda dA_i \begin{pmatrix} -ik_1 A_{g1} Y_1^{ig} e^{-ik_1 h} - ik_2 B_{g1} Y_2^{ig} e^{-ik_2 h} - ik_3 C_{g1} Y_3^{ig} e^{-ik_3 h} \\ -ik_4 D_{g1} Y_4^{ig} e^{-ik_4 h} + ik_5 A_{g2} Y_5^{ig} + ik_6 B_{g2} Y_6^{ig} \\ +ik_7 C_{g2} Y_7^{ig} + ik_8 D_{g2} Y_8^{ig} \end{pmatrix} \\
q_{o2} &= \lambda dA_o \begin{pmatrix} -ik_1 A_{g1} Y_1^{og} e^{-ik_1 h} - ik_2 B_{g1} Y_2^{og} e^{-ik_2 h} - ik_3 C_{g1} Y_3^{og} e^{-ik_3 h} \\ -ik_4 D_{g1} Y_4^{og} e^{-ik_4 h} + ik_5 A_{g2} Y_5^{og} + ik_6 B_{g2} Y_6^{og} \\ +ik_7 C_{g2} Y_7^{og} + ik_8 D_{g2} Y_8^{og} \end{pmatrix} \\
q_{g2} &= \lambda_g dA_g \begin{pmatrix} -ik_1 A_{g1} e^{-ik_1 h} - ik_2 B_{g1} e^{-ik_2 h} - ik_3 C_{g1} e^{-ik_3 h} \\ -ik_4 D_{g1} e^{-ik_4 h} + ik_5 A_{g2} + ik_6 B_{g2} \\ +ik_7 C_{g2} + ik_8 D_{g2} \end{pmatrix} \\
q_{s2} &= \lambda_s dA_s \begin{pmatrix} -ik_1 A_{g1} Y_1^{sg} e^{-ik_1 h} - ik_2 B_{g1} Y_2^{sg} e^{-ik_2 h} - ik_3 C_{g1} Y_3^{sg} e^{-ik_3 h} \\ -ik_4 D_{g1} Y_4^{sg} e^{-ik_4 h} + ik_5 A_{g2} Y_5^{sg} + ik_6 B_{g2} Y_6^{sg} \\ +ik_7 C_{g2} Y_7^{sg} + ik_8 D_{g2} Y_8^{sg} \end{pmatrix}
\end{aligned}
\tag{4.54}
$$

In a matrix form:

$$
\begin{pmatrix} q_{i1} \\ q_{o1} \\ q_{g1} \\ q_{s1} \\ q_{i2} \\ q_{o2} \\ q_{g2} \\ q_{s2} \end{pmatrix} = \begin{pmatrix} b_{11} & b_{12} & b_{13} & b_{14} & b_{15} & b_{16} & b_{17} & b_{18} \\ b_{21} & b_{22} & b_{23} & b_{24} & b_{25} & b_{26} & b_{27} & b_{28} \\ b_{31} & b_{32} & b_{33} & b_{34} & b_{35} & b_{36} & b_{37} & b_{38} \\ b_{41} & b_{42} & b_{43} & b_{44} & b_{45} & b_{46} & b_{47} & b_{48} \\ b_{51} & b_{52} & b_{53} & b_{54} & b_{55} & b_{56} & b_{57} & b_{58} \\ b_{61} & b_{62} & b_{63} & b_{64} & b_{65} & b_{66} & b_{67} & b_{68} \\ b_{71} & b_{72} & b_{73} & b_{74} & b_{75} & b_{76} & b_{77} & b_{78} \\ b_{88} & b_{82} & b_{83} & b_{84} & b_{85} & b_{86} & b_{87} & b_{88} \end{pmatrix} \begin{pmatrix} A_{g1} \\ B_{g1} \\ C_{g1} \\ D_{g1} \\ A_{g2} \\ B_{g2} \\ C_{g2} \\ D_{g2} \end{pmatrix} \tag{4.55}
$$

where

$$
b_{11} = ik_1 Y_1^{ig}\ ,\ b_{12} = ik_2 Y_2^{ig}\ ,\ b_{13} = ik_3 Y_3^{ig}\ ,\ b_{14} = ik_4 Y_4^{ig}
$$

$$
b_{15} = -ik_5 Y_5^{ig} e^{-ik_5 h},\ b_{16} = -ik_6 Y_6^{ig} e^{-ik_6 h},\ b_{17} = -ik_7 Y_7^{ig} e^{-ik_7 h},\ b_{18} = -ik_8 Y_8^{ig} e^{-ik_8 h}
$$

$$b_{21} = ik_1 Y_1^{og} \ , b_{22} = ik_2 Y_2^{og} \ , b_{23} = ik_3 Y_3^{og} \ , b_{24} = ik_4 Y_4^{og}$$
$$b_{25} = -ik_5 Y_5^{og} e^{-ik_5 h}, b_{26} = -ik_6 Y_6^{og} e^{-ik_6 h}, b_{27} = -ik_7 Y_7^{og} e^{-ik_7 h}, b_{28} = -ik_8 Y_8^{og} e^{-ik_8 h}$$

$$b_{31} = ik_1 \ , b_{32} = ik_2 \ , b_{33} = ik_3 \ , b_{34} = ik_4$$
$$b_{35} = -ik_5 e^{-ik_5 h} \ , b_{36} = -ik_6 e^{-ik_6 h} \ , b_{37} = -ik_7 e^{-ik_7 h} \ , b_{38} = -ik_8 e^{-ik_8 h}$$

$$b_{41} = ik_1 Y_1^{sg} \ , b_{42} = ik_2 Y_2^{sg} \ , b_{43} = ik_3 Y_3^{sg} \ , b_{44} = ik_4 Y_4^{sg}$$
$$b_{45} = -ik_5 Y_5^{sg} e^{-ik_5 h}, b_{46} = -ik_6 Y_6^{sg} e^{-ik_6 h}, b_{47} = -ik_7 Y_7^{sg} e^{-ik_7 h}, b_{48} = -ik_8 Y_8^{sg} e^{-ik_8 h}$$

$$b_{51} = -ik_1 Y_1^{ig} e^{-ik_1 h} \ , b_{52} = -ik_2 Y_2^{ig} e^{-ik_2 h} \ , b_{53} = -ik_3 Y_3^{ig} e^{-ik_3 h} \ , b_{54} = -ik_4 Y_4^{ig} e^{-ik_4 h}$$
$$b_{55} = ik_5 Y_5^{ig} \ , b_{56} = ik_6 Y_6^{ig} \ , b_{57} = ik_7 Y_7^{ig} \ , b_{58} = ik_8 Y_8^{ig}$$

$$b_{61} = -ik_1 Y_1^{og} e^{-ik_1 h}, b_{62} = -ik_2 Y_2^{og} e^{-ik_2 h}, b_{63} = -ik_3 Y_3^{og} e^{-ik_3 h}, b_{64} = -ik_4 Y_4^{og} e^{-ik_4 h}$$
$$b_{65} = ik_5 Y_5^{og} \ , b_{66} = ik_6 Y_6^{og} \ , b_{67} = ik_7 Y_7^{og} \ , b_{68} = ik_8 Y_8^{og}$$

$$b_{71} = -ik_1 e^{-ik_1 h} \ , b_{72} = -ik_2 e^{-ik_2 h} \ , b_{73} = -ik_3 e^{-ik_3 h} \ , b_{74} = -ik_4 e^{-ik_4 h}$$
$$b_{75} = ik_5 \ , b_{76} = ik_6 \ , b_{77} = ik_7 \ , b_{78} = ik_8$$

$$b_{81} = -ik_1 Y_1^{sg} e^{-ik_1 h}, b_{82} = -ik_2 Y_2^{sg} e^{-ik_2 h}, b_{83} = -ik_3 Y_3^{sg} e^{-ik_3 h}, b_{84} = -ik_4 Y_4^{sg} e^{-ik_4 h}$$
$$b_{85} = ik_5 Y_5^{sg} \ , b_{86} = ik_6 Y_6^{sg} \ , b_{87} = ik_7 Y_7^{sg} \ , b_{88} = ik_8 Y_8^{sg}$$

Eq.(4.55) can be described as

$$\hat{\mathbf{q}}_{\text{node}} = \mathbf{M}\left(k, \omega_n\right)\mathbf{A} \tag{4.56}$$

Substituting Eq.(4.47) into Eq.(4.56), yields

$$\mathbf{K}\left(k, \omega_n\right)\hat{\mathbf{T}}_{\text{node}} = \hat{\mathbf{q}}_{\text{node}} \tag{4.57}$$

in which $\mathbf{K}\left(k, \omega_n\right) = \mathbf{M}\left(k, \omega_n\right)\mathbf{H}\left(k, \omega_n\right)^{-1}$, representing the spectral element stiffness matrix, in resemblance to that of the finite element method. However, the spectral element matrix is exact and frequency-dependent.

For a multilayer system, each layer is described by a spectral element. The assembly of the global matrix is done following the finite element method, in which matrices assembly is dictated by the elements and nodes numbers. In this assembly process, the way the nodes are numbered determines the locations of the coefficients in the global stiffness matrix.

Consider a borehole heat exchanger embedded in a two layer system shown schematically in Figure 4.4. The system is described by two spectral elements and three nodes, numbered as shown in the figure. Each node has four degrees of freedom, describing the temperatures in pipe-in, $\hat{T}_{\mathrm{i}}$, pipe-out, $\hat{T}_o$, grout, $\hat{T}_{\mathrm{g}}$, and soil film, $\hat{T}_{\mathrm{s}}$. The stiffness matrix for each element is described by Eq.(4.57). Using the finite element method, the global spectral element equation can then be described as

$$\begin{bmatrix} K_{11}^1 & K_{12}^1 & & \\ K_{21}^1 & K_{22}^1+K_{11}^2 & K_{12}^2 & \\ & K_{21}^2 & K_{22}^2 & \end{bmatrix}\begin{bmatrix} \hat{\mathbf{T}}_1 \\ \hat{\mathbf{T}}_2 \\ \hat{\mathbf{T}}_3 \end{bmatrix}=\begin{bmatrix} \hat{\mathbf{q}}_1 \\ \hat{\mathbf{q}}_2 \\ \hat{\mathbf{q}}_3 \end{bmatrix} \tag{4.58}$$

in which the matrix on the left-hand side of the equation is the global stiffness matrix, with the superscript indices indicating the layer (element) number. The vector on the left-hand side is the degrees of freedom vector, indicating the nodal temperatures that need to be determined; and the vector on the right-hand side is the force vector, indicating the corresponding nodal heat fluxes.

The solution of the global system of equations is conducted using the IMSL mathematical library subroutine, *lin_sol_gen*, which solves a general system of linear equations $\boldsymbol{Ax}=\boldsymbol{b}$, (IMSL 2019). Eq. (4.38) is solved using the IMSL subroutine, *DZPOCC*, which solves for the roots of a polynomial with complex coefficients. The reconstruction of the time domain is carried out using the inverse FFT algorithm.

Upon solving the nodal values, the temperature anywhere within the element can be determined by the inverse fast Fourier transform, as :

$$\mathbf{T}(z,t)=\sum\nolimits_n \begin{pmatrix} \mathbf{A}_1 e^{-ik_1 z}+\mathbf{B}_1 e^{-ik_2 z}+\mathbf{C}_1 e^{-ik_3 z}+\mathbf{D}_1 e^{-ik_4 z} \\ +\mathbf{A}_2 e^{-ik_5(L-z)}+\mathbf{B}_2 e^{-ik_6(L-z)}+\mathbf{C}_2 e^{-ik_7(L-z)}+\mathbf{D}_2 e^{-ik_8(L-z)} \end{pmatrix} e^{i\omega_n t} \tag{4.59}$$

where $\mathbf{T}(z,t)$ represents $T_i(z,t)$, $T_o(z,t)$, $T_{\mathrm{g}}(z,t)$ or $T_s(z,t)$ in the time domain. The integration constants in Eq. (4.59) are determined from Eq.(4.47).

Upon solving the temperatures in the BHE, the temperature in the time domain in the soil mass can be determined using Eq. (4.21), as

$$T_{\mathrm{soil}}(r,z,t)=\sum\nolimits_n \hat{T}_s(z,\omega)\frac{K_o(k_s r)}{K_o(k_s r_{\mathrm{b}})}e^{i\omega_n t} \tag{4.60}$$

4.7 Modelling multiple borehole heat exchangers: a superposition technique

A superposition technique for Dirichlet boundary conditions is developed to extend the model from a single BHE embedded in an axial symmetric, multilayer domain to multiple borehole heat exchangers embedded in a three-dimensional domain.

Eq. (4.21) is the solution of the soil heat equation due to a single BHE. Here, we extend this solution to multiple borehole heat exchangers.

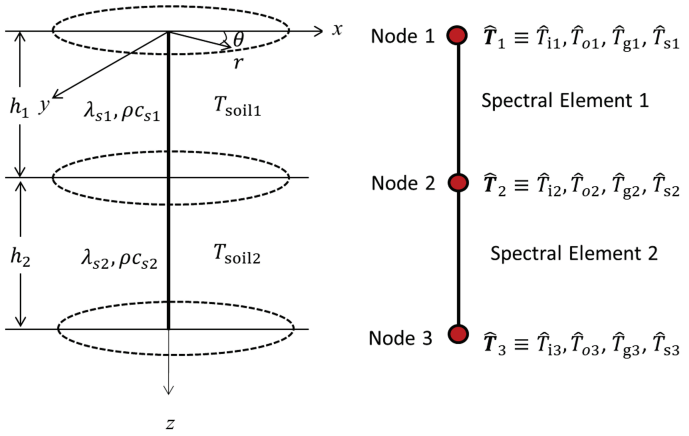

Figure 4.4: Two-layer system and its spectral element discretization

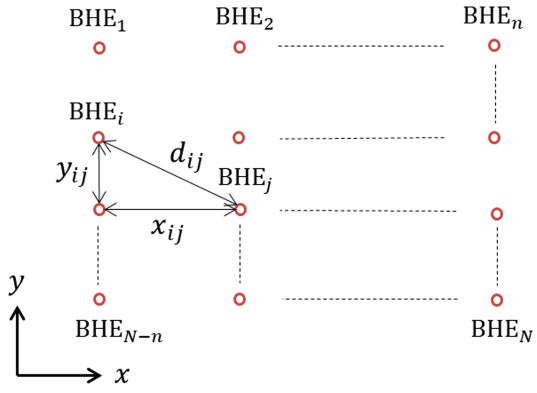

Figure 4.5: Multiple borehole heat exchangers configuration

Figure 4.5 shows a network of $n \times m$ borehole heat exchangers. The radial distance between BHE_i at $(x_i\ ,\ y_i)$ and BHE_j at $(x_j\ ,\ y_j)$ is calculated as

$$d_{ij} = \sqrt{x_{ij}^2 + y_{ij}^2} \tag{4.61}$$

in which $x_{ij} = |x_i - x_j|$ and $y_{ij} = |y_i - y_j|$.

As Eq. (4.21) imposes Dirichlet boundary condition at the boundary between the soil mass and the BHE, the superposition principle is not directly applicable. The superposition principle works directly for Neumann boundary conditions, and the temperature anywhere in the domain is calculated simply by the algebraic sum of temperatures aroused by heat fluxes from all heat sources. At steady state, the temperature will reach equilibrium and the heat fluxes become constant. For Dirichlet boundary conditions, however, the superposition works on condition that the prescribed temperature at a borehole must be made equal to the sum of temperatures aroused at its boundary by all boreholes, including itself. This entails modifying the temperature amplitudes at the boreholes and coupling them via a matrix technique, as described hereafter.

The temperature of a soil point at distance r from a BHE can be calculated using Eq.(4.21), which can be written in a general form as

$$\hat{T}_{\text{soil}}(r) = B\,K_o(k_s\,r) \tag{4.62}$$

For multiple borehole heat exchangers, and following the superposition principle, the temperature of a soil point at distances $r_1 \ldots r_N$ from N borehole heat exchangers can be described as

$$\hat{T}_{\text{soil}}(r) = B_1 K_o(k_s r_1) + B_2 K_o(k_s r_2) + \cdots + B_N K_o(k_s r_N) \tag{4.63}$$

As mentioned above, the temperature amplitudes ($B_1 \ldots B_N$) at the borehole heat exchangers need to be modified to take into consideration the effect of all involved boreholes. Solving Eq. (4.63) at the BHE locations, and upon imposing the boundary condition in Eq.(4.10), it yields

$$\begin{aligned}
\hat{T}_{s1} &= B_1 K_o(k_s r_b) + B_2 K_o(k_s d_{12}) + \cdots + B_N K_o(k_s d_{1N}) \\
\hat{T}_{s2} &= B_1 K_o(k_s d_{21}) + B_2 K_o(k_s r_b) + \cdots + B_N K_o(k_s d_{2N}) \\
&\vdots \qquad\qquad \vdots \qquad\qquad \vdots \\
\hat{T}_{sN} &= B_1 K_o(k_s d_{N1}) + B_2 K_o(k_s d_{N2}) + \cdots + B_N K_o(k_s r_b)
\end{aligned} \tag{4.64}$$

in which d_{12} is the distance between BHE_1 and BHE_2, etc., as shown in Figure 4.5.

In a matrix format, Eq. (4.64) becomes

$$\begin{pmatrix} \hat{T}_{s1} \\ \hat{T}_{s2} \\ \vdots \\ \hat{T}_{sN} \end{pmatrix} = \begin{pmatrix} K_o(k_s r_b) & K_o(k_s d_{12}) & \cdots & K_o(k_s d_{1N}) \\ K_o(k_s d_{21}) & K_o(k_s r_b) & \cdots & K_o(k_s d_{2N}) \\ \vdots & \vdots & \vdots & \vdots \\ K_o(k_s d_{N1}) & K_o(k_s d_{N2}) & \cdots & K_o(k_s r_b) \end{pmatrix} \begin{pmatrix} B_1 \\ B_2 \\ \vdots \\ B_N \end{pmatrix} \tag{4.65}$$

This equation states that the prescribed temperature at the borehole, $\hat{T}_{s1}$ for instant, is equal to its temperature plus temperatures generated by all other boreholes at its boundary. Its temperature, B_1 in this case, is not its prescribed value, but has to be determined by solving Eq. (4.65).

Eq. (4.65) can be expressed as

$$\hat{\mathbf{T}}_s = \mathbf{G}\,\mathbf{B} \tag{4.66}$$

Solving for **B**, gives

$$\mathbf{B} = \mathbf{G}^{-1}\hat{\mathbf{T}}_s \tag{4.67}$$

Upon substituting Eq. (4.67) into Eq.(4.63), the temperature at any radial point in the soil mass can be calculated.

4.8 Model verification

Analytical solution describing heat flow in multiple borehole heat exchangers embedded in a multilayer soil mass has not been introduced before. Accordingly, verification of the proposed model is done by comparing its computational results with those obtained from a detailed finite element model. The finite element package COMSOL Multiphysics (COMSOL 2019) is utilized. To reduce the CPU time of the finite element analysis, a relatively small geometry has been designed for this purpose.

A shallow geothermal system constituting four borehole heat exchangers embedded in a soil mass consisting of two soil layers with different thermal conductivity is modelled. The borehole heat exchangers are assumed 10 m long, constituting a single U-tube and grout. The soil mass is 10 m in depth and consisting of two layers, each 5 m in depth. It radially extends to infinity.

The borehole heat exchangers are configured as shown in Figure 4.6. Details of the material and geometrical parameters are given in Table 4.1. The initial temperature in all components is assumed 0 °C, and the temperature at the inlets of pipe-in (T_{in}) of the four borehole heat exchangers is prescribed to 20 °C.

The spectral element mesh consists of two, 2-node spectral elements. The use of two spectral elements is necessary because the geometry involves two soil layers with different physical parameters. The number of the borehole heat exchangers does not

influence the required number of spectral elements, as they are simulated by the superposition technique introduced in Section 4.7.

The finite element mesh, on the other hand, is made 60 m x 60 m x 10 m, and it consists of 494012, 3D tetrahedral elements, where along the BHE and in the surrounding soil mass, the mesh is made relatively fine. Figure 4.7 shows the finite element mesh and the top view at the boreholes region.

Table 4.1: Material and geometrical parameters of the verification example

Parameter	**Value**
Borehole:	
Borehole length	10 m
Borehole diameter	0.10 m
U-tube external diameter	0.03 m
U-tube thermal conductivity, λ_p	0.42 W/(mK)
Fluid:	
Density, ρ	1000 kg/m^3
Specific thermal capacity, c	4186 J/(kg.K)
Thermal conductivity, λ	0.56 W/(mK)
Dynamic viscosity, μ	0.001 Pa.s
Grout:	
Density, ρ_{g}	1420 kg/m^3
Specific thermal capacity, c_{g}	1197 J/(kg.K)
Thermal conductivity, λ_{g}	0.65 W/(m.K)
Soil:	
Film thickness	2 cm
density, ρ_{s}	1680 kg/m^3
Specific thermal capacity, c_s	400 J/(kg.K)
Thermal conductivity, λ_{s} at $z \geq -5m$	1 W/(m.K)
Thermal conductivity, λ_s at $z \leq -5m$	2 W/(m.K)

Figure 4.8 shows the temperature distributions in pipe-in, pipe-out and grout of one of the boreholes as obtained from the spectral element model and the finite element model, for short and long terms of operation. The figure shows a good match between the two results, though a deviation of less than 0.5 °C exists around the outlet of pipe-out. This deviation can be explained as a combination between the inaccuracy of the spectral element model due to the negligence of the radial dimension of the grout, and the typical inaccuracy of the finite element model due to the mesh size effect. Nevertheless, this deviation is relatively small and diminishes as time evolves.

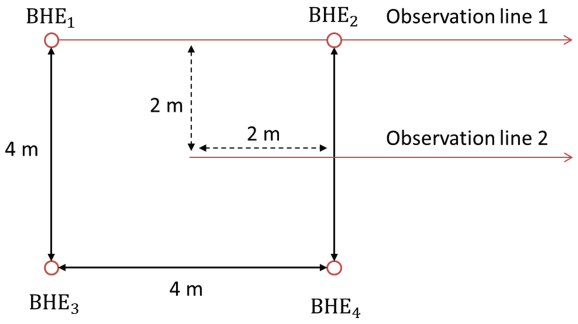

Figure 4.6: 4 borehole heat exchangers embedded in a two-layers soil mass

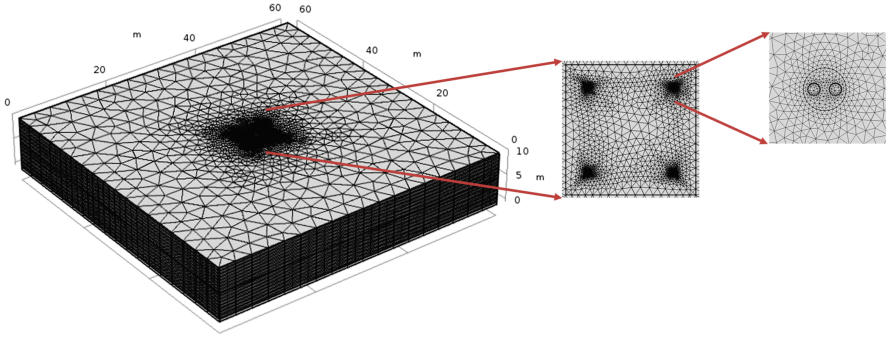

Figure 4.7: The finite element mesh

Physically, the figure shows a jump at the boundary between the upper and the lower soil layers due to the difference in their thermal conductivities. This demonstrates the capabilities of both computational techniques for simulating such a phenomenon.

Figures 4.9 and 4.10 show the radial soil temperature profile along Observation line 1 (see Figure 4.6), for the upper and lower soil layers, respectively. Similarly, Figures 4.11 and 4.12 show the radial soil temperature profile along Observation line 2. The figures show a good match between the two computational results. The small deviation between the results can be attributed to the finite element mesh size, which is relatively coarse in the radial direction. Nevertheless, this deviation is relatively small and diminishes as time evolves.

Physically, the figures show that the temperature profile along Observation line 1 exhibits a clear jump at BHE_1 and BHE_2 locations. This is not apparent along Observation line 2 because it is relatively far from the boreholes. Both models capture this behaviour properly.

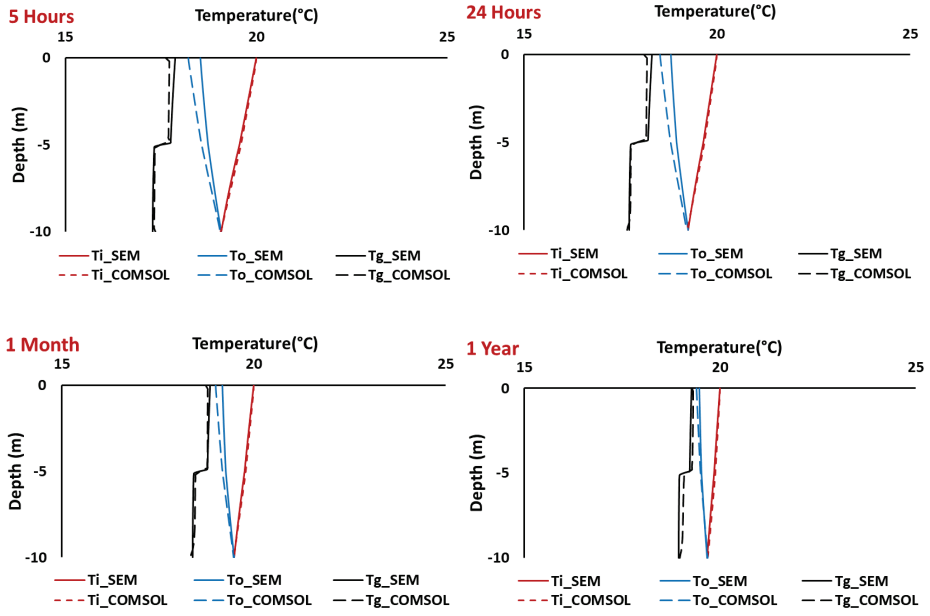

Figure 4.8: Temperature profile for pipe-in, pipe-out and grout for one of the 4 BHE's at different times

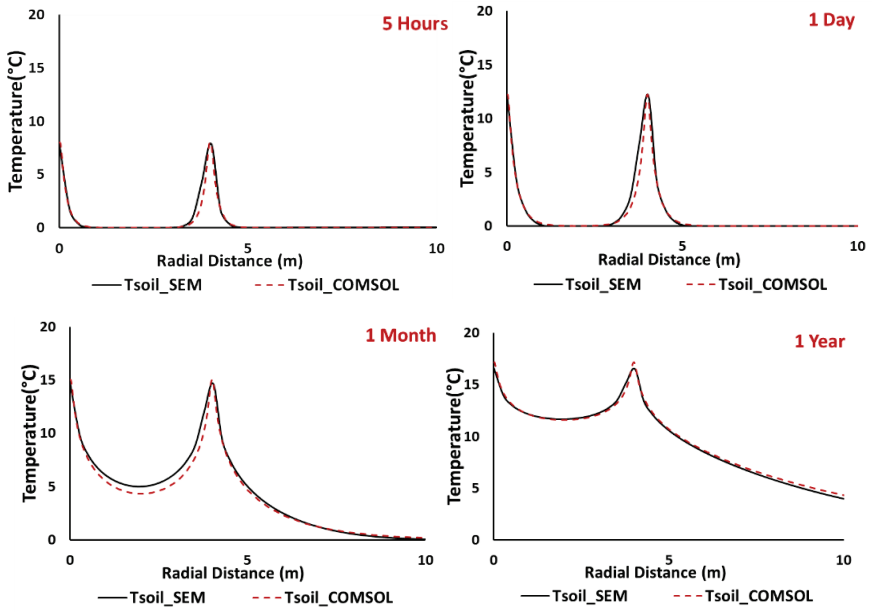

Figure 4.9: Radial temperature profile along Observation line1 for the top soil layer

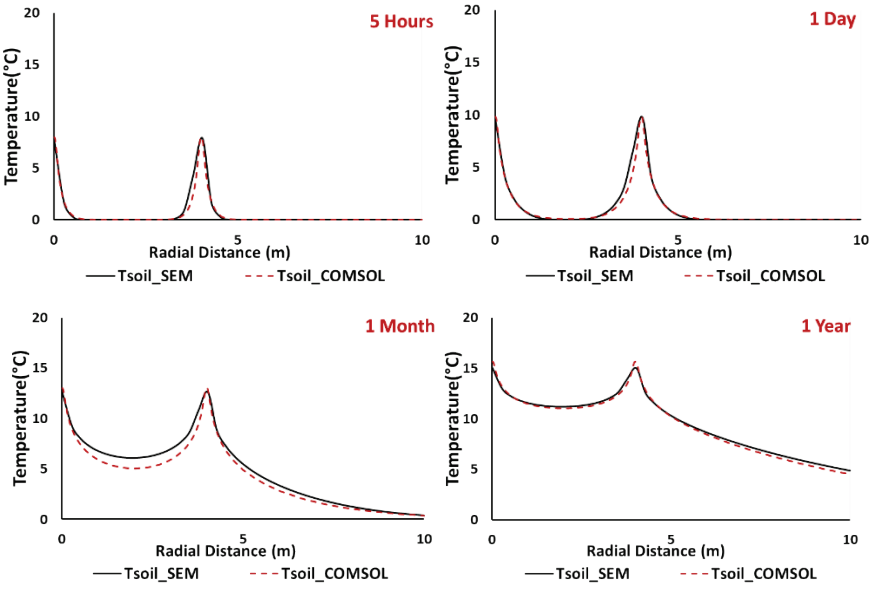

Figure 4.10: Radial temperature profile along Observation line 1 for the bottom soil layer

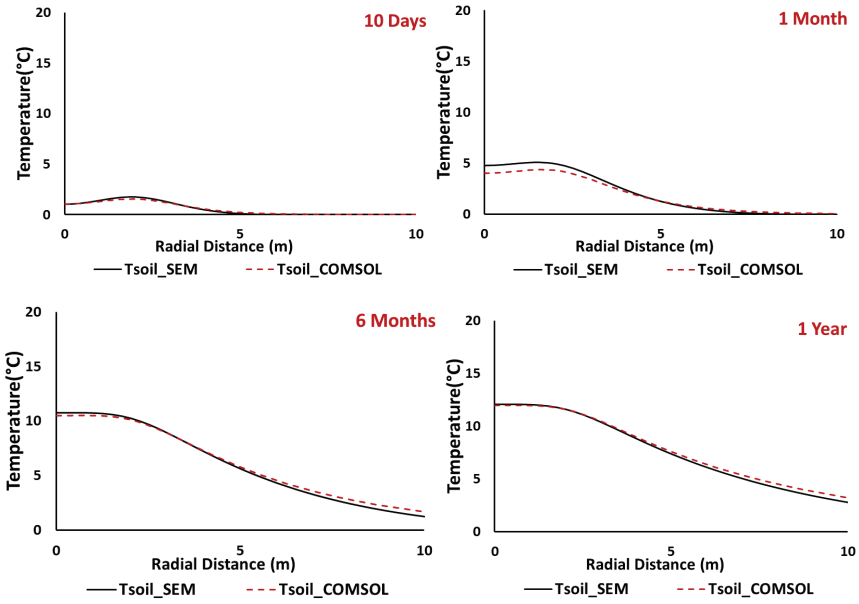

Figure 4.11: Radial temperature profile along Observation line 2 for the top soil layer

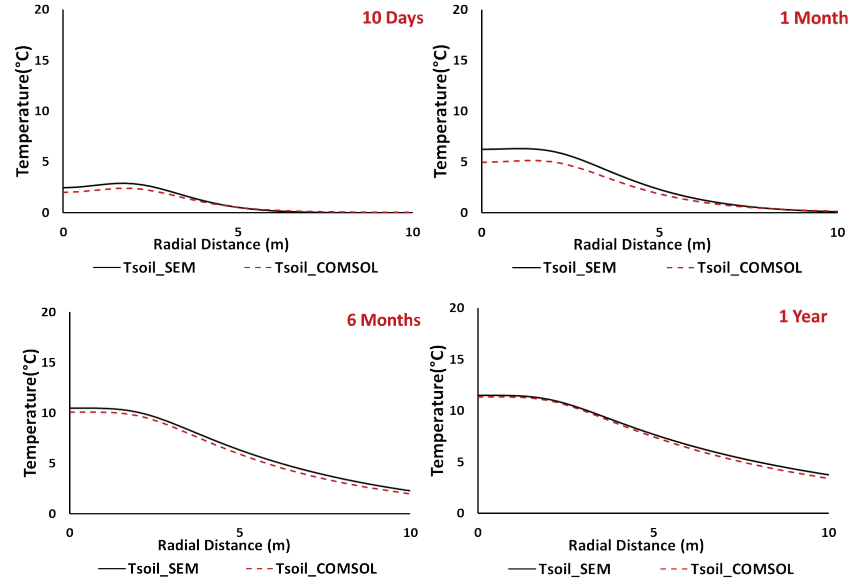

Figure 4.12: Radial temperature profile along Observation line 2 for the bottom soil layer

4.9 Numerical examples

To demonstrate the model computational capabilities in simulating complicated geometries, a numerical example illustrating heat flow in a 3D shallow geothermal system is introduced. The geothermal system is assumed to consist of 9, 100 m in length, borehole heat exchangers embedded in 5 soil layers with highly contrasted thermal properties. The soil thickness is 20 m for each.

A 3 x 3 BHE configuration as shown in Figure 4.13 is assumed. The material and geometrical parameters of the geothermal system are given in Table 4.2 and Figure 4.14. The initial temperature in all components is assumed 10 °C, and the temperature at the inlets of pipe-in of the 9 borehole heat exchangers is prescribed to 30 °C. The geometry is simulated using 5, 2-node spectral elements.

The proposed model allows the calculation of temperature distributions in all borehole heat exchangers without differentiation between inner, side and corner boreholes. Here, we present the computational results at the central BHE (BHE_5) and two soil points, indicated as observation points in Figure 4.13.

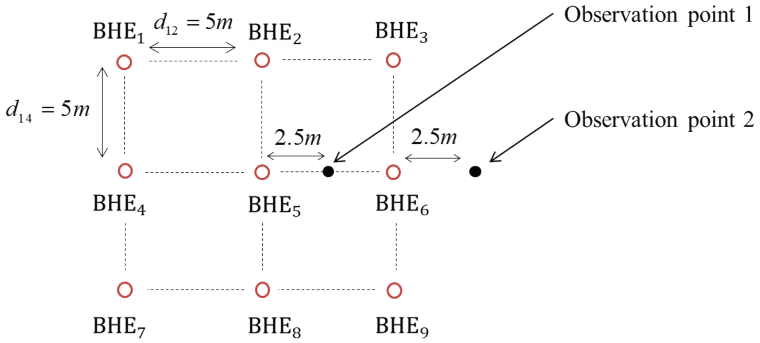

Figure 4.13: Borehole heat exchangers configuration

Figure 4.15 shows the temperature distributions in pipe-in, pipe-out and grout of BHE_5 on short and long terms of operation. The first figure shows that after 100 seconds, the fluid has travelled 50 m in pipe-in, giving rise to thermal interaction with the soil via the grout. As a result, the fluid in pipe-in cools down while the grout temperature rises up. Additionally, this figure shows an interesting increase in temperature in pipe-out despite the fact that the fluid hasn't reached it yet. This increase in temperature is due to heat conduction occurring as a result of its direct contact with the grout. At latter times, Figure 4.15 shows the effect of the layers thermal conductivities on the temperature distribution in the grout and its influence on pipe-in and pipe-out.

Table 4.2. Material and geometrical parameters of the numerical example

Parameter	Value	Parameter	Value
Borehole:		**Soil:**	
Borehole length	100 m	Film thickness	0.02 m
Borehole diameter	0.1 m	Density , ρ_s	1680 kg/m^3
Pipe external diameter	0.03 m	Specific thermal capacity , c_s	400 J/(kg.K)
Pipe thermal conductivity	0.42 W/(mK)		
Fluid:		$\mathbf{0 \geq z \geq -20m}$	
Density, ρ	1000 kg/m^3	Thermal conductivity, λ_s	2.5 W/(m.K)
Specific thermal capacity, c	4186 J/(kg.K)	$\mathbf{-20 \geq z \geq -40m}$	
Thermal conductivity, λ	0.56 W/(mK)	Thermal conductivity, λ_s	1 W/(m.K)
Dynamic viscosity, μ	0.001 Pa.s	$\mathbf{-40 \geq z \geq -60m}$	
Velocity, u	0.5 m/s	Thermal conductivity, λ_s	4 W/(m.K)
Grout:		$\mathbf{-60 \geq z \geq -80m}$	
Density, ρ_g	1420 kg/m^3	Thermal conductivity, λ_s	0.5 W/(m.K)
Specific thermal capacity, c_g	1197 J/(kg.K)	$\mathbf{-80 \geq z \geq -100m}$	
Thermal conductivity, λ_g	0.62 W/(m.K)	Thermal conductivity, λ_s	3 W/(m.K)

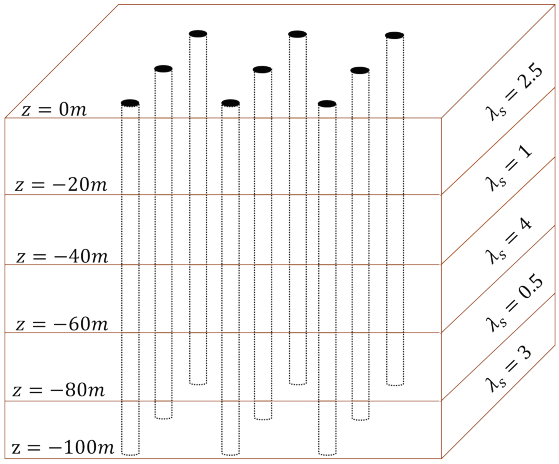

Figure 4.14: A schematic representation of the geometry of the numerical example

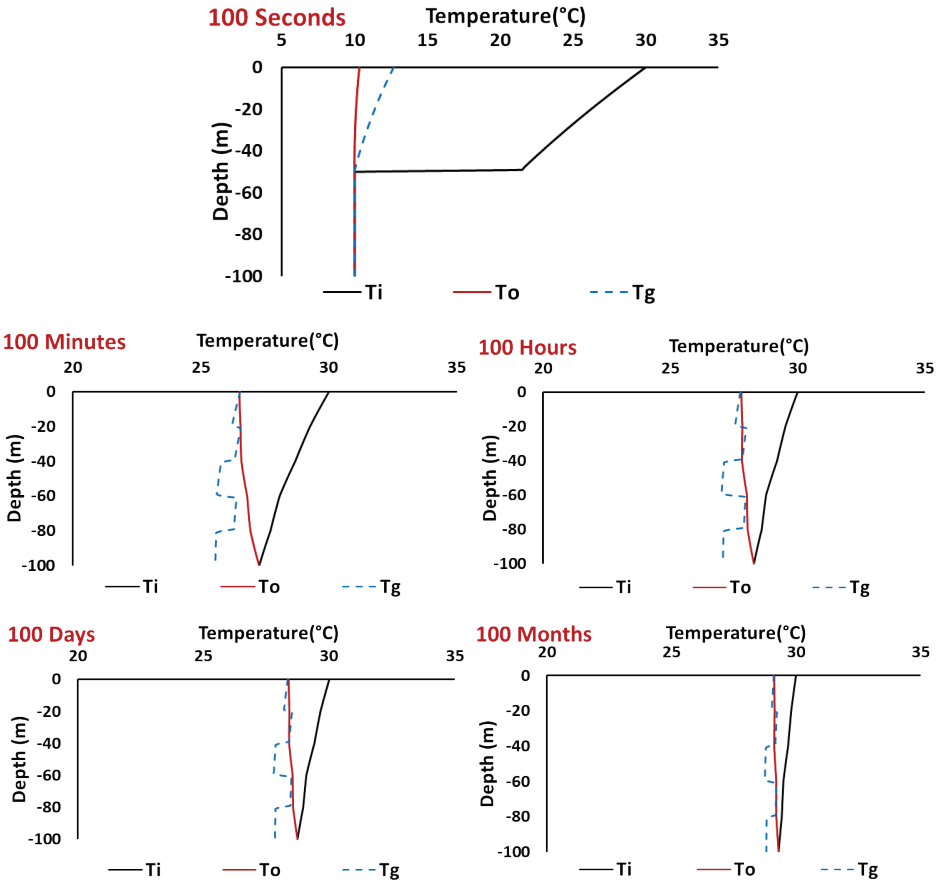

Figure 4.15: Temperature in pipe-in, pipe-out and grout for BHE_5 at different times

Figure 4.16 shows the vertical temperature profile in the soil mass at Observation Points 1 and 2, for short and long terms. The figure shows clearly the jumps in temperatures at the boundaries between layers. The figure also shows an interesting flip in the direction of the temperature jumps at longer terms. In the short term, layers with relatively higher thermal conductivities exhibit faster heat flow, as manifested by the advancing temperature fronts in layers 1, 3 and 5 (see 100 hours and 50 days profiles). In the long term, layers with lower thermal conductivities exhibit advancing temperature fronts (see 50 months and 10 years profiles for layers 2 and 4). The reason for this flip is that layers with relatively high thermal conductivities exhibit, at the beginning, faster heat flow, but, later on, faster thermal dissipation. In the contrary, layers with relatively low thermal conductivities exhibit slower heat flow at the beginning and slower thermal dissipation later on. This phenomenon has also been captured and discussed by Abdelaziz et al, (2014).

Capturing these physical phenomena exhibits clearly the capability of the model to describe the complex nature of heat flow in multiple borehole heat exchangers embedded in multilayer systems.

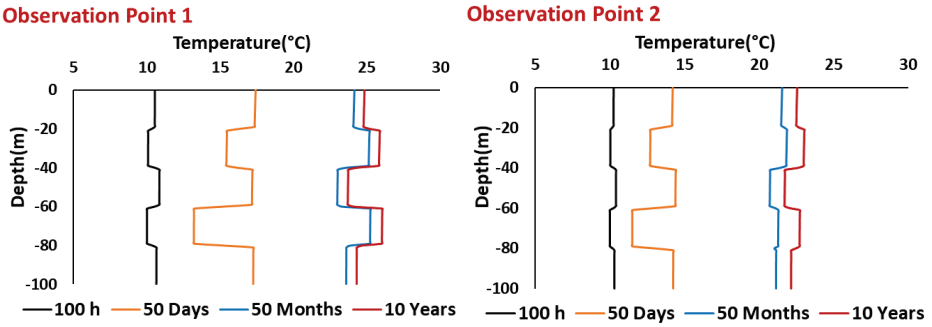

Figure 4.16: Vertical soil temperature profiles at different times at observation points 1 and 2

4.10 Soil-film thickness

In this section, we highlight the independence of the temperature distributions in the BHE components and the soil mass on the soil film thickness.

To minimize the effect of the soil film thickness on the temperature distributions, the thermal interaction coefficients must be appropriately formulated. In pursuit of this, the thermal interaction coefficients given in Section 2.3 are proved to be the most appropriate. Using these coefficients, we here demonstrate the model-independency on the soil film via a numerical example. The geometry and material properties, together with the initial and boundary conditions, are as for the numerical example given in Section 4.9.

Figure 4.17 shows the temperature distributions in pipe-in, pipe-out, grout and soil film for a single BHE at 0.5 hour, 5 hours, 5 days and 5 months, using 1 mm, 10 mm, 20 mm and 30 mm soil film thicknesses. The figure clearly shows that the soil film thickness has practically no effect on the temperature distributions except at 0.5 hour where there is a deviation of around 1 - 2 °C between 1 mm and 30 mm, mainly in the lower thermal conductivity layers.

Figure 4.18 shows the corresponding temperature distributions in the soil mass in the third layer. Obviously, the temperature distribution in the soil mass has not been affected by the soil film thickness, except at 0.5 hour where there is little deviation between 1 mm and 30 mm soil film thicknesses.

4.11 Conclusions

In this chapter, a spectral element model for the simulation of transient conduction-convection heat flow in a three-dimensional shallow geothermal system consisting of multiple borehole heat exchangers embedded in a multilayer soil mass is introduced. The model shares the exactness and computational efficiency of the analytical models, and a great extent of generality in describing the geometry and initial and boundary conditions of the numerical techniques. It can describe heat flow is any number of borehole heat exchangers with any layout configuration, embedded in any number of soil layers using minimal CPU time and capacity.

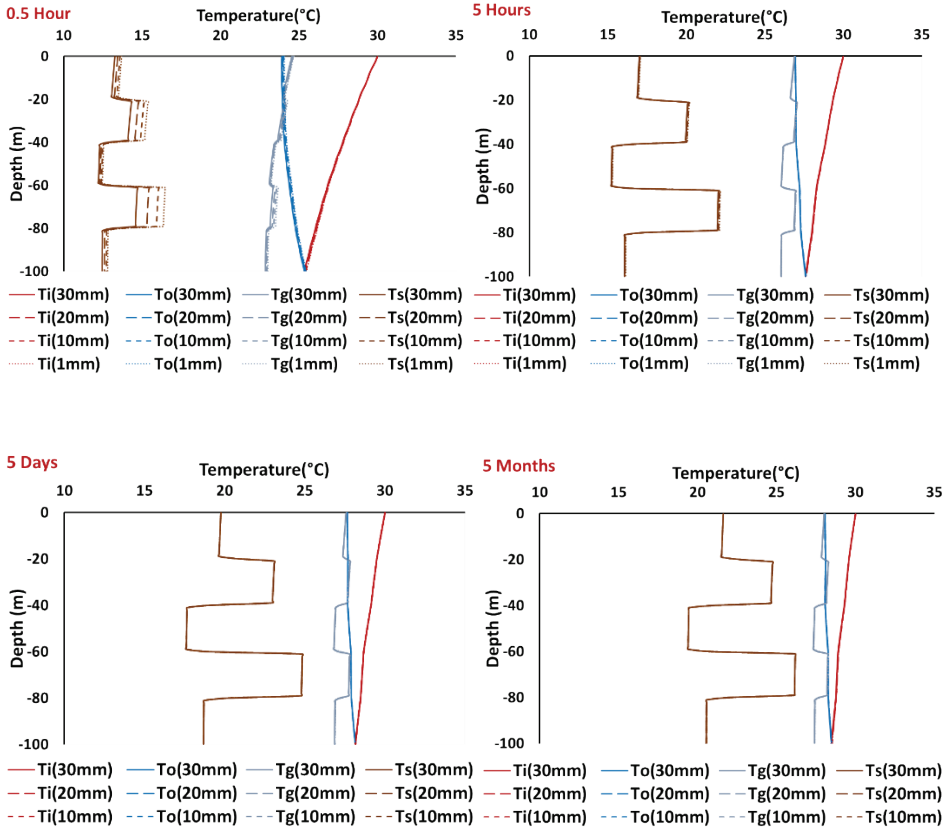

Figure 4.17: Pipe-in, pipe-out, grout and soil film temperature distributions using different soil film thicknesses at different times

The key for obtaining such an exact, computationally efficient and practically general model is the innovative mix between the conceptual model, the mathematical model and the solution technique. The link between 1D domain (for the borehole), axial symmetric 2D domain (for a homogeneous soil layer) and 3D domain (for multiple layers), together with the use of the soil film, makes the conceptual model mathematically feasible. Changing the BHE-soil non-homogeneous differential equations to homogenous differential equations (see Eqs. (4.4) and (4.23)) together with the matrix formulation for coupling the boreholes (see Eq. (4.63)), makes the mathematical model solvable. The use of the spectral element method for modelling multilayer systems together with the superposition technique for modelling multiple borehole heat exchangers makes the solution technique fit to the physics of the problem and computationally efficient.

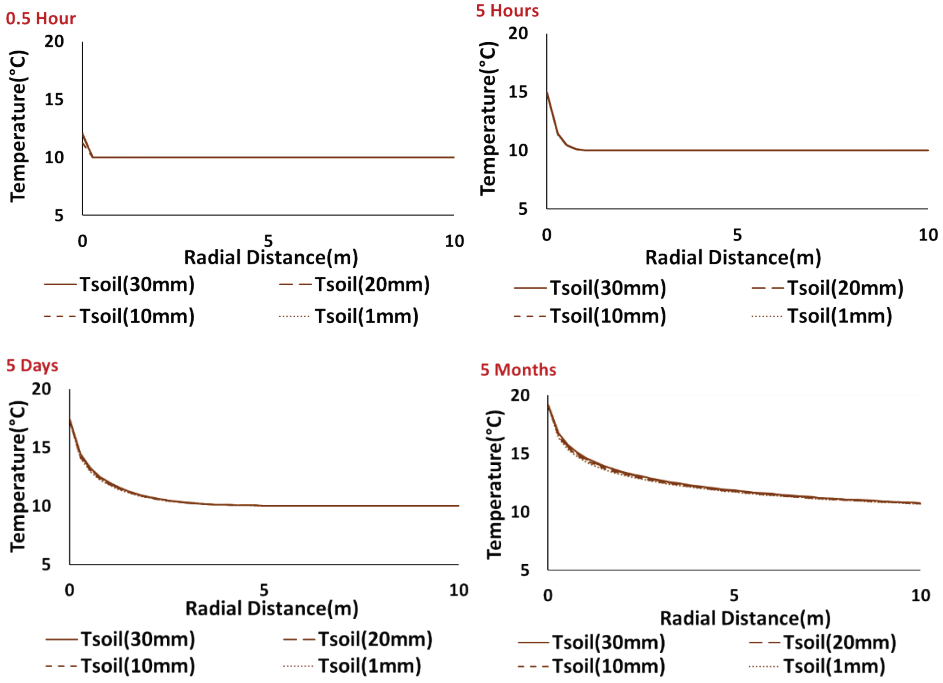

Figure 4.18: Soil radial temperature distribution in the third layer using different soil film thickness at different times

5

Analysis of short-to-long term heat flow in GSHP systems based on heat pump power

This chapter introduces a semi-analytical model based on the spectral element method for three-dimensional, short-to-long term heat flow in multiple borehole, multilayer ground source heat pump systems. The model is distinguished by its computational technique for expressing the input signal at the boundary of the borehole heat exchanger, giving rise to two important engineering features. First, the calculation can be conducted from seconds to years in a single run. This is achieved by discretizing the input signal at the inlet boundary of the borehole heat exchanger using a tailored fast Fourier transform with multiple time-stepping algorithm. Second, the calculation can be conducted using a Neumann boundary condition, instead of the commonly utilized Dirichlet boundary condition. This is achieved by mathematically relating the heat pump power to the heat flux at the inlet of the borehole heat exchanger, allowing direct use of the heat pump power signal as input instead of the inlet temperature. These features make the model computationally efficient that can readily be utilized for system design and included in inverse calculations. The two features are discussed in detail, verified against experimental measurements, and their functionality is highlighted by numerical examples.

This chapter is based on BniLam N., Al-Khoury R. (2019). Analysis of short-to-long term heat flow in GSHP systems based on heat pump power. Applied Thermal Engineering. Available online 19 October 2019, 114561

5.1 Introduction

The ground source heat pump (GSHP) technology can play an important role in boosting the economy and improving the environment. It relies on energy gain from shallow depths, which are available nearly everywhere, and its operation produces minimal CO_2 emission into the atmosphere. As a result, this technology is booming, and geothermal engineers are endeavouring to make it more efficient and economic. Several European projects are specifically designed to develop more accurate and reliable computational models aiming to optimize the efficiency of this technology; see for example Horizon Projects (2010).

Presently, there are a considerable number of computational models describing heat flow in GSHP systems using different solution methods and adopting a wide range of physical and geometrical complexities. Cui et. al. (2018) gave a comprehensive review on the available computational models for GSHP systems. Nevertheless, despite the presence of a large number of models and softwares, there are yet two important engineering features that need to be addressed in a more effective way: short-to-long term analysis of system performance, and analysis directly based on the heat pump power. This chapter addresses these two features by introducing a computational technique enabling their implementation within the spectral element framework. Hereafter, we highlight the significance of these two features and how they are treated in this work.

Feature 1: Short-to-long term analysis is important to evaluate the system performance at different times of the days and years. Heating and cooling of buildings includes periods of switching ON and OFF, and during the GSHP lifetime, hourly, daily and seasonal periods of switching ON and OFF take place intensely. This operational requirement severely restricts the calculations such that if detailed transient analysis is sought, the long term performance of the system will be difficult to pursue, but if the global lifetime analysis is sought, the short term performance will be overlooked. As a consequence, the calculations are usually conducted for either short term or long term. This problem is in particular manifested in the numerical models and tools. COMSOL Multiphysics (COMSOL 2019), FEFLOW finite element package (FEFLOW 2019), and, to a lesser extent, ABAQUS finite element package (ABAQUS 2019) and TOUGH2 finite difference code (Pruess et al, 1999), are the most commonly utilized numerical tools for this purpose. These tools can provide advanced numerical facilities, but are severely restricted in conducting detailed short-to-long term analysis. The demand for a fine mesh due to the geometrical disproportionality of the system and the need for small time steps for the short term analysis make the CPU demands unrealistic for analysing the long term performance of the system, especially if the analysis is intended for daily engineering practice.

Analytical and semi-analytical models are not exemption, and the majority of models are mainly suitable for either short term analysis or long term. Attempts to model short-to-long term performance of GSHP systems rely either on the Fast Fourier Transform (FFT) or the step response functions. Marcotte and Pasquier (2008a), and Zhang et. al. (2018)

introduced, among others, semi-analytical models based on FFT. The FFT algorithm is rather efficient and employing it enables studying the performance of the system for as many time steps as required. However, the standard FFT is formulated for constant time stepping schemes. Depending on the size of the time step, the analysis can go for any desirable time span, yet, only one time step size is allowed: seconds, minutes, hours, days, months or years; not a combination of them. This characteristic restricts the standard FFT from utilization for short-to-long terms analysis; rather for either short term or long term.

Claesson and Javed (2011), and Li et al. (2014) introduced analytical models to calculate the temperature distribution in the system from minutes to decades. Claesson and Javed (2011) adopted a two-step solution. For the short term (the first 100 hours) they solve the conductive axial-symmetric heat equation analytically using Laplace transform; and for the long term, they use the line source solution. Li et al. (2014), on other hand, developed a temperature response function that combines the composite-medium line-source solution and the conventional ILS and FLS solutions using the matched asymptotic expansion technique. More details on both models can be found in Li and Fang (2016). Despite the effectiveness of these models, they are formulated based on the line heat source models which do not take the detailed conduction-convection heat flow in the borehole heat exchanger.

In this Chapter, we address detailed heat flow in an effectively 3D GSHP systems for short-to-long terms by tailoring the Fast Fourier Transform (FFT) algorithm to allow for the use of multiple time-stepping schemes. This feature facilitates the calculation of heat flow for any desired details, ranging from one second to years, done in a single run.

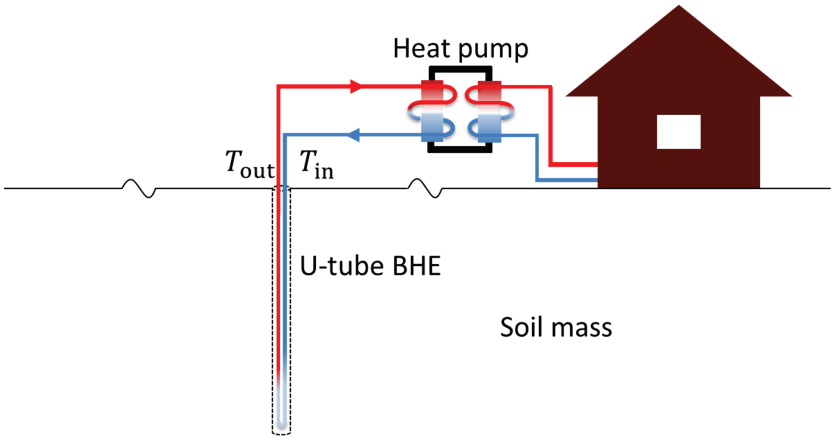

Figure 5.1: A schematic representation of a GSHP system (recall from Chapter 1)

Feature 2: Analysis based directly on the heat pump power is physically more realistic than that based on a prescribed temperature at the inlet of pipe-in. This temperature is a result of the heat pump operation; i.e. not known a priori. In engineering practice, the heat pump power is prescribed as a heat flux in models solely solving the heat flow in infinite and semi-infinite domains, such as the line and cylindrical heat source models. For instance, the heat pump power can directly be prescribed as a constant heat flow rate per unit length, q, in the well-known infinite line source model (Carslaw and Jaegar 1959):

$$T(r,t) \simeq T_0 + \frac{q}{4\pi\lambda_s}\left(\ln\frac{4\alpha t}{r^2} - \gamma\right) \tag{5.1}$$

in which $T(r,t)$ is the temperature of the medium at radial distance r from the heat line source, λ_s $(\mathrm{W/(m\,K)})$ is the solid domain thermal conductivity, $\alpha(\mathrm{m^2/s})$ is thermal diffusivity and $\gamma = 0.5772$, Euler's constant.

Models which calculate heat flow in the borehole hole exchanger (BHE), the heat pump power cannot directly be prescribed. Instead, the temperature of the circulating fluid coming out of the heat pump and entering the inlet of pipe-in is prescribed. This temperature is calculated using the power equation:

$$P = \dot{m}c\left(T_{\mathrm{in}}^{p} - T_{\mathrm{out}}^{p}\right) \tag{5.2}$$

in which $P(\mathrm{W})$ is the mean power of the heat pump, $\dot{m}(\mathrm{kg/s})$ is the mass flow rate of the circulating fluid, $c(\mathrm{J/(kg\,K)})$ is its specific heat capacity, $T_{\mathrm{in}}^{p}(\mathrm{K})$ is the fluid temperature entering the heat pump and $T_{\mathrm{out}}^{p}(\mathrm{K})$ is the fluid temperature leaving the heat pump. T_{in}^{p} is considered equal to the temperature T_{out} coming out of pipe-out of the BHE; and T_{out}^{p} is considered equal to the temperature T_{in} entering pipe-in of the BHE, see Figure 5.1. T_{in} is utilized as the Dirichlet boundary condition to the inlet of pipe-in from which the temperature distribution in the GSHP system is calculated. The procedure to calculate T_{in} from the heat pump power is given in Algorithm 5.1.

This algorithm has been implemented in several numerical tools, see for example Al-Khoury et al. (2010), Ozudogru et al. (2014) and Rui et al. (2018). A similar algorithm is utilized in semi-analytical tools such as EED (EED 2019, Eskilson 1987) and GLHEPRO (GLHEPRO 2019, Spitler, 2000). Despite the practical use of this algorithm, it suffers the shortcomings of the step response function in terms of its computational inefficiency and the overlooking of the details within the time steps.

In this chapter we address the use of heat pump power as a Neumann boundary condition by formulating a mathematical equation relating the heat pump power to the heat flux at the inlet of pipe-in. This feature allows the direct use of heating and cooling design specifications to calculate the temperature distribution in the system. In this case, T_{in} becomes unknown and needs to be computed, similar to T_{out} and all other temperatures at any geometrical point in the system.

5.2 Theoretical background of the model

The above mentioned two engineering features, short-to-long term analysis and analysis based on the heat pump power, are implemented in the computer code STAND, which stands for Shallow geoThermal Analysis aNd Design. This code constitutes a semi-analytical spectral element model capable of computing detailed heat flow in effectively three-dimensional GSHPs constituting multiple BHEs embedded in multilayer systems, subjected to arbitrary temporal Neumann or Dirichlet boundary conditions. The background theory of this model has been thoroughly presented Chapter 4.

The governing heat equations and initial conditions of a ground source heat pump consisting of a single U-tube borehole heat exchanger embedded in a soil mass, Figure 4.1, are presented in Section 4.3. The boundary condition, on the other hand, at the inlet of pipe-in might be any of two types:

a **Neumann boundary condition**:

$$q_i(0,t) = q_{\text{in}}(t) = -\lambda \frac{dT_i}{dz} dA_i \tag{5.3}$$

or a **Dirichlet boundary condition**:

$$T_i(0,t) = T_{\text{in}}(t) \tag{5.4}$$

where q_{in} is the heat flux and T_{in} is the prescribed inlet temperature, that might have any arbitrary distribution in time.

Algorithm 5.1: Prescribing T_{in} based on heat pump power

1: DO $n = 1$ to N (n : the time step)

2: Read ${}^{n+1}P\ ;\ \dot{m};\ c$

3: Calculate ${}^{n+1}T_{\text{out}}^{P}$ from Eq. (5.2) such that ${}^{n+1}P = \dot{m}c\left({}^{n}T_{\text{in}}^{p} - {}^{n+1}T_{\text{out}}^{p}\right)$, (where ${}^{n}T_{\text{in}}^{p}$ is known from the previous time step)

4: ${}^{n+1}T_{\text{in}} \leftarrow {}^{n+1}T_{\text{out}}^{P}$

5: Calculate GSHP temperature using ${}^{n+1}T_{\text{in}}$ as a prescribed temperature

6: Calculate ${}^{n+1}T_{\text{out}}$

7: ${}^{n+1}T_{\text{in}}^{P} \leftarrow {}^{n+1}T_{\text{out}}$

8: END DO

This initial and boundary value problem is solved using the spectral element method (Doyle 1997, Al-Khoury 2012b). This method combines the analytical solution for a homogeneous domain to the finite element matrix assembly technique for a heterogeneous domain. The resulting spectral element equation is similar to the algebraic finite element equation, such that

$$\mathbf{K}(\omega_n)\hat{\mathbf{T}} = \hat{\mathbf{q}} \tag{5.5}$$

in which $\mathbf{K}(\omega_n)$ represents the spectral element matrix, in resemblance to that of the finite element stiffness matrix, but here it is exact and frequency-dependent; $\hat{\boldsymbol{T}}$ is the nodal temperature vector and $\hat{\boldsymbol{q}}$ is the nodal heat flux vector.

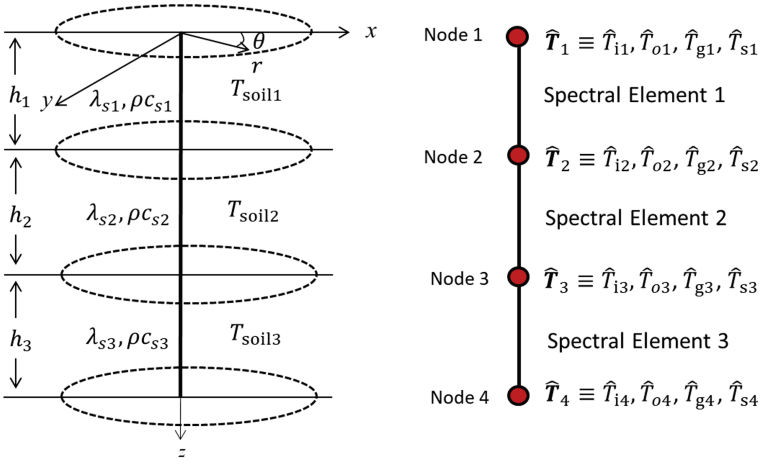

Figure 5.2: A three-layer system and its spectral element discretization

For a multilayer system, each layer is described by a spectral element. The assembly of the global matrix is done following the finite element method. If, for example, we have a borehole heat exchanger embedded in a three layer soil mass, shown schematically in Figure 5.2, the system is discretized by three spectral elements and four nodes. Each node has four degrees of freedom, describing the temperatures in pipe-in, $\hat{T}_{\mathrm{i}}$, pipe-out, $\hat{T}_o$, grout, $\hat{T}_{\mathrm{g}}$, and soil film, $\hat{T}_{\mathrm{s}}$. The stiffness matrix for each element is described by Eq.(5.5). Using the finite element mesh assembling technique, the global spectral element equation can then be described as

$$\begin{bmatrix} K_{11}^1 & K_{12}^1 & & \\ K_{21}^1 & K_{22}^1+K_{11}^2 & K_{12}^2 & \\ & K_{21}^2 & K_{22}^2+K_{11}^3 & K_{12}^3 \\ & & K_{21}^3 & K_{22}^3 \end{bmatrix} \begin{bmatrix} \hat{\mathbf{T}}_1 \\ \hat{\mathbf{T}}_2 \\ \hat{\mathbf{T}}_3 \\ \hat{\mathbf{T}}_4 \end{bmatrix} = \begin{bmatrix} \hat{\mathbf{q}}_1 \\ \hat{\mathbf{q}}_2 \\ \hat{\mathbf{q}}_3 \\ \hat{\mathbf{q}}_4 \end{bmatrix} \tag{5.6}$$

in which the matrix on the left-hand side is the global stiffness matrix, with the superscript indices indicating the element (layer) number. The vector on the left-hand side is the degrees of freedom vector, indicating the nodal temperatures that need to be determined; and the vector on the right-hand side is the corresponding nodal heat fluxes.

5.3 Tailored Fast Fourier Transform

The fast Fourier transform (FFT) entails transforming a given function in its original time (space) domain to a frequency (wave number) domain and reversing it back. It computes the discrete Fourier transform (DFT) in an exceptionally efficient manner and saves significant CPU time and capacity.

For a given data function $F(t_n)$ with N samples, the DFT can be expressed as:

Forward:

$$\hat{F}(\omega_k) = \sum_{n=0}^{N-1} F(t_n) e^{-i\omega_k t_n} \tag{5.7}$$

in which t_n is the discrete time sample, $\omega_k = 2\pi k/N$ is the discrete angular frequency and $k = 1, 2..., N-1$.

Inverse:

$$F(t_n) = \frac{1}{N} \sum_{k=0}^{N-1} \hat{F}(\omega_k) e^{i\omega_k t_n} \tag{5.8}$$

Standard FFT requires N to be a power of 2 and the sampling rate (time step) constant for the whole signal period. The latter constraint is adequate in many applications in engineering, but for solving heat transfer problems in GSHP systems, it can be restrictive. In this kind of systems, the designer is interested in the detailed thermal response of the GSHP at certain periods of switching ON and OFF the system, while at the same time needs to know its life time performance. If a detailed analysis with a sampling rate of one second is conducted for the life time of the system, which is typically 20 years, it would require more than 6.3×10^8 samples, which is practically unrealistic and can cause typical FFT numerical nuisances. If, on the other hand, an averaged analysis with a sampling rate of weeks or months is conducted, many important details on the hourly,

daily and seasonal performance would be missing, making such analysis not representative of the real system. As such, the standard FFT can be useful to GSHP systems for either detailed analysis of relatively short periods, or averaged analysis of relatively long periods; not both at the same time.

The short time Fourier transform (STFT) is an elegant extension to the FFT, such that it enables dividing a time signal with a non-uniform frequency spectrum into segments, followed by computing the FFT for each segment separately, Mertins (1999).

The STFT, for segment j, can be expressed as:

Forward:

$$\hat{F}^j\left(\omega_k\right)=\sum_{n=0}^{N-1}F^j\left(t_n\right)e^{-i\omega_k t_n} \tag{5.9}$$

Inverse:

$$F^j\left(t_n\right)=\frac{1}{N}\sum_{k=0}^{N-1}\hat{F}^j\left(\omega_k\right)e^{i\omega_k t_n} \tag{5.10}$$

Standard STFT requires equal interval segments and constant sampling rate to all segments. These requirements are adequate in communication and audio processing (Mertins 1999), but for GSHP systems, it is likewise restrictive.

To tackle this issue, we make use of the STFT idea to divide the time signal into segments, but tailor it to analyze segments with different time intervals and different sampling rates. Basically, we divide the signal into segments, use FFT with different time stepping rates (starting from small to large time steps), solve the system, and then link the reconstructed time domain of these segments via the Heaviside function, as illustrated hereafter.

The tailored FFT is expressed as:

Forward:

$$\hat{F}^j\left(\omega_k^j\right)=\sum_{n=0}^{N^j-1}F^j\left(t_n^j\right)e^{-i\omega_k^j t_n^j} \tag{5.11}$$

where N^j is the number of samples for segment j with time step t_n^j, and ω_k^j is the discrete angular sampling frequency of segment j, expressed as:

$$\omega_k^j=\frac{2\pi k}{\left(N^j t_n^j\right)} \tag{5.12}$$

Inverse:

$$F^j\left(t_n^j\right)=\frac{1}{N^j}\sum_{k=0}^{N^j-1}\hat{F}^j\left(\omega_k^j\right)e^{i\omega_k^j t_n^j} \tag{5.13}$$

Using the Heaviside function, the reconstructed time domain of the signal is described as

$$F\left(t_n\right)=\sum\nolimits_j H\left(t_n-t_n^j\right)F^j\left(t_n^j\right) \tag{5.14}$$

This equation expresses the time domain of a signal composed of $\sum_j N^j$ segments, put together. The algorithm of the tailored FFT can be summarized in Algorithm 5.2.

Algorithm 5.2: Tailored FFT

1:	DO	$j = 1$ to J (j : the time segment)
2:		Prescribe N^j, t_n^j
3:		Apply Forward tailored FFT, Eq.(5.11)
4:		Conduct STAND calculations
5:		Apply Inverse tailored FFT, Eq.(5.13)
6:		Aggregate the results with j-1 segment, Eq.(5.14)
7:	END DO	

The tailored FFT will be applied in the numerical example given in Section 5.6 to highlight the capability of the model to tackle the short-to-long time problems.

5.4 Heat flow analysis based on heat pump power

As indicated earlier, the heat pump power cannot directly be prescribed as a heat flux to models which simulate heat flow in the U-tubes. Here, we derive an equation relating the heat pump power to the prescribed heat flux at the inlet of pipe-in, Eq.(5.3).

The power gained (lost) by the U-tube is expressed as

$$dP=\dot{m}\,c\,dT_{\mathrm{i}} \tag{5.15}$$

Considering $\dot{m}=\rho uA$ with A is the U-tube cross sectional area, Eq. (5.15) can be written as

$$dT_{\mathrm{i}} = \frac{1}{\rho c u A} dP \tag{5.16}$$

The Neumann boundary condition at the inlet of pipe-in, Eq.(5.3), is

$$q_{in} = -\lambda \frac{dT_i}{dz} A \tag{5.17}$$

where λ (W/(m K)) is the thermal conductivity of the circulating fluid. Substituting dT_i of Eq. (5.16) into Eq. (5.17), and re-arranging, gives

$$q_{in} dz = -\frac{\lambda}{\rho c u} dP \tag{5.18}$$

This equation entails that whether convective heat flux or conductive, the temperature at the inlet of the U-tube must be unique

Integrating the left-hand side of this equation for a definite integral $0 \rightarrow 2L$ (with L being the BHE length, and $2L$ denoting the length of U-tube), and the right-hand side for $0 \rightarrow P$, leads to

$$q_{in} = -\frac{\lambda}{\rho c u} \frac{P}{2L} \tag{5.19}$$

which expresses the amount of heat transfer rate at the boundary of the U-tube when subjected to a heat pump power.

The interplay between Eq. (5.15) and (5.17) to produce Eq. (5.19) states that, in an adiabatic domain, the power gained by the U-tube (as a whole) is generated by a heat flux prescribed at the inlet of the U-tube. The heat flux at the boundary can be generated by any heat source, such as an electric heater or a heat pump.

As indicated above, Eq. (5.15) is valid for adiabatic processes, which occur without heat transfer between a thermodynamic system and its surrounding. Naturally, this is not the case for BHE, as it is composed of multiple components and is in thermal contact with its surrounding soil mass. In mechanical engineering, the power of complex heat exchangers, such as those involving multiple tubes and shell passes, is calculated using a correction factor that implicitly incorporate the thermal interactions among the heat exchanger components. Correction factors for several common configurations of mechanical heat exchangers are given in literature, see for example Pitts and Sissom (1997). Here, we apply a similar approach, by introducing a correction factor to Eq. (5.15), such that

$$dP = \varphi \dot{m} c dT_{\mathrm{i}} \tag{5.20}$$

where φ is a correction factor reflecting the non-adiabatic process of the GSHP, and can serve to cover any anomalies in measured data and description of physics. This implies that the inlet heat flux, Eq. (5.19), must be modified to read:

$$q_{in} = -\frac{\lambda}{\varphi \rho c u}\frac{P}{2L} \tag{5.21}$$

Normally, the heat pump power is not constant and varies with time due to electric voltage fluctuation and/or variation in its coefficient of performance (COP) (Al-Khoury 2012b), leading to:

$$q_{in}(t) = -\frac{\lambda}{\varphi \rho c u}\frac{P(t)}{2L} \tag{5.22}$$

This time dependent heat flux signal is implemented in the spectral analysis by first transforming it to the frequency domain and the resulted signal is applied to $\hat{q}_1$ on node 1 (Figure 5.2) on the right-hand side of Eq.(5.6).

To account for different BHE configurations, soil types and heat pumps, we determine the GSHP correction factor numerically, by calibrating the thermal power using Algorithm 5.3.

In Section 5.5 we validate this approach with experimental results and in Section 5.6 we utilize it in numerical examples.

5.5 Model verification

Beier et. al. (2011) presented a well-instrumented and documented experimental test set-up for a prototype ground source heat pump. They introduced experimental results and provided digital data for heat and fluid flow in a single U-tube, representing a borehole heat exchanger, embedded in a horizontal 1.8 m x 1.8 m x 18 m sandbox. The borehole is 18 m long, centered along the length of the box, Figure 5.3. They used an electric heater as a heat source. A fluid circulates through the closed loop and its temperature is measured at the inlet and outlet of the loop every 1 minute. A flow meter is used to measure the fluid flow rate through the loop. Details of the experimental test set-up can be found in their paper, referenced above. Table 5.1 lists the involved sandbox and borehole parameters.

Two experiments were conducted: a continuous heat pump operation; and an interrupted heat pump operation, in which the heat pump is switched OFF after 9 hours for 2 hours, followed by switching ON till the end of the experiment. Both experiments ran for about 50 hours. Using the provided digital data, we reproduced the experimental results by applying two calculation approaches: calculation based on prescribed T_{in}, and calculation based on prescribed heat pump power.

5.5.1 Calculation based on prescribed $T_{\mathbf{in}}$

Prescribing the temperature at the inlet of pipe-in is a common practice in analysing heat flow in GSHP systems (see for example Marcotte and Bernier 2019). In this calculation approach we set the measured temperature at the inlet of pipe-in as a prescribed T_{in} in the model, Eq. (5.4). Then, the temperature distributions along pipe-in, pipe-out and grout are calculated together with the temperature distribution in the surrounding soil mass. Figure 5.4 shows the measured temperature at the inlet of pipe-in and the computed and measured temperatures at the outlet of pipe-out, for both experiments. The two plots in the figure show an excellent match between the experimental and computed results. Equally, Figure 5.4b demonstrates the capability of the model to simulate accurately the switching OFF and ON the system in the interrupted operation experiment.

Algorithm 5.3: Tailored FFT & heat pump power prescription

1:	DO	$j = 1$ to J (j : the time segment)
2:		Prescribe N^j, t_n^j
3:		Transform the adiabatic form of the heat flux, Eq.(5.19), into the frequency domain and prescribe its magnitudes on node 1 in Eq.(5.6).
4:		Conduct STAND calculations
5:		Apply Inverse tailored FFT, Eq.(5.13)
6:		Compute the power from Eq.(5.2)
7:		Compare the specified heat pump power to the computed power, and calculate the correction factor, as $\varphi = \frac{\text{Computed power}}{\text{Input power}}$ (5.23)
8:		Insert the correction factor φ into Eq. (5.22)
9:		Transform Eq. (5.22), into the frequency domain and prescribe its magnitudes on node 1 in Eq.(5.6).
10:		Re-conduct the spectral analysis using STAND.
11:		Apply the inverse tailored FFT, Eq.(5.13).
12:		Aggregate the results with $j-1$ segment, Eq.(5.14)
13:	END DO	

It can be noted that the model could also detect the drop of the inlet temperature in the interrupted operation experiment, occurred between 1 and 5 hours, see the zoomed image in Figure 5.4b. The model properly captured its effect on the output temperature, but it is not clear why this drop in temperature has not been reflected in the measured data.

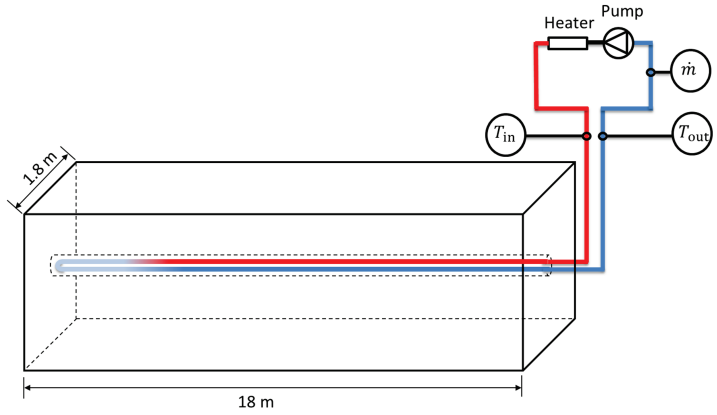

Figure 5.3: A scheme of the prototype GSHP experiment, conducted by Beier et.al (2011)

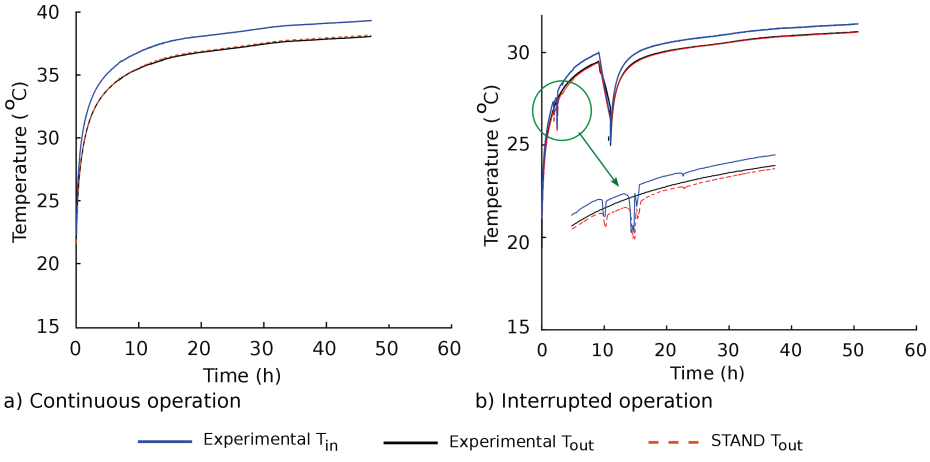

Figure 5.4: Measured and computed temperature variations in time based on prescribed inlet temperature

5.5.2 Calculation based on heat pump power

Calculation based on the heat pump power is conducted using the Algorithm 5.3, given in Section 5.4. Using this calculation approach the temperature distribution in the whole system is calculated, including T_{in}.

Table 5.1. Parameters of the prototype GSHP experiment (Beier et.al., 2011)

Parameter	Value
Borehole length	18.3 m
Borehole diameter	0.126 m
Pipe outer diameter	0.0668 m
Pipe inner diameter	0.0547 m
Pipe thermal conductivity	0.39 W/(mK)
Soil thermal conductivity	2.82 W/(mK)
Grout thermal conductivity	0.73 W/(mK)
Average fluid volumetric flow rate	0.197 L/s
Average heat input rate	1056 W

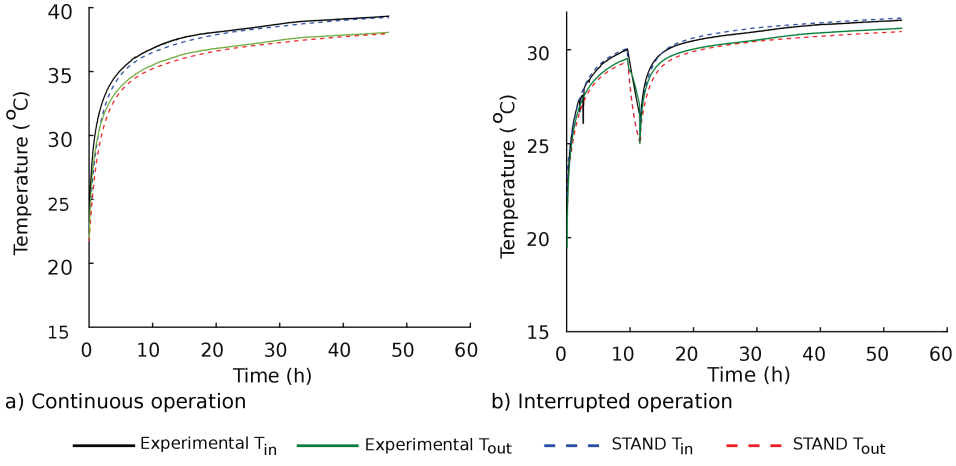

Figure 5.5: Measured and computed temperature variations in time based on heat pump power

Figure 5.5 shows the measured temperatures at the inlet of pipe-in and outlet of pipe-out, and their corresponding computed values for both experiments. The figure shows a good match between the experimental and computed results. Though, a closer look at the interrupted experiment reveals that the computed results overestimate ΔT ($T_{\mathrm{in}} - T_{\mathrm{out}}$) by a maximum 0.3℃ compared to the measured. This difference can be attributed to the error which might be introduced in calculating q_{in} in Eq.(5.22). Any variations in the measured fluid mass flow rate or deviations in the fluid density, specific heat and thermal conductivity can be reflected on the accuracy of q_{in} and hence on the computed temperature. Nevertheless, the correction factor accurately estimated the anomalies in measured data and uncertainties in several parameters that resulted to good agreement between the experimental data and the computed temperatures at all stages: the transient at the beginning, the interrupted and the steady state.

5.6 Numerical examples

To demonstrate the model computational capability in simulating realistic cases, a numerical example illustrating heat flow in a typical ground source heat pump is introduced. A 2 × 2 BHE layout configuration constituting boreholes, 100 m in length, embedded in three soil layers exhibiting different thermal conductivities is simulated, Figure 5.6. We studied three cases (Figure 5.7):

Case 1: one active BHE;
Case 2: four active BHEs, 5 m × 5 m configuration (denoted as $d = 5$ m);
Case 3: four active BHEs, 8 m × 8 m configuration (denoted as $d = 8$ m).

The material and geometrical parameters of the system are given in Table 5.2. The initial temperature in all components is assumed 12 °C.

The heat pump works with varying power, depending on hourly, days and nights, and seasonal demands. Figure 5.8a a shows the power demand over the year, where it is assumed that this power represents the thermal energy gained from the heat pump, without the additional power usually gained from the compressor, neither the variations due to the COP of the heat pump.

The day starts at 6:00 (6 am) and ends at 22:00 (10 pm) and the night starts at 22:00 and ends at 6:00. Within these, the system is operating ON for 60 minutes and OFF for 20 minutes. Figure 5.8b shows an example of the daily heat pump power for January. The year is divided into cold and warm months with varying thermal power demands. January till May, and October till December require heating; June requires neither heating nor cooling; and July till September are treated in two ways: with cooling (i.e. switching ON the heat pump in summer) and without cooling (i.e. switching OFF the heat pump for whole summer). The system is assumed to operate for 20 years. Any other operating scheme can also be considered.

Table 5.2. Material and geometrical parameters

Parameter	Value	Parameter	Value
Borehole:		**Soil**:	
Borehole length	100m	Film thickness	0.02m
Borehole diameter	0.126m	**Layer 1**: $0 \geq z \geq -30m$	
Pipe external diameter	0.0547m	Density , ρ_s	1100kg/m^3
Pipe thermal conductivity	0.38W/(mK)	Specific thermal capacity , c_s	1000J/(kg.K)
Fluid:		Thermal conductivity, λ_s	1. W/(m.K)
Density, ρ	1050kg/m^3		
Specific thermal capacity, c	3795J/(kg.K)	**Layer 2**: $-30 > z \geq -60m$	
Thermal conductivity, λ	0.5W/(m.K)	Density , ρ_s	1500kg/m^3
Dynamic viscosity, μ	0.0049Pa.s	Specific thermal capacity , c_s	1100J/(kg.K)
Velocity, u	0.5 m/s	Thermal conductivity, λ_s	2.5 W/(m.K)
Grout:			
Density, ρ_g	1200 kg/m^3	**Layer 3**: $-60 > z \geq -100m$	
Specific thermal capacity, c_g	2000J/(kg.K)	Density , ρ_s	1700kg/m^3
Thermal conductivity, λ_g	1. W/(m.K)	Specific thermal capacity , c_s	1200J/(kg.K)
		Thermal conductivity, λ_s	4. W/(m.K)

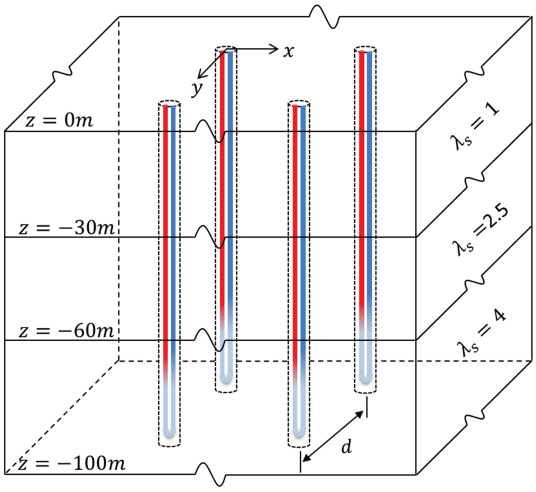

Figure 5.6: A scheme of GSHP consisting of 4 BHEs embedded in 3 soil layers

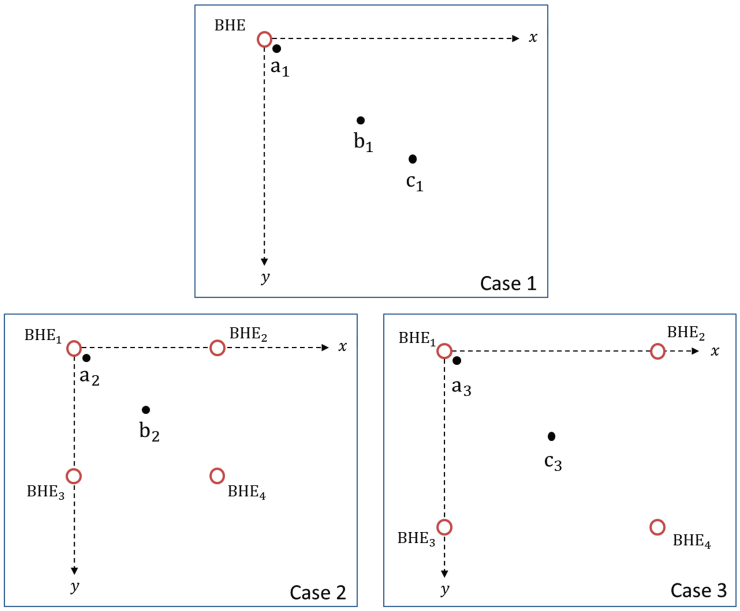

Figure 5.7: Case 1: one active BHE; Case 2: four active BHEs, 5 m × 5 m; Case 3: four active BHEs, 8 m × 8 m

The geometry is discretized using 3, 2-node spectral elements as schematically shown in Figure 5.2. The calculation is conducted using the tailored FFT with a multiple time stepping scheme, as the following:

Day 1: time step = 1 second.
Day 2 – end of Year 1: time step = 5 minutes.
Year 2 – end of Year 20: time step = 24 hours.

This scheme entails a very detailed analysis in the first day, a detailed analysis in the first year and a daily-averaged analysis for the rest. Other schemes can also be conducted, depending on the required details.

As indicated earlier, the model is capable of calculating the temperature distributions in all BHE components and in the soil mass in an effectively 3D space. Using the heat pump power option, even the temperature at the inlet of pipe-in, T_{in}, is calculated.

Figure 5.9 shows the soil temperature distributions for the 3 cases:

Case 1: One BHE is operating (Figure 5.7) in two options: cooling ON in summer, and cooling OFF in summer. The temperature is computed at a_1 (0.1, 0.1), b_1 (2.5, 2.5) and c_1 (4, 4). The computed results for these three points are shown in Figure 5.9a, Figure 5.9b, and Figure 5.9c, respectively.

Case 2: Four BHEs with 5 m × 5 m layout configuration (i.e. d = 5 m , Figures 5.6 and 5.7) in two options: cooling ON in summer, and cooling OFF in summer. The temperature is computed at a_2 (0.1, 0,1) and b_2 (2.5, 2.5). The computed results for these two points are shown in Figure 5.9a and Figure 5.9b, respectively.

Case 3: Four BHEs with 8 m × 8 m layout configuration (i.e. d= 8 m , Figures 5.6 and 5.7) in two options: cooling ON in summer, and cooling OFF in summer. The temperature is computed at a_3 (0.1, 0,1) and c_3 (4, 4). The computed results for these two points are shown in Figure 5.9a and Figure 5.9b, respectively.

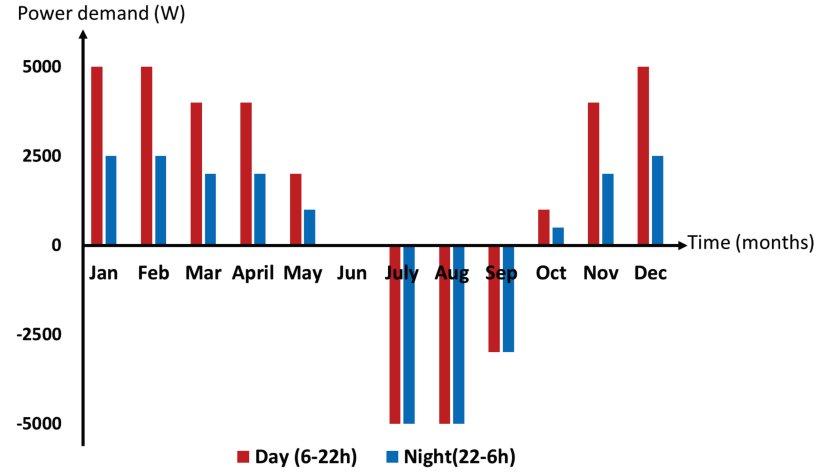

a) Yearly thermal power demand

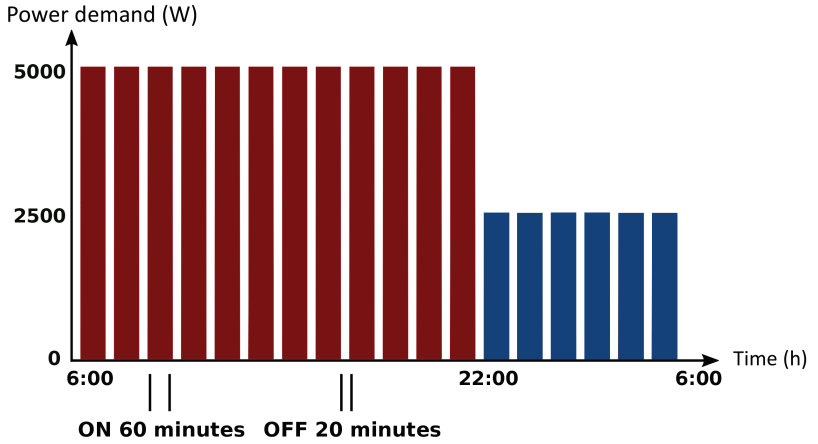

b) Daily thermal power demand for January

Figure 5.8: Power demand from the earth

Figure 5.9 clearly shows the effect of boreholes interactions on the soil temperature. At a short distance from the boreholes (a_1, a_2 and a_3) the soil temperature in the three cases is nearly the same for the cooling ON option, but for the cooling OFF, Cases 2 and 3 have clearly been affected. The soil temperature in these two cases is 3 °C lower than if only one BHE is operating after 20 years of operation.

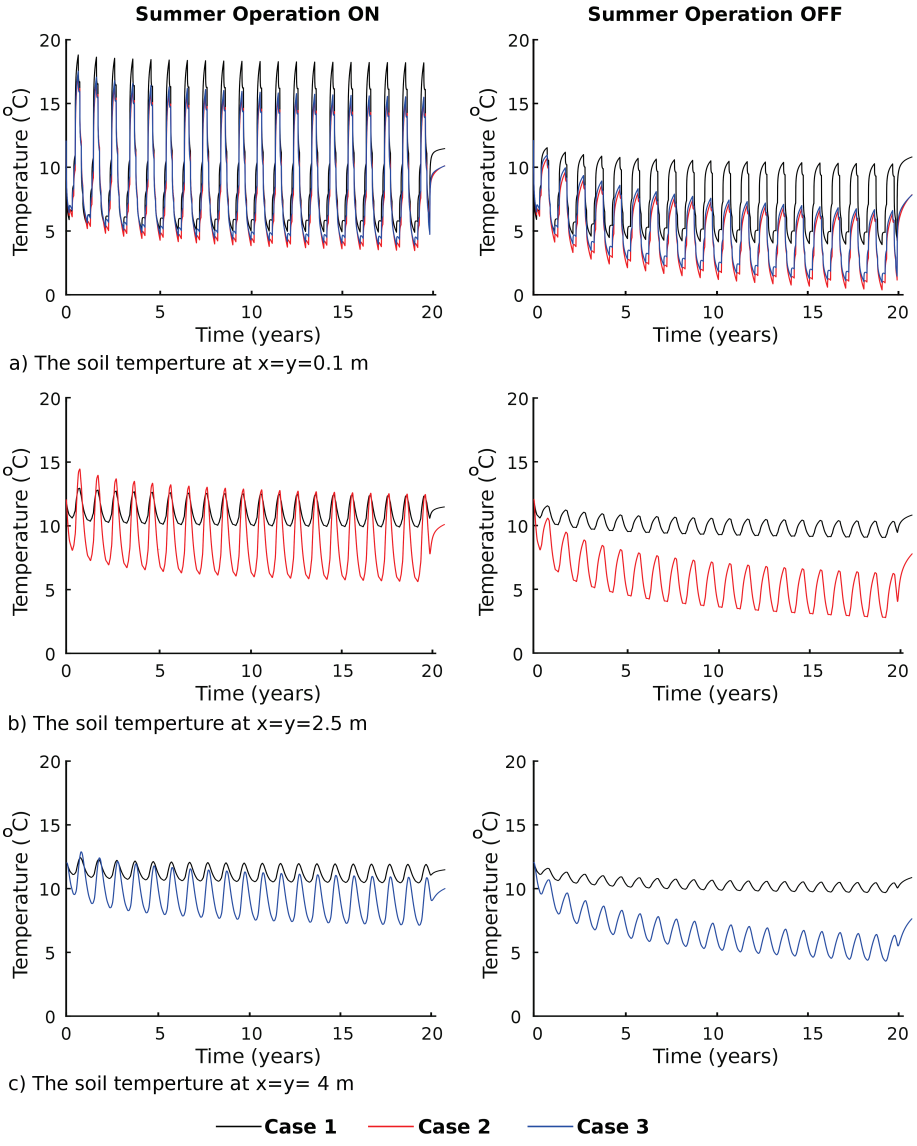

Figure 5.9 : Soil temperature at $z = 100$ m for Case1, Case 2 and Case 3

At relatively far distances from the BHE, b_1, b_2, c_1 and c_3, the effect of the borehole interactions are obvious. For Case 2, at point b_2, the temperature difference after 20 years of operation between a single BHE and 4 BHEs is 4.3 °C for the cooling ON option, and 7.0 °C for the cooling OFF. For Case 3, at point c_3, the temperatures were 3.3 °C and 5.4 °C, respectively.

Figure 5.9 also shows that the space between BHEs in a grid of neighbouring boreholes has a significant impact on the soil temperature. Likewise, cooling in summer is important for the soil mass to recover its thermal storage capacity.

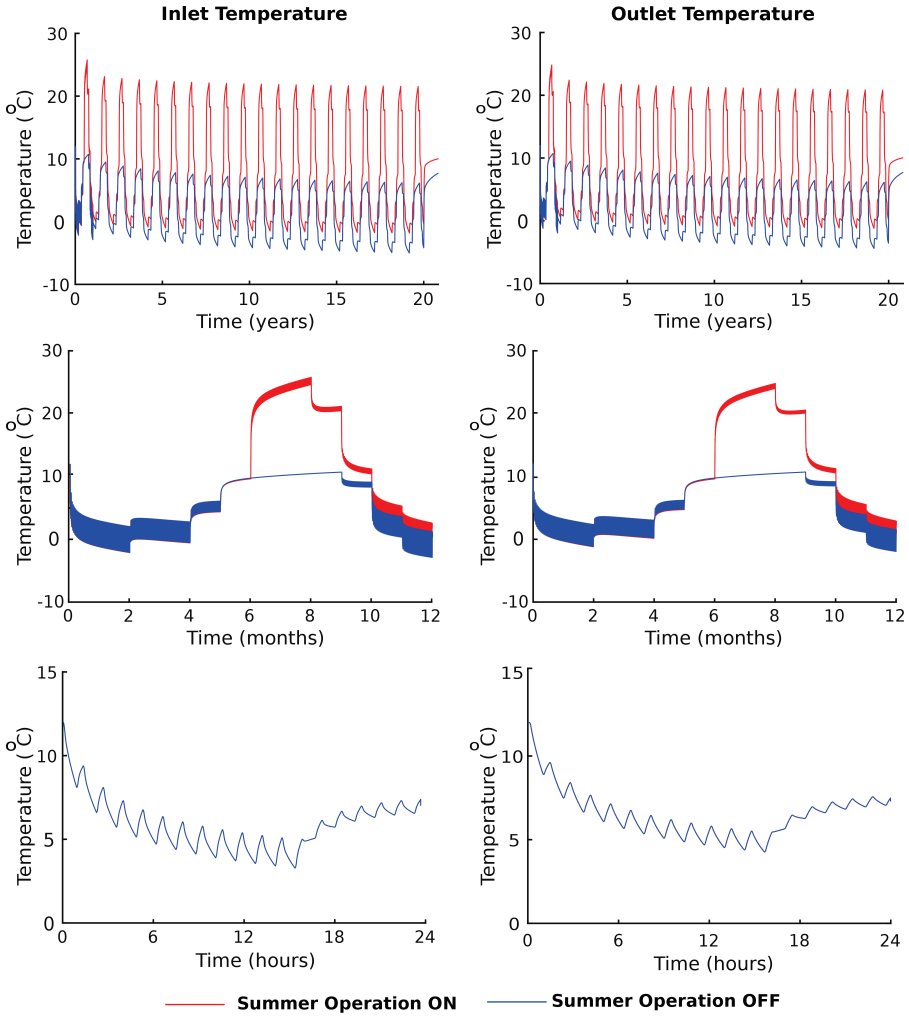

Figure 5.10 : Inlet and outlet temperatures for Case 2.

Figure 5.10 shows the computed temperature variations for Case 2 at the inlet of pipe-in (T_{in}) and outlet of pipe-out (T_{out}) for two options: cooling ON in summer; and cooling OFF in summer. The figure shows the computed results for 20 years, together with the zoomed results for the first year and first day. These results demonstrate the computational capability of the model to calculate the detailed performance of the system for short periods, and its performance for long period, all done in a single run.

Figure 5.10 also shows an important physical observation. Operating the geothermal system for cooling in summer helps the ground to recover its heat and thus makes the system more sustainable. This observation has been discussed in detail by Zhao et al. 2018. In this specific case, the decline of temperature between year 1 and year 20 for the cooling ON is 1.8 °C, but for the cooling OFF, it is 4.9 °C.

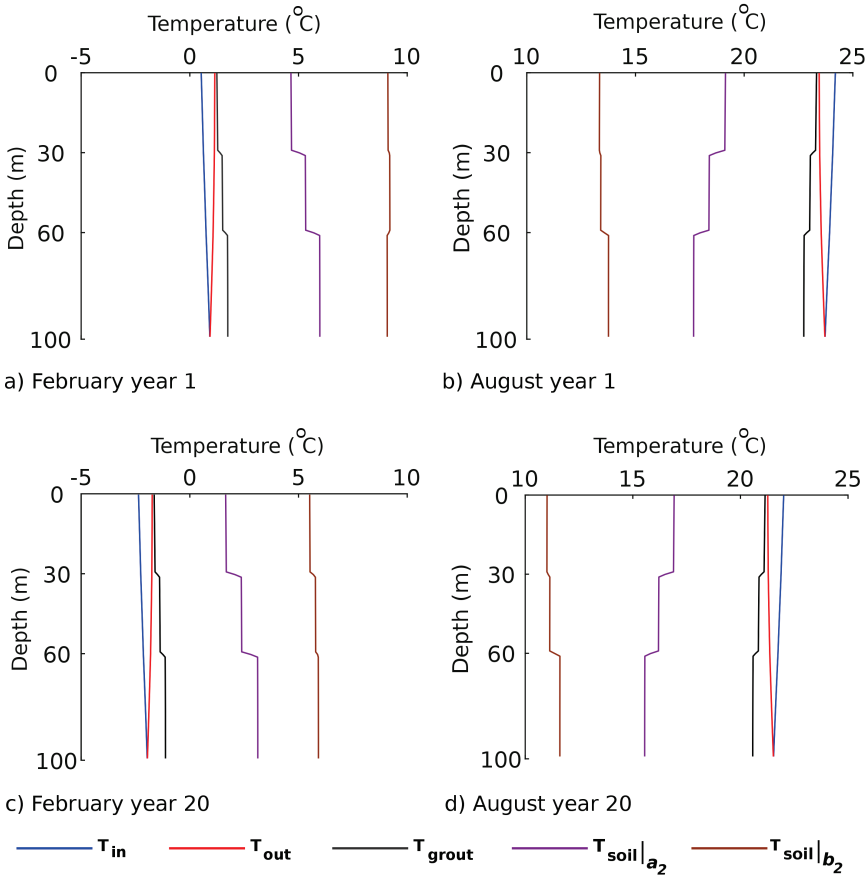

Figure 11: Vertical temperature distributions in pipe-in, pipe-out, grout and soil for Case 2

Figure 5.11 shows the vertical temperature distributions for Case 2 in pipe-in, pipe-out, grout and soil at a_2 and b_2 in February and August of year 1, and those in year 20. The summer cooling is ON. The figure shows the model capability to simulate the detailed effects of the soil thermal conductivity on the thermal propagation and contraction at different months of the year.

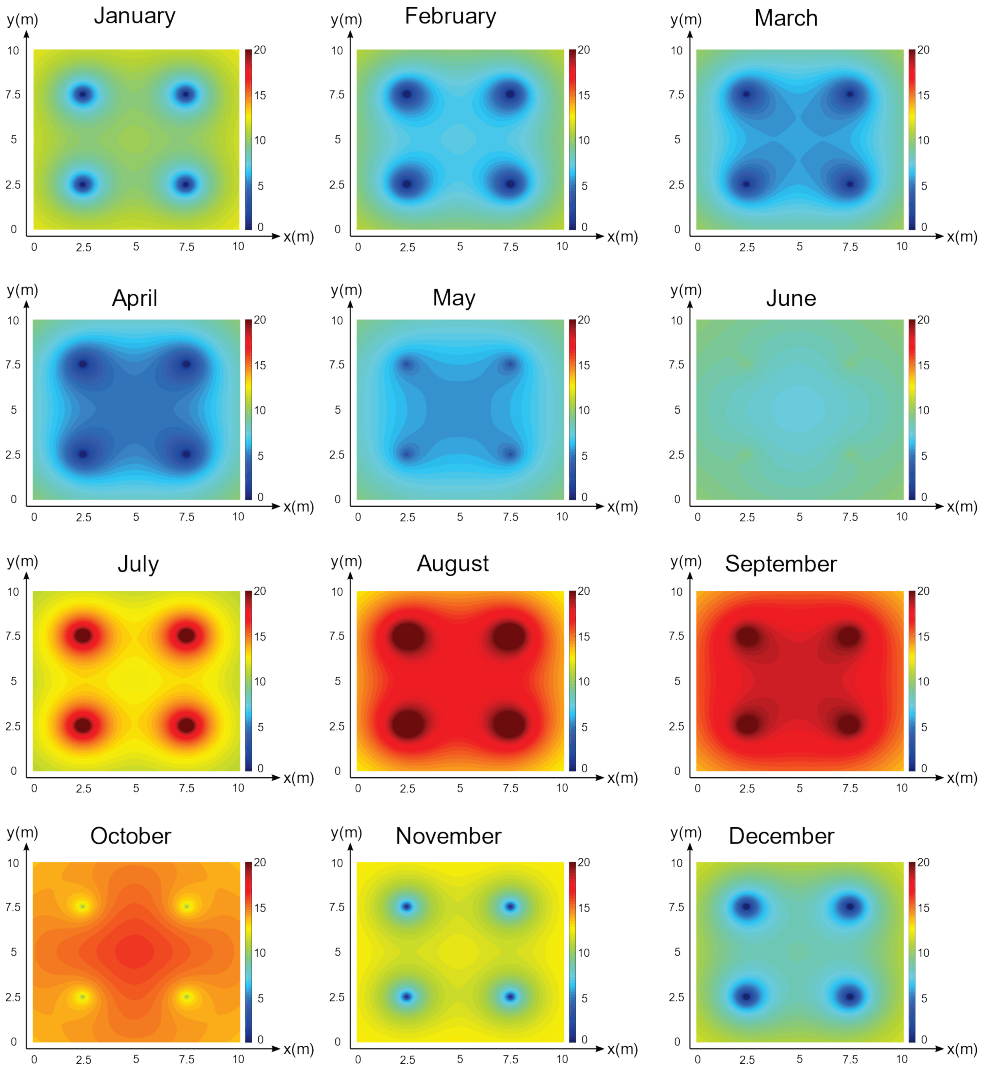

Figure 12: Soil temperature snapshots at $z = 100$ m for Case 2

Figure 5.12 shows the soil temperature snapshots at a $10\ \mathrm{m} \times 10\ \mathrm{m}$ cross-sectional area surrounding the bottom of the boreholes ($z = 100\ \mathrm{m}$) on the last day of the month, in the first 12 months of operation. The figure clearly shows the thermal interaction between boreholes and their effects on the soil mass at different times of the year.

It is worth mentioning here that although the model for a single borehole is axisymmetric, the use of the superposition principle has produced a significant spatial imbalance in the soil temperature distribution. However, by definition, the 2 x 2 BHE layout produces symmetric heat extraction rate for all BHEs. Any other layout such as 3 x 3 BHE or random distribution would produce unsymmetrical heat extraction rates. Kurevija et al. 2012, Gultekin et al. 2016 and You et al. 2018 have discussed this issue in detail. This topic will be the focus of a coming publication.

5.7 Conclusions

This chapter introduces a semi-analytical model for simulating heat flow in ground source heat pump systems, with emphasis on simulating short-to-long term heat flow using the heat pump power as input. The essential features of the model are:

1) It solves heat flow in effectively 3D geometries for any required temporal details. Detailed system operation from seconds to years can be handled in a single run. Hourly, daily and seasonally switching ON and OFF can be considered in the calculation.

2) It solves the system of equations using the heat pump power directly. Although in literature there are several models making use of the heat pump power to solve the system, they end up prescribing the Dirichlet boundary condition (T_{in}) at the inlet of the U-tube. Here, we prescribe the Neumann boundary condition (q_{in}), derived from the heat pump power. The Neumann boundary condition allows using the heat pump power directly, but would be realistic if the COP and the compressor effect are taken into consideration. This subject will be the focus of a future work.

Physically, the numerical example demonstrates that operating the heat pump in summer (i.e. cooling ON mode) helps the earth to recover its temperature, and hence increases the GSHP thermal efficiency.

6

A spectral model for heat flow with friction heat gain in geothermal borehole heat exchangers

This chapter introduces a semi-analytical model for the simulation of transient heat transfer with friction heat gain in a single U-tube geothermal borehole heat exchanger subjected to an arbitrary heat flux signal. The friction effect appears as a nonhomogeneous term in the governing equations, which constitutes a set of coupled partial differential equations describing heat flow in the three components of the borehole; pipe-in, pipe-out and grout. The spectral analysis has been utilized for discretizing the time domain, and the eigenfunction expansion for discretizing the spatial domain to solve the governing initial and boundary value problem. The proposed model combines the exactness of the analytical methods with an important extent of generality in describing the geometry and boundary conditions of the numerical methods. The model is verified analytically against a simplified one-dimensional solution. A numerical example is given to illustrate the effect of friction on heat transfer in the borehole heat exchanger for different fluid velocities and viscosities. The analysis shows; for the geometry, materials fluid velocities and viscosities, typically utilized in shallow geothermal systems; the friction is not really significant. However, the main advantage of this work is on the solution technique that can be useful for many other applications, including fluid flow in narrow pipes, high fluid velocities, high fluid viscosities, and pipes made of composite materials and of complex geometry. Also, the method can be useful for solving other nonhomogeneous coupled partial differential equations.

This chapter is based on BniLam N. and Al-Khoury R (2016). A spectral model for heat transfer with friction heat gain in geothermal borehole heat exchangers. Applied Mathematical Modelling Volume 40, Issues 15–16, Pages 7410-7421.

6.1 Introduction

Friction heat gain due to fluid flow in a pipe arises from the energy loss, which might be the result of the viscous force generated at the contact area between the fluid and the inner surface of the pipe. Friction energy loss can be significant in many engineering applications dealing with fluid flow in pipes, and has been given a significant attention, especially to those related to mechanical engineering. For geothermal engineering, however, this effect has not been considered. Two factors have motivated us to explore the effect of heat gain due to friction in shallow geothermal systems. First, shallow geothermal systems make use of the relatively low temperatures in shallow ground depths to generate heat. In this technology, every degree Celsius counts and made useful. Second, the friction is a function of length, which is particular in geothermal systems. The fluid in most U-tube borehole heat exchangers travels 200 m at every cycle.

Geothermal engineering is a relatively new field of physical sciences dealing with mining heat from shallow and deep earth formations. The borehole heat exchanger (BHE) is an important technology in this field that makes use of the widely available geothermal energy in shallow layers for heating and cooling of buildings and other facilities. It works by circulating a fluid, mostly water with antifreeze solution, through a U-tube (or a co-axial) polyethylene pipe that is inserted in a borehole. The borehole is filled with some grouted materials to fix the pipe and to ensure a good thermal interaction with the surrounding soil mass.

In shallow geothermal systems, in heating modes, gain of only few degrees centigrade from the ground is considered significant. This can make heat gain due to friction appealing and needs to be studied. Such a study might lead to improving the BHE technology, not merely the involved materials and the operation techniques. This constitutes the core subject of this work, which aims at studying the possible gain of heat from friction between the circulating fluid and the pipe.

Several computational models have been developed to simulate the thermal behavior of the BHE and the surrounding soil mass. These models vary from detailed numerical 3-D analysis to analytical solutions of simplified geometry and initial and boundary conditions. Due to the peculiarity of the involved geometry; which constitutes highly slender borehole heat exchangers embedded in a vast soil mass, and the presence of convection heat flow; the numerical models require extensive computational capacity and CPU time. Many numerical models have been introduced, such as those given in Yavuzturk et al. (1999), Al-Khoury and Bonnier (2006), He et al. (2011). Nevertheless, none of these models considered the friction heat gain due to fluid flow in the borehole heat exchanger.

In contrast, the analytical models require smaller computational capacity and much less CPU time. Several analytical and semi-analytical models with different complexity have been introduced, including those given in Carslaw and Jaeger (1947), Eskilson (1987), Gu and O'Neal (1995), Kavanaugh and Rafferty (1997), Zeng et al. (2002), Sutton et al. (2003), Diao et al. (2004), Al-Khoury (2010) and (2012a), Marcotte et al. (2010),

Molina-Giraldo et al. (2011), Pasquier and Marcotte (2013), Zanchini and Pulvirenti (2013), Erol et al. (2015). As for the numerical models, none of these models considered friction heat gain.

There is a large number of researches done on head loss due to friction in fluid flow in pipes. References Moody (1944), Brown (2002), Romeo et al. (2002), Imbrahim (2005), Siedel et al. (2015), are only few examples of research works in this field. However, it seems that there are only few computational models dealing explicitly with friction heat gain in pipes. In geothermal engineering, for instance, Ozudorgu et al (2014) have included heat gain into their governing equations, but did not explicitly study the effect of friction on heat flow. Saeid et al (2015) studied the effect of friction in heat flow in a low enthalpy deep wellbore, and found, for the studied flow rate and pipe roughness, insignificant gain of heat due to friction. In both works, the finite element method was utilized to solve the problem. No analytical solutions have been introduced for heat flow with friction, though, solutions of nonhomogeneous advective-diffusive transport equations, such as the one provided by Weigand (2004) or van Genuchten and Alves (1982), can be tailored and utilized to study friction heat gain. However, these solutions are designed for a one-dimensional object subjected to a mostly step force signal, and does not take into consideration the particular geometry of the pipe.

In this chapter, a semi-analytical solution for transient heat flow with friction heat gain in a single U-tube borehole heat exchanger, subjected to an arbitrary heat flux signal, is introduced. We utilize the spectral analysis and the eigenfunction expansion to solve the problem. The friction effect appears as a nonhomogeneous term in the governing equations, which constitutes a set of coupled partial differential equations. We make use of the solution provided in Al-Khoury (2010) and (2012a) to solve the homogeneous part of the solution, and extend it to solve the particular part of the solution.

6.2 Governing equations

Heat flow with friction heat gain in a single U-tube borehole heat exchanger, consisting of pipe-in, denoted as *i*; pipe-out, denoted as *o*; and grout, denoted as *g*, can be described as

Pipe-in

$$\rho c_r \frac{\partial T_i}{\partial t}\Delta V_i - \lambda_r \frac{\partial^2 T_i}{\partial z^2}\Delta V_i + \rho c_r u \frac{\partial T_i}{\partial z}\Delta V_i = b_{ig}(T_i - T_g)\Delta S_{ig} + \Delta Q_f \tag{6.1}$$

Pipe-out

$$\rho c_r \frac{\partial T_o}{\partial t}\Delta V_o - \lambda_r \frac{\partial^2 T_o}{\partial z^2}\Delta V_o - \rho c_r u \frac{\partial T_o}{\partial z}\Delta V_o = b_{og}(T_o - T_g)\Delta S_{og} + \Delta Q_f \tag{6.2}$$

Grout

$$\rho_g c_g \frac{\partial T_g}{\partial t}\Delta V_g - \lambda_g \frac{\partial^2 T_g}{\partial z^2}\Delta V_g = b_{ig}(T_g - T_i)\Delta S_{ig} + b_{og}(T_g - T_o)\Delta S_{og} \qquad (6.3)$$

in which the subscripts *r* and *g* represent the circulating fluid and the grout, respectively; T_i , T_o and T_g (K) are the cross-sectional average temperatures in pipe-in, pipe-out and grout, respectively; λ_r and $\lambda_g (W/mK)$ are the thermal conductivity of the circulating fluid and grout, respectively; $u(\mathrm{m/s})$ is the circulating fluid cross-sectional average velocity; $b_{ig}(\mathrm{W/m^2K})$ is the reciprocal of the thermal resistance between pipe-in and grout; $b_{og}(\mathrm{W/m^2K})$ is the reciprocal of the thermal resistance between pipe-out and grout; and $\rho c_r(\mathrm{J/m^3K})$ is the volume heat capacity, with $c_r(\mathrm{J/kgK})$ the specific heat, $\rho(\mathrm{kg/m^3})$ the mass density. $\Delta V_i, \Delta V_o$ and $\Delta V_g(\mathrm{m^3})$ are the partial volume of pipe-in, pipe-out and the grout respectively, and ΔS_{ig} and ΔS_{og} $(\mathrm{m^2})$ are the partial surface areas at the contact between pipe-in and grout, and pipe-out and grout, respectively. ΔQ_f is the change in heat flux due to friction between the circulating fluid and the pipe internal wall, derived below. For clarity of notation, in what follows, the subscript *r* will not be included

6.2.1 Initial and boundary conditions

For a single U-tube borehole heat exchanger, the initial and boundary conditions are typically:

$$\begin{aligned} &T_i(z,0) = T_o(z,0) = T_g(z,0) = T_{st}(\mathrm{z}) \\ &T_i(0,t) = T_{\mathrm{in}}(\mathrm{t}) \\ &T_i(L,t) = T_o(L,t) \end{aligned} \qquad (6.4)$$

$$-\lambda_g \frac{\partial T_g(z,t)}{\partial z} A_g - b_{ig}(T_g - T_i)\,\Delta S_{ig} - b_{og}(T_g - T_o)\,\Delta S_{og} = b_{gs}(T_g - T_{\mathrm{soil}})\Delta S_{gs} \qquad (6.5)$$

where T_{st} is the steady state soil temperature before operating the geothermal system; T_{in} is the fluid temperature at the inlet of pipe-in (z = 0), coming from the heat pump; T_{soil} is the soil temperature immediately surrounding the BHE; $b_{\mathrm{gs}}(\mathrm{W/m^2K})$ is the reciprocal of the thermal resistance between the grout and the soil; ΔS_{gs} $(\mathrm{m^2})$ is the partial surface area at the contact between the grout and the soil; A_{g} $(\mathrm{m^2})$ is the cross- sectional area of the grout; and L is the length of the BHE. At the bottom of the BHE, ($z = L$) the fluid temperature in pipe-in is equal to that in pipe-out, neglecting the elbow part because it is too small compared to the length.

Eqs. (6.1)-(6.3) and (6.5) state that, as physically occurring, the coupling between the BHE components, and between them and the soil formation occurs via the grout, which works as an intermediate medium that transfers heat from one component to another. Unlike the commonly utilized delta-circuit formulation, Eskilson (1987), heat flow in the grout is explicitly formulated.

6.2.2 Friction heat gain term, ΔQ_f

When a fluid moves in a pipe, it encounters frictional resistance due to the roughness of the inner surface of the pipe wall. This causes a loss of energy as a heat, which is equivalent to the loss of power consumed to overcome the viscous force at the contact surface between the fluid and the pipe.

Head loss in fluid flow in a pipe due to friction is commonly described using the Darcy–Weisbach equation, as

$$h_{\text{loss}} = f_D \frac{Lu^2}{2gd_i} \tag{6.6}$$

where L is the length of the pipe, d_i is its inner diameter, u is the average velocity of the fluid, g is the gravity and f_D is the Darcy friction factor, a dimensionless quantity. Several formulations describing f_D are available in literature. Here, we utilize the Colebrook equation, Colebrook (1938), for the turbulent flow. For laminar and turbulent flow, f_D is described as

$$f_D = \begin{cases} \dfrac{64}{\text{Re}} & \text{Re} < 2000 \\ \dfrac{1}{\sqrt{f_D}} = -2.0\log\left(\dfrac{e}{3.7d_i} + \dfrac{2.51}{\text{Re}\sqrt{f_D}}\right) & \text{Re} > 2000 \end{cases} \tag{6.7}$$

where e (m) is the tubing surface roughness, and Re is the Reynolds number, defined as

$$\text{Re} = \frac{\rho u d_i}{\mu} \tag{6.8}$$

where μ (Pa.s) is the dynamic viscosity.

The fluid pressure associated with the head loss is expressed as

$$\Delta P = \rho g h_{\text{loss}} = \frac{f_D \rho u^2 L}{2 d_i} \tag{6.9}$$

In fluid mechanics, the power loss is given by

$$\text{Power} = \Delta P V \tag{6.10}$$

where V(m^3/s) is the volumetric fluid rate.

As the heat gain due to friction is equivalent to the power loss, substituting Eq.(6.9) into Eq. (6.10), the heat gain can be described as

$$\Delta Q_f = \frac{f_D \rho u^3}{8} \Delta S \tag{6.11}$$

where ΔS is the inner surface area of the pipe at depth z.

6.3 Spectral analysis of BHE heat equations

Applying the Fourier transform to Eqs.(6.1)-(6.3), gives

$$i\omega \rho c_r \hat{T}_i \Delta V_i - \lambda_r \frac{d^2 \hat{T}_i}{dz^2} \Delta V_i + \rho c_r u \frac{d\hat{T}_i}{dz} \Delta V_i = b_{ig} (\hat{T}_i - \hat{T}_g) \Delta S_{ig} + \Delta \hat{Q}_f \tag{6.12}$$

$$i\omega \rho c_r \hat{T}_o \Delta V_o - \lambda_r \frac{d^2 \hat{T}_o}{dz^2} \Delta V_o - \rho c_r u \frac{d\hat{T}_o}{dz} \Delta V_o = b_{og} (\hat{T}_o - \hat{T}_g) \Delta S_{og} + \Delta \hat{Q}_f \tag{6.13}$$

$$i\omega \rho_g c_g \hat{T}_g \Delta V_g - \lambda_g \frac{d^2 \hat{T}_g}{dz^2} \Delta V_g = b_{ig} (\hat{T}_g - \hat{T}_i) \Delta S_{ig} + b_{og} (\hat{T}_g - \hat{T}_o) \Delta S_{og} \tag{6.14}$$

in which the transformed quantity is defined as $T \Leftrightarrow \hat{T}$. These equations are ordinary differential equations, two of which are nonhomogeneous. Solution of these nonhomogeneous equations is conducted by solving separately the homogenous part and the particular part, and then summed together algebraically.

6.3.1 Homogeneous solution

The homogeneous solution of Eqs.(6.12)-(6.14) is given in details in Al-Khoury (2010) and (2012a).

6.3.2 Particular solution

As for the homogeneous solution, the particular solution of Eqs. (6.12) and (6.13) can be represented by an exponential complex function of the form Doyle (1997):

$$\hat{T}_{pi} = C_i e^{-ikz}, \quad \hat{T}_{po} = C_o e^{ikz}, \quad \hat{T}_{pg} = C_g e^{-ikz} \tag{6.15}$$

where $\hat{T}_{pi}, \hat{T}_{po}$ and $\hat{T}_{pg}$ are the particular temperature frequency response of pipe-in, pipe-out and grout respectively.

Also, as for the homogeneous solution, the BHE system can be divided into two sub-systems: pipe-in – grout and pipe-out – grout.

Pipe-in – grout

The particular solution of pipe in-grout equations, Eq. (6.12), can be expressed as

$$\begin{aligned} \hat{T}_{pi} &= C_{i1} e^{-ik_1 z} + C_{i2} e^{-ik_2 z} \\ \hat{T}_{pgi} &= C_{gi1} e^{-ik_1 z} + C_{gi2} e^{-ik_2 z} \end{aligned} \tag{6.16}$$

where $\hat{T}_{pi}$ and $\hat{T}_{pgi}$ are the particular temperature frequency response of pipe-in and grout respectively. $C_{i1} \ldots C_{gi2}$ are integration constants that need to be determined. $\hat{T}_{pi}$ and $\hat{T}_{pgi}$ are coupled via Eq.(6.14), as

$$i\omega\rho_g c_g \hat{T}_{pgi} \Delta V_g - \lambda_g \frac{d^2 \hat{T}_{pgi}}{dz^2} \Delta dV_g - b_{ig} (\hat{T}_{pgi} - \hat{T}_{pi}) \Delta S_{ig} = 0 \tag{6.17}$$

which is the corresponding particular heat equation of the grout in contact with pipe-in only. Substituting Eq.(6.16) into Eq.(6.17) gives

$$\begin{aligned} C_{gi1} &= \alpha_{gi1} C_{i1} \\ C_{gi2} &= \alpha_{gi2} C_{i2} \end{aligned} \tag{6.18}$$

where

$$\begin{aligned} \alpha_{gi1} &= \frac{-b_{ig} \Delta S_{ig}}{i\omega\rho_g c_g \Delta V_g + k_1^2 \lambda_g \Delta V_g - b_{ig} \Delta S_{ig}} \\ \alpha_{gi2} &= \frac{-b_{ig} \Delta S_{ig}}{i\omega\rho_g c_g \Delta V_g + k_2^2 \lambda_g \Delta V_g - b_{ig} \Delta S_{ig}} \end{aligned} \tag{6.19}$$

Substituting Eq.(6.16) into Eq.(6.12), and with some mathematical arrangements, gives

$$((i\omega\rho c\Delta V_i + \lambda {k_1}^2 \Delta V_i - ik_1\rho cu\,\Delta V_i - b_{ig}\Delta S_{ig})\,C_{i1} + b_{ig}\Delta S_{ig}C_{gi1})e^{-ik_1 z} +$$
$$((i\omega\rho c\Delta V_i + \lambda {k_2}^2 \Delta V_i - ik_2\rho cu\,\Delta V_i - b_{ig}\Delta S_{ig})\,C_{i2} + b_{ig}\Delta S_{ig}C_{gi2})e^{-ik_2 z} = \Delta\hat{Q}_f \tag{6.20}$$

Substituting Eq.(6.18) into Eq.(6.20) yields

$$((i\omega\rho c\Delta V_i + \lambda {k_1}^2 \Delta V_i - ik_1\rho cu\,\Delta V_i - b_{ig}\Delta S_{ig}) + b_{ig}\Delta S_{ig}\alpha_{gi1})C_{i1}\,e^{-ik_1 z} +$$
$$((i\omega\rho c\Delta V_i + \lambda {k_2}^2 \Delta V_i - ik_2\rho cu\,\Delta V_i - b_{ig}\Delta S_{ig}) + b_{ig}\Delta S_{ig}\alpha_{gi2})C_{i2}e^{-ik_2 z} = \Delta\hat{Q}_f \tag{6.21}$$

At $z = 0$, the heat gain due to friction is zero. Thus, the first equation of Eq.(6.16) gives

$$C_{i1} + C_{i2} = 0 \tag{6.22}$$

Applying Eq.(6.22) to Eq.(6.21) yields

$$C_{i1} = \frac{\Delta\hat{Q}_f}{\alpha_{i1} - \alpha_{i2}}$$
$$C_{i2} = \frac{\Delta\hat{Q}_f}{\alpha_{i2} - \alpha_{i1}} \tag{6.23}$$

where

$$\alpha_{i1} = (i\omega\rho c\Delta V_i + \lambda {k_1}^2 \Delta V_i - ik_1\rho cu\,\Delta V_i - b_{ig}\Delta S_{ig} + b_{ig}\Delta S_{ig}\alpha_{gi1})e^{-ik_1 z}$$
$$\alpha_{i2} = (i\omega\rho c\Delta V_i + \lambda {k_2}^2 \Delta V_i - ik_2\rho cu\Delta V_i - b_{ig}\Delta S_{ig} + b_{ig}\Delta S_{ig}\alpha_{gi2})e^{-ik_2 z} \tag{6.24}$$

Pipe-out – grout

Pipe-out is a continuation of pipe-in at z=L, and as the friction is a function of the length travelled by the fluid, the particular solution of pipe-out can be expressed as

$$\hat{T}_{po} = C_{o1}e^{-ik_1(2L-z)} + C_{o2}e^{-ik_2(2L-z)}$$
$$\hat{T}_{pgo} = C_{go1}e^{-ik_1(2L-z)} + C_{go2}e^{-ik_2(2L-z)} \tag{6.25}$$

where $\hat{T}_{po}$ and $\hat{T}_{pgo}$ are the particular temperature frequency response of pipe-out and grout respectively. C_{o1}... C_{go2} are integration constants that need to be determined. $\hat{T}_{po}$ and $\hat{T}_{pgo}$ are coupled via Eq.(6.14), as

$$i\omega\rho_g c_g \hat{T}_{pgo}\Delta V_g - \lambda_g \frac{d^2\hat{T}_{pgo}}{dz^2}\Delta V_g - b_{og}(\hat{T}_{pgo} - \hat{T}_{po})\Delta S_{og} = 0 \tag{6.26}$$

which is the corresponding particular heat equation of the grout in contact with pipe-out only.

Substituting Eq.(6.25) into Eq.(6.26) gives

$$\begin{aligned} C_{go1} &= \alpha_{go1} C_{o1} \\ C_{go2} &= \alpha_{go2} C_{o2} \end{aligned} \tag{6.27}$$

where

$$\begin{aligned} \alpha_{go1} &= \frac{-b_{og}\Delta S_{og}}{i\omega\rho_g c_g \Delta V_g + k_1{}^2 \lambda_g \Delta V_g - b_{og}\Delta S_{og}} \\ \alpha_{go2} &= \frac{-b_{og}\Delta S_{og}}{i\omega\rho_g c_g \Delta V_g + k_2{}^2 \lambda_g \Delta V_g - b_{og}\Delta S_{og}} \end{aligned} \tag{6.28}$$

Similar to pipe-in, substituting Eq.(6.25) and (6.27) into Eq.(6.13), yields

$$\begin{aligned} C_{o1} &= \frac{\Delta\hat{Q}_f}{\alpha_{o1} - \alpha_{o2}} \\ C_{o2} &= \frac{\Delta\hat{Q}_f}{\alpha_{o2} - \alpha_{o1}} \end{aligned} \tag{6.29}$$

where

$$\begin{aligned} \alpha_{o1} &= (i\omega\rho c\Delta V_o + \lambda k_1{}^2 \Delta V_o - ik_1\rho cu\Delta V_o - b_{og}\Delta S_{og} + b_{og}\Delta S_{og}\alpha_{go1})e^{-ik_1(2L-z)} \\ \alpha_{o2} &= (i\omega\rho c\Delta V_o + \lambda k_2{}^2 \Delta V_o - ik_2\rho cu\Delta V_o - b_{og}\Delta S_{og} + b_{og}\Delta S_{og}\alpha_{go2})e^{-ik_2(2L-z)} \end{aligned} \tag{6.30}$$

Grout

The particular solution of the grout is considered as an average value of the particular solutions of $\hat{T}_{pgi}$, Eq. (6.16), and $\hat{T}_{pgo}$, Eq. (6.25), represented as

$$\hat{T}_{pg} = \frac{1}{2}\left(\hat{T}_{pgi} + \hat{T}_{pgo}\right) \tag{6.31}$$

6.3.3 General solution of BHE heat equations

The general solution of the single U-tube BHE heat equations can be obtained by summing over the homogeneous and particular solutions for all involved eigenfunctions and frequencies, as

Pipe-in

$$T_i(z,t)=\sum_n\left(A_i\,e^{-ik_1 z}+B_i\,e^{-ik_2 z}+C_{i1}\,e^{-ik_1 z}+C_{i2}\,e^{-ik_2 z}\right)e^{i\omega_n t} \tag{6.32}$$

Pipe-out

$$T_o(z,t)=\sum_n\left(A_o\,e^{ik_1 z}+B_o\,e^{ik_2 z}+C_{o1}\,e^{-ik_1(2L-z)}+C_{o2}\,e^{-ik_2(2L-z)}\right)e^{i\omega_n t} \tag{6.33}$$

Grout

$$T_g(z,t)=\frac{1}{2}\sum_n\begin{bmatrix}\left(A_{ig}+A_{og}+C_{gi1}\right)e^{-ik_1 z}+\left(B_{ig}+B_{og}+C_{gi2}\right)e^{-ik_2 z}\\+C_{go1}e^{-ik_1(2L-z)}+C_{go2}e^{-ik_2(2L-z)}\end{bmatrix}e^{i\omega_n t} \tag{6.34}$$

where A_{ig}, A_{og}, B_{ig}, and B_{og} are the homogeneous solution integration constants; defined in Al-Khoury (2010), and C_{gi1}, C_{gi2}, C_{go1}, C_{go2} are defined in Eqs.(6.18) and (6.27) .

6.4 Model Verification

Exact solution describing heat flow with friction heat gain in a single U-tube BHE does not exist. Accordingly, verification of the model accuracy is done by comparing its computational results with those obtained from an analytical solution of a simplified case. The van Genuchten and Alves (1982) solution of a one-dimensional advective-dispersive solute transport equation including a nonhomogeneous term is utilized for this purpose.

van Genuchten and Alves solved the following one-dimension partial differential equation

$$R\frac{\partial c}{\partial t}-D\frac{\partial^2 c}{\partial z^2}+F\frac{\partial c}{\partial z}+\mu c-\gamma=0 \tag{6.35}$$

with the following initial and boundary conditions:

$$
\begin{aligned}
&c(z,0) = A(z) = \frac{\gamma}{\mu} + \left(C_{\text{int}} - \frac{\gamma}{\mu} \right) e^{\frac{(F-\overline{u})}{2D} z} \\
&c(0,t) = \begin{cases} C_{in} & 0 < t < t_o \\ 0 & t > t_o \end{cases} \\
&\frac{\partial c}{\partial z}(\infty,t) = 0
\end{aligned}
\tag{6.36}
$$

where R, D, F, μ *and* γ are constants, and $\overline{u} = F\sqrt{1 + \frac{4\mu D}{F^2}}$. The initial value, $A(z)$ in Eq.(6.36), is determined by solving the steady state condition of Eq. (6.35). In this way, the nonhomogeneous term will be included in the initial condition, and there is no need to solve for the particular solution. This is possible because γ is independent of time.

The solution of this problem is

$$
c(z,t) = A(z) + \frac{1}{2}(C_{in} - C_{\text{int}}) \left(\begin{array}{l} e^{\frac{(F-\overline{u})}{2D} z} \operatorname{erfc}\left[\dfrac{Rz - \overline{u}t}{2(DRt)^{\frac{1}{2}}} \right] \\ + e^{\frac{(F+\overline{u})}{2D} z} \operatorname{erfc}\left[\dfrac{Rz + \overline{u}t}{2(DRt)^{\frac{1}{2}}} \right] \end{array} \right) \quad 0 < t \le t_o \tag{6.37}
$$

and

$$
\begin{aligned}
c(z,t) = A(z) + \frac{1}{2}(C_{in} - C_{\text{int}}) &\left(e^{\frac{(F-\overline{u})}{2D} z} \operatorname{erfc}\left[\frac{Rz - \overline{u}t}{2(DRt)^{\frac{1}{2}}} \right] + e^{\frac{(F+\overline{u})}{2D} z} \operatorname{erfc}\left[\frac{Rz + \overline{u}t}{2(DRt)^{\frac{1}{2}}} \right] \right) - \\
&\frac{1}{2} C_{in} \left(e^{\frac{(F-\overline{u})}{2D} z} \operatorname{erfc}\left[\frac{Rz - \overline{u}(t - t_o)}{2(DR(t - t_o))^{\frac{1}{2}}} \right] + e^{\frac{(F+\overline{u})}{2D} z} \operatorname{erfc}\left[\frac{Rz + \overline{u}(t - t_o)}{2(DR(t - t_o))^{\frac{1}{2}}} \right] \right) \quad t > t_0
\end{aligned}
\tag{6.38}
$$

To compare with the proposed spectral model, the van Genuchten and Alves parameters need to be adjusted to match the physical parameters of the model. Comparing Eq.(6.1) to Eq.(6.35), these parameters are adjusted such that:

$$R = \rho c \Delta V_i, \qquad D = \lambda_r \Delta V_i,$$
$$F = \rho c_r u \Delta V_i, \qquad \mu = -b_{ig} \Delta S_{ig} \tag{6.39}$$
$$\gamma = \Delta Q_f - \mu T_g, \qquad C_{\text{int}} = T_{st}, \qquad C_{in} = T_{in}$$

We utilized the two models to solve heat flow with heat gain due to friction in an insulated heat pipe. The geometry and material parameters are as the following:

Pipe length = 100m
Pipe radius, r_i = 0.016 m
Fluid ρc = 4.1298E6 J/m^3 K
Fluid λ = 0.56 W/m K
Fluid velocity, u = 1 and 20 m/s

The initial steady state temperature, and the temperature at the pipe inlet are:

$$T_{st}(t=0,z) = 10\,^\circ C$$
$$T_{in}(t,z=0) = \begin{cases} 40\,^\circ C & 0 < t \le 1000\,s \\ 0\,^\circ C & 1000 < t < \infty\,s \end{cases} \tag{6.40}$$

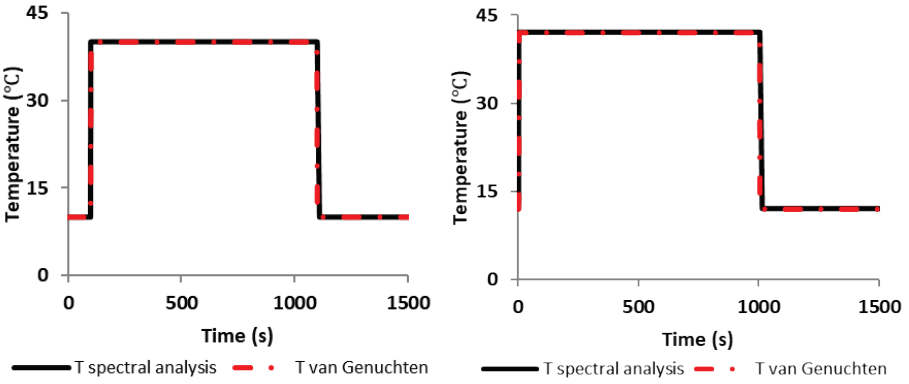

(a) (b)

Figure 6.1: Spectral model vs. van Genuchten and Alves solution with time at z=100m. (a) the fluid flow u=1m/s, (b) the fluid flow u=20 m/s

In the spectral model, T_{in} is equal to $T_{st} + \Delta T_{in}$, where, in this case, ΔT_{in} = 30 ºC. The coefficient of the thermal interaction between the pipe and the surrounding material (grout in the spectral model), b_{ig} , was made relatively small (0.1 W/m^{2}K) to insure insulation. The input temperature time histories of T_{in} and T_{st} were transformed to the frequency domain using the forward FFT. 4096 samples, with a sample rate of 1s, were used, giving a time window of 4096s.

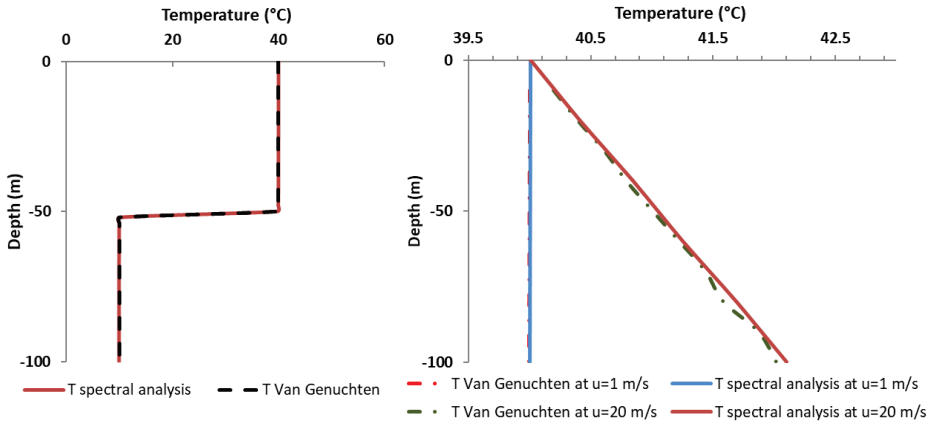

(a) (b)

Figure 6.2: (a) Spectral model vs. van Genuchten and Alves solution along the pipe at time=50s with fluid average velocity u=1m/s. (b) Spectral model vs. van Genuchten and Alves solution along the pipe at time=500s

The calculation results of the temperature at z = 100m, as calculated by the van Genuchten and Alves solution and the spectral model, are shown in Figure 6.1. Figure 6.2a shows the temperature distributions along the pipe after 50s with fluid average velocity equals to 1m/s, and Figure 6.2b shows the temperature distributions along the pipe after 500s for both velocities. Apparently, the two results are nearly identical for both fluid flow average velocities and along the depth of the pipe, though the van Genuchten and Alves solution exhibited some oscillation in the high velocity case.

Physically, Figure 6.2 shows that with a relatively small fluid flow velocity, the temperature does not change along the pipe, while it increases by more than 2 °C for the high velocity case. As b_{ig} is relatively small, the pipe is effectively insulated, and this increase in temperature from the top to the bottom is merely due to friction.

6.5 Numerical Examples

As discussed earlier, the proposed spectral model is capable of calculating the temperature distribution in all BHE components and in the surrounding soil mass (not shown in this chapter) for short and long terms. Here, we introduce numerical examples illustrating its computational capabilities for analyzing an in-time varying signal for a relatively long term. The material and geometrical properties are given in Table 6.1.

The initial temperature in the soil and the borehole is assumed 10°C. The air temperature is also set to 10 °C (see Al-Khoury 2012b). The fluid temperature at the inlet is assumed to vary between on and off, as

$$T_{in} = \begin{cases} 20 & t < 30\,\text{day} \\ 10 & 30\,\text{day} \le t < 45\,\text{day} \\ 18 & 45\,\text{day} \le t < 75\,\text{day} \\ 10 & 75\,\text{day} \le t < 90\,\text{day} \\ 16 & 90\,\text{day} \le t < 120\,\text{day} \\ 10 & 120\,\text{day} \le t \end{cases} \tag{6.41}$$

where it can be seen that the BHE has a 15 days off after every 30 days of operation.

Table 6.1: Material and geometrical parameters

Parameter	Value
Borehole:	
Borehole length	100 m
Borehole diameter	0.127 m
Pipe inner diameter	0.032 m
Pipe wall thickness	0.0029 m
Pipe roughness	3 E-6
Pipe thermal conductivity	0.42 W/(mK)
Grout:	
Grout density	1420 kg/m^3
Grout thermal conductivity	0.6 W/(m.K)
Grout specific thermal capacity	1197 J/(kg.K)
Soil:	
Soil density	1680 kg/m^3
Soil thermal conductivity	2.15 W/(m.K)
Soil specific thermal capacity	400 J/(kg.K)

Frequency discretization of T_{in}, ΔQ_f and T_{air} signals was conducted using the forward FFT with 16,384 (2^{14}) samples and a sample rate of 1 hour, giving a time window of approximately 22 months. Spatial discretization of the soil mass was conducted using 100 Bessel function roots. It is worth mentioning that, as the friction term is a function of fluid velocity and its effect vanishes by stopping the system operation, it must be discretized using FFT. Its time distribution is equivalent to the T_{in} signal, but its magnitude, for any specific z, is determined from Eq. (6.11).

The thermal coefficients b_{ig}, b_{og} and b_{gs} are determined based on Al-Khoury (2012a) and (2012b) thermal resistance formulation.

The effects of fluid velocities and viscosities are studied hereafter.

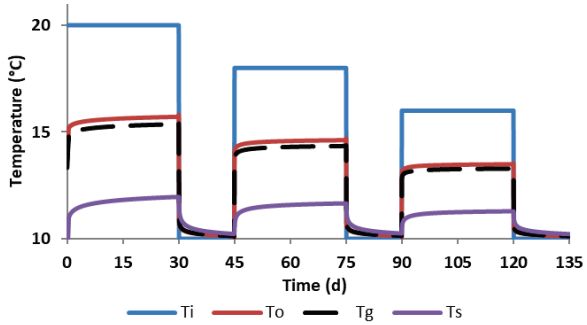

(a)

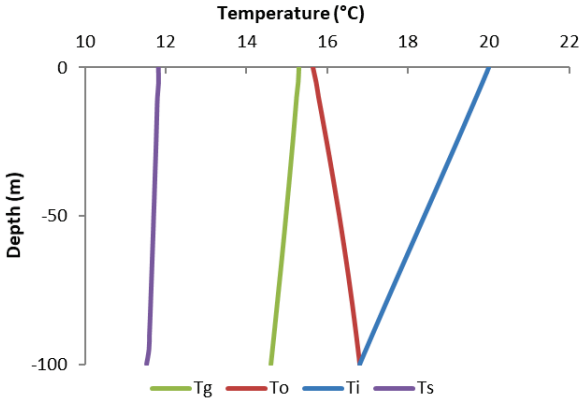

(b)

Figure 6.3:(a) Temperature variations for BHE components and soil vs. time for u=0.5 m/s with $b_{ig} = b_{og} = 126.53$ and $b_{gs} = 27.52$ W/(m^{2}K). (b) Temperature distributions for BHE components and soil along the z-axes, for u=0.5 m/s after 20 days with $b_{ig} = b_{og} = 126.53$ and $b_{gs} = 27.52$ W/(m^{2}K).

6.5.1 Fluid velocity effect

To study the effect of velocity, two fluid velocities are assumed: 0.5 and 5 m/s. The thermal parameter for the circulating fluid is shown in Table 6.2.

Figure 6.3a shows the temperature variations with no friction versus time for fluid velocity 0.5 m/s at z = 0. Figure 6.3b shows the temperature distributions along the BHE. Analysis with friction heat gain (not shown in the figure) reveals that, for this fluid velocity, the difference is negligible.

Table 6.2: the circulating fluid thermal parameters

Parameter	Value
Fluid density	1000 kg/m^3
Fluid thermal conductivity	0.56 W/(mK)
Fluid specific thermal capacity	4186 J/(kg.K)
Fluid dynamic viscosity	0.001 Pa.s
Fluid velocities	0.5 and 5 m/s

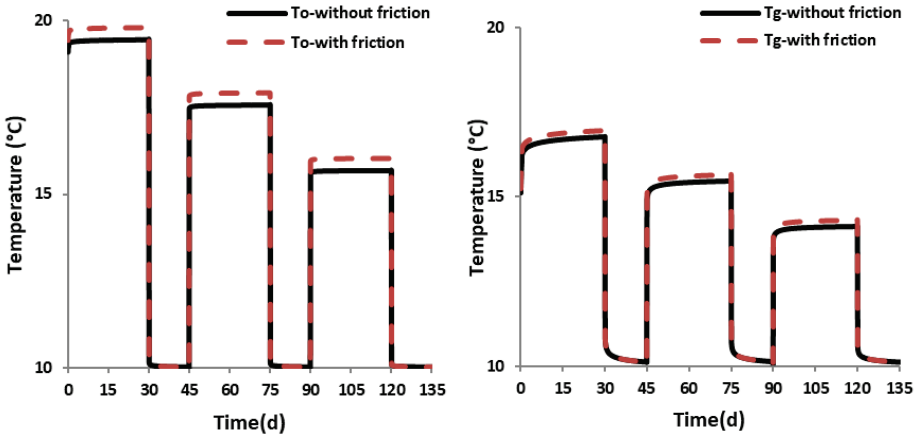

(a) (b)

Figure 6.4: Temperature variations in pipe-out and grout vs. time with and without friction for u=5 m/s with $b_{ig} = b_{og} = 132.26$ and $b_{gs} = 27.4\ \mathrm{W/(m^2K)}$. (a) fluid temperature at the outlet, (b) grout temperature at the surface

Figure 6.4 shows the temperature variations with and without friction versus time for pipe-out (T_o) and grout (T_g), for a fluid velocity equals to 5 m/s. The figure reveals that the temperature in pipe-out increased by approximately 0.4 °C and in the grout increased by approximately 0.2 °C. Apparently, the friction effect is higher for this flow rate.

6.5.2 Fluid viscosity effect

To study the effect of viscosity, two solutions with different viscosities are assumed: 30% propylene glycol solution, and a solution with a 0.5 Pa.s viscosity. The thermal parameter for the 30% propylene glycol solution is shown in Table 6.3.

Figure 6.5 shows the fluid temperature at the outlet of pipe-out (T_o), for both: with friction and without friction. Apparently, the viscosity of this solution has no effect on the friction.

Table 6.3: 30% propylene glycol thermal parameters

Parameter	Value
30% propylene glycol: at 15 ^oC	
Fluid density	1031 kg/m^3
Fluid thermal conductivity	0.426 W/(mK)
Fluid specific thermal capacity	3834 J/(kg.K)
Fluid dynamic viscosity	0.00369 Pa.s
Fluid velocity	0.5 m/s

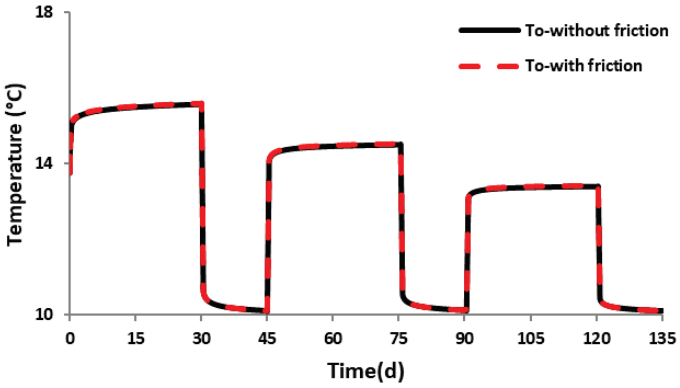

Figure 6.5: Outlet temperature of BHE with 30% propylene glycol solution

Suppose, for the sake of argument, we use a solution with 0.5 Pa.s viscosity, with thermal parameters given in Table 6.4. All other geometrical and thermal parameters are similar to the previous case. Figure 6.6 shows the temperature variations with and without friction versus time for pipe-out (T_o) and grout (T_g), The figure reveals that the temperature in pipe-out increased by approximatly 1 ˚C and in the grout increased by approximately 0.5 ˚C. Apparently, the friction effect is higher for highly viscous fluids.

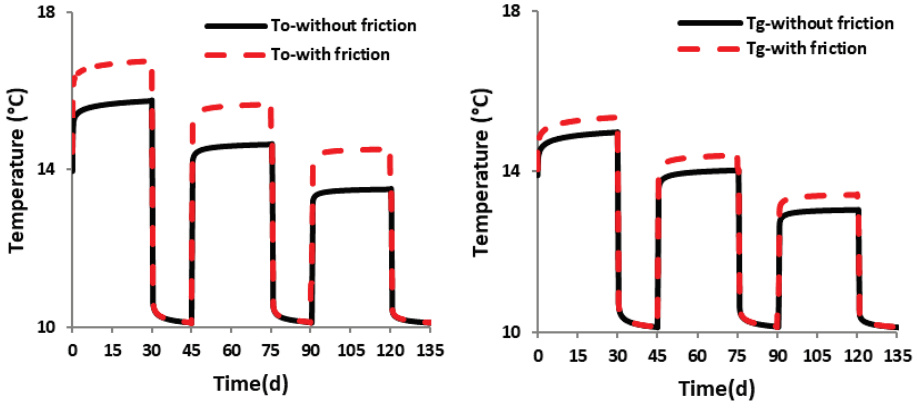

Figure 6: Temperature variations in pipe-out and grout vs. time with and without friction, for u=.5 m/s, $\mu = 0.5\ pa.s$, $b_{ig} = b_{og} = 128.89$ and $b_{gs} = 27.47$ W/ (m^2K). (a) fluid temperature at BHE outlet , (b) grout temperature at surface

Table 6.4: A solution with high viscosity

Parameter	Value
Fluid density	1000. kg/m^3
Fluid thermal conductivity	0.56 W/(mK)
Fluid specific thermal capacity	4186 J/(kg.K)
Fluid dynamic viscosity	0.5 Pa.s
Fluid velocity	0.5 m/s

6.6 Conclusions

A semi-analytical model for the simulation of transient heat transfer with friction heat gain in a single U-tube geothermal borehole heat exchanger subjected to an arbitrary force signal has been derived and tested. The friction effect appears as a nonhomogeneous term in the governing equations, which constitutes a set of coupled partial differential equations describing heat flow in the three components of the borehole; pipe-in, pipe-out and grout. The spectral analysis is utilized to discretize the time domain; and the eigenfunction expansion is utilized to discretize the spatial domain. The model is verified analytically against a simplified one-dimensional transport equation given by van Genuchten and Alves. A numerical example is given to illustrate the effect of friction on heat transfer for different fluid velocities, and viscosities. The analysis shows that; for the geometry, materials, fluid velocities and viscosities, typically utilized for shallow geothermal systems; the friction is not really significant. However, the main advantage of this work is on the solution technique that can be useful for many other applications, including fluid flow in narrow pipes, high fluid velocities, high fluid viscosities, and pipes with composite materials. Also, the method can be useful for solving other nonhomogeneous coupled partial differential equations.

The proposed model combines the exactness of the analytical methods with a great extent of generality in describing the geometry and boundary conditions of the numerical methods. The CPU time for calculating temperature distributions in all involved shallow geothermal system components; using 16,384 FFT samples, for the time domain, and 100 Fourier-Bessel series samples, for the spatial domain; is in the order of 1 second in a normal Intel PC. As the solution is highly accurate and computationally efficient, it can be suitable for inverse problems.

Part II

Parameter Identification of GSHP Systems:

Inverse Calculations

7

Parameter Identification Algorithm for Ground Source Heat Pump Systems

This chapter introduces a new parameter identification (PI) algorithm for estimating effective and detailed thermal parameters of ground source heat pump systems using data obtained from the well-known thermal response test. The PI comprises an iterative scheme coupling a semi-analytical forward model to an inverse model. The forward model is formulated based on the spectral element method to simulate transient 3D heat flow in ground source heat pump (GSHP) systems, and the inverse model is formulated based on the interior-point optimization method to minimize the system objective function. Compared to existing interpretation tools for the thermal response test, the proposed PI algorithm has several advanced features, including: it can handle fluctuating heat pump power and inlet temperatures; interpret data obtained from multiple heat injection or extraction signals; produce accurate backcalculation for short and long duration experiments; and handle multilayer systems. The PI algorithm is tested against synthesized data, using a wide range of random noise, and versus an available laboratory experiment. The computational results show that the PI algorithm is accurate, stable and exhibiting relatively high convergence rate.

This chapter is based on BniLam and Al-Khoury (submitted), Parameter Identification Algorithm for Ground Source Heat Pump Systems.

7.1 Introduction

The use of the ground source heat pump technology for heating and cooling of buildings is rapidly rising worldwide, and engineers are striving to improve its design. Efficient design of a GSHP system depends in part on the accuracy of the thermal parameters of the borehole heat exchanger and the soil mass (Witte et al. 2002), and in another on the optimization of the energetic, exergetic and economic performance of the system as a whole (Ozgener and Hepbasli 2007; Conti 2015; and Verrax 2018). This chapter focuses on the first part.

Thermal parameters of the borehole heat exchanger (BHE) components are usually known a priori, but thermal parameters of the soil mass and the borehole thermal resistance are not readily known and need to be determined. Laboratory and field experiments have been devised for estimating the soil thermal parameters. Thermal properties estimated from laboratory experiments are in principle more accurate. However, the drawback in here is that only a small volume of the soil is tested, ignoring the inhomogeneity of the soil layers. Also, disturbances in the soil samples can lead to erroneous estimate (Witte et al. 2002). Following this, the in-situ Thermal Response Test (TRT), first introduced by Mogensen (1983), has become the tool for estimating the GSHP parameters. The TRT became popular because in addition to determining the thermal properties of the soil without the need for taking samples to the lab, it determines the borehole thermal interaction coefficient, a property that is quite difficult to be quantified in the lab.

An important element of the thermal response test is the interpretation procedure of the measured data. This experiment is relatively expensive but can only be useful if the utilized parameter identification algorithm is able to produce accurate estimate of the involved thermal parameters. Basically, parameter identification algorithms employ forward and inverse models to obtain effective or detailed parameters, depending on the rigor of the algorithm. The forward model is a mathematical expression which describes the physical system and predicts the response of the system for any given values of the model parameters. The inverse model is a mathematical optimization algorithm designed for inferring the values of the model parameters from measured and theoretical response quantities. The competence of a parameter identification algorithm depends on several factors, including:

a) the adequacy of the forward model to describe the physics of the problem, and its computational efficiency in utilization in iterative schemes for inverse calculations, and

b) the consistency, stability and convergence rate and uniqueness of the inverse model for solving the objective functions.

Based on these factors, parameter identification algorithms utilized for TRT interpretation can be put in three categories:

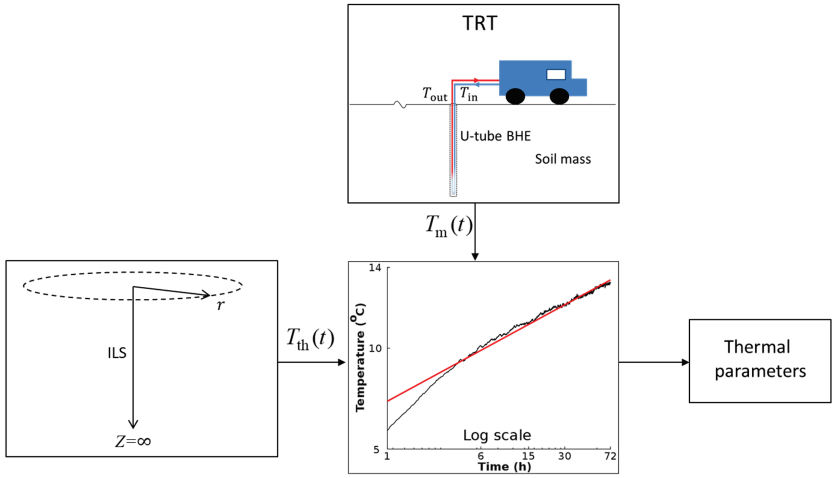

Figure 7.1: A schematic representation of the Forward analytical – Inverse graphical interpretation (GI) algorithm

1) Forward analytical – Inverse graphical interpretation (GI) algorithm (also denoted as curve fitting method). This algorithm employs the well-known infinite line source (ILS) model (Ingersoll et al. 1954) for the forward calculation. The inverse calculation is conducted via curve fitting of the measured data to estimate the effective soil thermal conductivity and borehole thermal resistance, as shown in Figure 7.1. This method is widely used because of its simplicity, simple mathematical tools (such as MS Excel) can be used to interpret the measured data. Works fall in this category, among many others, are: Witte et al. (2002); Busso et al. (2003); Sanner et al. (2005) and (2008); Witte (2013); Focaccia et al. (2013); and Bujok et al. (2014). In Section 7.2 we discuss this algorithm in detail, and in Section 7.4 we examine its performance. The study shows that this algorithm has fundamental shortcomings, mainly in its non-uniqueness in determining two physical parameters (soil thermal conductivity and borehole thermal resistance) from one equation.

2) Forward analytical – Inverse optimization algorithms. This kind of algorithms employ analytical models such as the infinite line source (ILS), infinite cylindrical source (ICS) (Ingersoll et al. 1954), thermal resistance and capacitance (TRC) (Pasquier and Marcotte 2014), or alike, for the forward calculation. The inverse calculation is conducted using some sort of optimization techniques, as shown in Figure 7.2. Works fall in this category, among others, are: Fujii et al (2009); Li and Lai (2012); Wagner et al. (2013); Raymond and Lamarche (2013); Choi and Ooka (2015); Pasquier (2015) and (2018); and Pasquier et al. (2019). In this category, the use of optimization techniques for minimizing the system objective functions overcomes some of the shortcomings of the previous category. However, most of the

analytical forward models are not formulated to describe the detailed heat flow in the GSHP systems, making backcalculations based on such models limited in accuracy.

3) Forward numerical – Inverse optimization algorithms. This kind of algorithms employ numerical solutions based on the finite element method, finite difference method or finite volume method for the forward calculation. The inverse calculation is conducted using some sort of optimization techniques, as shown in Figure 7.3. Works fall in this category, among others, are: Spitler et al. (2000), Austin et al. (2000); Wagner and Clauser (2005); Witte and van Gelder (2006); Signorelli et al. (2007); and Marcotte and Pasquier (2008b). In general, the parameter identification models of this category are more advanced, but the use of the numerical models for forward calculations make them computationally inefficient for utilization in iterative schemes for inverse problems.

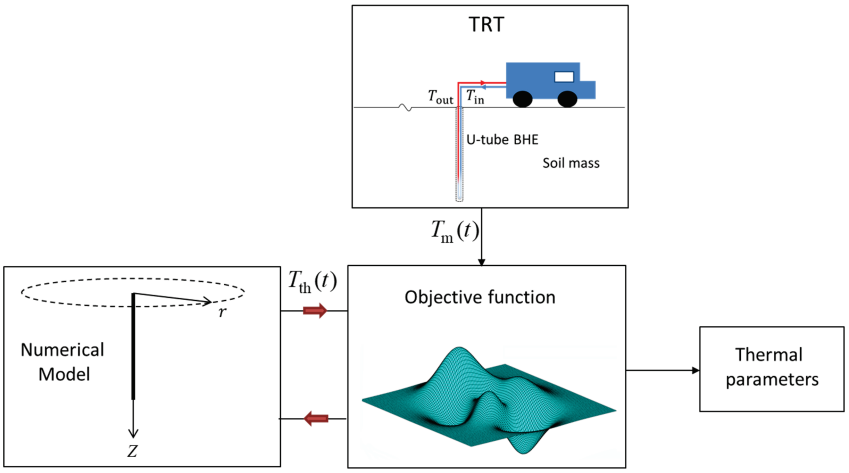

Figure 7.2: A schematic representation of the Forward analytical – Inverse optimization algorithms

Despite the bulk of research work in this field, there are yet many challenges that affect the accuracy of the TRT interpretation procedures, including:

A) Heat pump power fluctuation

Heat pumps used in GSHP systems usually produce fluctuating thermal loads, leading eventually to fluctuations in the measured inlet and outlet temperatures. As it will be shown in Section 7.2 and the subsequent sections, the GI algorithm is directly related to the heat power, and if this power is not constant, the temperature can be misrepresented, giving rise to inaccurate curve fitting. Two solutions have been employed for this problem. One is modifying the hardware by using electric resistance

heaters for heating the circulating fluid (Sanner et al. 2005, Sauer et al. 2012); and another is modifying the interpretation method by using numerical forward models which are usually capable of handling fluctuated heat fluxes. Witte and van Gelder (2006), for instance, employed TRNSYS simulator to estimate the soil thermal parameters using a time varying heat flux injection. Raymond et al. (2011) and Choi and Ooka (2015) tackled this problem by using a temporal superposition technique combining the ILS model to an optimization algorithm.

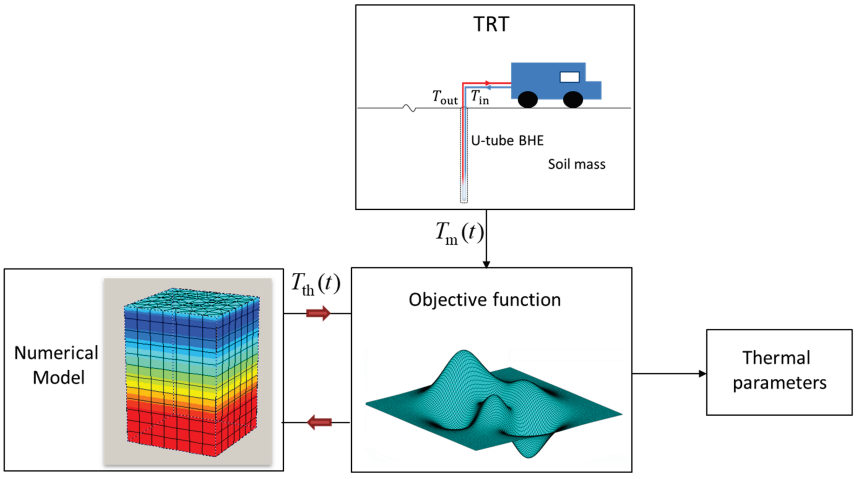

Figure 7.3: A schematic representation of the Forward numerical – Inverse optimization algorithms

B) TRT duration

In practice, the TRT is conducted for 72 hours in an effort to let the system reaches the steady state and guarantee better interpretation (Witte and van Gelder 2006). This duration is particularly crucial for the GI algorithm, as will be explained in Section 7.2 and verified in Section 7.4. However, performing the experiment for 72 hours can be expensive. Spitler et al. (2000) have shown that the cost of performing TRT increases significantly with the increase of the TRT duration. As a consequence, recently, several studies are initiated to investigate the possibility of shortening the TRT duration. Bujok et al. (2014) performed several TRT in a field containing 16 boreholes to analyze the effect of shortening the TRT durations on the accuracy of the thermal parameter identification. Their study shows that shortening the test to 24 hours can bring an acceptable amount of inaccuracy. Pasquier (2018) introduced an interpretation technique that can make use of the measured temperatures during the first three hours to produce an effective thermal conductivity accurate within 10% of a reference value.

C) Nonhomogeneous soil mass

Most TRT parameter identification algorithms assume that the soil mass consists of a homogeneous layer, which can be described by effective soil thermal conductivity and borehole thermal resistance. Obviously, this assumption is not realistic as the borehole can go as deep as 200 m into the ground, which most probably consists of layers with varying soil types, geometry and thermal properties (Witte and van Gelder 2006, Spitler and Gehlin 2015). An attempt to backcalculate the thermal properties of a multilayer system necessities two main requirements:

1) The TRT needs to include temperature measurements, not only at the inlet and outlet of the borehole, but also along its depth. Currently, this is gradually becoming a common practice, especially by the introduction of what is known as the Distributed Thermal Response Test (DTRT), where measurements are made along the BHE using optical fiber (Fujii et al. 2009, Acuña and Palm 2013, Vélez Márquez et al. 2018).

2) The forward model needs to be able to simulate multilayer systems. Raymond and Lamarche (2013) presented a noteworthy attempt to estimate the thermal parameters of a multilayer soil mass system. They utilized the MLU simulator (an analytical tool for hydraulic pumping test in layered domains) for the forward calculation. The inverse calculation is conducted using the Levenberg–Marquardt algorithm (Marquardt 1963). They backcalculated thermal parameters for three layers and showed that the results were, for most cases, within 20% accuracy.

As indicated above, these challenges have been addressed in the literature, but most of the models can only deal with one or two challenges at a time. In this chapter we address these challenges, together with the possibility to identify parameters other than the conventional thermal conductivity and borehole thermal resistance. We introduce a new parameter identification (PI) algorithm capable of estimating effective and detailed thermal parameters of GSHP systems. The PI comprises an iterative scheme, coupling a semi-analytical forward model to an inverse model.

The forward model is formulated based on the spectral element method (Doyle 1997) and the superposition principle to simulate transient 3D heat flow in multiple borehole heat exchangers embedded in multilayer systems. The spectral element method (SEM) solves linear partial differential equations for a homogeneous domain analytically, and for a layered domain it solves the governing equations by means of the finite element technique. It elegantly combines the exactness of the analytical methods to a great extent of generality of the numerical methods in describing the geometry and boundary conditions. It requires one element per layer, making the mesh size equivalent to the number of layers. These features make the proposed forward model accurate and computationally efficient, and thus suitable for utilization in iterative schemes for inverse problems.

The inverse model is formulated based on the interior-point method (IPM), a technique capable of optimizing multi-dimensional, sparse linear, quadratic or general nonlinear objective functions and constraints (Byrd et. al. 1999). Optimization algorithms based on the IPM are usually implemented on the basis of the predictor-corrector technique, Cholesky decomposition and Newton's method. These features make the inverse model capable of identifying multiple variables problems with relatively high convergence rate. Details of the PI algorithm is given in Section 7.3, followed by verifications and analyses in Section 7.4 and 7.5. But first, we elaborate on the current GI algorithm.

7.2 Current Graphical Interpretation (GI) algorithm

The GI algorithm estimates the effective soil thermal conductivity and borehole thermal resistance based on the infinite line source model (ILS) and the least square curve fitting method. For a sufficiently long time, Carslaw and Jaegar (1959) solved the ILS partial differential equation for a constant heat flow rate per unit length, q, giving:

$$T(r,t) \simeq T_0 + \frac{q}{4\pi\lambda}\left(\ln\frac{4\alpha t}{r^2} - \gamma\right) \tag{7.1}$$

in which $T(r,t)$ is the temperature of the medium (soil mass in this case) at radial distance r from the heat line source, λ (W/(m. k)) is the medium thermal conductivity, $\alpha(\mathrm{m}^2/\mathrm{s})$ is the thermal diffusivity and $\gamma = 0.5772$ is Euler's constant.

At the borehole boundary surface, $r = r_b$, the borehole temperature is related to the average fluid temperature via (Eskilson 1987, and Wagner and Clauser 2005):

$$\overline{T}(t) = T\big|_{r=r_b} + qR_b \tag{7.2}$$

where

$$\overline{T}(t) = \frac{T_{\mathrm{in}}(t) + T_{\mathrm{out}}(t)}{2} \tag{7.3}$$

in which $T_{\mathrm{in}}(t)$ and $T_{\mathrm{out}}(t)$ are the inlet and outlet temperatures, and R_b is the borehole thermal resistance between the fluid and the borehole wall.

Substituting Eq.(7.1) into Eq.(7.2) , and rearrangement, gives

$$\overline{T}(t) = \frac{q}{4\pi\lambda}\ln(t) + \left[qR_b + \frac{q}{4\pi\lambda}\left(\ln\frac{4\alpha}{r_b^2} - \gamma\right)\right] + T_0 \tag{7.4}$$

In a compact format, Eq. (7.4) can be written as

$$\overline{T}(t) = a\ln(t) + b \tag{7.5}$$

which represents a line in a semi-log scale with a its slope and b its $\bar{T}$-intercept. Relating a to the coefficient of the first term on the right-hand side of Eq. (7.4), and knowing the heat pump q, the soil thermal conductivity λ can readily be determined. Then, relating b to the second and third terms on the right-hand side of Eq. (7.4), and known λ from the previous step together with all other known parameters, R_b can be determined.

Apparently, the GI algorithm is easy to implement, making it attractive for daily engineering practice. However, it suffers from fundamental shortcomings, including:

1. This method is undetermined. It entails determining two physical parameters from one equation in two steps; not by solving two equations simultaneously. An error in determining λ would inevitably lead to error in R_b. Basically, the parameter identification procedure requires either determinate systems (the number of equations is equal to the number of unknowns) or over-determinate systems (the number of equations is more than the number of unknowns).
2. The time when the curve fitting begins can have a crucial effect on the values of a and b, and hence on λ and R_b.
3. The solution given in Eq. (7.1), provided by Craslaw and jaeger (1959), is applicable for "sufficiently" long time, necessitating conducting the experiment for several days to be valid.

7.3 Proposed PI algorithm

The proposed PI algorithm consists of a forward model to an inverse model, described hereafter.

7.3.1 Forward model

The background theory of the forward model has been thoroughly presented in Chapter 4. The governing heat equations and initial conditions of a ground source heat pump consisting of a single U-tube borehole heat exchanger embedded in a soil mass, Figure 4.1, are presented in Section 4.3. The boundary condition at the inlet of pipe-in might be any of two types:

a **Neumann boundary condition:**

$$q_i(0,t) = q_{\text{in}}(t) = -\lambda \frac{dT_i}{dz} dA_i \tag{7.6}$$

or a **Dirichlet boundary condition**:

$$T_i(0,t) = T_{\text{in}}(t) \tag{7.7}$$

where q_{in} is the prescribed heat flux and T_{in} is the prescribed inlet temperature, that might have any arbitrary distribution in time.

Eqs. (4.1)-(4.4) are coupled via local thermal interaction terms describing heat flow at the contact surfaces between neighboring BHE components. At the boundary between pipe-in and grout the heat flow is described in terms of the thermal interaction coefficient, b_{ig}, which can be expressed as:

$$b_{ig} = \frac{1}{dS_{ig}\, R_{ig}} \tag{7.8}$$

where dS_{ig} is the surface area of pipe-in in contact with the grout, and R_{ig} is the corresponding thermal resistance, expressed analytically as

$$R_{ig} = R_{\text{convection}} + R_{\text{pipe material}} = \frac{1}{2\pi r_i L \bar{h}} + \frac{\ln\left(r_o / r_i\right)}{2\pi L \lambda_{\text{p}}} \tag{7.9}$$

in which r_i and r_o are the inner and outer radius of pipe-in, respectively; L is the length of the spectral element; λ_{p} is the thermal conductivity of pipe-in material; and $\bar{h} = \text{Nu}\lambda / D$ is the convective heat transfer coefficient, where D is the inner diameter of the pipe, Nu and λ are the Nusselt Number and thermal conductivity of the circulating fluid. A similar formulation is used for b_{og}, pipe out – grout thermal interaction.

The thermal interaction coefficient for the soil film – soil mass is expressed as

$$b_{ss} = \frac{1}{dS_s\, R_{ss}} \tag{7.10}$$

where dS_s is the surface area of the soil film in contact with the soil mass, and R_{ss} is the corresponding thermal resistance, expressed analytically as

$$R_{ss} = \frac{\ln\left(r_{\text{f}} / r_{\text{b}}\right)}{2\pi L \lambda_s} \tag{7.11}$$

in which r_{f} is the radius of the soil film and r_{b} is the borehole radius. The thermal interaction coefficient for grout –soil film is expressed as

$$b_{gs} = \frac{1}{dS_{gs}\, R_{gs}} \tag{7.12}$$

where dS_{gs} is the surface area of grout in contact with the soil film, and R_{gs} is the corresponding thermal resistance. Unlike R_{ig}, R_{og} and R_{ss}, R_{gs} does not have an analytical expression due to the acentric positions of pipe-in and pipe-out inside the grout. This coefficient is usually approximated using an equivalent centric pipe with an

equivalent cross-sectional area of pipe-in and pipe-out (Al-Khoury 2012b, Section 2.3). Here, R_{gs} is backcalculated using the inverse model.

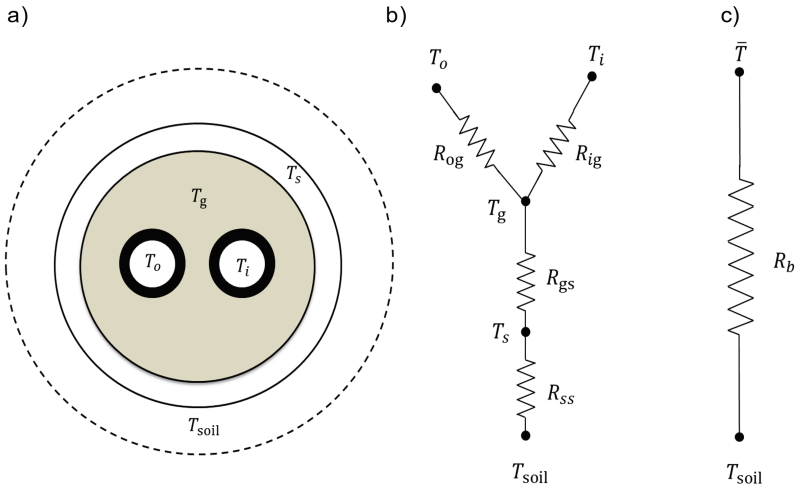

Figure 7.4: **a) BHE-soil top view, b) BHE-soil Y–configuration thermal circuit, c) equivalent borehole thermal resistance.**

The above local thermal interaction terms are unique to this model, Eqs. (4.1)-(4.4). Different models can have different local thermal interaction arrangements and formulations. Nevertheless, regardless of the local interaction terms, models that are utilized to interpret the thermal response test (TRT) are required to back calculate the borehole thermal resistance, R_b. The usual practice is to lump the local thermal interaction coefficients into an equivalent coefficient using some sort of arrangements, such as the Delta– or Y–configuration analogy to Ohm's law (Al-Khoury 2012b). The governing BHE heat equations (Eqs. (4.1)-(4.4)) are a typical Y– configuration, where pipe-in and pipe-out are interacting with each other via the grout, which is in contact with the soil, Figure 7.4a. Figure 7.4b shows the thermal resistance configuration, where R_{ig} and R_{og} are in parallel to each other and in series with R_{gs} and R_{ss}. The equivalent thermal resistance for this configuration is given in Figure 7.4c that can be expressed as

$$R_b = R_{ig} \parallel R_{og} + R_{gs} + R_{ss} \tag{7.13}$$

where R_{ig}, R_{og} and R_{ss} are determined analytically using Eqs. (7.9) and (7.11), respectively, and R_{gs} is backcalculated.

7.3.2 Inverse model

The procedure for parameter identification entails minimizing the objective function of a system subjected to predefined constraints, such that:

$$\begin{aligned} &\text{minimize} \quad f(\mathbf{x}) \\ &\text{subjected} \quad \mathbf{x} \in \Omega \end{aligned} \tag{7.14}$$

where $f(\mathbf{x})$ is the objective function that needs to be minimized; $\mathbf{x} = [x_1, x_2, \dots]$ is the vector of the unknown parameters that need to be estimated, such as the soil thermal conductivity and the borehole thermal resistance; and Ω represent the constraints of $\mathbf{x}$.

For a ground source heat pump, the objective function can be expressed as the Euclidean distance (norm 2) between the measured and computed temperatures. Using the spectral analysis, the Euclidean distance is described in the frequency domain, as

$$\begin{aligned} f(\mathbf{x}) &= \left\| \hat{T}_{\mathrm{m}}(\omega, z) - \hat{T}_{\mathrm{th}}(\omega, z, \mathbf{x}) \right\|_2 \\ &= \left(\sum\nolimits_n \left| \hat{T}_{\mathrm{m}}(\omega_n, z) - \hat{T}_{\mathrm{th}}(\omega_n, z, \mathbf{x}) \right|^2 \right)^{1/2} \end{aligned} \tag{7.15}$$

in which $\hat{T}_{\mathrm{m}}(\omega_n, z)$ is the frequency transformed measured temperature, as typically obtained from TRT, and $\hat{T}_{th}(\omega_n, z, \mathbf{x})$ is its equivalent theoretical temperature, as computed by the forward model. Theoretically, $\hat{T}_{\mathrm{m}}(\omega_n, z)$ and $\hat{T}_{th}(\omega_n, z, \mathbf{x})$ can be at any frequency, ω_n, at any depth, z, and for any component of the GSHP system, including the soil mass. However, in typical TRT, only the temperatures at the inlet of pipe-in and outlet of pipe-out are measured. The summation over n in Eq. (7.15) indicates that the objective function can contain any number of frequencies. This constitutes an important advantage of the spectral analysis compared to the time domain. In the time domain the whole signal must be considered and the whole system must be calculated in every iteration, while in the spectral analysis the system can be calculated for only few frequencies. This stems from the fundamental property of the frequency domain which describes the characteristic of the system to respond to a range of frequencies regardless of the time of occurrences. In the time domain, the sequence of occurrences determines the response of the physical system, specifically for that event. The verification and numerical examples given in later sections are conducted using 20 frequencies for each reading set.

Solving the objective function, Eq. (7.15), requires a minimization algorithm capable of solving complex, multidimensional, nonlinear equations. In this work, we employ the Interior-point optimization algorithm (Bonnans et. al. 2006), which can handle large and sparse problems. It satisfies bounds at all iterations and can recover from NAN (Not a Number) or Inf (Infinity) results. This algorithm has been implemented and optimized in the MATLAB nonlinear programming solver called $fmincon$ (MathWorks 2019). The

proposed PI algorithm can be summarized in a computer program (see PROGRAM PI Algorithm).

PROGRAM PI Algorithm

1: Transform measured temperatures into frequency domain: $\hat{T}_{\mathrm{m}}(\omega_n, z)$

2: Set initial values for the required parameter: $\mathbf{x}^o$

3: **Call** $fmincon$

4: Loop_z **DO** $m = 1, M$; M is the number of temperature readings along BHE or in soil

5: Loop_freq **DO** $n = 1, N$; N is the number of selected frequencies

6: Calculate $\hat{T}_{\mathrm{th}}(\omega_n, z, \mathbf{x})$ using the forward model, Section 3.1

7: **ENDDO** Loop_freq

8: **ENDDO** Loop_z

9: Calculate the objective function, Eq. (7.15):

$$f(\mathbf{x}) = \left\{ \sum_{n=1}^{N} \left| \hat{T}_{\mathrm{m}}(\omega_n, z) - \hat{T}_{\mathrm{th}}(\omega_n, z, \mathbf{x}) \right|^2 \right\}^{1/2}$$

10: **IF** $f(\mathbf{x}) > \varepsilon$; ε some tolerance

$fmincon$ determines new guess for **x**

GOTO Loop_z

ENDIF

11: Output **x**

ENDPROGRAM PI Algorithm

7.4 Performance of PI algorithm

The performance of the proposed PI algorithm is examined by means of numerical experiments using synthetic data generated by the forward model to represent measurements of a typical TRT experiment. Synthetic data is usually smooth, but to make it comparable to measured data, random noise with different contamination levels is applied. The advantage of using synthetic data is that the input parameters are known a

priori that enables quantifiable verification of the inverse model. The PI algorithm is tested in terms of its accuracy; stability, which is a measure of the ability of an algorithm to converge even in the presence of contaminated data; and convergence rate, which is a measure of the speed at which a convergence sequence reaches the desired accuracy.

Table 7.1: BHE material and physical parameters

Parameter	Value
Borehole:	
Borehole length	100 m
Borehole diameter	0.1 m
Pipe external diameter	0.03 m
Pipe thermal conductivity	0.42 W/(mK)
Fluid:	
Density, ρ	1000 kg/m^3
Specific thermal capacity, c	4186 J/(kg. K)
Thermal conductivity, λ	0.56 W/(m. K)
Dynamic viscosity, μ	0.001 Pa. s
Velocity, u	0.5 m/s
Grout:	
Density, ρ_g	1400 kg/m^3
Specific thermal capacity, c_g	2000 J/(kg. K)
Thermal conductivity, λ_g	0.8 W/(m. K)

Typical TRT heat pumps exhibit fluctuations in their power signal, with standard deviation (std) ranging between 2% and 10% (Beier et. al. 2011 and Witte et. al. 2002). To mimic this, we contaminate the synthetic heat pump power using an additive white Gaussian noise (AWGN), such that

$$P_{\text{con}} = P_{\text{sy}} + \eta(t, \text{std}) \tag{7.16}$$

in which P_{con} is the contaminated heat pump signal, P_{sy} is the synthetic heat pump power and η is a zero-mean random AWGN with standard deviation, std. Here, the synthetic heat pump power is assumed 5000 W. To generate a wide range of randomness, we apply 150 random AWGN with three levels of std:

$$\text{std} = \begin{cases} 100 \\ 300 \\ 500 \end{cases} \text{W} \tag{7.17}$$

The heat pump is assumed to be connected to a 100 m BHE, constituting a single U-tube embedded in a soil mass. Details of the BHE parameters are given in Table 7.1. Two numerical TRT experiments have been conducted: 1) for a BHE embedded in a half space; and 2) for a BHE embedded in a three-layer system. Parameter identifications have been performed on the contaminated data using the GI method and the proposed PI algorithm. We compare the performance of these two algorithms based on:

1. accuracy in predicting the parameters;
2. noise effect;
3. duration of experiment; and
4. number of backcalculated parameters.

7.4.1 Numerical TRT in a half space

In this set up, the BHE is assumed to be embedded in a half space constituting a homogeneous soil layer with thermal conductivity $\lambda_s = 2$ (W/mK), and volumetric heat capacity $\rho_s c_s = 2.6$ (MJ/m^{3}K).

150 numerical TRT experiments were conducted for 72 hours. They were divided into three sets, each representing 50 numerical experiments subjected to randomly contaminated power signal (Eq. (7.16)) with a specific standard deviation (Eq. (7.17)). Figure 7.5 shows an example of one of the three sets. It shows randomly contaminated power with 300 W standard deviation (Figure 7.5a), and the associated computed inlet and outlet temperatures (Figure 7.5b). This figure evidently demonstrates that the use of AWGN makes the synthetic data comparable to measured data.

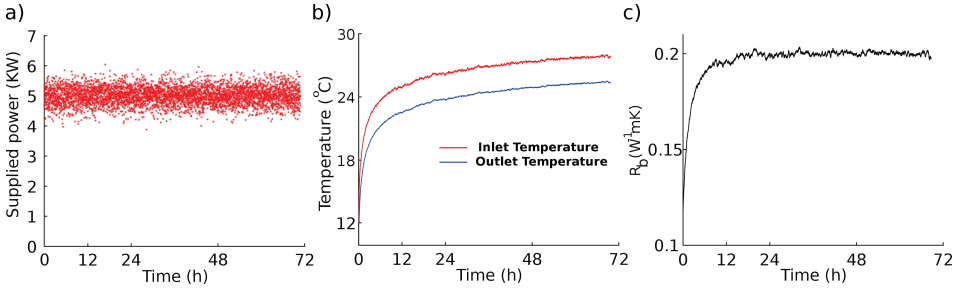

Figure 7.5: a) thermal power with std $= 300\ W$, b) inlet and outlet temperatures, c) borehole thermal resistance: Eq.(7.18) .

The borehole thermal resistance is calculated based on the forward model results, via (Raymond and Lamarche 2013):

$$R_b = \frac{\overline{T} - T_b}{q} \tag{7.18}$$

where $\overline{T}$ is the average fluid temperature (Eq. (7.3)), and T_b the borehole temperature (T_s in Eq.(4.3)). Figure (7.5c) is a plot of R_b versus time, which clearly shows that, upon the end of the transient period, R_b becomes nearly constant at 0.2 (mK)/W.

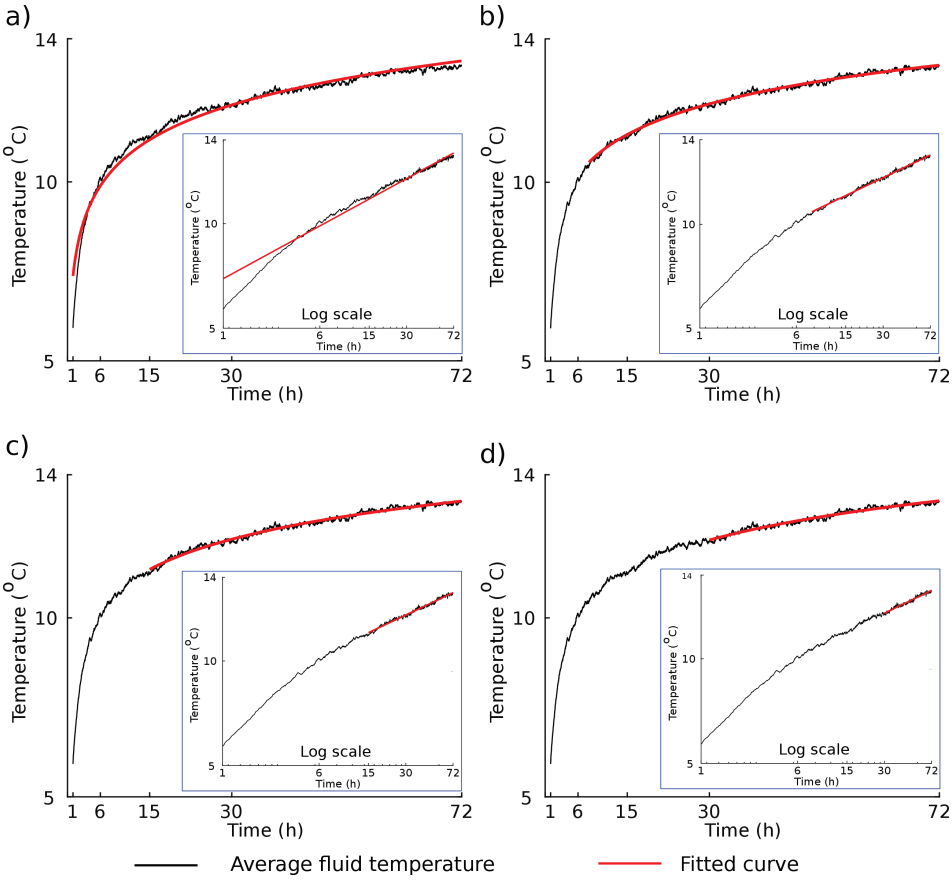

Figure 7.6: Average fluid temperature and fitted curves for different fitting start time: a) 1 h, b) 6 h, c) 15 h and d) 30 h.

The backcalculation is carried out using both the GI algorithm and the proposed PI algorithm.

A. Backcalculation based on GI algorithm

The GI algorithm is utilized to backcalculate the effective soil thermal conductivity, λ_s, and the borehole thermal resistance, R_b, for the 150 numerical experiments. Figure 7.6 shows an example of one of the numerical experiments, generated from processing the computed results of Figure 7.5. It displays the average fluid temperature $\bar{T}$ versus time, along with the best fitted curves. Four fitted curves, depending on the start time, were conducted: after 1 h; after 6 h; after 15 h; and after 30 h. The fitted curves are shown in normal scale plots and in semi-log scale plots (inside the blue boxes). Obviously, the fitted curve which starts after 1 h is the least accurate due to the high transient gradient at the beginning of the experiment.

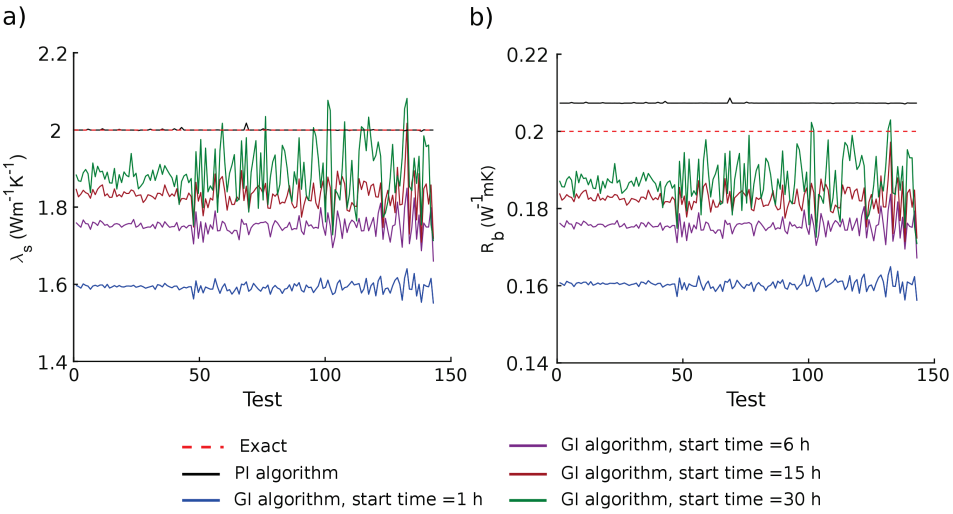

Figure 7.7: a) backcalculated soil thermal conductivity, b) backcalculated borehole thermal resistance.

Figure 7.7 presents the backcalculated results of these four fitted curves. Apparently, the GI algorithm exhibits dependency on both the start time of fitting and the noise level. Knowing the input values ($\lambda_s = 2\,\mathrm{W/mK}; R_b = 0.2\,\mathrm{mK/W}$) the figure qualitatively indicates that the fitted curve which starts after 30 h and $\mathrm{std} = 100\,\mathrm{W}$ gave the best estimate. We use the boxplots as a means for descriptive statistics to observe the estimation errors of the best fitted curve case based on five quantities: minimum, first quartile, median, third quartile, and maximum. Figure 7.8 shows boxplots of the 30 h

fitting case; and Table 7.2 presents the associated statistical values. The following can be deduced from the boxplots:

1) The median error decreases with increasing noise,
2) The interquartile range (IQR , box size) increases with noise level: $IQR_{100W} = 1.2; IQR_{300W} = 5.5; IQR_{500W} = 5.7$.
3) The gap between the minimum and maximum increases with increasing noise: $MM_{100W} = 3.9; MM_{300W} = 10.3; MM_{500W} = 14.3$.
4) Noise level $100\ W$ has three outliers, while others do not have.

These observations indicate that the GI algorithm depends strongly on the noise level.

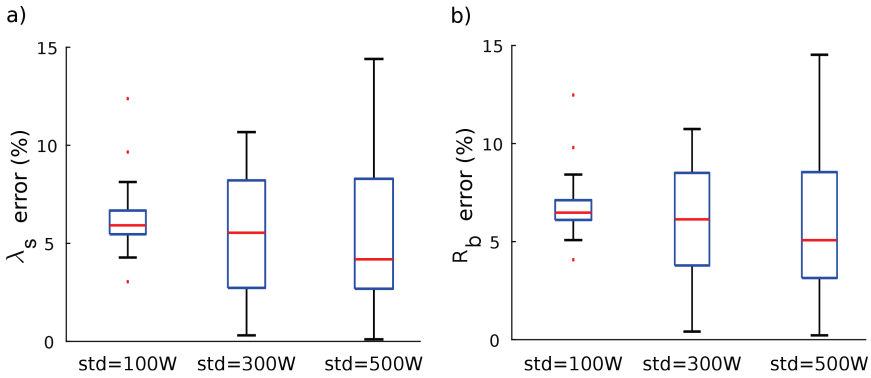

Figure 7.8: Boxplot of estimated error of GI algorithm started at 30 h: a) soil thermal conductivity, b) borehole thermal resistance, for GI algorithm started at 30 hours.

Table 7.2: Statistical values of Figure 7.8

Noise level	Minimum (%)	First quartile (%)	Median (%)	Third quartile (%)	Maximum (%)
std = 100 W	4.2	5.4	5.9	6.6	8.1
std = 300W	0.3	2.7	5.5	8.2	10.6
std = 500W	0.1	2.6	4.1	8.3	14.4

It is worth noting that the error in the backcalculated borehole thermal resistance has the same statistical description as that for the thermal conductivity (see Figure 7.8a and Figure 7.8b). This proves the argument which was raised in Section 7.2. As the estimation of R_b using the GI algorithm is dependent on λ_s, the error in estimating λ_s is reflected on R_b.

B. Backcalculation based on PI algorithm

Here, the proposed PI algorithm was utilized to backcalculate λ_s and R_b from the 150 numerical experiments. Figure 7.7 shows the backcalculated results (black lines). The estimated λ_s is 1.99 W/mK (input value is 2 W/mK), and R_b is 0.207 mK/W (input value is 0.2 mK/W). The figure also shows that the PI algorithm is stable such that it demonstrates minor oscillations with noise.

Figure 7.9 shows the convergence rate of one of the experiments with std $= 300\ W$. It shows that both parameters were identified in 25 iterations. This relatively high convergence rate can be attributed to several reasons, including the use of the spectral element method for the forward calculation, and the use of the interior-point optimization algorithm and the Euclidean norm for the inverse calculation. 20 frequencies were utilized and on average it took 5 seconds in a normal laptop for the whole backcalculation procedure.

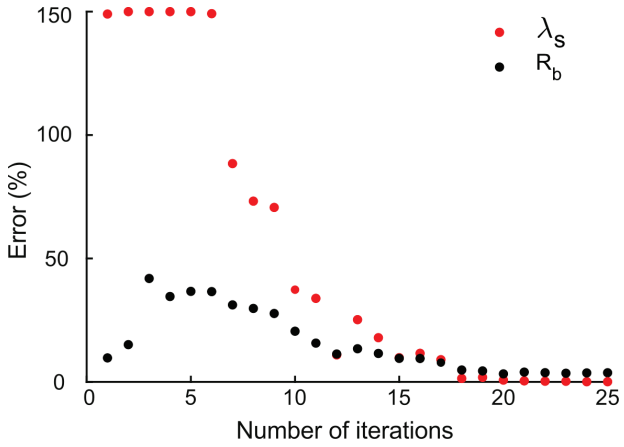

Figure 7.9: Convergence rate of PI algorithm

7.4.2 Numerical TRT in a layered system

In this section, we investigate a numerical TRT for a BHE embedded in a three-layer soil mass. Figure 7.10 shows the geometry and material properties of the soil layers. The BHE physical and thermal properties are as those given in the previous example. Also, 150 numerical experiments with heat pump power and noise levels as for the previous example were conducted. The borehole thermal resistance is calculated using Eq. (7.18).

We examined the PI algorithm in two ways: 1) effective parameter identification, where we estimate the thermal parameters assuming that the soil mass consists of a single layer which can be descried by an effective thermal conductivity and borehole thermal resistance; and 2) detailed parameter identification, where we estimate the thermal parameters of all layers, assuming that sufficient temperature readings along the pipe are available.

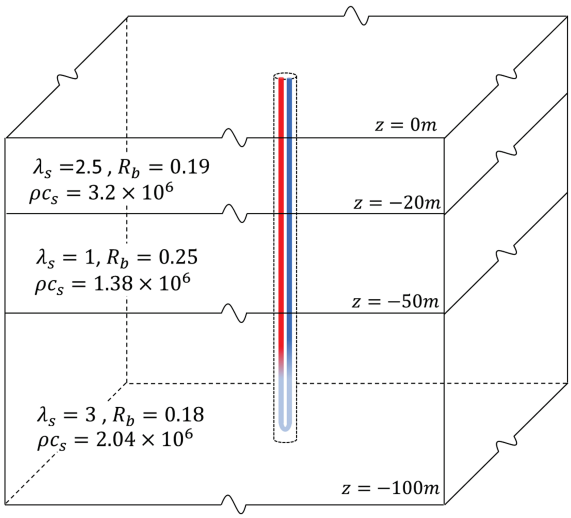

Figure 7.10: Schematic presentation of a BHE embedded in a three-layer soil mass

A. Effective parameter identification

Conventional parameter identification using TRT measurements is based on estimating the thermal conductivity and borehole thermal resistance of the soil mass from the inlet and outlet temperatures. The soil mass is assumed half space, characterized by effective (average) thermal parameters.

The average thermal conductivity of the soil mass, as given in Figure 7.10, can readily be calculated to give 2.16 W/mK, and the average borehole thermal resistance to give 0.206 mK/W. If the layer thicknesses are considered, calculation of the weighted averages would give 2.3 W/mK and 0.203 mK/W, respectively.

Figure 7.11 shows the backcalculated effective parameters using both the proposed PI algorithm and the GI algorithm. The backcalculation due to the PI algorithm gave 2.188 W/mK for the thermal conductivity, and 0.187 W/mK for the borehole thermal resistance; which are close to both averages of the input values. Additionally, the figure reveals that the PI algorithm has minor oscillations for all noise levels. On the other hand, the GI algorithm gave different results depending on the start time of the curve fitting and the noise level. In all cases it gave underestimated values.

We furthermore examined the performance of the PI algorithm for different experiment durations: 12, 24, 48 and 72 hours. Table 7.3 presents the estimated values of the effective λ_s and R_b, backcalculated from the PI algorithm and GI algorithm for different curve fitting periods (from 1, 6, 15 and 30 hours). This independency on the duration of the experiment is attributed to the capability of the forward model to simulate the highly transient period at the beginning of the experiment, and to the choice of the minimization procedure. On the other hand, the GI algorithm gave varying estimates with somewhat better performance for the longer experiment duration and shorter curve fitting. This explains why the TRT is conducted in practice for 72 hours.

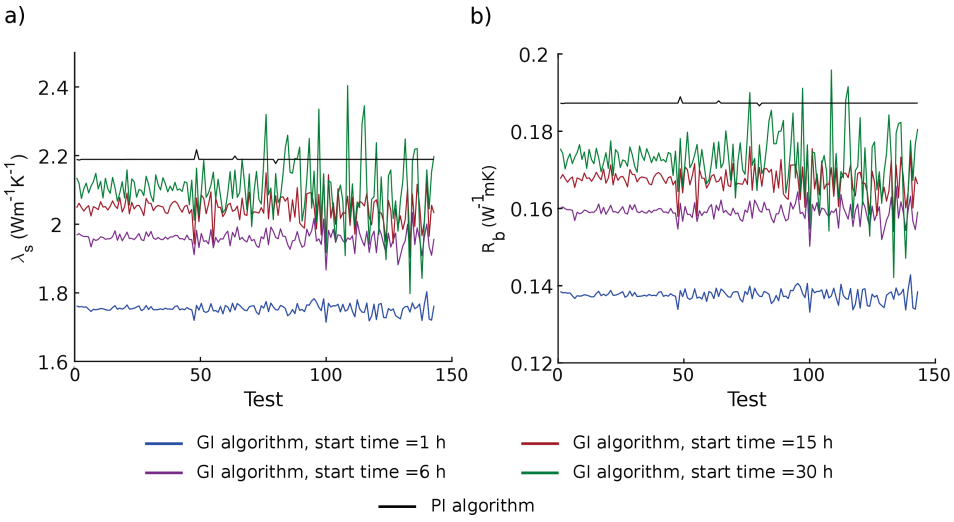

Figure 7.11: a) estimated soil thermal conductivity, b) estimated borehole thermal resistance

B. Detailed parameter identification

Detailed parameter identification entails estimating the thermal parameters of all involved layers and/or parameters including the volumetric heat capacities, $\rho_s c_s$.

As mentioned earlier, the basic principle of the parameter identification is that the system of equations must be either determinate or over-determinate. This implies that the number of measured set of readings must be equal or more than to the number of backcalculated parameters. To estimate the thermal parameters of the three-layer system of Figure 7.10, we assume that we have four measurement sets along the BHE. One set is the standard inlet and outlet temperatures, and the other three measurement sets are taken in the U-tube, on the middle of each layer. We backcalculate nine parameters: λ_s and R_b for each layer together with their associated volumetric heat capacities, $\rho_s c_s$. The TRT operation time is assumed 12 hours.

Table 7.4 shows the estimated parameters compared to the exact (input values). It reveals that the estimated thermal conductivities for the three layers are nearly exact, the borehole thermal resistances have a maximum 5.5% error, and the volumetric heat capacities have a maximum 4.6% error.

Table 7.3: Parameter estimation for different TRT durations

Period	PI algorithm		GI starts at 1h		GI starts at 6h		GI starts at 15h		GI starts at 30h	
	λ_s	R_b	λ_s	R_b	λ_s	R_b	λ_s	R_b	λ_s	R_b
12 h	2.188	0.187	1.35	0.1	1.61	0.13	___	___	____	____
24 h	2.187	0.187	1.51	0.116	1.77	0.144	1.85	0.15	____	____
48 h	2.184	0.187	1.67	0.13	1.9	0.154	1.95	0.16	1.84	0.149
72 h	2.188	0.187	1.76	0.138	1.96	0.159	2.02	0.165	2.11	0.17

7.5 Model verification

Witte et al. (2002) and Witte and van Gelder (2006) had conducted several in-situ thermal response tests to backcalculate the thermal conductivities of a multilayer soil mass. The borehole heat exchanger is 30 m in depth and 0.25 m in diameter, filled with soil materials of the surroundings, and embedded in which a U-tube, 0.025 m in diameter. The working fluid in the U-tube consists of water with 17% ethylene glycol solution. Detailed description of the geometry and materials can be found in Witte et al. (2002). Figure 7.12 and Table 7.5 (Column *TRT*) give an overview of the geometry and show that the soil mass consists of 8 layers of different soil types and thicknesses.

Table 7.4: PI algorithm, detailed parameter identification

	λ_s		R_b		$\rho_s c_s$	
	Exact	**Estimated**	**Exact**	**Estimated**	**Exact**	**Estimated**
Layer1	2.5	2.49	0.19	0.2	3.3M	3.2M
Layer 2	1	0.99	0.25	0.24	1.4M	1.38M
Layer 3	3	2.99	0.18	0.19	2.14M	2.04M

Witte et al. (2002) also provided the range of thermal conductivities of each soil type, as given in literature, and laboratory results for nine soil samples taken from the site. Witte and van Gelder (2006) conducted non-conventional experiments comprising three successive heat pump power pulses: two for heat injection and one for heat extraction. The power pulses lasted 96 hours, followed by a switching off period until 169 hours. The heat pump power together with the temperatures at the inlet and outlet of the U-tube were recorded for 169 hours every 4 minutes. Figure 7.13a shows the heat pump power versus time.

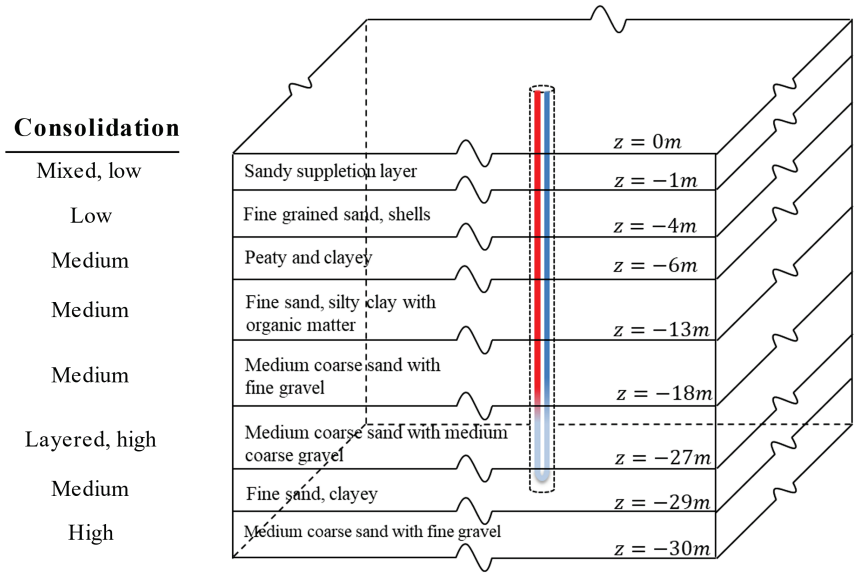

Figure 7.12: Schematic presentation of the TRT given by Witte et.al. (2002)

Here, we make use of Witte and van Gelder (2006) TRT measurement to backcalculate the thermal conductivities of the involved soil layers with two varying complexities:

1. Effective parameter identification of the average soil thermal conductivity, assuming that all soil layers can be grouped into one. The backcalculation results are given in Table 7.5 (Column *Parameter Identification*). The effective thermal conductivity is estimated to be 2.01 $(\mathrm{W/mK})$. This estimation falls between the weighted average of the minimum (1.19 $\mathrm{W/mK}$) and maximum 3.4 $(\mathrm{W/mK})$, obtained from the literatures. It also compares well with the average laboratory results; 2.1 $(\mathrm{W/mK})$, given by Witte et. al. (2002).
2. Detailed parameter identification of thermal conductivities of all layers using the measured inlet and outlet temperatures, and eight synthetic fluid temperatures obtained from the forward model along pipe-in and pipe-out. Synthetic data was utilized because no measurements were made along the BHE. Nevertheless, they are computed using the measured inlet temperature, which intrinsically involves noise. The backcalculation results are given in Table 7.5 (Column *Parameter Identification*). It shows that the backcalculated thermal conductivities are rather close to the laboratory results. The weighted average of the backcalculated values of all layers is 2.16 $(\mathrm{W/mK})$.

Figure 7.13b shows the measured inlet and outlet temperatures, together with the theoretical outlet temperature calculated based on the backcalculated thermal conductivities. The theoretical outlet temperatures were calculated in two ways: based on the effective thermal conductivity 2.01 $(\mathrm{W/mk})$, and based on the detailed thermal conductivities, as given in Table 7.5 (Column *Parameter Identification*)**.** The figure obviously shows a very good matching between the measured temperatures and the computed from both ways. This gives the impression that backcalculating the effective thermal conductivity is sufficient to produce accurate results; avoiding thus the need for detailed backcalculations. This argument has been highlighted in literature, see for example Lee (2011). However, matching accurately the fluid outlet temperature does not necessarily reflect the accuracy in calculating the temperature distribution in the soil mass. Figure 13c shows the associated temperature profiles in the soil mass in the $z-$direction, $10\ \mathrm{cm}$ away from the BHE. The temperature profiles are computed at the end of heat injection to the soil and the end of heat extraction. The figure clearly shows that calculations based on the detailed parameter identification exhibit different temperature distributions in the soil layers, depending on their thermal conductivities. This implies that relying on the effective thermal parameters might be useful for individual GSHP systems, but for regional GSHP systems where the thermal interaction between adjacent boreholes is crucial, knowing the detailed thermal properties of the soil layers is unavoidable.

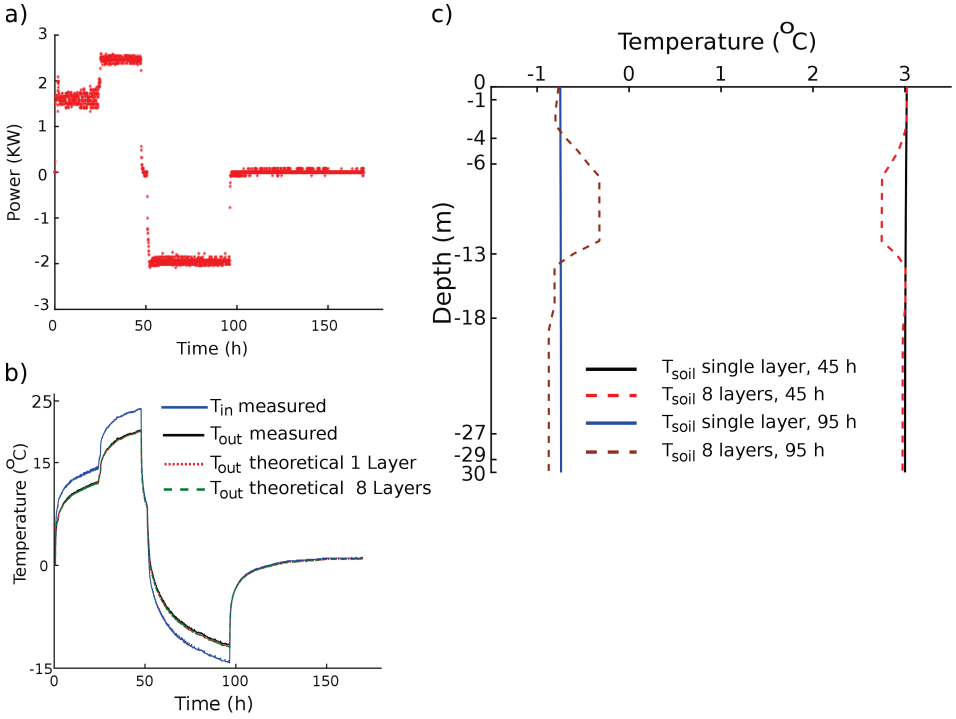

Figure 13: a) supplied power, b) inlet and outlet temperatures, c) soil temperature in z direction at radial distance 10 *cm* from the BHE.

7.6 Conclusions

A new parameter identification algorithm has been introduced for estimating effective and detailed thermal parameters of ground source heat pump systems. The algorithm constitutes a semi-analytical forward model based on the spectral element method and an inverse model based on the interior-point optimization.

Important features of the PI algorithm are:

1. It can handle fluctuating heat pump power.
2. It can interpret data obtained from multiple heat extraction or injection pulses for heating or cooling modes.
3. It can produce accurate backcalculation for short and long duration experiments.
4. It can handle multilayer systems.
5. It can identify multiple parameters.

6. It is accurate and computationally efficient, stable and has a high convergence rate. Additionally, the numerical experiment on the multilayer system and the verification example demonstrated that the proposed PI algorithm has remarkable uniqueness even for multiple parameter identification. These features (accuracy, computational efficiency, stability, high convergence rate and uniqueness) constitute the essence of any parameter identification technique. They are manifested in the proposed algorithm due to the novel coupling between the spectral element method and the interior-point optimization method together with the Euclidean norm.

In practice, these features can help in:

1. Reducing the TRT cost by applying short duration experiments. The proposed forward model is accurate at both, the highly transient period of TRT and its steady state. This makes the backcalculation possible for almost any duration.
2. Facilitating better GSHP design. Knowing the detailed soil mass parameters yields accurate calculation of the temperature distribution in the soil mass, making the PI particularly suitable for regional GSHP systems design. Combining this parameter identification technique to a heat pump optimization tool such as that of Jin and Spitler (2002), and to energetic, exergetic and economic performance optimization tools, such as those of Ozgener and Hepbasli (2007), Conti (2015) and Verrax (2018), would lead to optimal GSHP designs.

The proposed PI algorithm can be extended to include features to consider the initial soil temperature gradient and groundwater flow in the forward model, and options to estimate the actual BHE length after installation and the thicknesses of the soil layers in the inverse model.

Table 7.5: TRT field and laboratory data versus backcalculated.

TRT (Witteet. al. 2002)						Parameter Identification	
Layers			*Range from literature*		*Laboratory samples*	*Effective estimation*	*Detailed estimation (8 readings)*
	Soil type	**Thickness(m)**	**Min**	**Max**			
1	Sandy suppletion layer	1	1.11	1.25	2.265		2.1
2	Fine grained sand, shells	3	0.58	1.75	2.535		2.26
3	Peaty and clayey	2	0.9	1.32	1.39*		1.5
4	Fine sand, silty clay with organic matter	7	____	____	1.091		1.13
5	Medium coarse sand with fine gravel	5	1.73	5.02	2.447	2.01	2.34
6	Medium coarse sand with medium coarse gravel	9	1.73	5.02	2.78		2.79
7	Fine sand, clayey	2	1.34	4.8	____		2.8
8	Medium coarse sand with fine gravel	1	1.73	5.02	2.868		2.85
	Weighted average		**1.19**	**3.4**	**2.1****		**2.16**

*This value is the mean of two readings at 4 and 6 meters.
**Normal average of all the values

8

Conclusions and Outlook

8.1 Conclusions

This thesis deals with modelling heat flow in ground source heat pumps (GSHP). GSHP is a well-established technology that utilizes the vastly available shallow geothermal energy for the heating and cooling of buildings. The GSHP systems have many advantages, including low CO_2 emissions, long lifetime (typically up to tens of years) and low costs for operation and maintenance. Even though the GSHP industry is relatively matured and efficient in extracting the shallow geothermal energy, accurate and efficient computational modelling of GSHP systems is still lagging. The design of this system is not yet optimal and requires further development.

Several computational models have been developed to simulate the heat flow in GSHP systems. These models vary from detailed numerical 3D analyses to analytical solutions. Due to the peculiarity of the involved geometry (which constitutes highly slender borehole heat exchangers embedded in a vast soil mass, and the convection heat flow mechanism) the numerical models require extensive computational capacity and CPU time. The analytical models, on the other hand, are computationally efficient but their accuracy suffers from the over-simplified geometry and initial and boundary conditions. This thesis aims to bridge the gap between the numerical models in their generality and the analytical models in their computational efficiency.

The proposed semi-analytical model is comprehensive in describing the physics of the problem and efficient in its computations. It can simulate heat flow in an effectively 3D GSHP system constituting multiple borehole heat exchangers embedded in multilayer soil mass. The heat flow, in a multilayer system, is formulated based on the spectral element method. The thermal interaction between multiple borehole heat exchangers, on the other hand, is formulated based on the superposition principle. The model possesses the exactness and computational efficiency of the analytical models, and (to a great extent) also the generality of numerical techniques in describing the geometry as well as initial

and boundary conditions. The key for obtaining such an exact, computationally efficient and practically general model is the unique mix adopted in this thesis between the conceptual model, the mathematical formulation and the solution technique:

1) The conceptual model includes coupling a 1D domain (representing the borehole heat exchanger) to an axial symmetric 2D domain (representing a homogeneous soil layer) and a 3D domain (representing multiple borehole heat exchangers embedded in multilayers soil mass). This coupling makes the model computationally more efficient compared to detailed numerical 3D models.

2) The mathematical formulation is designed to describe heat flow in all GSHP components, including the detailed heat equations of the individual borehole heat exchangers components and the soil mass (as well as their thermal interactions). This formulation results to a comprehensive description of the involved physical features of the system.

3) The solution technique is designed to be accurate and computationally efficient. The use of the spectral element method for modelling multilayer systems together with the superposition technique for modelling multiple borehole heat exchangers makes the solution technique fit for this problem. It enables the simulation of heat flow in effectively 3D GSHP systems subjected to any arbitrary time dependant boundary condition. It gives accurate computation of the governing equations and makes the model suitable for forward and inverse calculations.

From the engineering point of view, the findings in this thesis can provide engineers with the means to have an in-depth knowledge of this technology, including:

a) The model allows the calculations of the temperature distribution in all BHE components and in soil layers. This feature allows engineers to analyse and design ground source heat exchangers with great details.

b) The calculation can be done for short to long term, covering hourly, daily and seasonally switching ON and OFF scenarios. This feature facilitates the calculation of heat flow for any desired details, ranging from one second to years, done in a single run.

c) The model allows the calculations of any arbitrary layout configuration of the borehole heat exchangers and any number of soil layers. This feature is essential for optimizing the layout configuration in a larger region and avoids conflicts among neighbouring users.

d) The calculation can be done based on prescribing heat flux derived from the heat pump power, as given by HVAC engineers. This feature allows the direct use of heating and cooling design specifications to calculate the temperature distribution in the system, including the inlet temperature and all other temperatures at any geometrical point in the system.

e) The inverse model can handle the following:

i. It can handle fluctuating heat pump power.

ii. It can interpret data obtained from multiple heat extraction or injection pulses.

iii. It can interpret data obtained at any spatial point in the GSHP system, including the surrounding soil mass.

iv. It can produce accurate backcalculations for short and long duration experiments.

v. It can handle multilayer systems.

vi. It can identify multiple parameters.

vii. It is accurate, computationally efficient, stable and has a high convergence rate.

With further elaborations on the engineering aspects, these features can help engineers to improve their design method and make this technology more efficient and economic.

8.2 Outlook

The proposed semi-analytical model is designed to be comprehensive in describing the physics and efficient in its computation. However, the model can be extended to include several features, such as:

a) The effect of ground water flow on heat flow in GSHP systems.

b) The soil temperature vertical gradient.

c) Thermal interaction between the soil and air temperatures.

d) The optimization process, in this thesis, has been applied for parameter identification problems. The same optimization process can be considered for GSHP systems' design. The model can be used to optimize the size and the cost of GSHP systems. Furthermore, constraints (such as regulations set by authorities) can also be considered.

e) The proposed PI algorithm can be extended to include more features such as: estimating the initial soil temperature gradient, the actual BHE length after installation and the thickness of the soil layers.

References

ABAQUS(2019): https://www.simuleon.com/ (accessed November 2019).

Abdelaziz S.L., Ozudogru T.Y., Olgun C.G. and Martin J.R. (2014). Multilayer finite line source model for vertical heat exchangers. Geothermics 51 (2014) 406–416.

Acuña J. and Palm B. (2013). Distributed thermal response tests on pipe-in-pipe borehole heat exchangers. Applied Energy 109 (2013) 312–320.

Al-Khoury R. (2010). Spectral framework for geothermal borehole heat exchangers. International Journal for Numerical Methods for Heat and Fluid Flow 20(7) 773-793.

Al-Khoury R. (2012a). A spectral model for shallow geothermal systems. International Journal for Numerical Methods for Heat and Fluid Flow 22(1) 49-72.

Al-Khoury R. (2012b). Computational Modeling of Shallow Geothermal Systems. CRC Press/Taylor & Francis Group.

Al-Khoury R. and Bonnier P.G. (2006). Efficient finite element formulation for geothermal heating systems. Part II: Transient. International Journal for Numerical Methods in Engineering. 67 (5) 725–745.

Al-Khoury R., Kölbel T. and Schramedei R. (2010). Efficient numerical modeling of borehole heat exchangers. Computers and Geosciences. 36(10) 1301-1315.

Austin W., Yavuzturk C. and Spitler J. D. (2000). Development of An In-Situ System For Measuring Ground Thermal Properties. ASHRAE Transactions. 106(1): 365-379.

Bandyopadhyay G., Gosnold W. and Mann M. (2008). Analytical and semi-analytical solutions for short-time transient response of ground heat exchangers. Energy and Buildings. 40(10) 1816–1824.

Beier R. A., Smith M. D. and Spitler J. D. (2011). Reference data sets for vertical borehole ground heat exchanger models and thermal response test analysis. Geothermics. 40(1) 79-85.

BniLam N. and Al-Khoury R. (2016). Transient heat conduction in an infinite medium subjected to multiple cylindrical heat sources: An application to shallow geothermal systems. Renewable Energy 97(2016) 145-154.

BniLam N. and Al-Khoury R. (2017). A spectral element model for nonhomogeneous heat flow in shallow geothermal systems. International Journal of Heat and Mass Transfer 104(2017) 703-717.

BniLam N., Al-Khoury R., Shiri A. and Sluys L. J. (2018). A semi-analytical model for detailed 3D heat flow in shallow geothermal systems. International Journal of Heat and Mass Transfer 123(2018) 911-927.

Bonnans J. F., Gilbert J. C., Lemaréchal C. and Sagastizábal C. A. (2006). Numerical optimization: Theoretical and practical aspects. Universitext.

Brown G. O. (2002). The history of the Darcy-Weisbach equation for pipe flow resistance. Environmental and Water Resources History Journal 38(7) 34-43.

Bujok P., Grycz D., Klempa M., Kunz A. and Porzer M. (2014). Assessment of the influence of shortening the duration of TRT (thermal response test) on the precision of measured values. Energy 64 (2014) 120-129

Busso A., Georgiev A. and Roth P., (2003). Underground thermal energy storage – first thermal response test in south America. RIO 3 - World Climate and Energy Event, 1-5 December 2003, Rio de Janeiro, Brazil.

Byrd, R.H., Hribar M. E., and Nocedal J. (1999). An Interior Point Algorithm for Large-Scale Nonlinear Programming. SIAM Journal on Optimization, Vol 9, No. 4, pp. 877–900.

Carslaw H. S. and Jaeger J. C. (1947). Heat conduction in solids. Claremore Press, Oxford University Press, London, UK.

Carslaw H. S. and Jaeger J. C. (1959). Conduction of Heat in Solids. (2nd ed). Oxford University Press, London, UK.

Choi W. and Ooka R. (2015). Interpretation of disturbed data in thermal response tests using the infinite line source model and numerical parameter estimation method. Applied Energy 148(2015) 476–488.

Claesson J. and Javed S. (2011). An analytical method to calculate borehole fluid temperatures for time-scales from minutes to decades. ASHRAE Transactions 117(2) 279-288.

Colebrook C. (1938). Turbulent flow in pipes, with particular reference to the transition region between the smooth and rough pipe laws. Journal of the Institution of Civil Engineers, London 11(4) 133-156.

COMSOL (2019). http://www.comsol.com/comsol-multiphysics (accessed November 2019).

Conti P. Sustainable design of ground-source heat pump systems: optimization of operative life performances: Universit`a di Pisa; 2015.

Cui Y., Zhu J., Twaha S. and Riffat S. (2018). A comprehensive review on 2D and 3D models of vertical ground heat exchangers. Renewable and Sustainable Energy Reviews 94(2018) 84-114.

Deerman J.D. and Kavanaugh S.P. (1991). Simulation of vertical U-tube ground-coupled heat pump systems using the cylindrical heat source solution. ASHRAE Transactions. 97 (1) 287-295.

Diao N., Li Q. and Fang Z. (2004). Heat transfer in ground heat exchangers with groundwater advection. International Journal of Thermal Sciences 43(12) 1203-1211.

Diersch, H. J. G., Bauer D., Heidemann W., Ruhaak W. and Schatzl P. (2011a). Finite element modeling of borehole heat exchanger systems: Part 1. Fundamentals. Computers and Geosciences 37(8), 1122-1135.

Diersch, H. J. G., Bauer D., Heidemann W., Ruhaak W. and Schatzl P. (2011b). Finite element modeling of borehole heat exchanger systems Part 2. Numerical simulation. Computers and Geosciences 37(8), 1136-1147.

Doyle J. F. (1988). Spectral analysis of coupled thermoelastic waves. Journal of Thermal Stresses 11 (3) 175–185.

Doyle J. F. (1997). Wave Propagation in Structures: Spectral Analysis Using Fast Discrete Fourier Transforms. Springer-Verlag, New York.

EED (2019): https://buildingphysics.com/eed-2/ . (accessed November 2019).

Erol S., Hashemi M. A. and François B. (2015). Analytical solution of discontinuous heat extraction for sustainability and recovery aspects of borehole heat exchangers. International Journal of Thermal Sciences 88 (2015) 47-58.

Eskilson P. (1987), Thermal Analysis of Heat Extraction Boreholes. Doctoral Thesis, University of Lund, Department of Mathematical Physics. Lund, Sweden.

Eskilson P. and Claesson J. (1988). Simulation model for thermally interacting heat extraction boreholes. Numerical Heat Transfer 13 (1988) 149–165.

European Commission (2016). Communication from The Commission to the European Parliament, The Council, The European Economic and Social Committee and The Committee of The Regions: An EU Strategy on Heating and Cooling. Brussels, 16.2.2016

Fagan M. J. (1992). Finite Element Analysis: Theory and Practice, Longman Singapore, Berlin.

FEFLOW (2019): https://www.mikepoweredbydhi.com/products/feflow/geothermal-energy .(accessed November 2019).

Focaccia S., Tinti F. and Bruno R. (2013). A software tool for geostatistical analysis of thermal response test data: GA-TRT. Computers and Geosciences 59(2013)163–170.

Fujii H., Okubo H., Nishi K., Itoi R., Ohyama K. and Shibata K. (2009). An improved thermal response test for U-tube ground heat exchanger based on optical fiber thermometers. Geothermics 38(2009) 399–406

GLHEPRO (2019): https://hvac.okstate.edu/glhepro/overview (accessed November 2019).

Gu Y. and O'Neal D. L. (1995). An analytical solution to transient heat conduction in a composite region with a cylindrical heat source. ASME Journal of Solar Energy Engineering 117(3) 242-248.

Gultekin A., Aydin M. and Sisman A. (2016). Thermal performance analysis of multiple borehole heat exchangers. Energy Conversion and Management 122 (2016) 544–551.

He M., Rees S. and Shao L. (2011). Simulation of a domestic ground source heat pump system using a three-dimensional numerical borehole heat exchanger model. Journal of Building Performance Simulation. 4 (2) 141–155.

Horizon Projects (2010). https://www.geothermalresearch.eu/active-geothermal-projects/horizon2020-projects/ (accessed November 2019)

Imbrahim C. (2005). Simplified equations calculates head losses in commercial pipes. The Journal of American Science 1(1), 1-2.

IMSL(2019) Numerical Libraries http://www.roguewave.com/products-services/imsl-numerical-libraries (accessed November 2019)

Ingersoll L. R., Zobel O. J. and Ingersoll A. C. (1954). Heat Conduction with Engineering, Geological, and other Applications Revised edition. University of Wisconsin press.

Javed S. and Claesson J. (2011). New analytical and numerical solutions for the short-term analysis of vertical ground heat exchangers. ASHRAE Trans. 117(1) 3–12.

Jin H, Spitler J. (2002). A Parameter Estimation Based Model of Water-to-Water Heat Pumps for Use in Energy Calculation Programs. ASHRAE Transactions. Volume 108.

Kavanaugh S. P. and Rafferty K. (1997). Ground-Source Heat Pumps. Design of Geothermal Systems for Commercial and Institutional Buildings, ASHRAE, Atlanta.

Kurevija T., Vulin D. and Krapec V. (2012). Effect of borehole array geometry and thermal interferences on geothermal heat pump system. Energy Conversion and Management 60 (2012) 134–142.

Lamarche L. and Beauchamp B. (2007). New solutions for the short-time analysis of geothermal vertical boreholes. International Journal of Heat and Mass Transfer 50 (2007) 1408–1419.

Lee C. K and Lam H. N. (2008). Computer simulation of borehole ground heat exchangers for geothermal heat pump systems. Renewable Energy 33(6), 1286-1296.

Lee C. K. (2011). Effects of multiple ground layers on thermal response test analysis and ground-source heat pump simulation. Applied Energy 88 (2011) 4405–4410

Lee U. (2009). Spectral Element Method in Structural Dynamics. Wiley, Singapore.

Li M. and Lai A. C. (2012). Parameter estimation of in-situ thermal response tests for borehole ground heat exchangers. International Journal of Heat and Mass Transfer 55(9–10), 2615–2624.

Li M. K. and Fang Z. (2016). Analytical methods for thermal analysis of vertical ground heat exchangers. Woodhead publishing Edition. Woodhead Publishing Series in Energy, Rees, Simon, pp. 157–183.

Li M., Li P., Chan V. and Lai A. C. K. (2014). Full-scale temperature response function (G-function) for heat transfer by borehole ground heat exchangers (GHEs) from sub-hour to decades. Applied Energy 136 (2014) 197–205.

Maple (2019), http://www.maplesoft.com/products/maple/ (accessed November 2019).

Marcotte B. and Bernier M. (2019). Experimental validation of a TRC model for a double U-tube borehole with two independent circuits. Applied Thermal Engineering 162 (2019) 114229.

Marcotte D. and Pasquier P. (2008a). Fast fluid and ground temperature computation for geothermal ground-loop heat exchanger systems. Geothermics 37(2008) 651– 665.

Marcotte D. and Pasquier P. (2008b). On the estimation of thermal resistance in borehole thermal conductivity test. Renew. Energy 33(11), 2407–2415.

Marcotte D., Pasquier P., Sheriff F. and Bernier M. (2010). The importance of axial effects for borehole design of geothermal heat-pump systems. Renewable Energy 35(4) 763–770.

Marquardt D. (1963). "An Algorithm for Least-Squares Estimation of Nonlinear Parameters". SIAM Journal on Applied Mathematics. 11 (2).

MathWorks, (2019). https://nl.mathworks.com/help/optim/ug/fmincon.html (accessed November 2019).

MATLAB(2019). https://nl.mathworks.com/campaigns/products/ppc/google/matlab-trialrequest.html?s_eid=ppc_2537840002&q=matlab (accessed November 2019)

Mertins A. (1999). Signal Analysis: Wavelets, Filter Banks, Time-Frequency Transforms and Applications. John Wiley & Sons Ltd.

Mogensen P. (1983). Fluid to duct wall heat transfer in duct system heat storages. Document Swedish Council for Building Research 16(1983) 652-657.

Molina-Giraldo N., Bayer P., Blum P., Zhu K. and Fang Z. (2011). A moving finite line source model to simulate borehole heat exchangers with groundwater advection. International Journal of Thermal Sciences. 50(12) 2506-2513.

Moody L. F. (1944). Friction factors for pipe flow. Transactions ASME 66 (8), 671.

Nabi M. and Al-Khoury R. (2012a). An efficient finite volume model for shallow geothermal systems. Part I: Model formulation. Computers and Geosciences. 49(2012) 290-296.

Nabi M. and Al-Khoury R. (2012b). An efficient finite volume model for shallow geothermal systems—Part II: Verification, validation and grid convergence. Computers and Geosciences. 49(2012) 297-307.

Ozgener O, Hepbasli A (2007). Modeling and performance evaluation of ground source (geothermal) heat pump systems. Energy and Buildings. Volume 39, Issue 1, Pages 66-75.

Ozudogru T. Y., Olgun C. G. and Senol A. (2014). 3D numerical modeling of vertical geothermal heat exchangers. Geothermics, 51(2014) 312-324.

Pasquier P. (2015). Stochastic interpretation of thermal response test with TRT-S Interp. Computers and Geosciences 75(2015)73–87

Pasquier P. (2018). Interpretation of the first hours of a thermal response test using the time derivative of the temperature. Applied Energy 213 (2018) 56–75

Pasquier P. and Marcotte D. (2013). Efficient computation of heat flux signals to ensure the reproduction of prescribed temperatures at several interacting heat sources. Applied Thermal Engineering 59(2013) 515-526.

Pasquier P. and Marcotte D. (2014). Joint use of quasi- 3D response model and spectral method to simulate borehole heat exchanger. Geothermics 51(2014)281–299.

Pasquier P., Zarrella A. and Marcotte D. (2019). A multi-objective optimization strategy to reduce correlation and uncertainty for thermal response test analysis. Geothermics 79(2019) 176-187.

Patera A. (1984). A spectral element method for fluid dynamics: Laminar flow in a channel expansion. Journal of Computational Physics 54 (3) 468–488.

Pitts D. and Sissom L. (1997). Schaum's Outline of Heat Transfer. 2nd Edition, Singapore; McGraw-Hill.

Pruess K., Oldenburg C. and Moridis G. (1999). TOUGH2 User's Guide, Version 2.0. Lawrence Berkeley National Laboratory Report LBNL-43134, Berkeley, CA, November 1999.

Raymond J. and Lamarche L. (2013). Simulation of thermal response tests in a layered subsurface. Applied Energy 109 (2013) 293–301.

Raymond J., Therrien R. and Gosselin L. (2011). Borehole temperature evolution during thermal response tests. Geothermics 40 (2011) 69–78

Rees S. J. (2016). An introduction to ground-source heat pump technology. Woodhead publishing Edition. Woodhead Publishing Series in Energy, Rees, Simon, pp. 1–25.

Romeo E., Royo C. and Monzón A. (2002). Improved explicit equations for estimation of the friction factor in rough and smooth pipes. Chemical Engineering Journal 86(2002) 369–374.

Rui Y., Garber D. and Yin M. (2018). Modelling ground source heat pump system by an integrated simulation programme. Applied Thermal Engineering 134 (2018) 450–459.

Saeid S., Al-Khoury R., Hamidreza M. N. and Michael A. H. (2015). A prototype design model for deep low-enthalpy hydrothermal systems. Renewable Energy 77(2015) 408-422.

Sanner B., Hellström G., Spitler J. and Gehlin S. (2005). Thermal Response Test – Current Status and World-Wide Application. Proceedings World Geothermal Congress. Antalya, Turkey.

Sanner B., Mands E., Sauer M. K. and Grundmann E. (2008). Thermal response test, a routine method to determine thermal ground properties for GSHP design. 9th International IEA Heat Pump Conference, 20 – 22 May 2008, Zürich, Switzerland.

Sauer M., Sanner B., Mands E., Grundmann E. and Fernández A. (2012). Thermal Response Test: Practical experience and extended range of application. The 12th International Conference on Energy Storage. Lleida, Spain.

Siedel B., Sartre V. and Lefevre F. (2015). Complete analytical model of a loop heat pipe with a flat evaporator. International Journal of Thermal Sciences 89(2015) 372–386.

Signorelli S., Bassetti S., Pahud D. and Kohl T. (2007). Numerical evaluation of thermal response tests. Geothermics 36(2) 141-166.

Spitler J. D. and Gehlin S. E. A. (2015). Thermal response testing for ground source heat pump systems—An historical review. Renewable and Sustainable Energy Reviews 50(2015)1125–1137.

Spitler, J. D. (2000). GLHEPRO -- A Design Tool for Commercial Building Ground Loop Heat Exchangers. Proceedings of the Fourth International Heat Pumps in Cold Climates Conference, Aylmer, Québec. August 17-18, 2000.

Spitler, J. D., Yavuzturk C. and Rees S. J. (2000). In Situ Measurement of Ground Thermal Properties. Proceedings of Terrastock 2000, Vol. 1, Stuttgart, pp. 165-170.

Sutton M. G., Nutter D. W. and Couvillion R. J. (2003). A ground resistance for vertical bore heat exchangers with groundwater flow. Journal of Energy Resources Technology 125(2003) 183-189.

Van Genuchten M. Th. and Alves W. J., (1982). Analytical solutions of the one-dimensional convective-dispersive solute transport equation. U.S. Department of Agriculture, Technical Bulletin No. 1661.

Vélez Márquez M.I., Raymond J., Blessent D., Philippe M., Simon N., Bour O. and Lamarche L. (2018). Distributed Thermal Response Tests Using a Heating Cable and Fiber Optic Temperature Sensing. Energies 11(11), 3059.

Verrax P. (2018). Model Predictive Control Applied to Ground Source Heat Pumps. Stockholm: KTH Royal Institute of Technology. Master thesis.

Wagner R. and Clauser C. (2005). Evaluating thermal response tests using parameter estimation for thermal conductivity and thermal capacity. Journal of Geophysics and Engineering 2(4) 349–356.

Wagner V., Blum P., Kübert M. and Bayer P. (2013). Analytical approach to ground water influenced thermal response tests of grouted borehole heat exchangers. Geothermics 46(2013) 22–31.

Weigand B. (2004). Analytical methods for heat transfer and fluid flow. By Springer.

Witte H. J. L. (2013). Error analysis of thermal response tests. Applied Energy 109(2013) 302–311.

Witte H. J. L. (2016). In situ estimation of ground thermal properties. Advances in Ground-Source Heat Pump Systems. Woodhead publishing Edition. Woodhead Publishing Series in Energy, Rees, Simon, pp. 97–116.

Witte H. J. L. ,van Gelder G. J. and Spitler J. D. (2002). In Situ Measurement of Ground Thermal Conductivity: A Dutch Perspective. ASHRAE Transactions. 108(2002) Part I.

Witte H. J. L. and van Gelder A.J. (2006). Geothermal Response Tests using Controlled Multi-Power Level Heating and Cooling Pulses (MPL-HCP): Quantifying Ground Water Effects on Heat Transport Around a Borehole Heat Exchanger. SiteSeer.

Yavuzturk C., Spitler J. and Rees S., (1999). A transient two-dimensional finite volume model for the simulation of vertical U-tube ground heat exchangers, ASHRAE Transactions 105 (2), 465–474.

You T., Li X., Cao S. and Yang H. (2018). Soil thermal imbalance of ground source heat pump systems with spiral-coil energy pile groups under seepage conditions and various influential factors. Energy Conversion and Management 178 (2018) 123–136.

Zanchini E. and Pulvirenti B. (2013). An analytical solution for the temperature field around a cylindrical surface subjected to a time dependent heat flux. International Journal of Heat and Mass Transfer 66(2013) 906-910.

Zeng H. Y., Diao N. R., and Fang Z. H. (2002). A finite line-source model for boreholes in geothermal heat exchangers. Heat Transfer—Asian Research, 31(7), 558-567.

Zeng H., Diao N. and Fang Z. (2003). Heat transfer analysis of boreholes in vertical ground heat exchangers. International Journal of Heat and Mass Transfer 46 (2003) 4467–4481.

Zhang C., Guo Z., Liu Y., Cong X. and Peng D. (2014). A review on thermal response test of ground-coupled heat pump systems. Renewable Sustainable Energy Rev; 40:851–67.

Zhang L., Huang G., Zhang Q. and Wang J. (2018). An hourly simulation method for the energy performance of an office building served by a ground-coupled heat pump system. Renewable Energy 126(2018) 495-508.

Zhao Z., Shen R., Feng W., Zhang Y. and Zhang Y. (2018). Soil Thermal Balance Analysis for a Ground Source Heat Pump System in a Hot-Summer and Cold-Winter Region. Energies 11(5) 1206.

Acknowledgements

Finishing this thesis has been my ultimate goal for the last few years. It was a very rewarding, incredibly tough and surprisingly amazing experience in the way that it shaped me to be the person that I am today. I have learnt that through dedication and hard work I can achieve even more than I thought I could. Nevertheless, finalizing this thesis would never have been possible without the help and the support of the wonderful people around me.

The first person that I wish to acknowledge is my co-promotor, my mentor and my friend **Dr. Rafid Al-Khoury**. Finishing this thesis would have never been possible without Rafid. He always provided me with support, day and night. We shared the joyful moments when the model worked, and we brainstormed together when it didn't work. He was extremely enthusiastic regarding our research and always encouraged me to achieve more. I learnt from him how to be passionate and critical about my research. Many thanks to Rafid ánd his family for their support and friendship.

I would like to thank my promotor **Prof. dr. Bert Sluys** for giving me the opportunity to join his research group. From the first day on, he always supported and encouraged me. His insightful advice on my research has been very precious to me.

Besides my supervisors, I would like to thank my friends **Luis Magalhaes Pereira** and **Mehdi Musivand Arzanfudi**, both whom were my colleagues at TU Delft. Discussing research problems with them was often the way for me to find solutions, and our meetings outside of work were often the way for me to wind down and relax.

I would also like to thank my colleagues in the IDLab and the Cosys-lab research groups (University of Antwerp). In particular, I want to thank **Prof. Maarten Weyn** and **Prof. Jan Steckel**. Maarten's support was important to me in finalizing this thesis, and Jan was always there whenever I needed his advice. A lot of thanks to you both.

During my first year in The Netherlands, my uncle and aunt, **Sadeq** and **Ibtisam**, took me into their home and treated me as a part of their family. They helped me settle into my new surroundings. Thank you for all that you did! Without your sandwiches I would have starved in this first year.

I also want to thank my family-in-law: **John**, **Sylvia**, **Giel**, **Anniek**, **Ruben**, **Maaike** and **Marijn**. John, I enjoy our talks about watches and technology. I almost did not have the time to finish my PhD after you introduced me to CataWiki. Sylvia and Giel, thank you so much for always making me feel welcome in your home and for having the best Dutch

cookies. Anniek, Ruben and the boys; I love your sense of humor and thank you for always showing an interest in my work. And Maaike and Marijn; thanks for cheering with me when one of our articles got published, and for distracting me with FIFA when the situation called for it.

I cannot begin to describe the role that my family in Baghdad has played in all of this, even though they are far away: My parents **Hussein** and **Fadeelah**, and my brothers and sisters **Weyam**, **Ali**, **Hayder** and **Reyam**, have all been there for me throughout. Before I started my PhD, I took a trip together with just my parents, which has since remained a memory of great comfort and joy to all of us. I do not see them as often as I wish, but our phone calls are always the highlight of any day. To both my parents I want to say: I love you so much and thank you for all that you have done to support me.
Thank you also to my sister Weyam, who is the most loving and caring person I know. To Ali, you are the greatest storyteller and never fail to make me laugh; thank you for keeping me in the loop on all the heaviest and greasiest of Baghdadi cuisine. Hayder, I offer you so many thanks for all your help over the years and for tirelessly braving the Iraqi bureaucracy for me when I could not be there to do it myself. Finally, to Reyam, my baby sister: thank you for being the loving person that you are and for always being there when I visit our home.
I am most grateful that the distance from my family has not resulted in a distance in our connection; rather I feel closer and more attached to them than ever before.

One year into my PhD I met **Saskia**, who is now my wife, which is an event that I feel defines this period of my life. Ever since we met, she has become my love, my friend and my buddy. I clearly remember meeting and admiring her for the first time, and thinking she was way out of my league. But for reasons unknown to me, she decided to stick around, for which I am deeply grateful! She is smart, wise, independent and likes sweets more than she should (the sweets-thing is a direct quote, so I will not get in trouble for mentioning this). Her passion to read amazed me from the start and she introduced me to many new universes such as Harry Potter, Star Wars and Star Trek. We face everything together and we have so much fun, laughing at random inside jokes which make sense to no one but us. Saskia, thank you very much for all the effort that you spent to make this thesis possible. Thank you, a lot, for being my private English editor and English to Dutch translator, even though it sometimes made you grumpy. My Sas, I cannot imagine what my life would be like without you.

Noori Bni Lam

Breda, Jan 2020

List of Publications

1. BniLam N. and Al-Khoury R. (2016). A spectral model for heat transfer with friction heat gain in geothermal borehole heat exchangers. Applied Mathematical Modelling Volume 40, Issues 15–16, Pages 7410-7421.

2. BniLam N. and Al-Khoury R. (2016). Transient heat conduction in an infinite medium subjected to multiple cylindrical heat sources: An application to shallow geothermal systems. Renewable Energy, Volume 97, Pages 145-154.

3. BniLam N. and Al-Khoury R. (2017). A spectral element model for nonhomogeneous heat flow in shallow geothermal systems. International Journal of Heat and Mass Transfer Volume 104, Pages 703-717.

4. BniLam N., Al-Khoury R., Shiri A. and Sluys L.J., (2018). A semi-analytical model for detailed 3D heat flow in shallow geothermal systems. International Journal of Heat and Mass Transfer Volume 123, Pages 911-927.

5. BniLam N., Al-Khoury R. (2019). Analysis of short-to-long term heat flow in GSHP systems based on heat pump power. Applied Thermal Engineering. Available online 19 October 2019, 114561.

6. BniLam N., Al-Khoury R. (submitted). Parameter Identification Algorithm for Ground Source Heat Pump Systems.

About the Author

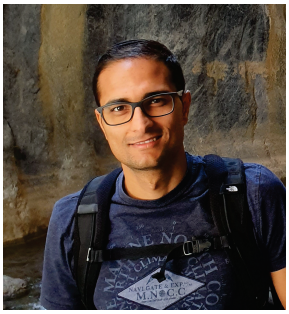

Noori Hussein Noori Bni Lam was born on the 13th of May 1987 in Baghdad, Iraq. He received his B.Sc. and his M.Sc. degrees in Electronics and Communication Engineering from Baghdad University, Iraq, in 2009 and 2012, respectively. He occupied two positions in Iraq, the first was as a communication engineer at the National Communications and Media Commission (CMC) until 2012. The second position was as a teacher assistant at Al-Mansour University College until 2014.

In late 2014, Noori enrolled in his first PhD position at Delft University of Technology, The Netherlands. Here he was a part of the Materials, Mechanics, Management and Design (3MD) department. He developed a spectral element model to simulate the thermal response of Ground Source Heat Pump (GSHP) systems.

Noori is currently a teacher assistant at the University of Antwerp, Belgium, where he is also pursuing his second PhD degree at the imec-IDLab research group. His research there focuses on estimating the Angle of Arrival (AoA) of the received signals. Furthermore, his main objective is to develop AoA-based localization systems for Internet of Thing (IoT) applications.